ANTENNA SUBTRACTIVE-MASK SHAPE SYNTHESIS INCORPORATING MODEL ORDER REDUCTION

JACOB MARTIRE

Thesis submitted to the University of Ottawa
in partial fulfillment of the requirements for the degree of

Doctorate in Philosophy
in Electrical and Computer Engineering

School of Electrical Engineering and Computer Science
Faculty of Engineering
University of Ottawa

Abstract

Antenna shape synthesis is an advanced design methodology that treats the geometrical shape of radiating structures as free variables, constrained solely by the underlying electromagnetic physics. This approach significantly expands the antenna design space and enables the discovery of high-performance structures that differ from conventional antenna geometries. However, the prohibitive computational cost associated with repeated full-wave simulations during the optimization process has limited the practical adoption of shape synthesis in industry.

This thesis addresses this challenge by introducing model order reduction (MOR) techniques to accelerate the electromagnetic analysis within shape synthesis workflows. Specifically, a novel adaptation of MOR is developed and applied to the electric field integral equation (EFIE) discretized via the Method of Moments (MoM) using the spatial-domain free-space Green's function for perfectly conducting objects. The proposed reduced-order model achieves substantial reductions in computational time compared to traditional MoM solutions, with the efficiency gains becoming particularly pronounced as the number of frequency points increases.

Leveraging this accelerated forward solver, a new subtractive mask-based shape synthesis method is proposed. In this approach, a genetic algorithm systematically identifies and removes groups of basis functions corresponding to geometric regions (masks) on the antenna mesh, while enforcing complex multi-objective performance criteria. The resulting methodology enables the design of unconventional, high-performance antennas in a matter of hours or days rather than weeks, markedly improving the feasibility of shape synthesis for practical applications.

Furthermore, the developed MOR framework is shown to be effective beyond shape synthesis. A novel antenna-circuit co-simulation technique is presented that incorporates the driving beamforming circuitry directly into a single matrix formulation.

The effectiveness of both the reduced-order model and the proposed synthesis and co-simulation techniques is demonstrated through multiple numerical examples, confirming significant improvements in computational efficiency while maintaining high accuracy. This work contributes new tools that enhance the practicality of advanced antenna design methods and opens pathways for the more widespread industrial application of antenna shape synthesis.

Acknowledgements

I would like to express the utmost gratitude to my supervisors, Prof. Derek McNamara and Prof. Emad Gad, for their expertise and guidance throughout the entirety of my graduate studies. Their encouragement and support have been truly unwavering.

Of course, I would also like to thank my parents for everything they have done for me over the years. Hopefully this thesis will convince them there is more to antenna design than bending coat hangers.

Table of Contents

List of Figures

List of Tables

List of Acronyms

ABS	Adaptive Binary Search
AR	Axial Ratio
BFN	Beamforming Network
BSIM	Berkely Short-Channel IGFET Model
BW	Beamwidth
CEM	Computational Electromagnetic
DGTD	Discontinuous Galerkin Time-Domain
DSP	Digital Signal Processing
EFIE	Electric Field Integral Equation
EM	Electromagnetic
FB	Fractional Bandwidth
FEM	Finite Element Method
FETD	Finite-Element Time-Domain
GA	Genetic Algorithm
HPBW	Half-Power Beamwidth
HSPICE	High-Performance Simulation Program with Integrated Circuit Emphasis
KCL	Kirchhoff's Current Law
MNA	Modified Nodal Analysis
MoM	Method of Moments
MOR	Model Order Reduction
NMOS	N-Type Metal Oxide Semiconductor
OMC	Odd Minimum Check
PEC	Perfect Electrical Conductor
PMOS	P-Type Metal Oxide Semiconductor
PWTD	Plane Wave Time Domain
RF	Radio Frequency
ROM	Reduced Order Model
RWG	Rao-Wilton-Glisson
SMSS	Subtractive-Mask Shape Synthesis
SMW	Sherman-Morrison-Woodbury
SVD	Singular Value Decomposition
TD-AIM	Time-Domain Adaptive Integral Method
VF	Vector Fitting

CHAPTER 1

Introduction

The long-term goal to which the research described in this thesis contributes towards is in the acceleration of the automated antenna shape synthesis process to the point where it becomes viable in engineering practice. It does so in three ways: (a) By developing a reduced order model for the full-wave field simulation of conducting antennas that is essential in such shape synthesis. (b) By developing a new technique to incorporate this new field-MOR capability with existing circuit analysis methods, which will be an asset in future integrated antenna work. (c) By proposing and implementing a novel subtractive-mask shape synthesis (SMSS) algorithm.

The method of moments (MoM) is a widely used numerical technique in computational electromagnetics for finding the frequency domain solution to electromagnetic (EM) scattering problems [PETE 07]. It is often the preferred method of analyzing antennas due its ability to handle unbounded domains. This is because the MoM solves for the current distribution on the scatterers using an integral equation in which a Green's function accounts for wave propagation over any distance [PETE 07]. The current distribution can then be used to compute field quantities, resulting in a fixed problem size for a given geometry. This is in contrast to another widely used numerical technique known as the finite element method (FEM) which solves for the fields directly but requires the discretization of the medium in which the fields are desired, yielding a problem size that can rapidly grow far beyond that of the MoM. Despite the suitable nature of the MoM to antenna problems, the computational time required to run many EM simulations, as is necessary in the design of any antenna system, but particularly in optimization-type problems such as the shape synthesis of radiating structures, has proven to be restrictive. The first item of research presented in this thesis is thus on improving the efficiency of MoM simulations, in particular those of EM scattering from perfect electrical conductors (PEC). This goal is achieved by substantially adapting model order reduction (MOR) techniques commonly used in circuit simulation to the MoM to construct an approximate, but accurate, problem of significantly lesser size. The reduced order model can in turn be solved very quickly at any number of frequencies. It is this novel approach that forms the groundwork for the other two contributions of this research, namely the new antenna-circuit co-simulation technique and subtractive-mask shape synthesis method. The structure of this work progresses as described below, where everything beyond *Chapter 2* constitutes the new contribution.

Chapter 2 covers background material relevant to the topics of this thesis described in later chapters, allowing for this work to be correctly placed amongst the existing literature. The chapter begins by covering antenna fundamentals and important performance indices that will be referred to throughout. This is followed by a brief, but mathematically comprehensive, outline of the particular MoM formulation of interest. Then, an overview of the modified nodal analysis (MNA) circuit representation is presented, followed by an extensive review of the MOR technique in the context of linear circuit analysis, employing the aforementioned circuit representation. A review of the MOR technique is then expanded upon when handling circuits with multiple ports. The mathematical portion of the chapter is then concluded by a brief summary of the Chebyshev approximation of functions, which will prove to be an important stepping stone in the MoM-MOR formulation of *Chapter 3*, along with a short overview of the vector fitting technique that will be used in *Chapter 4*. The final three sections of this chapter then cover existing literature pertaining to the application of MOR to the MoM, field-circuit co-simulation techniques, and shape synthesis methods for antennas.

Chapter 3 provides the new mathematical procedure and derivation for the application of MOR to the MoM formulation of EM scattering from PEC objects. The MoM matrix equation is first adapted using a Chebyshev approximation to suit the demands of the MOR technique. This approximation comes with drawbacks which are mitigated by a novel efficient MOR procedure devised specifically for this type of problem. The methodology is then verified for accuracy through two examples, one of small size and one of significantly larger size, to highlight the wide variety of problem that this method can handle. Furthermore, the computation time needed to compute these solutions for various numbers of frequencies are compared to traditional MoM simulation times, thereby fully characterizing the improved computational efficiency of the new MoM-MOR approach.

Chapter 4 then introduces a novel formulation for simultaneously simulating antenna arrays along with their feeding circuitry. This combines a MoM field solution along with the MNA circuit formulation for linear lumped elements into a single matrix equation that links the voltages from the circuit with those that drive the antenna elements along with the exchange of currents from the circuitry to the antenna via the feed locations. The result is a single matrix formulation that solves for all of the MNA circuit and MoM field unknowns at once, constituting a new method that is first detailed here. The method is also well-suited for MOR which proves again to offer a significant reduction in computation time, while also permitting the inclusion of nonlinear elements in the circuitry via a novel sequential co-simulation technique. Furthermore, the reduced order models of the antenna structures are circuit independent and can thus be connected with any circuit for a combined circuit/full-wave solution, potentially justifying the creation of a “bank” of reduced order models. The need for a simulation technique such as this one has stemmed from the ever-growing demand for higher frequency applications, resulting in tightly integrated arrays which do not easily allow for measurements at individual element ports due to limited access. It has thus become increasingly common for measurements to consider both the antenna array and its transceiver circuitry. The formulation described above is derived and tested for its accuracy. Examples validating this approach are also shown in this chapter.

Chapter 5 then details the subtractive-mask shape synthesis approach for antennas and explains its advantages over other techniques. This is a new synthesis approach that improves upon previous subtractive techniques by not necessitating a re-meshing of the structure between iterations, yielding substantial improvements in efficiency. Furthermore, the very large number of MoM analyses that must be performed in any thorough optimization problem such as this benefits perfectly from the field-MOR technique devised in *Chapter 3*. Three antenna optimization examples will be covered and used to highlight firstly both the speed and accuracy of using MOR, secondly the accuracy of the shaping approach itself via a fabricated design with measurements, and finally how this approach can comfortably handle problems with many optimization metrics and thus a complex objective function.

Chapter 6 concludes the thesis and provides a summary of the contributions that have been made, along with areas for future research.

CHAPTER 2

Review of Existing Background Concepts

2.1 INTRODUCTION

In order to place the work of this thesis in context and hence be able to indicate how it has made contributions to the field of antenna analysis and synthesis, the present chapter will cover relevant existing background concepts. It will begin by reviewing various antenna performance indices, followed by the moment method analysis of scattering from perfectly conducting objects. Then the fundamentals of MNA circuit formulation, the use of MOR in linear circuit analysis, and the expansion of MOR to multi-port linear circuits along with the clustered approach will be summarized. This chapter will then cover the Chebyshev approximation of functions over a specified interval, vector fitting, and finally a review of existing contributions pertaining to the application of MOR to the method of moments, existing field-circuit co-simulation methods, and existing shape synthesis methods for antennas, as follows:

- Section 2.2: Antenna Fundamentals and Performance Indices
- Section 2.3: Method of Moments Analysis of Electromagnetic Scattering from Perfectly Conducting Objects
- Section 2.4: Modified Nodal Analysis Circuit Formulation
- Section 2.5: Model Order Reduction in Linear Circuit Analysis
- Section 2.6: Multi-Port MOR and the Clustered Approach to MOR in Linear Circuit Analysis
- Section 2.7: Chebyshev Approximation
- Section 2.8: Vector Fitting

- Section 2.9: Existing Contributions Pertaining to the Application of MOR to Computational Electromagnetics

- Section 2.10: Field-Circuit Co-Simulation Methods

- Section 2.11: Shape Synthesis Methods for Antennas

Throughout this chapter, as well as in those that follow it, the bolding of symbols is used to indicate matrix quantities, while overlines are used to denote field vectors.

2.2 ANTENNA FUNDAMENTALS AND PERFORMANCE INDICES

2.2.1 Introductory Remarks

Antennas are structures designed to radiate or receive electromagnetic waves. They act as transformers that convert guided waves propagating through distributed circuits to radiated electromagnetic waves in the surrounding medium, or vice versa. As such, they are an integral part of any wireless system. The upcoming sections will define important antenna performance metrics which will be referred to at various points throughout this thesis. Such definitions can be found in a plethora of antenna textbooks (e.g. [BALA 05] and [VISS 12]).

2.2.2 Antenna Power Budget and Equivalent Circuit

Figure 2.2-1 (top) illustrates an antenna in transmit mode fed by a transmission line. A certain amount of incident power P_{inc} travels along the transmission line towards the antenna port depending on the matching between the transmitter and the transmission line. Upon reaching the antenna terminals, a mismatch between the transmission line and the antenna causes some of the incident power to be reflected P_{refl} back towards the transmitter. The remainder of the incident power P_{in} is accepted by the antenna. Figure 2.2-1 (bottom) shows the equivalent circuit of an antenna in transmit mode. Resistance R_{rad} models the power radiated by the antenna, resistance R_{loss} models the power lost on the antenna structure, and X_{in} is the reactance at the antenna port. The input impedance at the antenna port is thus

$$Z_{in} = (R_{rad} + R_{loss}) + jX_{in}. \tag{2.2-1}$$

The radiated power and power lost are thus

$$P_{rad} = \frac{1}{2}|I_{in}|^2 R_{rad} \tag{2.2-2}$$

and

$$P_{loss} = \frac{1}{2}|I_{in}|^2 R_{loss} \tag{2.2-3}$$

respectively, where I_{in} is the current at the antenna terminals as depicted in Figure 2.2-1. The reflection coefficient at the antenna input terminals and the voltage standing wave ratio are then defined, respectively, as

$$\Gamma_{in} = \frac{Z_{in} - Z_0}{Z_{in} + Z_0} \tag{2.2-4}$$

and

$$VSWR = \frac{1 + |\Gamma_{in}|}{1 - |\Gamma_{in}|} \tag{2.2-5}$$

where Z_0 is the characteristic impedance of the transmission line. A mismatch factor of $(1 - |\Gamma_{in}|^2)$ can then be used to relate the power accepted by the antenna to the power incident upon its terminals, namely

$$P_{in} = P_{inc} - P_{refl} = (1 - |\Gamma_{in}|^2)P_{inc}. \tag{2.2-6}$$

To lessen the amount of reflected power at the antenna port, a matching network is often designed and placed between the transmission line and the radiator. This matching network is then included as part of the antenna and thus the antenna terminals would now be situated between the transmission line and the matching network.

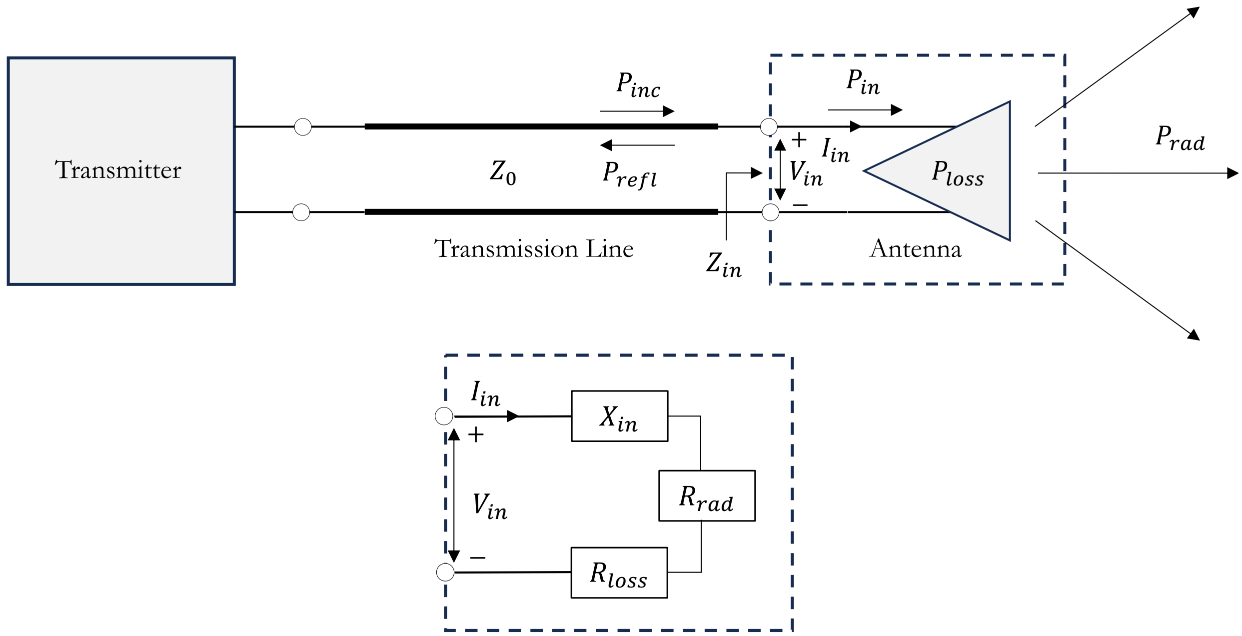

Figure 2.2-1. Transmit mode antenna power budget (top) and equivalent circuit (bottom).

2.2.3 Radiation Efficiency

The radiation efficiency of an antenna is the ratio of the power radiated by the antenna to the power it accepts. The radiation efficiency can thus be written as

$$e_{rad} = \frac{P_{rad}}{P_{in}} = \frac{P_{rad}}{P_{rad+}P_{loss}} = \frac{R_{rad}}{R_{rad+}R_{loss}}. \quad (2.2\text{-}7)$$

It is desirable to have $R_{rad} \gg R_{loss}$, and $R_{in} = R_{rad} + R_{loss}$ and X_{in} close to the characteristic impedance of the transmission line Z_0 and close to zero, respectively, to facilitate matching. If $X_{in} \approx 0$ at a particular frequency without a matching network, then it is said that the antenna is self-resonant at that frequency.

2.2.4 Electromagnetic Fields and the Poynting Vector

Any electromagnetic field can be expressed as its spherical coordinate (r, θ, ϕ) components as

$$\bar{E}(r,\theta,\phi) = E_r(r,\theta,\phi)\hat{r} + E_\theta(r,\theta,\phi)\hat{\theta} + E_\phi(r,\theta,\phi)\hat{\phi} \tag{2.2-8}$$

and

$$\bar{H}(r,\theta,\phi) = H_r(r,\theta,\phi)\hat{r} + H_\theta(r,\theta,\phi)\hat{\theta} + H_\phi(r,\theta,\phi)\hat{\phi}. \tag{2.2-9}$$

The complex Poynting vector at a point describes the power associated with an electromagnetic wave and is given as

$$\bar{\mathcal{S}}(r,\theta,\phi) = \frac{1}{2}\{\bar{E}(r,\theta,\phi) \times \bar{H}^*(r,\theta,\phi)\}. \tag{2.2-10}$$

The time-averaged Poynting vector represents the average power density at a given point (r,θ,ϕ) and is given by

$$\bar{S}(r,\theta,\phi) = \frac{1}{2}Re\{\bar{E}(r,\theta,\phi) \times \bar{H}^*(r,\theta,\phi)\}. \tag{2.2-11}$$

The average radiated power P_{rad} can then be determined by integrating the time-averaged radiated power density over a closed surface S that surrounds the antenna.

$$\begin{aligned} P_{rad} &= \oiint_S \bar{S}(r,\theta,\phi) \cdot d\bar{S} = \oiint_S \bar{S}(r,\theta,\phi) \cdot \hat{r}dS \\ &= \int_0^{2\pi}\int_0^{\pi} [\bar{S}(r,\theta,\phi) \cdot \hat{r}]\, r^2 sin\theta d\theta d\phi \end{aligned} \tag{2.2-12}$$

2.2.5 Field Regions

The space surrounding the antenna can be divided into three regions based on the behaviour of the fields. The reactive near-field region is that immediately surrounding the antenna where the fields mostly do not radiate but rather the reactive field predominates. The radiating near-field or Fresnel region lies just further than the reactive near-field region. In this region, the fields predominantly radiate, and the angular field distribution depends on the distance from the antenna. The far-zone region extends from the furthest point of the radiating near-field to infinity. In this region, the angular distribution of the fields are essentially independent of the distance from the antenna. For larger antennas, the radius at which the far-zone begins can be approximated by

$$R = \frac{2D^2}{\lambda} \tag{2.2-13}$$

where D is the largest linear dimension of the antenna. In the far-zone region the fields take the following forms.

$$E_r(r,\theta,\phi) = \hat{r} \cdot \bar{E}(r,\theta,\phi) \approx 0 \tag{2.2-14}$$

$$H_r(r,\theta,\phi) = \hat{r} \cdot \bar{H}(r,\theta,\phi) \approx 0 \tag{2.2-15}$$

$$E_\theta(r,\theta,\phi) = F_\theta(\theta,\phi)\frac{e^{-jkr}}{r} \tag{2.2-16}$$

$$E_\phi(r,\theta,\phi) = F_\phi(\theta,\phi)\frac{e^{-jkr}}{r} \tag{2.2-17}$$

The electric field in the far zone can thus be written in its entirety as

$$\bar{E}(r,\theta,\phi) = \bar{F}(\theta,\phi)\frac{e^{-jkr}}{r} = \left[F_\theta(\theta,\phi)\hat{\theta} + F_\phi(\theta,\phi)\hat{\phi}\right]\frac{e^{-jkr}}{r}. \tag{2.2-18}$$

Setting the radial components of the electric and magnetic fields to zero in Maxwell's curl equations results in the following relationship between the far-zone electric and magnetic fields

$$\bar{H}(r,\theta,\phi) = \frac{1}{\eta_o}\hat{r} \times \bar{E}(r,\theta,\phi) = \frac{1}{\eta_o}\hat{r} \times \bar{F}(\theta,\phi)\frac{e^{-jkr}}{r} \tag{2.2-19}$$

where $\eta_o = \sqrt{\mu_o/\varepsilon_o}$.

2.2.6 Far-Zone Quantities

When the observation point is in the far-zone of the antenna the average radiated power density in (2.2-11) becomes

$$\bar{S}(r,\theta,\phi) = S(r,\theta,\phi)\hat{r} = \frac{|\bar{F}(\theta,\phi)|^2}{2\eta_o r^2}\hat{r}. \tag{2.2-20}$$

The radiated power in the far-zone can then be found as

$$\begin{aligned} P_{rad} &= \int_0^{2\pi}\int_0^{\pi} S(r,\theta,\phi)\, r^2 sin\theta d\theta d\phi \\ &= \frac{1}{2\eta_o}\int_0^{2\pi}\int_0^{\pi} |\bar{F}(\theta,\phi)|^2\, sin\theta d\theta d\phi. \end{aligned} \tag{2.2-21}$$

The radiation intensity in a given direction is defined as the power radiated from an antenna per unit solid angle in that direction. Radiation intensity is a far-zone quantity and is related to the far-zone average radiated power density as

$$U(\theta,\phi) = r^2 S(r,\theta,\phi) = \frac{|\bar{F}(\theta,\phi)|^2}{2\eta_o}. \tag{2.2-22}$$

The radiated power in the far-zone can be written in terms of the radiation intensity as

$$P_{rad} = \int_0^{2\pi}\int_0^{\pi} U(\theta,\phi)\, sin\theta d\theta d\phi. \tag{2.2-23}$$

The radiation pattern of an antenna typically refers to the radiation intensity in decibels normalized to its maximum value occurring in direction (θ_o,ϕ_o).

$$U_{norm}^{[dB]}(\theta,\phi) = 10\log\left(\frac{|\bar{F}(\theta,\phi)|^2}{|\bar{F}(\theta_o,\phi_o)|^2}\right) = 20\log\left(\frac{|\bar{F}(\theta,\phi)|}{|\bar{F}(\theta_o,\phi_o)|}\right) \tag{2.2-24}$$

The directivity of an antenna is also a far-zone quantity. It is a measure of the amount of energy concentrated in the main beam of an antenna pattern or can mathematically be stated as the ratio of the radiation intensity in a particular direction to the spatially averaged radiation intensity U_{avg} of the antenna. Directivity is computed as follows.

$$D(\theta, \phi) = \frac{U(\theta, \phi)}{U_{avg}} = \frac{4\pi U(\theta, \phi)}{P_{rad}} \tag{2.2-25}$$

Directivity is measured in dBi, where the "i" refers to an isotropic radiator. An isotropic radiator is one which radiates equally in all directions. Such a radiator is not physically possible, however theoretically, its directivity would be 1, and thus directivity can be considered measured relative to it.

$$D^{[dBi]}(\theta, \phi) = 10 \log[D(\theta, \phi)] \tag{2.2-26}$$

Since the far-field vector in (2.2-22) can be split into both θ and ϕ components, so can the radiation intensity as $U_\theta(\theta, \phi)$ and $U_\phi(\theta, \phi)$, and thus the directivity. This yields partial directivities given by

$$D_\theta(\theta, \phi) = \frac{4\pi U_\theta(\theta, \phi)}{P_{rad}} \tag{2.2-27}$$

and

$$D_\phi(\theta, \phi) = \frac{4\pi U_\phi(\theta, \phi)}{P_{rad}}. \tag{2.2-28}$$

The directivity shown in (2.2-25) is thus considered to be the total directivity and is of course the sum of (2.2-27) and (2.2-28). Gain is a parameter very similar to directivity; however, it also considers any losses within the antenna. It is defined as

$$G(\theta, \phi) = e_{rad} D(\theta, \phi) \tag{2.2-29}$$

and has partial gains defined in the same manner as (2.2-29), however using the partial directivities in (2.2-27) and (2.2-28) instead of the total directivity.

2.2.7 Beamwidth

Beamwidth is defined as the angular separation between two points on opposite sides of the pattern maximum. Concerning antennas, several different beamwidth quantities are defined. The one which will be mentioned in this thesis, and which is one of the most widely used, is the half-power beamwidth (HPBW) or known equivalently as the 3 dB beamwidth. The HPBW is the angle between two directions in a plane containing the direction of the maximum beam whose radiation intensities are half that of the beam maximum. Figure 2.2-2 shows a generalized example of a normalized radiation intensity polar plot in which the HPBW is labelled.

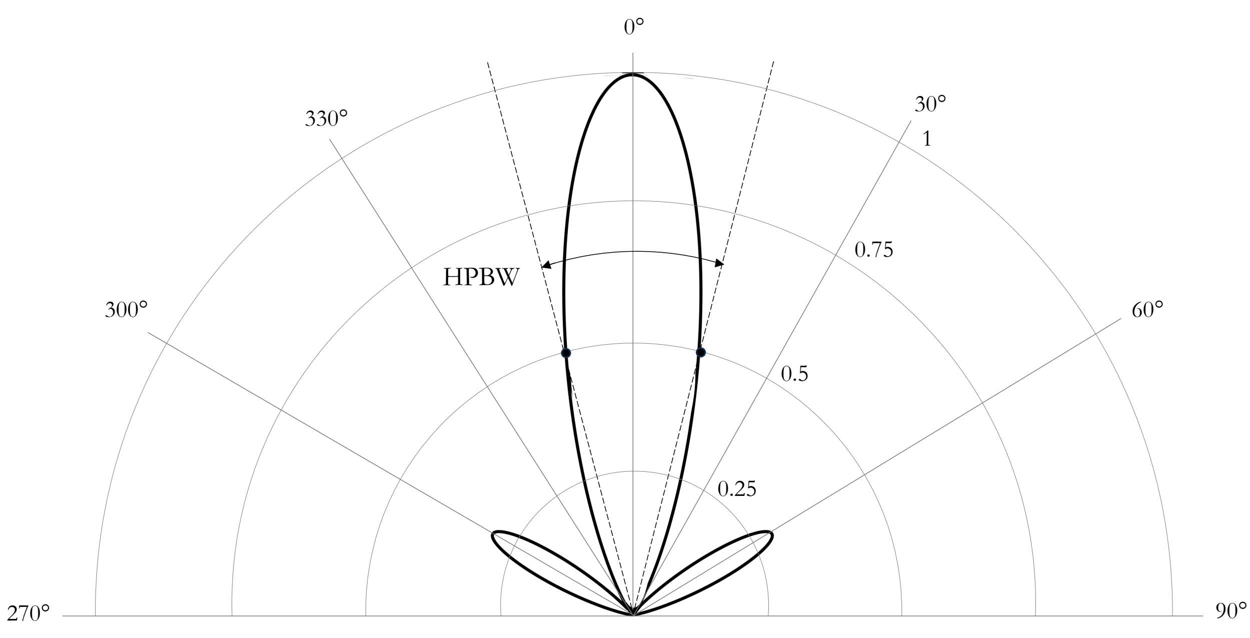

Figure 2.2-2. Illustration depicting HPBW using a linear scale.

2.2.8 Polarization

The polarization of an electromagnetic field is defined by the variation in the direction of the electric field vector with respect to time. More precisely, the polarization of the wave is traced by the locus of the tip of the electric field vector in time when viewed from the antenna at a fixed position in space (a plane transverse to $\hat{r}$). In the most general case, a wave will have an elliptical polarization, however in specific cases can also be linearly or circularly polarized. The axial ratio (AR) is the ratio of the major axis to the minor axis of the general polarization ellipse. AR is a quantity dependent on direction in space and can be calculated by first calculating the linear polarization ratio

$$\rho_l(\theta,\phi) = \frac{F_\phi(\theta,\phi)}{F_\theta(\theta,\phi)} \tag{2.2-30}$$

and then the circular polarization ratio

$$\rho_c(\theta,\phi) = \frac{1 + j\rho_l(\theta,\phi)}{1 - j\rho_l(\theta,\phi)}. \tag{2.2-31}$$

AR is then given by

$$AR(\theta,\phi) = \frac{|\rho_c(\theta,\phi)| + 1}{|\rho_c(\theta,\phi)| - 1}. \tag{2.2-32}$$

If $|AR(\theta,\phi)| = 1$ then the antenna is circularly polarized and if $|AR(\theta,\phi)| \to \infty$ then the polarization is linear. AR is also often expressed in decibels as

$$AR^{[dB]}(\theta,\phi) = 20\log[|AR(\theta,\phi)|]. \tag{2.2-33}$$

Antenna systems are typically designed with a specific polarization in mind for some directional coverage. This is referred to as the principal polarization or co-polarization. These systems however will always have some unwanted other polarization, referred to as the cross-polarization. The co- and cross-polarizations can be described by unit vectors $\hat{u}_{co}(\theta,\phi)$ and $\hat{u}_{cr}(\theta,\phi)$, respectively. These unit vectors must be orthogonal such that $\hat{u}_{co}(\theta,\phi) \cdot \hat{u}_{cr}^*(\theta,\phi) = 0$ and must have unity magnitudes. The co- and cross-polarized far-zone radiated fields are then

$$F_{co}(\theta,\phi) = \bar{F}(\theta,\phi) \cdot \hat{u}_{co}{}^{*}(\theta,\phi) \tag{2.2-34}$$

and

$$F_{cr}(\theta,\phi) = \bar{F}(\theta,\phi) \cdot \hat{u}_{cr}{}^{*}(\theta,\phi) \tag{2.2-35}$$

respectively, such that

$$\bar{F}(\theta,\phi) = F_{co}(\theta,\phi)\hat{u}_{co}(\theta,\phi) + F_{cr}(\theta,\phi)\hat{u}_{cr}(\theta,\phi). \tag{2.2-36}$$

2.2.9 Bandwidth

The bandwidth of an antenna is the range of frequencies over which the performance of the antenna is acceptable given particular criteria. The bandwidth of an antenna varies depending on the criteria in question and therefore what bandwidth is being referred to must be distinguished. This is the case as the range of frequencies in which an antenna conforms to acceptable bounds may not be the same for, say, the input reflection coefficient as it is for the total directivity. The absolute bandwidth of an antenna satisfying certain metrics between a minimum frequency f_{min} and a maximum frequency f_{max} is defined as

$$\Delta f = f_{max} - f_{min}. \tag{2.2-37}$$

The fractional bandwidth (FB) of the antenna is then defined as the ratio of the absolute bandwidth to the center frequency f_o and is typically expressed as a percentage.

$$FB = \frac{\Delta f}{f_o} = 2\left(\frac{f_{max} - f_{min}}{f_{max} + f_{min}}\right) \tag{2.2-38}$$

2.2.10 Mutual Coupling Between Two Antennas

Mutual coupling between antennas or between antenna elements in an array refers to the interactions these radiating elements have with each other. For example, in the case of a transmit array with two elements, when there is no mutual coupling, each element will radiate a wave which when added vectorially yields the overall radiation pattern of the array. When there is mutual coupling between these elements, some of the power transmitted by the first element will induce currents on the second element. These currents are partly accepted by the second element through its port, while the rest are scattered back towards the first element. The scattered waves from the second element back onto the first will distort the transmitted field distribution of the first element, as well as its input impedance. The effect of mutual coupling is then compounded further when additionally considering the effects of the second element in a manner similar to what was just discussed for the first element. It is thus often desirable to minimize the effect of mutual coupling to avoid these complications which effect antenna performance.

When analyzing the mutual coupling of any two antennas, they can be considered equivalently as a two-port network with currents and voltages defined at each port as is shown in Figure 2.2-3.

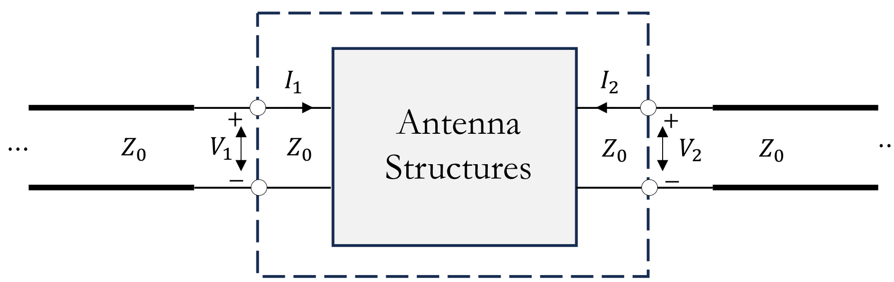

Figure 2.2-3. Two-port network representation of two antennas.

The interaction between the antennas can be described via admittance parameters relating their respective port quantities as

$$Y_{11} = \frac{I_1}{V_1}\bigg|_{V_2=0} \qquad Y_{12} = \frac{I_1}{V_2}\bigg|_{V_1=0} \qquad Y_{21} = \frac{I_2}{V_1}\bigg|_{V_2=0} \qquad Y_{11} = \frac{I_2}{V_2}\bigg|_{V_1=0}. \tag{2.2-39}$$

Admittance parameters are simple to compute using the method of moments since a port voltage can be easily set to zero in the right-hand vector of the matrix formulation in (2.3-20) covered in the next section. Admittance parameters can then be related to scattering parameters assuming real equal characteristic impedances Z_0 as

$$S_{11} = \frac{(1 - Z_0 Y_{11})(1 + Z_0 Y_{22}) + Z_0^2 Y_{12} Y_{21}}{\Delta} \quad (2.2\text{-}40)$$

$$S_{12} = \frac{-2Z_0 Y_{12}}{\Delta} \qquad S_{21} = \frac{-2Z_0 Y_{21}}{\Delta} \quad (2.2\text{-}41)$$

$$S_{22} = \frac{(1 + Z_0 Y_{11})(1 - Z_0 Y_{22}) + Z_0^2 Y_{12} Y_{21}}{\Delta} \quad (2.2\text{-}42)$$

where

$$\Delta = (1 + Z_0 Y_{11})(1 + Z_0 Y_{22}) - Z_0^2 Y_{12} Y_{21}. \quad (2.2\text{-}43)$$

2.3 METHOD OF MOMENTS ANALYSIS OF ELECTROMAGNETIC SCATTERING FROM PERFECTLY CONDUCTING OBJECTS

2.3.1 Introductory Remarks

The MoM is a numerical technique used to solve integral equation models of electromagnetic systems. The MoM solves for the current densities induced on scatterers which can then be used to compute secondary parameters such as the scattered and total electric and magnetic fields. This section will cover the particular MoM formulation relevant to this thesis.

2.3.2 Electric Field Integral Equation Formulation

This formulation will consider an electric field integral equation as its starting point, as magnetic field integral equations are only applicable to closed conducting objects [RAO 82]. The electric field integral equation stems from the boundary condition which denotes that the tangential electric field must be equal to zero at all points on the surface of a perfect electric conductor defined as S,

$$\hat{n}(\bar{r}) \times \bar{E}(\bar{r}) = 0 \quad (2.3\text{-}1)$$

where $\bar{r}$ are vectors spanning from the origin to points on the surface of S, $\hat{n}$ is a normal unit vector outwardly directed from the surface of the perfect electric conductor, and $\bar{E}$ is the total electric field. This total electric field can be written as the sum of the incident and scattered fields.

$$\hat{n}(\bar{r}) \times \left[\bar{E}^{inc}(\bar{r}) + \bar{E}^{scat}(\bar{r})\right] = 0 \tag{2.3-2}$$

The incident electric field is that which is generated by any impressed sources in the absence of the scatterers. This field exists at all points, including inside the scatterers, and is responsible for inducing surface currents, $\bar{J}$, on the PEC. The scattered electric field is then the electric field which arises from these induced surface currents [PETE 97]. Equation (2.3-2) can then be expanded and rearranged as follows.

$$\hat{n}(\bar{r}) \times \bar{E}^{scat}(\bar{r}) = -\hat{n}(\bar{r}) \times \bar{E}^{inc}(\bar{r}) \tag{2.3-3}$$

The electric field integral equation can finally be written as

$$\hat{n}(\bar{r}) \times \bar{E}^{scat}\{\bar{r}, \bar{J}\} = -\hat{n}(\bar{r}) \times \bar{E}^{inc}(\bar{r}) \qquad \bar{r} \epsilon \mathcal{S} \tag{2.3-4}$$

where $\bar{E}^{scat}\{\bar{r}, \bar{J}\}$ denotes the scattered field due to the induced currents $\bar{J}$ evaluated at points $\bar{r}$. This scattered field quantity is that in (2.3-4) which contains the integral and can be expressed as

$$\bar{E}^{scat}(\bar{r}) = -j\omega\bar{A}(\bar{r}) - \nabla\Phi(\bar{r}) \tag{2.3-5}$$

where the magnetic vector potential and the electric scalar potential are defined respectively as

$$\bar{A}(\bar{r}, \bar{r}') = \frac{\mu}{4\pi}\int_{\mathcal{S}} \bar{J}(\bar{r})\frac{e^{-jk|\bar{r}-\bar{r}\prime|}}{|\bar{r}-\bar{r}'|}d\mathcal{S}' \tag{2.3-6}$$

$$\Phi(\bar{r}, \bar{r}') = \frac{1}{4\pi\varepsilon}\int_{\mathcal{S}} \rho_e(\bar{r})\frac{e^{-jk|\bar{r}-\bar{r}\prime|}}{|\bar{r}-\bar{r}'|}d\mathcal{S}' \tag{2.3-7}$$

and $\bar{r}'$ are vectors spanning from the origin to source points on $\mathcal{S}$, $k = \omega\sqrt{\mu\varepsilon}$, with μ and ε being the permittivity and permeability respectively of the surrounding medium, and ρ_e being the surface charge density [RAO 82]. In these equations, the quantity $e^{-jk|\bar{r}-\bar{r}\prime|}(4\pi|\bar{r}-\bar{r}'|)^{-1}$ is known as the free space Green's function. The surface current density and the surface charge density can be related through the continuity equation,

$$\rho_e(\bar{r}) = \frac{j}{\omega}\nabla\cdot\bar{J}(\bar{r}). \tag{2.3-8}$$

Substitution of (2.3-8) into (2.3-7) yields an alternative form of the electric scalar potential, namely

$$\Phi(\bar{r},\bar{r}') = \frac{j}{4\pi\omega\varepsilon}\int_S \left(\nabla_s\cdot\bar{J}(\bar{r})\right)\frac{e^{-jk|\bar{r}-\bar{r}\prime|}}{|\bar{r}-\bar{r}'|}\,d\mathcal{S}'. \tag{2.3-9}$$

The final electric field integral equation can thus be written by substituting (2.3-5) into (2.3-4).

$$j\omega\bar{A}_{tan}(\bar{r},\bar{r}') + \nabla\Phi(\bar{r},\bar{r}')_{tan} = \bar{E}_{tan}^{inc}(\bar{r}) \tag{2.3-10}$$

The tan subscript refers to the tangential component of the scattered and incident fields, thus replacing the unit vector cross products in (2.3-4) [JOHN 90].

2.3.3 Meshing of the Geometry

To apply the method of moments the geometry on which the unknown surface current density exists must be divided into subsections forming a mesh. For the purpose of this work, the geometry will be meshed using 2D triangular elements. In order to ensure that the mesh density is fine enough to obtain accurate results, the length of the triangle edges will be approximately one tenth of a wavelength. When meshing a geometry, all of the geometrical information is stored in tables. This allows one to easily relate each element with its three nodes, node coordinates, and three edges. Figure 2.3-1 shows an example of the meshing of a PEC patch antenna and ground plane whose dimensions are defined in [HERS 98]. This structure will be revisited in later sections.

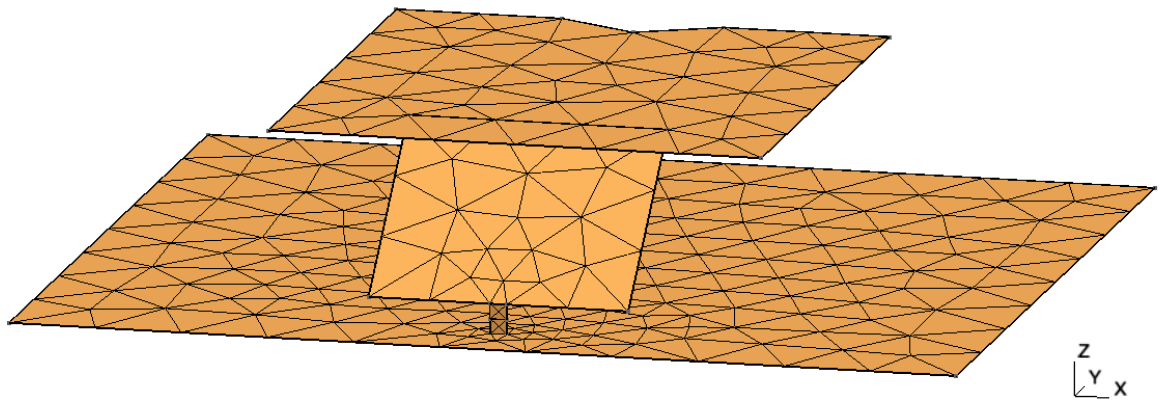

Figure 2.3-1. Mesh of a PEC patch antenna and ground plane constructed using Gmsh [GEUZ 09].

2.3.4 Expansion and Weighting Functions

To solve the integral equation in (2.3-10) and determine the current distribution, $\bar{J}$ is represented in the following form,

$$\bar{J}(\bar{r}) \approx \sum_{n=1}^{N} \bar{f}_n I_n(\bar{r}) \tag{2.3-11}$$

where the I_n are unknown coefficients and the $\bar{f}_n(\bar{r})$ are a set of known expansion functions (terminology which is used interchangeably with "basis functions"). This form allows for efficient numerical computation. The expansion functions that will be used in this thesis are RWG expansion functions defined as follows [RAO 82].

$$\bar{f}_n(\bar{r}) = \begin{cases} \frac{l_n}{2A_n^{\pm}} \bar{\rho}_n^{\pm} & \bar{r} \in T_n^{\pm} \\ 0 & otherwise \end{cases} \tag{2.3-12}$$

Each inter-element edge (an edge shared by two triangles in the mesh) has an associated expansion function. One triangle attached to the common edge is denoted the plus triangle while the other is the minus triangle. l_n in (2.3-12) is the length of the n^{th} edge in the mesh, $A_n^{\pm}$ is the area of the plus or minus triangle on either side of the n^{th} edge, and $\bar{\rho}_n^{\pm}$ are the vectors defined below in Figure 2.3-2.

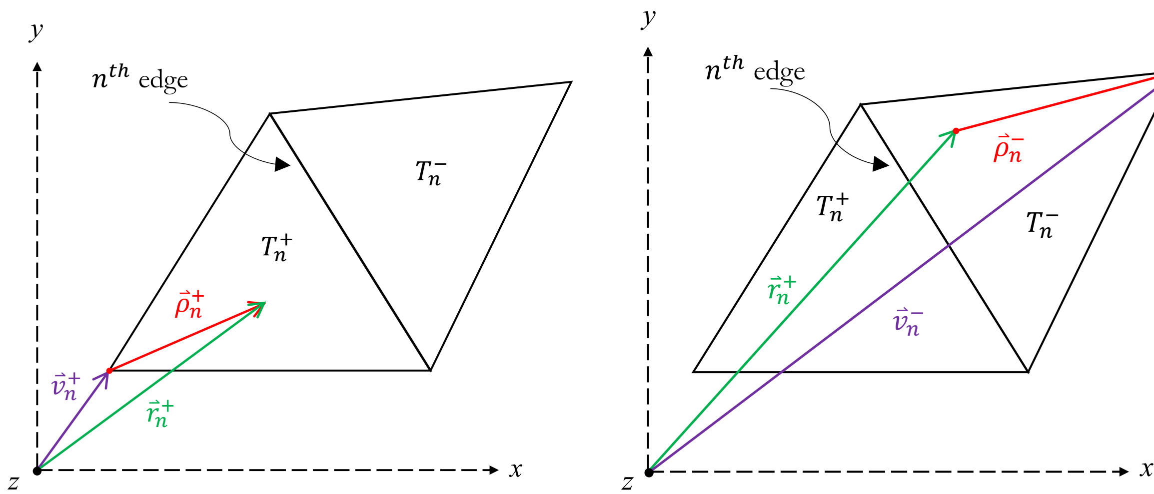

Figure 2.3-2. RWG expansion function defined on the *n*-th inter-element edge where $\bar{\rho}_n \in T_n^+$ (left) and $\bar{\rho}_n \in T_n^-$ (right).

The $\bar{\rho}_n^{\pm}$ vectors in Figure 2.3-2 are constructed via the $\bar{r}_n^{\pm}$ and $\bar{v}_n^{\pm}$ vectors which span from the origin to a point within the $T_n^{\pm}$ triangle and to the vertex of the $T_n^{\pm}$, respectively.

$$\bar{\rho}_n^+ = \bar{r}_n^+ - \bar{v}_n^+ \tag{2.3-13}$$

$$\bar{\rho}_n^- = -\bar{r}_n^- + \bar{v}_n^- \tag{2.3-14}$$

The advantage of using RWG expansion functions is that the current representation is free of fictitious line or point charges. These same expansion functions will also be used as the weighting functions [RAO 82].

2.3.5 Matrix Equation Formulation

The moment method matrix equation can be constructed by introducing the symmetric product.

$$\langle \bar{u}, \bar{v} \rangle = \int_S \bar{u} \cdot \bar{v} \, dS \tag{2.3-15}$$

Applying the above symmetric product to the EFIE in (2.3-10) and the weighting functions $\bar{f}_m$

yields

$$j\omega\langle \bar{A}(\bar{r},\bar{r}')_{tan}, \bar{f}_m\rangle + \langle \nabla\Phi(\bar{r},\bar{r}')_{tan}, \bar{f}_m\rangle = \langle \bar{E}^{inc}_{tan}(\bar{r}), \bar{f}_m\rangle. \tag{2.3-16}$$

Applying integration by parts to the scalar potential term in (2.3-16) results in the following approximation [RAO 82].

$$\langle \nabla\Phi(\bar{r},\bar{r}')_{tan}, \bar{f}_m\rangle \approx l_m[\Phi^-_{mn}(\bar{r}^{c+}_m) - \Phi^+_{mn}(\bar{r}^{c-}_m)] \tag{2.3-17}$$

This approximation also averages the scalar potential over each triangle by its value at the centroid, hence the vectors $\bar{r}^{c-}_m$ and $\bar{r}^{c+}_m$. Similarly, the magnetic vector potential term and the incident field term in (2.3-16) can be approximated, respectively, as [RAO 82]

$$\langle \bar{A}(\bar{r},\bar{r}')_{tan}, \bar{f}_m\rangle \approx l_m\left[\bar{A}(\bar{r}^{c+}_m)\cdot\frac{\bar{\rho}^{c+}_m}{2} + \vec{A}(\bar{r}^{c-}_m)\cdot\frac{\bar{\rho}^{c-}_m}{2}\right] \tag{2.3-18}$$

$$\langle \bar{E}^{inc}_{tan}(\bar{r}), \bar{f}_m\rangle \approx l_m\left[\bar{E}^{inc}(\bar{r}^{c+}_m)\cdot\frac{\bar{\rho}^{c+}_m}{2} + \bar{E}^{inc}(\bar{r}^{c-}_m)\cdot\frac{\bar{\rho}^{c-}_m}{2}\right] \tag{2.3-19}$$

where $\bar{\rho}^{c\pm}_m$ and $\bar{r}^{c\pm}_m$ are defined in Figure 2.3-2 however are pertaining specifically to the centroid of the minus or plus triangle. (2.3-17)-(2.3-19) can now be substituted into (2.3-16) yielding an $N_e \times N_e$ system of linear equations which can be written in the form,

$$\boldsymbol{ZI} = \boldsymbol{V} \tag{2.3-20}$$

where $\boldsymbol{Z}$ is an $N_e \times N_e$ matrix, and $\boldsymbol{I}$ and $\boldsymbol{V}$ are $N_e \times 1$ column vectors (N_e being equal to the number of inter-element edges in the mesh). Elements in $\boldsymbol{Z}$ and $\boldsymbol{V}$ are thus given by

$$Z_{mn} = l_m\left[j\omega\left(\bar{A}^+_{mn}\cdot\frac{\bar{\rho}^{c+}_m}{2} + \bar{A}^-_{mn}\cdot\frac{\bar{\rho}^{c-}_m}{2}\right) + \Phi^-_{mn} - \Phi^+_{mn}\right] \tag{2.3-21}$$

$$V_m = l_m \left[\bar{E}^{inc}(\bar{r}_m^{c+}) \cdot \frac{\bar{\rho}_m^{c+}}{2} + \bar{E}^{inc}(\bar{r}_m^{c-}) \cdot \frac{\bar{\rho}_m^{c-}}{2} \right] \tag{2.3-22}$$

and the magnetic vector potential and electric scalar potential are defined as

$$\begin{aligned} \bar{A}_{mn}^{\pm} = \frac{\mu}{4\pi} \Bigg[& \frac{l_n}{2A_n^+} \int_{T_n^+} \bar{\rho}_n^+ \left(\bar{r}_n^{+'}\right) \frac{e^{-jk\left|\bar{r}_m^{C\pm} - \bar{r}_n^{+'}\right|}}{\left|\bar{r}_m^{C\pm} - \bar{r}_n^{+'}\right|} dS' \\ & + \frac{l_n}{2A_n^-} \int_{T_n^-} \bar{\rho}_n^- \left(\bar{r}_n^{-'}\right) \frac{e^{-jk\left|\bar{r}_m^{C\pm} - \bar{r}_n^{-'}\right|}}{\left|\bar{r}_m^{C\pm} - \bar{r}_n^{-'}\right|} dS' \Bigg] \end{aligned} \tag{2.3-23}$$

$$\Phi_{mn}^{\pm} = \frac{j}{4\pi\omega\varepsilon} \left[\frac{l_n}{A_n^+} \int_{T_n^+} \frac{e^{-jk\left|\bar{r}_m^{C\pm} - \bar{r}_n^{+'}\right|}}{\left|\bar{r}_m^{C\pm} - \bar{r}_n^{+'}\right|} dS' - \frac{l_n}{A_n^-} \int_{T_n^-} \frac{e^{-jk\left|\bar{r}_m^{C\pm} - \bar{r}_n^{-'}\right|}}{\left|\bar{r}_m^{C\pm} - \bar{r}_n^{-'}\right|} dS' \right] \tag{2.3-24}$$

where l_n is the length of the n^{th} edge, $A_n^{\pm}$ is the area of the plus or minus triangle associated with the n^{th} edge, $\bar{\rho}_n^+\left(\bar{r}_n^{+'}\right)$ is a vector spanning from the vertex opposite the n^{th} edge in the T_n^+ triangle to a point $\left(x_n^{+'}, y_n^{+'}\right)$ in the T_n^+ triangle ($\bar{r}_n^{\pm'}$ is a vector from the origin to a point (x', y', z') in the $T_n^{\pm}$ triangle. The integrals in (2.3-23) and (2.3-24) are with respect to this primed coordinate), and $\bar{\rho}_n^-\left(\bar{r}_n^{-'}\right)$ is a vector spanning from a point $\left(x_n^{-'}, y_n^{-'}\right)$ in the T_n^- triangle to the vertex opposite the n^{th} edge in the T_n^- triangle [MAKA 02]. The integration over the plus and minus triangles in equations (2.3-23) and (2.3-24) must be evaluated numerically. This will be done by dividing each triangle into nine sub-triangles using barycentric subdivision and using the centroids of each sub-triangle as sample points.

$$\int_{T_n^{\pm}} f\left(\bar{r}_n^{\pm'}\right) dS' = \frac{A_n^{\pm}}{9} \sum_{p=1}^{9} f\left(\bar{r}_{n_p}^{c\pm}\right) \tag{2.3-25}$$

$\bar{r}_{n_p}^{c}$ in (2.3-25) is a vector spanning from the origin to the centroid of the p^{th} sub-triangle. An example of the barycentric subdivision of a triangle into nine sub-triangles is shown in Figure 2.3-3.

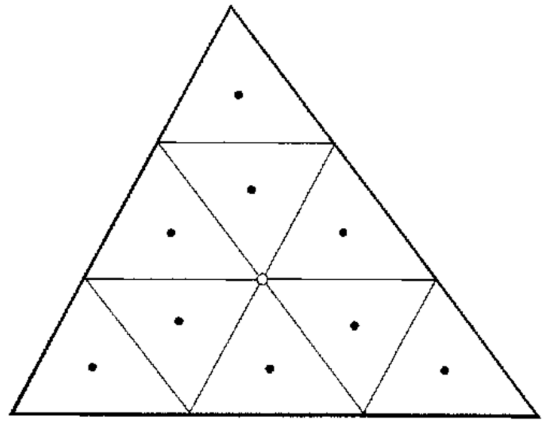

Figure 2.3-3. Barycentric subdivision of a triangle into nine sub-triangles. The triangle's midpoint is shown by a white circle while the midpoint of each sub-triangle is shown by a black dot [MAKA 02].

Finally, once the matrix equation in (2.3-20) has been solved, the coefficients in ***I*** can be substituted into (2.3-11) to obtain the electric current density on the PEC scatterers.

2.3.6 Delta Gap Feeding Model

For all simulated examples shown throughout this thesis the antennas will be fed via a feeding edge model where a voltage is applied across a gap of negligible width. For convenience, the gap is taken to coincide with one or more inter-element edges such that there are one or more RWG expansion functions associated with these edges. Relating this to equation (2.3-22), the incident electric field will exist only on the chosen edges and will thus be zero elsewhere. Representing the voltage across the gap as V, the electric field within the gap is [MAKA 02]

$$\bar{E}^{inc} = \frac{V}{\Delta}\hat{\tau} = V\delta\left(\bar{r} - \bar{r}_{gap}\right)\hat{\tau} \qquad (2.3\text{-}26)$$

where Δ is the width of the gap, $\bar{r}_{gap}$ is the location of the centre of the gap, and $\hat{\tau}$ is a unit vector depicting the direction of the electric field across the gap. As the width of the gap in (2.3-26) becomes infinitesimally small, the electric field can be represented by a delta function approximation. The integral of the electric field in (2.3-26) over the gap, or over the edges, is thus the applied voltage. Applying this to the symmetric product on the right side of equation (2.3-16) yields

$$
\begin{aligned}
V_m = \langle \bar{E}^{inc}, \bar{f}_m \rangle &= \int_{T_m^+ + T_m^-} \bar{E}^{inc} \cdot \bar{f}_m d\mathcal{S} \\
&= V \int_{T_m^+ - T_m^-} \delta\left(\bar{r} - \bar{r}_{gap}\right) \hat{\tau} \cdot \bar{f}_m d\mathcal{S} = l_m V
\end{aligned}
\tag{2.3-27}
$$

for the edge element $\bar{f}_m$ over which the voltage gap is applied and

$$
V_m = \langle \bar{E}^{inc}, \bar{f}_m \rangle = \int 0 \cdot \bar{f}_m d\mathcal{S} = 0 \tag{2.3-28}
$$

elsewhere. (2.3-27) makes use of the property that the component of an RWG expansion function normal to an edge is always equal to one [RAO 82]. The right-side vector $\boldsymbol{V}$ in the matrix equation in (2.3-20) will thus be entirely zeros other than entries in the rows corresponding to the one or more feeding edges. More than one feeding edge is required when the delta gap spans multiple edges. For examples in later sections, if not specified otherwise, the voltage V in (2.3-27) will be set to 1 V.

2.4 MODIFIED NODAL ANALYSIS CIRCUIT FORMULATION

Modified nodal analysis (MNA) is a method used in circuit analysis to automatically formulate general circuit equations which can be used to solve for nodal voltages and branch currents. The basic idea stems from identifying the contribution of each circuit element to a circuit's overall matrix equation formed through the application of Kirchhoff's Current Law (KCL) at each of the circuit nodes. The general form of the circuit matrix equation is the system of differential equations seen below.

$$
\boldsymbol{G}\boldsymbol{x}(t) + \boldsymbol{C}\frac{\partial \boldsymbol{x}(t)}{\partial t} + \boldsymbol{F}\big(\boldsymbol{x}(t)\big) = \boldsymbol{b}(t) \tag{2.4-1}
$$

Matrices $\boldsymbol{G}$ and $\boldsymbol{C}$ are $N_k \times N_k$ and vectors $\boldsymbol{x}(t)$, $\boldsymbol{b}(t)$, and $\boldsymbol{F}(\boldsymbol{x}(t))$ are $N_k \times 1$, where N_k represents the number of unknowns in the system. The $\boldsymbol{G}$ and $\boldsymbol{C}$ matrices are the conductance and susceptance matrices respectively, the $\boldsymbol{b}(t)$ vector is referred to as the source or input vector, $\boldsymbol{F}(\boldsymbol{x}(t))$ contains nonlinear functions of $\boldsymbol{x}(t)$, and $\boldsymbol{x}(t)$ is the solution [NOUR 13b], [ACHA 01]. Should the circuit contain no nonlinear elements, equation (2.4-1) can be written in the Laplace-domain as

$$(\boldsymbol{G} + s\boldsymbol{C})\boldsymbol{x}(s) = \boldsymbol{b}(s) \tag{2.4-2}$$

where $s = j\omega$. As an example, consider the RC circuit in Figure 2.4-1.

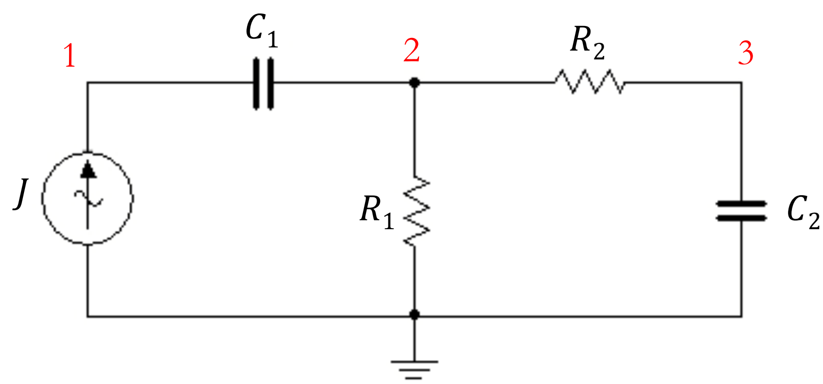

Figure 2.4-1. RC circuit.

The number of nodes in the circuit excluding the reference node must first be identified. This circuit has three non-reference nodes which are numbered in red. Writing a KCL at each of these nodes results in the following equations.

$$-J + sC_1(v_1 - v_2) = 0 \tag{2.4-3}$$

$$sC_1(v_2 - v_1) + \frac{v_2}{R_1} + \frac{v_2 - v_3}{R_2} = 0 \tag{2.4-4}$$

$$sC_2v_3 + \frac{v_3 - v_2}{R_2} = 0 \tag{2.4-5}$$

Rewriting the above equations in matrix form yields

$$\left(\begin{bmatrix} 0 & 0 & 0 \\ 0 & g_1 + g_2 & -g_2 \\ 0 & -g_2 & g_2 \end{bmatrix} + s\begin{bmatrix} C_1 & -C_1 & 0 \\ -C_1 & C_1 & 0 \\ 0 & 0 & C_2 \end{bmatrix}\right)\begin{bmatrix} v_1 \\ v_2 \\ v_3 \end{bmatrix} = \begin{bmatrix} J \\ 0 \\ 0 \end{bmatrix} \tag{2.4-6}$$

where g is the conductance of resistor R. From (2.4-6), it can be seen that resistors only contribute to the $\boldsymbol{G}$ matrix and capacitors contribute only to the $\boldsymbol{C}$ matrix. Also, all three elements only effect the rows and columns in (2.4-6) which correspond to the nodes which that particular element is connected to. As such, the contribution of each element to the matrix equation can be generalized via element "stamps." The resistor stamp can be seen in the figure below.

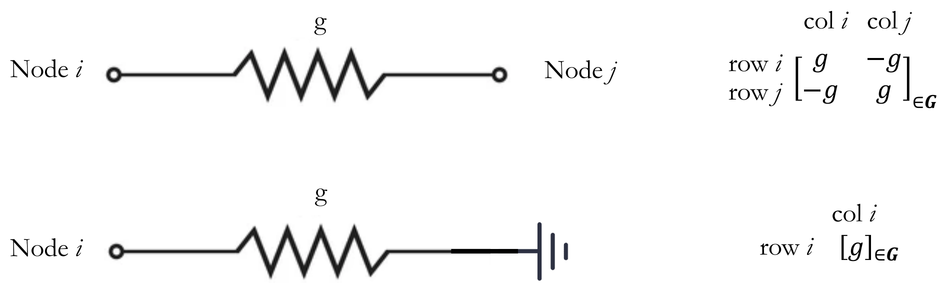

Figure 2.4-2. MNA resistor stamp.

Similar stamps can be developed for the capacitor and current source from the above example, while stamps for inductors, voltage sources, and dependent sources can be found in much the same way. The term "modified" in modified nodal analysis refers to modifications which need to be made to the matrix equation to accommodate certain elements. For example, there is no Ohm's law for a voltage source, hence the current through voltage sources must be added as an additional unknown in the $\boldsymbol{x}(t)$ vector while the voltage difference across the source yields the additional equation needed to accommodate this extra unknown.

Ultimately, the MNA formulation allows for the development of programs which can automatically generate the circuit equations. The only information that the program would need as an input is a list of every element in the circuit, their values, and which nodes they are connected to. Such a list is typically referred to as a circuit netlist. Further and more detailed information on the MNA formulation can be found in [NAJM 10].

2.5 MODEL ORDER REDUCTION IN LINEAR CIRCUIT ANALYSIS

2.5.1 Introductory Remarks

Model order reduction (MOR) is a technique which is applied to systems described by large matrices in the form of a set of differential equations. MOR seeks to reduce the computational complexity of using such large systems in numerical simulations by effectively reducing the degrees of freedom of the original system of equations to create a reduced order model (ROM) of considerably lesser size that preserves the system's fidelity (within a satisfactory error bound).

2.5.2 Overview of the MOR Technique

Let us assume that N_k first order ordinary differential equations represented by a Laplace-domain matrix equation can be written in the form

$$\boldsymbol{M}(s)\boldsymbol{X}(s) = \boldsymbol{b}(s) \tag{2.5-1}$$

where $\boldsymbol{M}$ is a matrix of size $N_k \times N_k$, and $\boldsymbol{X}(s)$ and $\boldsymbol{b}(s)$ are column vectors of size $N_k \times 1$, $\boldsymbol{X}(s)$ being the unknown vector. Furthermore, let us assume that the matrix $\boldsymbol{M}$ can be separated in the following way,

$$(\boldsymbol{G} + s\boldsymbol{C})\boldsymbol{X}(s) = \boldsymbol{b}(s) \tag{2.5-2}$$

such that neither $N_k \times N_k$ matrices $\boldsymbol{G}$ nor $\boldsymbol{C}$ contain any elements which are dependent on s, where $s = j\omega$. Recall this form as the form used to represent linear circuits using the MNA formulation. The exact solution to (2.5-1) or (2.5-2) at, for example, N_f frequencies, would require the total $(\boldsymbol{G} + s\boldsymbol{C})$ matrix to be inverted N_f times (or equivalently would require N_f LU decompositions). Alternatively, the solution vector can be approximated by a Taylor series expansion centered at $s = 0$ as

$$\boldsymbol{X}(s) = \sum_{n=0}^{\infty} \boldsymbol{M}_n s^n = \boldsymbol{M}_0 + \boldsymbol{M}_1 s + \boldsymbol{M}_2 s^2 + \boldsymbol{M}_3 s^3 + \cdots \tag{2.5-3}$$

where $\boldsymbol{M}_n$ are the moments of $\boldsymbol{X}(s)$ which are column vectors of size $N_k \times 1$ [ACHA 01], [ANTO 01].

Given an impulse response, $\boldsymbol{b}(s) = [0 \quad \cdots \quad 1 \quad \cdots \quad 0]^{\mathrm{T}}$, the moments can be computed as derivatives of the solution vector $\boldsymbol{X}(s)$ at expansion point $s_0 = 0$ as

$$\boldsymbol{M}_n = \frac{1}{n!}\frac{\partial \boldsymbol{X}(s)}{\partial s^n}\bigg|_{s=0}. \tag{2.5-4}$$

Alternatively, by substituting (2.5-3) into (2.5-2) and equating like powers of s, the moment $\boldsymbol{M}_0$ (the DC solution) can first be computed as

$$\boldsymbol{M}_0 = \boldsymbol{G}^{-1}\boldsymbol{b} \tag{2.5-5}$$

and can then be used in the recursive relationship

$$\boldsymbol{G}\boldsymbol{M}_n = -\boldsymbol{C}\boldsymbol{M}_{n-1} \tag{2.5-6}$$

to compute all other moments [ACHA 01]. One can notice from the above equations that the computation of all of the moments requires just one matrix inverse. As such, with the moments computed, (2.5-3) can be used to approximate the solution of $\boldsymbol{X}$ at any number of frequencies, say the previously mentioned N_f frequencies, while only requiring the inversion of the $\boldsymbol{G}$ matrix once. Equivalently, the moments can be computed in terms of the matrix $\boldsymbol{A}$ and vector $\boldsymbol{R}$ as follows [ACHA 01, NOUR 14],

$$\boldsymbol{M}_i = \boldsymbol{A}^i\boldsymbol{R} \tag{2.5-7}$$

where

$$\boldsymbol{A} = -\boldsymbol{G}^{-1}\boldsymbol{C} \tag{2.5-8}$$

$$\boldsymbol{R} = \boldsymbol{G}^{-1}\boldsymbol{b}. \tag{2.5-9}$$

It can be found, however, that the moments of $\boldsymbol{X}$, the sequence $\{\boldsymbol{R}, \boldsymbol{AR}, \boldsymbol{A}^2\boldsymbol{R}, \boldsymbol{A}^3\boldsymbol{R}, \dots\}$, converges to an eigenvector corresponding to the largest eigenvalue of matrix $\boldsymbol{A}$. This convergence means that after a certain number of moments are computed (typically fewer than 10), no more useful information is obtained by computing additional moments. As such, the direct computation of the moments of $\boldsymbol{X}$ is considered an ill-conditioned numerical process, rendering the approximation in (2.5-3) undesirable [ANTO 01, NOUR 14]. However, since (2.5-3) shows that the solution vector $\boldsymbol{X}$ can be written as a linear combination of the moments, it can be said that $\boldsymbol{X}$ is a vector in the space spanned by the moments. This particular subspace which is spanned by the moments is called the Krylov Subspace and is represented as

$$\kappa_r(\boldsymbol{A}, \boldsymbol{R}, \boldsymbol{q}) = Span\{\boldsymbol{R}, \boldsymbol{AR}, \boldsymbol{A}^2\boldsymbol{R}, \dots \boldsymbol{A}^{q-1}\boldsymbol{R}\} \tag{2.5-10}$$

where matrix $\boldsymbol{Q}$ is defined as an orthogonal basis of the Krylov Subspace [ACHA 01, NOUR 14]. It is this matrix $\boldsymbol{Q}$ which allows one to reduce the size of the $\boldsymbol{G}$ and $\boldsymbol{C}$ matrices in (2.5-2) such that the system of equations can be approximated by a system of lesser dimension. The theorem used to find the orthogonal basis $\boldsymbol{Q}$ is the following. If $\boldsymbol{Q}$ is an orthogonal basis of $\kappa_r(\boldsymbol{A}, \boldsymbol{R}, \boldsymbol{q})$, then $\boldsymbol{AQ} = \boldsymbol{QH}$, where $\boldsymbol{H}$ is an upper-Hessenberg matrix [ACHA 01]. Recall that the moments themselves are ill-conditioned, thus methods such as the Gram-Schmidt algorithm for determining the orthogonal basis of a subspace will not be applicable here, as the moments themselves cannot be computed. The above theorem is more clearly written as

$$\boldsymbol{AQ} = \boldsymbol{QH} \rightarrow \boldsymbol{A}[\boldsymbol{q}_1 \quad \boldsymbol{q}_2 \quad \boldsymbol{q}_3 \quad \cdots] = [\boldsymbol{q}_1 \quad \boldsymbol{q}_2 \quad \boldsymbol{q}_3 \quad \cdots]\begin{bmatrix} h_{11} & h_{12} & h_{13} & \cdots \\ h_{21} & h_{22} & h_{23} & \cdots \\ 0 & h_{32} & h_{33} & \cdots \\ 0 & 0 & h_{34} & \cdots \\ \vdots & \vdots & \vdots & \ddots \end{bmatrix} \tag{2.5-11}$$

where $\boldsymbol{Q}$ is $N_k \times N_q$ and $\boldsymbol{H}$ is $N_q \times N_q$ (N_q being the number of columns of orthogonal matrix $\boldsymbol{Q}$ which determines the size of the reduced model). In order to determine the vectors $\boldsymbol{q}_i$ which form the orthogonal matrix $\boldsymbol{Q}$, Arnoldi's Algorithm is used, which is a modified version of the Gram-Schmidt Algorithm that utilizes the theorem in (2.5-11). This algorithm starts by defining the first column of $\boldsymbol{Q}$ as follows.

$$\boldsymbol{q}_1 = \frac{\boldsymbol{R}}{\|\boldsymbol{R}\|} \tag{2.5-12}$$

Evaluating (2.5-11) firstly yields

$$\boldsymbol{A}\boldsymbol{q}_1 = h_{11}\boldsymbol{q}_1 + h_{21}\boldsymbol{q}_2 \tag{2.5-13}$$

which when pre-multiplied by the transpose of $\boldsymbol{q}_1$ gives

$$\boldsymbol{q}_1{}^{\mathrm{T}}\boldsymbol{A}\boldsymbol{q}_1 = \boldsymbol{q}_1{}^{\mathrm{T}}h_{11}\boldsymbol{q}_1 + \boldsymbol{q}_1{}^{\mathrm{T}}h_{21}\boldsymbol{q}_2. \tag{2.5-14}$$

Since an orthogonal basis is formed of orthogonal column vectors, (2.5-14) simplifies to

$$\boldsymbol{q}_1{}^{\mathrm{T}}\boldsymbol{A}\boldsymbol{q}_1 = h_{11}. \tag{2.5-15}$$

Next, the vector $\boldsymbol{w}$ is defined in Figure 2.5-1.

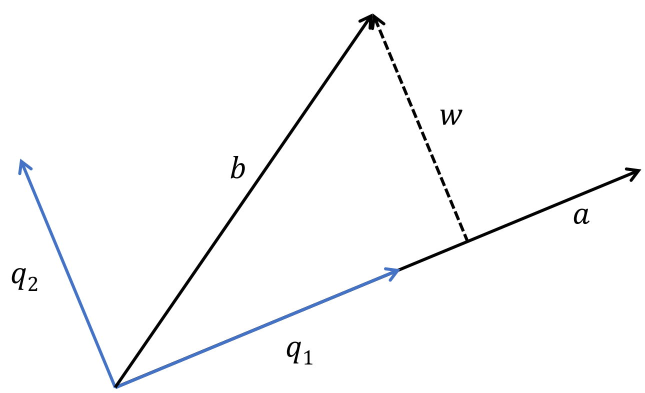

Figure 2.5-1. Vector diagram of the first two columns of $\boldsymbol{Q}$.

Figure 2.5-1 shows that the vector $\boldsymbol{w}$, which has the same magnitude and direction of vector $\boldsymbol{q}_2$, is simply the difference between the vector $\boldsymbol{b}$ and the projection of vector $\boldsymbol{b}$ onto vector $\boldsymbol{q}_1$.

$$\boldsymbol{w} = \boldsymbol{b} - \langle \boldsymbol{b}, \boldsymbol{q}_1 \rangle \boldsymbol{q}_1 \tag{2.5-16}$$

Vectors $\boldsymbol{a}$ and $\boldsymbol{b}$ in Figure 2.5-1 represent two moment vectors which span the subspace, and that are not orthogonal. Since vector $\boldsymbol{R}$ forms the first moment $\boldsymbol{M}_0$, (2.5-12) defines the first vector in matrix $\boldsymbol{Q}$ as being in the direction of the first moment $\boldsymbol{a}$. The second moment $\boldsymbol{b}$ is of course in the direction of the second moment, which from (2.5-10) is known to be $\boldsymbol{AR}$, and thus in the direction of $\boldsymbol{Aq}_1$. Thus, replacing $\boldsymbol{Aq}_1$ in (2.5-15) with $\boldsymbol{b}$ and substituting into (2.5-16) yields $\boldsymbol{w}$ and thus $\boldsymbol{q}_2$ as follows [ACHA 01].

$$\boldsymbol{w} = \boldsymbol{Aq}_1 - h_{11}\boldsymbol{q}_1 \tag{2.5-17}$$

$$\boldsymbol{q}_2 = \frac{\boldsymbol{w}}{\|\boldsymbol{w}\|} \tag{2.5-18}$$

This process can then be repeated for however many columns of $\boldsymbol{Q}$ are chosen. Arnoldi's Algorithm is summarized below in Figure 2.5-2 which will run for $N_q - 1$ iterations.

Require: $\boldsymbol{R}$, $\boldsymbol{A}$, and N_q

Initialize: $\boldsymbol{q_1} \leftarrow \boldsymbol{R}/\|\boldsymbol{R}\|$
for $j = 1$ **to** $N_q - 1$ **do**
    $\boldsymbol{z} = \boldsymbol{Aq}_j$
    for $i = 1$ **to** j
        $h_{ij} = \boldsymbol{q}_i^{\mathrm{T}}\boldsymbol{z}$
        $\boldsymbol{z} = \boldsymbol{z} - h_{ij}\boldsymbol{q}_i$
    end
    $h_{j+1,j} = \|\boldsymbol{z}\|$
    if $h_{j+1,j} = 0$
        quit
    else
        $\boldsymbol{q}_{j+1} = \boldsymbol{z}/h_{j+1,j}$
    end if
end for

Figure 2.5-2. Arnoldi Algorithm Pseudocode [ACHA 01].

The $\boldsymbol{Q}$ matrix can then be used to reduce $\boldsymbol{G}$, $\boldsymbol{C}$, and $\boldsymbol{b}$ to $N_q \times N_q$ matrices and an $N_q \times 1$ vector, respectively [NOUR 14].

$$\widehat{\boldsymbol{G}} = \boldsymbol{Q}^{\mathrm{T}}\boldsymbol{GQ} \tag{2.5-19}$$

$$\widehat{\boldsymbol{C}} = \boldsymbol{Q}^{\mathrm{T}}\boldsymbol{CQ} \tag{2.5-20}$$

$$\widehat{\boldsymbol{b}} = \boldsymbol{Q}^{\mathrm{T}}\boldsymbol{b} \tag{2.5-21}$$

The reduced approximation of the unknown vector $\boldsymbol{X}$ can then be found by solving the reduced matrix equation

$$\left(\widehat{\boldsymbol{G}} + s\widehat{\boldsymbol{C}}\right)\widehat{\boldsymbol{X}} = \widehat{\boldsymbol{b}}. \tag{2.5-22}$$

The final full approximation $\boldsymbol{X}_{app}$ of the unknown vector $\boldsymbol{X}$ can then be found by pre-multiplying the reduced $\widehat{\boldsymbol{X}}$ vector by matrix $\boldsymbol{Q}$ [ACHA 01], [NOUR 14].

$$\boldsymbol{X}_{app} = \boldsymbol{Q}\widehat{\boldsymbol{X}} \approx \boldsymbol{X} \tag{2.5-23}$$

In total, computing the $\boldsymbol{Q}$ matrix requires only one matrix inverse (the $\boldsymbol{G}$ matrix in order to compute $\boldsymbol{A}$ and $\boldsymbol{R}$) and is independent of frequency, thus does not have to be recomputed at each frequency. This allows for a significant reduction in the size of the original matrix equation that is to be solved, and hence faster computation times.

2.5.3 Linearization of Higher Order Matrix Polynomials

In the previous section it was assumed that the matrix $\boldsymbol{M}$ in (2.5-1) could be separated into a first order polynomial in terms of s. This section will cover the procedure that is used to apply model order reduction to higher order polynomials.

As an example, assume the equation in (2.5-1) can be written as follows.

$$(\boldsymbol{G} + s\boldsymbol{C}_1 + s^2\boldsymbol{C}_2 + s^3\boldsymbol{C}_3)\boldsymbol{X}(s) = \boldsymbol{b}(s) \tag{2.5-24}$$

For each additional order of s, a new unknown variable must be defined.

$$\boldsymbol{X}_a(s) = s\boldsymbol{X}(s) \tag{2.5-25}$$

$$\boldsymbol{X}_b(s) = s^2\boldsymbol{X}(s) = s\boldsymbol{X}_a(s) \tag{2.5-26}$$

Equation (2.5-24) can then be expanded and rewritten as follows.

$$\boldsymbol{G}\boldsymbol{X}(s) + s\boldsymbol{C}_1\boldsymbol{X}(s) + s\boldsymbol{C}_2\boldsymbol{X}_a(s) + s\boldsymbol{C}_3\boldsymbol{X}_b(s) = \boldsymbol{b}(s) \tag{2.5-27}$$

Rearranging (2.5-25) and (2.5-26) yields

$$\boldsymbol{X}_a(s) - s\boldsymbol{X}(s) = 0 \tag{2.5-28}$$

$$\boldsymbol{X}_b(s) - s\boldsymbol{X}_a(s) = 0 \tag{2.5-29}$$

which along with (2.5-27) can then be put in matrix form

$$\begin{bmatrix} \boldsymbol{G} + s\boldsymbol{C}_1 & s\boldsymbol{C}_2 & s\boldsymbol{C}_3 \\ -s & \mathbb{I}_{N_k} & \boldsymbol{0} \\ \boldsymbol{0} & -s & \mathbb{I}_{N_k} \end{bmatrix} \begin{bmatrix} \boldsymbol{X}(s) \\ \boldsymbol{X}_a(s) \\ \boldsymbol{X}_b(s) \end{bmatrix} = \begin{bmatrix} \boldsymbol{b}(s) \\ \boldsymbol{0} \\ \boldsymbol{0} \end{bmatrix} \tag{2.5-30}$$

where $\mathbb{I}_{N_k}$ is an identity matrix of size $N_k \times N_k$. Equation (2.5-30) is now entirely in terms of s and thus can be written in the form of (2.5-2) [NOUR 20].

$$\left(\begin{bmatrix} \boldsymbol{G} & \boldsymbol{0} & \boldsymbol{0} \\ \boldsymbol{0} & \mathbb{I}_{N_k} & \boldsymbol{0} \\ \boldsymbol{0} & \boldsymbol{0} & \mathbb{I}_{N_k} \end{bmatrix} + s \begin{bmatrix} \boldsymbol{C_1} & \boldsymbol{C_2} & \boldsymbol{C_3} \\ -\mathbb{I}_{N_k} & \boldsymbol{0} & \boldsymbol{0} \\ \boldsymbol{0} & -\mathbb{I}_{N_k} & \boldsymbol{0} \end{bmatrix} \right) \begin{bmatrix} \boldsymbol{X}(s) \\ \boldsymbol{X}_a(s) \\ \boldsymbol{X}_b(s) \end{bmatrix} = \begin{bmatrix} \boldsymbol{b}(s) \\ \boldsymbol{0} \\ \boldsymbol{0} \end{bmatrix} \tag{2.5-31}$$

Equation (2.5-31) is now in the correct form required for the MOR process described in the previous section. Once the approximate unknown vector $\boldsymbol{X}_{app}$ is solved for, rows $N_k + 1$ to $3N_k$ can be discarded, as it is only $\boldsymbol{X}$ in (2.5-31) which contains relevant information. Furthermore, although the system has increased in size, and thus the equivalent $\boldsymbol{G}$ matrix which must be inverted for MOR has increased in size, one can observe that the additional elements in (2.5-31) are all identity matrices. Given that the inverse of a diagonal matrix of matrices is the inverse of each of its matrix elements, and the inverse of an identity matrix is itself, the computation time required to invert this new $\boldsymbol{G}$ matrix is comparable to that of the single $\boldsymbol{G}$ matrix in (2.5-2).

2.6 MULTI-PORT MODEL ORDER REDUCTION AND ITS CLUSTERED APPROACH IN CIRCUIT ANALYSIS

The MOR procedure described in *Section 2.5* assumed that the reduced order model was computed from that of a single-port circuit as $\boldsymbol{b}(s)$ was defined to have only a single column. The result from this formulation is a reduced order model which is only valid for the particular set of excitations included in this source vector (unless the circuit has only one source). The seminal work on the application of MOR methods to circuit analysis allowed the use of multiple external ports, and such "multiport" MOR implies that the construction of the reduced order model via $\boldsymbol{Q}$ considers excitations from every port simultaneously. This is represented in the MNA equations by modifying the right side of (2.5-2) as follows

$$(\boldsymbol{G} + s\boldsymbol{C})\boldsymbol{X}(s) = \boldsymbol{B}_c\boldsymbol{U}(s) \tag{2.6-1}$$

where $\boldsymbol{U}(s)$ is a vector of size $N_p \times 1$ describing the Laplace-domain independent stimuli (current or voltage sources) in the circuit and $\boldsymbol{B}_c$ is a matrix containing either ones or zeros that maps the independent sources to the space of the circuit variables and is of size $N_k \times N_p$, equivalently stated as $\{0,1\}^{N_k \times N_p}$, with N_p being the number of ports. Including multi-port excitations in the form of (2.6-1) does not change the MOR process described in *Section 2.5*, however all columns on the right side of (2.6-1) are now used in the determination of $\boldsymbol{Q}$, leading to a reduced order model which now need not be recomputed for every new set of port excitations. This $\boldsymbol{Q}$ is computed using the same Arnoldi algorithm described in Figure 2.5-2, however the moments of $\boldsymbol{X}(s)$ in (2.5-3) are now block moments of size $N_k \times N_p$ whose columns are vector moments, one for each column of $\boldsymbol{B}_c$. Because of this, $\boldsymbol{Q}$, which considers all N_p ports of the circuit simultaneously, is now of size $N_k \times N_q N_p$ and the reduced order model is now of size $N_q N_p \times N_q N_p$. It is therefore evident that the effectiveness of the MOR technique degrades when the number of external ports increases.

This limitation spurred the development of the clustered MOR approach in [NOUR 13a]. This adaptation of multi-port MOR works by grouping the N_p ports into "clusters" and applying the principle of superposition [BENN 08] to achieve the same outcome as conventional multi-port

MOR but using single-port reduced order models instead (should each cluster contain a single-port, which it will for the work in this thesis) as follows

$$\boldsymbol{X}(s) = \sum_{i=1}^{N_p} \boldsymbol{X}_i(s) \tag{2.6-2}$$

where $\boldsymbol{X}_i(s)$ are solutions to the systems

$$(\boldsymbol{G} + s\boldsymbol{C})\boldsymbol{X}_i(s) = \boldsymbol{B}_{c,i}U_i, \quad i = 1, 2, \cdots, N_p \tag{2.6-3}$$

and $\boldsymbol{B}_{c,i}$ is the i^{th} column of $\boldsymbol{B_c}$ and U_i is the i^{th} component of $\boldsymbol{U}(s)$. This approach thus results in N_p single-port reduced order models of size $N_q \times N_q$ as opposed to the above-mentioned single reduced-order model of size $N_qN_p \times N_qN_p$. These single-port models are faster to compute given their smaller overall size, and result in a multi-port model that is more efficient to invert. The reason is that to consider each cluster simultaneously, the single-port models are arranged block diagonally which leads to inversions of $O({N_q}^3 N_p)$ rather than $O\left((N_qN_p)^3\right)$. This idea will be clarified further as its application to this thesis is discussed in *Chapter 4*.

2.7 CHEBYSHEV APPROXIMATION

The Chebyshev approximation is based on a sequence of Chebyshev polynomials which can be used to approximate a given mathematical function. The Chebyshev polynomial of degree *k* is given by

$$T_k(x) = \cos\left(k cos^{-1}(x)\right). \tag{2.7-1}$$

The first 11 Chebyshev polynomials are summarized in Table 2.7-1. Trigonometric identities can be combined with the expression in (2.7-1) to yield polynomials as opposed to trigonometric functions. The recursive expression

$$T_k(x) = 2xT_{k-1}(x) - T_{k-2}(x) \tag{2.7-2}$$

allows for the computation of a given Chebyshev polynomial from the previous two. The Chebyshev polynomials can then be used to approximate a function f as follows,

$$f(x) \approx \left[\sum_{k=0}^{N-1} c_k T_k(x)\right] - \frac{1}{2} c_0 \tag{2.7-3}$$

where the coefficients c_k are computed as

$$c_k = \frac{2}{N} \sum_{i=1}^{N} f\left[cos\left(\frac{\pi\left(i-\frac{1}{2}\right)}{N}\right)\right] cos\left(\frac{\pi k\left(i-\frac{1}{2}\right)}{N}\right) \qquad k = 0, 1, 2, \cdots, N-1. \tag{2.7-4}$$

Table 2.7-1. The first eleven Chebyshev polynomials.

k	Chebyshev Polynomial
0	1
1	x
2	$2x^2 - 1$
3	$4x^3 - 3x$
4	$8x^4 - 8x^2 + 1$
5	$16x^5 - 20x^3 + 5x$
6	$32x^6 - 48x^4 + 18x^2 - 1$
7	$64x^7 - 112x^5 + 56x^3 - 7x$
8	$128x^8 - 256x^6 + 160x^4 - 32x^2 + 1$
9	$256x^9 - 576x^7 + 432x^5 - 120x^3 + 9x$
10	$512x^{10} - 1280x^8 + 1120x^6 - 400x^4 + 50x^2 - 1$

For an arbitrary fixed value of N, (2.7-3) approximates the function f for values of x in the interval from $[-1, 1]$, which is where the zeros of $T_k(x)$ are located. In order to make use of this approximation for a different interval of x, say $[a, b]$, the following change of variables and modifications must be made.

$$\hat{x} = \frac{x - \Delta_p}{\Delta_m} \tag{2.7-5}$$

$$\Delta_m = \frac{1}{2}(b - a) \tag{2.7-6}$$

$$\Delta_p = \frac{1}{2}(b + a) \tag{2.7-7}$$

$$f(\hat{x}) \approx \left[\sum_{k=0}^{N-1} c_k T_k(\hat{x})\right] - \frac{1}{2}c_0 \tag{2.7-8}$$

Further details regarding Chebyshev approximations can be found in [PRES 92]. The need for Chebyshev approximations in this work will become apparent in *Chapter 3*.

2.8 VECTOR FITTING

Vector fitting (VF) is an algorithm used to create reduced order models of linear time-invariant systems based on their sampled response. These samples may come from experimental measurements or numerical simulations, and as such, VF is considered to be a data-driven approach to reduction. VF essentially seeks to determine an approximation of the rational transfer function $H(s)$, $\widetilde{H}(s)$, in the Laplace domain relating the input $U(s)$ to the output $Y(s)$ as

$$Y(s) = H(s)U(s) \tag{2.8-1}$$

given k measurements of the transfer function as [TRIV 20]

$$\widetilde{H}(j\omega_k) \simeq H(j\omega_k),\ \ k = 1, \dots, \bar{k}. \tag{2.8-2}$$

The following form is then chosen for the approximation $\widetilde{H}(s)$.

$$\widetilde{H}(s) = \frac{n(s)}{d(s)} = \frac{c_0^{(i)} + \sum_{n=1}^{\tilde{n}} \frac{c_n^{(i)}}{s - p_n^{(0)}}}{1 + \sum_{n=1}^{\tilde{n}} \frac{d_n^{(i)}}{s - p_n^{(0)}}} \tag{2.8-3}$$

The VF algorithm then seeks to determine the coefficients c_n and d_n of the above rational function of order $\tilde{n}$ and set of initial poles $p_n^{(0)}$ by minimizing the error function

$$e^2 = \frac{1}{\bar{k}} \sum_{k=1}^{\bar{k}} \left| H_k - \widetilde{H}(j\omega_k) \right|^2. \tag{2.8-4}$$

Substituting (2.8-3) into (2.8-4) and performing various mathematical manipulations covered in detail in [TRIV 20] leads to the actual vector fitting error function used to fit the model iteratively to the given samples,

$$\left(e_{SK}^{(i)}\right)^2 = \frac{1}{\bar{k}} \sum_{k=1}^{\bar{k}} \left| H_k \left(1 + \sum_{n=1}^{\tilde{n}} \frac{w_n^{(i)}}{j\omega_k - p_n^{(i-1)}} \right) - \left(r_0^{(i)} + \sum_{n=1}^{\tilde{n}} \frac{r_n^{(i)}}{j\omega_k - p_n^{(i-1)}} \right) \right|^2 \tag{2.8-5}$$

where p_n and r_n are the poles and residues of the model $\widetilde{H}(s)$. For multiple inputs and multiple outputs, (2.8-5) is updated as follows

$$\left(e_{SK}^{(i)}\right)^2 = \frac{1}{\bar{k}\bar{q}\bar{m}} \sum_{k=1}^{\bar{k}} \left\| \boldsymbol{H}_k \left(1 + \sum_{n=1}^{\tilde{n}} \frac{w_n^{(i)}}{j\omega_k - p_n^{(i-1)}} \right) - \left(\boldsymbol{R}_0^{(i)} + \sum_{n=1}^{\tilde{n}} \frac{\boldsymbol{R}_n^{(i)}}{j\omega_k - p_n^{(i-1)}} \right) \right\|_F^2 \tag{2.8-6}$$

where given samples $\boldsymbol{H}_k$ are matrices of size $\bar{q} \times \bar{m}$, $\|.\|_F$ is the Frobenius norm, and $\boldsymbol{R}_n^{(i)} \in \mathbb{C}^{\bar{q} \times \bar{m}}$. For the purposes of this thesis, it is of interest to utilize a real-valued formulation of VF, that is, one whose resulting poles and residues of the approximate transfer function are either real or complex-conjugate pairs. To ensure this condition, the approximate transfer function model is updated to the following form [TRIV 20]

$$\widetilde{\boldsymbol{H}}(s) = \boldsymbol{R}_0 + \sum_{n=1}^{\tilde{n}_r} \frac{\boldsymbol{R}_n}{s - p_n} + \sum_{n=\tilde{n}_r+1}^{\tilde{n}_r+\tilde{n}_c} \left[\frac{\boldsymbol{R}_n}{s - p_n} + \frac{\boldsymbol{R}_n^*}{s - p_n^*}\right] \tag{2.8-7}$$

where $\tilde{n}_r$ is the number of real poles and $\tilde{n}_c$ is the number of pairs of complex conjugate poles. The form of model in (2.8-7) can be easily converted into various representations depending on the scenario. One such representations that will be used in *Chapter 4* of this thesis is

$$\widetilde{\boldsymbol{H}}(s) = \boldsymbol{D} + \boldsymbol{C}\left(s\mathbb{I}_{N_A} - \boldsymbol{A}\right)^{-1}\boldsymbol{B} \tag{2.8-8}$$

which uses the state-space coefficient matrices $\boldsymbol{A}$, $\boldsymbol{B}$, $\boldsymbol{C}$, and $\boldsymbol{D}$ where

$$\boldsymbol{A} = \begin{bmatrix} \boldsymbol{A}_1 & & \\ & \ddots & \\ & & \boldsymbol{A}_{\tilde{n}_r+\tilde{n}_c} \end{bmatrix}, \boldsymbol{B} = \begin{bmatrix} \boldsymbol{B}_1 \\ \vdots \\ \boldsymbol{B}_{\tilde{n}_r+\tilde{n}_c} \end{bmatrix}, \boldsymbol{C} = [\boldsymbol{C}_1 \quad \dots \quad \boldsymbol{C}_{\tilde{n}_r+\tilde{n}_c}], \boldsymbol{D} = \boldsymbol{R}_0 \tag{2.8-9}$$

and $\mathbb{I}_{N_A}$ is an identity matrix equal to the size of $\boldsymbol{A}$. The mathematical procedure through which the poles and residues from (2.8-7) are used to compute the state-space coefficient matrices in (2.8-9) is described in [TRIV 20].

2.9 EXISTING APPLICATIONS OF MOR IN CEM

Model order reduction techniques for the analysis of lumped circuits can be considered well-established. This is not so for field analysis methods of CEM that result in a matrix equation similar to that in (2.3-20). The majority of mathematical-based reduction techniques (as opposed to those driven by physical insight [DAI 17]) are used in conjunction with the finite element method (FEM) (e.g. [JIN 21], [IOAN 21], [KUMA 18]). As was mentioned in *Chapter 1*, the method of moments in most cases is more desirable for antenna applications since it naturally handles problems with unbounded domains.

Reference [WEIL 01] adopts an MOR approach in a MoM framework for the field analysis of frequency selective surfaces (FSS). It uses the spectral-domain form of the modified Green's function for a planar infinite periodic surface (restricted to plane-wave excitation), Hermite polynomial interpolation of the MoM matrix over frequency in a manner appropriate to the particular spectral-domain formulation (although details are not given), rooftop basis functions, and establishes the reduced-order model via an Arnoldi algorithm. The work in this thesis instead uses the spatial-domain free-space Green's function that is suited to more general geometries and excitations, Chebyshev interpolation of the MoM matrix, and RWG basis functions.

References [HOCH 14], [GAN 19], and [CHEN 22] employ singular value decomposition (SVD) to develop reduced-order modes of the scattering operator. The approaches used in these works can be viewed as a form of *data-driven* model order reduction since they utilize the system's input-output behaviour to create the reduced model. In contrast, the Arnoldi-like MOR detailed throughout this work is a *matrix-driven* approach, relying on the Arnoldi iterative process for construction of basis vectors that approximate the action of a left-hand matrix on a right-hand vector. For MoM analysis with antenna arrays, generating data or "snapshots" of the system behaviour can be computationally expensive due to the density and large size of the problem matrix. This challenge is addressed in the MOR formulation in this work, while additionally allowing for easy integration into a field-circuit co-simulation framework, delivering significant benefits. Antenna-circuit co-simulation will be discussed in *Chapter 4*.

2.10 FIELD-CIRCUIT CO-SIMULATION METHODS

Work on field-circuit co-simulation has been briefly reviewed in [JIN 19] within the context of multi-physics problems generally. The former differs from some other multi-physics problems in that the temporal variations in the circuit model and the field model are of the same order and so requires their "two-way simultaneous coupling" [JIN 19]. Almost all accurate field-circuit co-simulation work of a general nature has utilized differential equation-based field analysis via the finite-element time-domain (FETD) method or discontinuous Galerkin time-domain (DGTD) method (e.g. [WANG 09], [LI 14], [ZHAN 22a]). In these field analysis formulations, the discretized operator matrices are sparse and reminiscent of those of circuit analysis, and so can be readily inter-connected to the similar lumped circuit analysis side. Time-domain integral equation modelling via the MoM for field analysis has successfully been used in [AYGÜ 04], [YILM 05], and [ZHAN 16]. Although the plane-wave time-domain (PWTD) and time-domain adaptive integral method (TD-AIM) are used for computational acceleration of the field analysis in [AYGÜ

04] and [YILM 05], respectively, I am not aware of any co-simulation approaches that use the MoM with MOR, which is done in this thesis and is shown to provide significant acceleration. A few commercially available simulators allow some level of field-circuit co-simulation. However, specific details on the computational methods involved, ways in which these have perhaps been accelerated, and so forth, are for obvious proprietary reasons not openly accessible. It is thus not possible to comment on these here.

2.11 SHAPE SYNTHESIS METHODS FOR ANTENNAS

Antenna design is typically done by selecting geometries from a group of well documented components, via insight or intuition, and arranging them in such a way to adhere to physical design constraints. Repeated computational electromagnetic (CEM) full-wave analysis is then performed to optimize the design such that its behaviour is sufficiently close to that which is desired. This is typically being done using optimization algorithms which can adjust prescribed features of the design. While the number of well documented components/designs is always expanding with ongoing research, this method of design is limited by what is currently known. Shape synthesis of antennas is not restricted by such a limitation. After constraints are set regarding material and the space the design may occupy, the shape synthesis approach essentially allows the electromagnetic physics to create the geometry/orientation of material needed to obtain the required performance. This is done by specifying an objective function that simultaneously incorporates each of the antenna metrics that are to be optimized. The layout of the material constituting the antenna is then iteratively modified to shape the structure around fixed port locations. CEM full-wave analysis is then used to compute the objective function of each structural iteration in order to quantify its performance. Shape synthesis techniques differ in the methodology they employ to create each new structure, as well as by the choice of optimization algorithm. As of now, the nomenclature used to describe such techniques has not yet become standardized in the microwave engineering field. This thesis will therefore refer to any automated changing of the material distribution, by the methods to be briefly reviewed below, as shape synthesis, thus encompassing what others have called “shape optimization” [TOIV 10], “topology optimization” or “inverse design” [GEDE 23].

Shape synthesis methods for antennas can generally be placed into two categories, discrete pixelation methods and gradient-based methods. Existing discrete pixelation shaping techniques function by subdividing an initial material structure into pixels. These pixels are then assigned values of either one or zero, indicating whether that pixel consists of conducting material (typically PEC) or not (free space), respectively. In works utilizing discrete pixelation and the MoM, such as in [JOHN 99], [AOKI 11], and [ALAK 21], the optimization variables take the values of the material properties in each pixel which correspond with the mesh elements used for the CEM analysis. While this technique yields results which are readily manufacturable in the sense that the material properties are clearly defined over the entire structure, in order to achieve an acceptable resolution so as to permit either narrow strips of conductor or narrow gaps of air, the dimensions of the pixels must be sufficiently small and thus the total number of optimization variables can become very large. Consequently, non-gradient optimization algorithms will struggle to find global minima in the objective function and an increasingly dense mesh will lead to larger and thus more computationally cumbersome repeated CEM analyses. Several discrete pixelation methods have been introduced in order to try to overcome these issues by redefining what are used as pixels. One such approach is the "subtractive" shape synthesis technique [MOHA 22]. This method was developed with regards to numerous observations regarding prior shaping methods and geometries of conventional designs (e.g. microstrip filters [HONG 04], waveguide filters [JIN 21]). Those being that discrete pixelation methods often reveal small groups of pixels that contribute little to the performance of the circuit, resulting in negligible difference in performance between a pixelated and its corresponding "smoothed" layout, and that much of the microwave circuit library can be arrived at by starting with a section of material and then subtracting material away in various shapes. It is these "subtractive shapes" which make up the discrete pixels in this method. As such, it is the size and location of these shapes (relatively few of them) on the starting surface which are designated as optimization variables. These shapes are systematically excised from the starting material distribution to generate the desired antenna/microwave circuit layout. The number of optimization variables used in this technique is thus significantly reduced given that they are no longer tied to mesh elements making non-gradient optimizers (e.g. genetic algorithms) viable, while the geometrical resolution becomes essentially infinite. This method hints that far more degrees of freedom are often used in shape synthesis (to ensure fine geometrical resolution) than are actually necessary for a given design problem. The disadvantage to such a technique is that each successive structure generated (as a result of altering the subtractive shapes) by the optimizer must be re-meshed in order to compute the objective function via the CEM analysis. Another form of discrete-pixelation is shown in [CAPE 19], [CAPE 23a], and [CAPE 23b] where pixels are selected to be individual basis functions. These individual basis functions are then added to or removed from an initial structure one at a time, evaluating the resulting objective function each time, and selecting the one which most improves the performance to be added or removed permanently. Every possible addition or removal is then revaluated given the initial structure now including this first permanent change until a second permanent alteration is made. This process is repeated until the objective function can no longer be improved. The initial structure is defined iteratively by a global genetic algorithm which uses the aforementioned process as a local optimization step within each global individual. The removal/addition of single basis functions can be done quickly via various mathematical tricks, such as the application of the Sherman-Morrison-Woodbury formula to the inversion of the impedance matrix, so as to not necessitate full matrix inverses upon the removal of a basis function. The limitations of this method however dawn from the enormous number of times the objective function must be computed along with the resulting shape of the structure. Each basis function addition/removal requires computation of the objective function which can be exceedingly cumbersome for problems involving complex objective functions that balance several performance metrics over many frequencies, this burden being further emphasized in medium- to large-sized problems with many basis functions. Additionally, the removal of a single basis function is equivalent physically to cutting a narrow slit in the conducting material. This can result in a final structure that is littered with small slits yielding it difficult to fabricate.

Gradient-based methods or continuous versions of pixelation-based methods, reviewed instructively (albeit in a magneto-quasistatic context) in [LUCC 22], are those which allow for a continuous variation in the material properties (e.g. conductivity [HASS 14], [TUCE 23]; relative permittivity [HAMM 25], [MOLE 18], [HADJ 25], [HAMM 22]) of the pixels, permitting the use of gradient-based optimization algorithms which are adept at handling an enormous number of design variables. These methods depend on the following two conditions to achieve this. Foremost is the ability to rapidly compute the gradient of the objective function with respect to each of the design variables (e.g. the conductivity of the material in each pixel). This has been accomplished through the use of so-called adjoint sensitivity techniques [LUCC 22]. Computationally rapid means of determining such gradient information, for density-based approaches, has been available for quantities such as port parameters [NIKO 06], modal fields [HAMM 25], radiated fields [GHAS 13], [WANG 25], [WANG 17], [GUO 23], [WHIT 22], and more recently directly for antenna gain [TUCE 24], but their use with composite objective functions such as those in [KHAN 22] has not appeared. Secondly, the formulation must be such that it penalizes designs that do not have material distributions that are binary. So-called filtering and projection (e.g. [GEDE 23]) are needed to nudge the final design towards a binary one, and often some post-processing of the shaped object is needed to realize complete binarization. In electromagnetics-related devices relying on localized energy storage (resonances) for device operation, or similar, the use of such projection may lead to less-than-optimal solutions, as observed in [HASS 14], [TUCE 23]. Work on overcoming such a problem is ongoing [HAMM 25], [TUCE 25]. Intuition may lead one to surmise that a method similar to the subtractive shape synthesis technique described earlier that uses geometrical parameters as the design variables would alleviate the need for the above filtering and projection. However, computationally efficient means of obtaining gradient information directly in terms of geometrical variables, on par with that of the material-density-based route, is not readily available [NIKO 04], [KATA 14], especially in the integral equation CEM of interest here.

The various advantages, and drawbacks, of these methods will be touched on and referenced further in *Chapter 5*.

2.12 CONCLUDING REMARKS

The purpose of this chapter was to relay background information to the reader that is important in understanding and contextualizing the contributions this thesis will present in the chapters that follow. First, *Sections 2.2* through *2.3* covered antenna fundamentals and performance indices along with the MoM analysis of EM scattering from PEC objects. These concepts form the foundation of the work that will be presented in all of the upcoming chapters, as the ultimate goal of this work is to increase the viability of historically long antenna shaping CEM optimization and analysis routines caused by repeated laborious MoM matrix solving. Next, the MNA circuit formulation, MOR applied to linear circuit analysis, and multi-port MOR and its clustered alternative in circuit analysis were covered in *Sections 2.4* through *2.6*. These sections serve as an introduction to MOR and will be referenced heavily throughout the thesis. It is this technique that we wish (albeit with the considerable developments that comprise *Chapter 3*) to apply to the MoM to contribute to the aforementioned computational acceleration. *Section 2.7* then highlighted the basics of the Chebyshev approximation of functions over a specified interval. As will be seen in *Chapter 3*, the Chebyshev approximation will prove to be a crucial stepping stone in the application of MOR to the MoM. The Chebyshev approximation was then followed in *Section 2.8* by a brief overview of those aspects of vector fitting relevant to this thesis. This algorithm will be used in *Chapter 4* when non-linear circuit elements are introduced into the antenna-circuit co-simulation framework. Finally, *Sections 2.9* through 2*.11* offered a literature review of prior contributions pertaining to the application of MOR to CEM work, field-circuit co-simulation methods, and shape synthesis methods for antennas. These sections detailed existing works that are most relevant to the new contributions that will be presented in *Chapters 3* through *5*, respectively. They also highlighted the drawbacks or gaps in the literature that this thesis will seek to address or fill. In addition, *Section 2.11* also covered the motivation for antenna shape synthesis, as well as detailing its general methodology in a variety of implementations. This will have hopefully provided the reader with sufficient understanding of the advantages of antenna shape synthesis that make it a highly promising form of design, but also its disadvantages that have thus far limited it from widespread use.

CHAPTER 3

Application of Model Order Reduction to the Method of Moments

3.1 INTRODUCTION

Among other topics, the previous chapter reviewed an existing MoM formulation, the notion of MOR used in linear circuit analysis, and the Chebyshev approximation employed to approximate a certain function over a specific interval by a series of Chebyshev polynomials and their coefficients. This chapter seeks to adopt and combine these three concepts in order to develop a MoM solution to model the electromagnetic radiation/scattering from PEC objects which applies MOR techniques. The ultimate objective of this formulation is to decrease the computational burden associated with solving the MoM matrix equation especially when this needs to be done at many frequencies. This will be achieved in this chapter by developing an "approximation" of the MoM matrix elements and subsequent application of MOR to the modified matrix equation, as follows:

- Section 3.2: Approximation of the Moment Method Matrix
- Section 3.3: Application of Model Order Reduction to the Modified Matrix Equation
- Section 3.4: Verification of the Model Order Reduction Solution
- Section 3.5: Concluding Remarks

3.2 APPROXIMATION OF THE MOMENT METHOD MATRIX

In order to apply the principles of model order reduction described in *Section 2.5* to the moment method solution of *Section 2.3*, it is evident that the impedance matrix $\boldsymbol{Z}(s)$ in equation (2.3-20) must be decomposed into a power series with respect to frequency as follows,

$$\boldsymbol{Z}(s) = \boldsymbol{Z}_0 + s\boldsymbol{Z}_1 + s^2\boldsymbol{Z}_2 + \cdots + s^{N-1}\boldsymbol{Z}_{N-1} \tag{3.2-1}$$

where $s = j\omega$. For ease of understanding, the key equations found at the end of *Section 2.3.5* are repeated again here.

$$Z_{mn} = l_m j\omega\left(\bar{A}_{mn}^{+}\cdot\frac{\bar{\rho}_m^{c+}}{2} + \bar{A}_{mn}^{-}\cdot\frac{\bar{\rho}_m^{c-}}{2}\right) + \Phi_{mn}^{-} - \Phi_{mn}^{+} \tag{3.2-2}$$

$$\begin{aligned}\bar{A}_{mn}^{\pm} = \frac{\mu}{4\pi}\Bigg[&\frac{l_n}{2A_n^{+}}\int_{T_n^{+}}\bar{\rho}_n^{+}(\bar{r}_n^{+\prime})\frac{e^{-jk\left|\bar{r}_m^{C\pm}-\bar{r}_n^{+\prime}\right|}}{\left|\bar{r}_m^{C\pm}-\bar{r}_n^{+\prime}\right|}dS' \\ &+\frac{l_n}{2A_n^{-}}\int_{T_n^{-}}\bar{\rho}_n^{-}(\bar{r}_n^{-\prime})\frac{e^{-jk\left|\bar{r}_m^{C\pm}-\bar{r}_n^{-\prime}\right|}}{\left|\bar{r}_m^{C\pm}-\bar{r}_n^{-\prime}\right|}dS'\Bigg]\end{aligned} \tag{3.2-3}$$

$$\Phi_{mn}^{\pm} = \frac{j}{4\pi\omega\varepsilon}\left[\frac{l_n}{A_n^{+}}\int_{T_n^{+}}\frac{e^{-jk\left|\bar{r}_m^{C\pm}-\bar{r}_n^{+\prime}\right|}}{\left|\bar{r}_m^{C\pm}-\bar{r}_n^{+\prime}\right|}dS' - \frac{l_n}{A_n^{-}}\int_{T_n^{-}}\frac{e^{-jk\left|\bar{r}_m^{C\pm}-\bar{r}_n^{-\prime}\right|}}{\left|\bar{r}_m^{C\pm}-\bar{r}_n^{-\prime}\right|}dS'\right] \tag{3.2-4}$$

As is seen from the above three equations, the frequency dependencies in the magnetic vector potential and the electric scalar potential are found primarily inside of exponential functions. Thus, in order to represent $\boldsymbol{Z}(s)$ in the form depicted in (3.2-1), each exponential term in (3.2-3) and (3.2-4) must be approximated by a polynomial in terms of s. The approximation that will be used is the Chebyshev approximation described in *Section 2.7*. This approximation allows for the exponential terms in the above equations to be written as,

$$e^{-s\xi^{\pm}} \approx \left[\sum_{k=0}^{N_c-1} c_k T_k(s)\right] - \frac{1}{2}c_0 \tag{3.2-5}$$

where $T_k(s)$ are the Chebyshev polynomials defined in Table 2.7-1, as well as in equations (2.7-1) and (2.7-2), N_c is the number of Chebyshev polynomials selected for the approximation, $\xi^{\pm}$ is

$$\xi^{\pm} = \sqrt{\mu\varepsilon}\left|\vec{r}_m^{C\pm} - \vec{r}_n^{\pm\prime}\right| \tag{3.2-6}$$

given $k = \omega\sqrt{\mu\varepsilon}$ and with the "$\pm$" in $\xi^{\pm}$ corresponding to the appropriate "+" or "$-$" of the second term, while c_k are the Chebyshev polynomial coefficients seen in (2.7-4), which are defined once more considering the specific exponential function of interest as

$$c_k = \frac{2}{N_c}\sum_{i=1}^{N_c} e^{-\left(\cos\left(\frac{\pi\left(i-\frac{1}{2}\right)}{N_c}\right)\Delta_m+\Delta_p\right)\xi^{\pm}} \cos\left(\frac{\pi k\left(i-\frac{1}{2}\right)}{N_c}\right) \qquad k = 0, 1, 2, \cdots, N_c - 1. \tag{3.2-7}$$

Recall that the Chebyshev approximation yields results over an interval of $[-1, 1]$. Thus, the inclusion of the variables Δ_m and Δ_p in (3.2-7) are used to approximate the function over an arbitrary interval of s, $[s_{min}, s_{max}]$. These variables were defined in (2.7-6) and (2.7-7). Applying (3.2-5), the exponential terms in (3.2-3) and (3.2-4) can be approximated by a polynomial in terms of s and coefficients $b_i(\xi^{\pm})$.

$$e^{-s\xi^{\pm}} \approx b_0(\xi^{\pm}) + b_1(\xi^{\pm})s + b_2(\xi^{\pm})s^2 + \cdots + b_{N_c-1}(\xi^{\pm})s^{N_c-1} = \sum_{d=0}^{N_c-1} b_d(\xi^{\pm})s^d \tag{3.2-8}$$

Next, the integration in equations (3.2-3) and (3.2-4) is handled via the method described in *Section 2.3.5* and specifically that described in equation (2.3-25), which is repeated below.

$$\int_{T_n^{\pm}} f\left(\bar{r}_n^{\pm\prime}\right)dS' = \frac{A_n^{\pm}}{9}\sum_{p=1}^{9} f\left(\bar{r}_{n_p}^{c\pm}\right) \tag{3.2-9}$$

Substituting (3.2-8) and (3.2-9) into (3.2-3) and (3.2-4) yields,

$$\bar{A}_{mn}^{\pm} = \frac{\eta l_n}{72\pi}\left[\sum_{p=1}^{9}\left(\frac{\bar{\rho}_n^{+}\left(\bar{r}_{n_p}^{C+}\right)}{\xi^{+}}\sum_{d=0}^{N_c-1}\left[b_d(\xi^{+})s^d\right] + \frac{\bar{\rho}_n^{-}\left(\bar{r}_{n_p}^{C-}\right)}{\xi^{-}}\sum_{d=0}^{N_c-1}\left[b_d(\xi^{-})s^d\right]\right)\right] \tag{3.2-10}$$

and

$$\Phi_{mn}^{\pm} = \frac{-l_n}{36\pi s\varepsilon\sqrt{\mu\varepsilon}}\left[\sum_{p=1}^{9}\left(\frac{1}{\xi^{+}}\sum_{d=0}^{N_c-1}[b_d(\xi^{+})s^d] - \frac{1}{\xi^{-}}\sum_{d=0}^{N_c-1}[b_d(\xi^{-})s^d]\right)\right] \tag{3.2-11}$$

where $b_d(\xi^{+})$ and $b_d(\xi^{-})$ are equivalent to $b_d(\xi^{\pm})$ however with the "+" or "–" of the second term now explicitly defined, yielding

$$\xi^{+} = \sqrt{\mu\varepsilon}\left|\vec{r}_m^{\,C\pm} - \vec{r}_{n_p}^{\,c+'}\right| \qquad \xi^{-} = \sqrt{\mu\varepsilon}\left|\vec{r}_m^{\,C\pm} - \vec{r}_{n_p}^{\,c-'}\right|, \tag{3.2-12}$$

and $\eta = \sqrt{\mu/\varepsilon}$. The vector $\vec{r}_{n_p}^{\,c\pm'}$ spans from the origin to the centre of the p^{th} sub triangle within the plus or minus triangle associated with the n^{th} edge. It is important to note that the coefficients $b_d(\xi^{\pm})$ are found by expanding the summation in (3.2-5) and collecting like powers of s. Since s must be excluded from the computation of the $\boldsymbol{Z}_i$ matrices in (3.2-1), the summation,

$$\sum_{d=0}^{N_c-1}[b_d(\xi^{\pm})s^d] \tag{3.2-13}$$

would be represented by a vector of computed coefficients as follows,

$$\boldsymbol{B} = \begin{bmatrix} b_0(\xi^{\pm}) \\ b_1(\xi^{\pm}) \\ b_2(\xi^{\pm}) \\ \vdots \\ b_{N_c-1}(\xi^{\pm}) \end{bmatrix} \tag{3.2-14}$$

with the understanding that $b_d(\xi^{\pm})$ is the coefficient of s^d. Substituting $\boldsymbol{B}$ into (3.2-10) and (3.2-11) results in the following four equations,

$$\overline{\boldsymbol{A}}_{mn}^{+} = \frac{\eta l_n}{72\pi}\left[\sum_{p=1}^{9}\left(\frac{\bar{\rho}_n^{+}\left(\bar{r}_{n_p}^{C+}\right)}{\xi^{++}}\boldsymbol{B}^{++} + \frac{\bar{\rho}_n^{-}\left(\bar{r}_{n_p}^{C-}\right)}{\xi^{+-}}\boldsymbol{B}^{+-}\right)\right] \tag{3.2-15}$$

$$\overline{\boldsymbol{A}}_{mn}^{-} = \frac{\eta l_n}{72\pi}\left[\sum_{p=1}^{9}\left(\frac{\bar{\rho}_n^{+}\left(\bar{r}_{n_p}^{C+}\right)}{\xi^{-+}}\boldsymbol{B}^{-+} + \frac{\bar{\rho}_n^{-}\left(\bar{r}_{n_p}^{C-}\right)}{\xi^{--}}\boldsymbol{B}^{--}\right)\right] \tag{3.2-16}$$

$$\boldsymbol{\Phi}_{mn}^{+} = \frac{-l_n}{36\pi s\varepsilon\sqrt{\mu\varepsilon}}\left[\sum_{p=1}^{9}\left(\frac{1}{\xi^{++}(\mu\varepsilon)^{-\frac{1}{2}}}\boldsymbol{B}^{++} - \frac{1}{\xi^{+-}(\mu\varepsilon)^{-\frac{1}{2}}}\boldsymbol{B}^{+-}\right)\right] \tag{3.2-17}$$

$$\boldsymbol{\Phi}_{mn}^{-} = \frac{-l_n}{36\pi s\varepsilon\sqrt{\mu\varepsilon}}\left[\sum_{p=1}^{9}\left(\frac{1}{\xi^{-+}}\boldsymbol{B}^{-+} - \frac{1}{\xi^{--}}\boldsymbol{B}^{--}\right)\right] \tag{3.2-18}$$

where an additional plus or minus superscript has been added now that the plus and minus component of the magnetic vector potential and the electric scalar potential have been explicitly separated, yielding

$$\begin{aligned} \xi^{++} &= \sqrt{\mu\varepsilon}\left|\vec{r}_m^{C+} - \vec{r}_{n_p}^{c+'}\right| \qquad \xi^{+-} = \sqrt{\mu\varepsilon}\left|\vec{r}_m^{C+} - \vec{r}_{n_p}^{c-'}\right| \\ \xi^{-+} &= \sqrt{\mu\varepsilon}\left|\vec{r}_m^{C-} - \vec{r}_{n_p}^{c+'}\right| \qquad \xi^{--} = \sqrt{\mu\varepsilon}\left|\vec{r}_m^{C-} - \vec{r}_{n_p}^{c-'}\right|. \end{aligned} \tag{3.2-19}$$

Each superscript combination of $\boldsymbol{B}$ is of course defined as in (3.2-14) however with the matching ξ defined above. The bolding of the vector and scalar potential symbols in (3.2-15)-(3.2-18) is to indicate that these are matrices. The vector potentials are matrices of size $N_c \times 3$ due to the x, y, and z components of $\bar{\rho}_n^{\pm}\left(\bar{r}_{n_p}^{C\pm}\right)$, while the scalar potentials are matrices of size $N_c \times 1$. These matrices can finally be substituted into (3.2-2).

$$Z_{mn} = l_m s\left(\overline{\boldsymbol{A}}_{mn}^{+} \cdot \frac{\bar{\rho}_m^{c+}}{2} + \overline{\boldsymbol{A}}_{mn}^{-} \cdot \frac{\bar{\rho}_m^{c-}}{2}\right) + \frac{1}{s}\left(\widehat{\boldsymbol{\Phi}}_{mn}^{-} - \widehat{\boldsymbol{\Phi}}_{mn}^{+}\right) \tag{3.2-20}$$

The scalar potential in equations (3.2-17) and (3.2-18) both have an s in the denominator. Equation (3.2-20) has factored this s out of these equations, thus yielding $\widehat{\boldsymbol{\Phi}}_{mn}^{\pm}$, where the "hat" denotes the scalar potentials with the removal of $\frac{1}{s}$. This $\frac{1}{s}$ in (3.2-20) is problematic since the model order reduction methods discussed in *Section 2.5* require a power series of the form seen in (3.2-1), containing no negative powers of s. This issue can be resolved by multiplying both sides of the matrix equation in (2.3-20) by s, yielding,

$$s\boldsymbol{Z}(s)\boldsymbol{I}(s) = s\boldsymbol{V}(s). \tag{3.2-21}$$

Incorporating the s on the left side of (3.2-21) into each element of $\boldsymbol{Z}(s)$ results in

$$Z_{mn} = l_m s^2 \left(\overline{\boldsymbol{A}}_{mn}^{+} \cdot \frac{\bar{\rho}_m^{c+}}{2} + \overline{\boldsymbol{A}}_{mn}^{-} \cdot \frac{\bar{\rho}_m^{c-}}{2} \right) + (\widehat{\boldsymbol{\Phi}}_{mn}^{-} - \widehat{\boldsymbol{\Phi}}_{mn}^{+}). \tag{3.2-22}$$

As a result of the s^2 in (3.2-22), the highest power in the series in (3.2-1) will thus be raised by two. For example, if the number of Chebyshev polynomials selected are four, Table 2.7-1 indicates that the highest power of s will be s^3. However, due to the s^2 in (3.2-22), the highest power will now be s^5, thus yielding six $\boldsymbol{Z}_i$ matrices in (3.2-1). As such, (3.2-1) will be adjusted as follows.

$$\boldsymbol{Z}(s) = \boldsymbol{Z}_0 + s\boldsymbol{Z}_1 + s^2\boldsymbol{Z}_2 + \cdots + s^{N_c+1}\boldsymbol{Z}_{N_c+1} \tag{3.2-23}$$

The final step to obtain the above form is to expand and collect similar power of s terms in (3.2-22). Recall that each of the vector and scalar potential terms is actually a matrix or vector containing coefficients of powers of s. This is summarized below where a dot product is computed with each row of $\overline{\boldsymbol{A}}_{mn}^{\pm}$.

$$\overline{\boldsymbol{A}}_{mn}^{+} \cdot \frac{\bar{\rho}_m^{c+}}{2} = \begin{bmatrix} A_{x_0}^{+(mn)} & A_{y_0}^{+(mn)} & A_{z_0}^{+(mn)} \\ A_{x_1}^{+(mn)} & A_{y_1}^{+(mn)} & A_{z_1}^{+(mn)} \\ A_{x_2}^{+(mn)} & A_{y_2}^{+(mn)} & A_{z_2}^{+(mn)} \\ \vdots & \vdots & \vdots \\ A_{x_{N_c-1}}^{+(mn)} & A_{y_{N_c-1}}^{+(mn)} & A_{z_{N_c-1}}^{+(mn)} \end{bmatrix} \frac{\bar{\rho}_m^{c+}}{2} = \begin{bmatrix} A_0^{+(mn)} \\ A_1^{+(mn)} \\ A_2^{+(mn)} \\ \vdots \\ A_{N_c-1}^{+(mn)} \end{bmatrix} \tag{3.2-24}$$

$$\overline{\boldsymbol{A}}_{mn}^{-} \cdot \frac{\bar{\rho}_m^{c-}}{2} = \begin{bmatrix} A_{x_0}^{-(mn)} & A_{y_0}^{-(mn)} & A_{z_0}^{-(mn)} \\ A_{x_1}^{-(mn)} & A_{y_1}^{-(mn)} & A_{z_1}^{-(mn)} \\ A_{x_2}^{-(mn)} & A_{y_2}^{-(mn)} & A_{z_2}^{-(mn)} \\ \vdots & \vdots & \vdots \\ A_{x_{N_c-1}}^{-(mn)} & A_{y_{N_c-1}}^{-(mn)} & A_{z_{N_c-1}}^{-(mn)} \end{bmatrix} \frac{\bar{\rho}_m^{c-}}{2} = \begin{bmatrix} A_0^{-(mn)} \\ A_1^{-(mn)} \\ A_2^{-(mn)} \\ \vdots \\ A_{N_c-1}^{-(mn)} \end{bmatrix} \tag{3.2-25}$$

$$\widehat{\boldsymbol{\Phi}}_{mn}^{+} = \begin{bmatrix} \widehat{\Phi}_0^{+(mn)} \\ \widehat{\Phi}_1^{+(mn)} \\ \widehat{\Phi}_2^{+(mn)} \\ \vdots \\ \widehat{\Phi}_{N_c-1}^{+(mn)} \end{bmatrix} \qquad \widehat{\boldsymbol{\Phi}}_{mn}^{-} = \begin{bmatrix} \widehat{\Phi}_0^{-(mn)} \\ \widehat{\Phi}_1^{-(mn)} \\ \widehat{\Phi}_2^{-(mn)} \\ \vdots \\ \widehat{\Phi}_{N_c-1}^{-(mn)} \end{bmatrix} \tag{3.2-26}$$

Computing and substituting (3.2-24)-(3.2-26) into (3.2-22) and simplifying and collecting like terms of s thus yields a power series expression of Z_{mn} in the following form, recalling that the vector notation above stemmed from that used for $\boldsymbol{B}$ in (3.2-14), which contained coefficients of powers of s used in the summation in (3.2-13) to approximate the exponential terms in the magnetic vector and electric scalar potentials.

$$Z_{mn} = Z_0^{(mn)} + sZ_1^{(mn)} + s^2 Z_2^{(mn)} + \cdots + s^{N_c+1} Z_{N_c+1}^{(mn)}. \tag{3.2-27}$$

Computing every combination of m and n and storing each $Z_i{}^{mn}$ in its respective matrix $\boldsymbol{Z}_i$ will finally yield an appropriate form of the $\boldsymbol{Z}$ matrix that can be used in model order reduction. The modified method of moments matrix equation can now finally be written as

$$\left[\boldsymbol{Z}_0 + s\boldsymbol{Z}_1 + s^2\boldsymbol{Z}_2 + \cdots + s^{N_c+1}\boldsymbol{Z}_{N_c+1}\right]\boldsymbol{I}(s) = s\boldsymbol{V}(s). \tag{3.2-28}$$

It is also worth noting that the $\boldsymbol{Z}_i$ matrices in (3.2-28) that are multiplied by large powers of s will contain very small values. To avoid encountering singularity issues when working with these matrices, they are normalized by powers of the speed of light and a normalization factor n_f

$$\boldsymbol{Z}_{i_{norm}} = \boldsymbol{Z}_i {n_f}^i c^i \tag{3.2-29}$$

for $i = 0, 1, 2, \cdots, N_c + 1$. An acceptable normalization factor was found through testing to be 180. To account for this normalization the set of frequencies s_{norm} are introduced.

$$s_{norm} = \frac{s}{n_f c} \tag{3.2-30}$$

It is thus understood that any instances of s which are multiplied by any matrix $\boldsymbol{Z}_i$ in the upcoming sections have been normalized.

3.3 APPLICATION OF MODEL ORDER REDUCTION TO THE MODIFIED MATRIX EQUATION

Now that the impedance matrix $\boldsymbol{Z}(s)$ has been written as a power series in terms of s, MOR can be used to compute a reduced matrix equation which can be solved quickly at many frequencies. However, it is evident from (3.2-22) that regardless of N_c, due to the s^2 in front of the vector potentials, the power series approximation for $\boldsymbol{Z}(s)$ will always be of order two or higher. MOR, however, requires the left side of the matrix equation to have only a linear polynomial of s. Therefore, the linearization technique in *Section 2.5.3* must be employed. Letting N_e be the total number of inter-element edges in the antenna mesh, this linearization is summarized below.

$$\begin{aligned}
&\left(\begin{bmatrix} \boldsymbol{Z}_0 & \boldsymbol{0} & \boldsymbol{0} & & \boldsymbol{0} \\ \boldsymbol{0} & \mathbb{I}_{N_e} & \boldsymbol{0} & \cdots & \\ \boldsymbol{0} & \boldsymbol{0} & \mathbb{I}_{N_e} & & \vdots \\ & \vdots & & \ddots & \\ \boldsymbol{0} & & \cdots & & \mathbb{I}_{N_e} \end{bmatrix}_{N_e(N_c+1)\times N_e(N_c+1)} \right. \\
&\left. + s \begin{bmatrix} \boldsymbol{Z}_1 & \boldsymbol{Z}_2 & \boldsymbol{Z}_3 & & \boldsymbol{Z}_{N_c+1} \\ -\mathbb{I}_{N_e} & \boldsymbol{0} & \boldsymbol{0} & \cdots & \\ \boldsymbol{0} & -\mathbb{I}_{N_e} & \boldsymbol{0} & & \vdots \\ & \vdots & & \ddots & \\ \boldsymbol{0} & \cdots & \boldsymbol{0} & -\mathbb{I}_{N_e} & \boldsymbol{0} \end{bmatrix}_{N_e(N_c+1)\times N_e(N_c+1)} \right) \begin{bmatrix} \boldsymbol{I}(s) \\ \boldsymbol{I}_1(s) \\ \boldsymbol{I}_2(s) \\ \vdots \\ \boldsymbol{I}_{N_c}(s) \end{bmatrix}_{N_e(N_c+1)\times 1} \\
&= s \begin{bmatrix} \boldsymbol{V}(s) \\ \boldsymbol{0} \\ \boldsymbol{0} \\ \vdots \\ \boldsymbol{0} \end{bmatrix}_{N_e(N_c+1)\times 1}
\end{aligned} \tag{3.3-1}$$

$\mathbb{I}_{N_e}$ is an identity matrix of size $N_e \times N_e$ and $\boldsymbol{I}_1(s) = s\boldsymbol{I}(s)$, $\boldsymbol{I}_2(s) = s\boldsymbol{I}_1(s)$, $\boldsymbol{I}_3(s) = s\boldsymbol{I}_2(s)$, …, $\boldsymbol{I}_{N_C}(s) = s\boldsymbol{I}_{N_c-1}(s)$. Equation (3.3-1) can then be written as follows,

$$(\boldsymbol{P} + s\boldsymbol{T})\tilde{\boldsymbol{I}}(s) = s\tilde{\boldsymbol{V}}(s) \tag{3.3-2}$$

where $\tilde{\boldsymbol{I}}(s)$ and $\tilde{\boldsymbol{V}}(s)$ have replaced $\boldsymbol{X}(s)$ and $\boldsymbol{b}(s)$ respectively from equation (2.5-2) and recalling that the right-side vector must be multiplied by s in order to remove the $\frac{1}{s}$ term from the power series representation of $\boldsymbol{Z}(s)$. The MOR derivation described in *Section 2.5.2* stems from a Taylor Series expansion of $\boldsymbol{X}(s)$ centred at zero, as is seen in equation (2.5-3). In antenna applications, s is defined at frequencies much higher than zero, thus requiring an MOR solution centered at an arbitrary frequency s_0 that is within the desired range of test frequencies. A Taylor Series expansion of $\tilde{\boldsymbol{I}}(s)$ centred around s_0 is thus expressed as follows,

$$\tilde{\boldsymbol{I}} = \sum_{i=0}^{\infty} \boldsymbol{M}_{i,s_0}(s - s_0)^i \tag{3.3-3}$$

where $\boldsymbol{M}_{i,s_0}$ is the i^{th} moment of $\tilde{\boldsymbol{I}}$ centred at s_0. Substituting (3.3-3) into (3.3-2) yields

$$(\boldsymbol{P} + s\boldsymbol{T}) \sum_{i=0}^{\infty} \boldsymbol{M}_{i,s_0}(s - s_0)^i = s\tilde{\boldsymbol{V}}. \tag{3.3-4}$$

Adding and subtracting $s_0\boldsymbol{T}$ to the left side and $s_0\tilde{\boldsymbol{V}}$ to the right side of (3.3-4) gives

$$(\boldsymbol{P} + s_0\boldsymbol{T} - s_0\boldsymbol{T} + s\boldsymbol{T}) \sum_{i=0}^{\infty} \boldsymbol{M}_{i,s_0}(s - s_0)^i = s\tilde{\boldsymbol{V}} - s_0\tilde{\boldsymbol{V}} + s_0\tilde{\boldsymbol{V}} \tag{3.3-5}$$

which can be rewritten as

$$(\boldsymbol{P} + (s - s_0)\boldsymbol{T} + s_0\boldsymbol{T}) \sum_{i=0}^{\infty} \boldsymbol{M}_{i,s_0}(s - s_0)^i = (s - s_0)\tilde{\boldsymbol{V}} + s_0\tilde{\boldsymbol{V}}. \tag{3.3-6}$$

Defining $\bar{s} = s - s_0$ then yields

$$(\boldsymbol{P} + \bar{s}\boldsymbol{T} + s_0\boldsymbol{T})\sum_{i=0}^{\infty}\boldsymbol{M}_{i,s_0}\bar{s}^i = \bar{s}\widetilde{\boldsymbol{V}} + s_0\widetilde{\boldsymbol{V}}. \tag{3.3-7}$$

Defining $\widetilde{\boldsymbol{P}} = \boldsymbol{P} + s_0\boldsymbol{T}$ finally results in

$$\left(\widetilde{\boldsymbol{P}} + \bar{s}\boldsymbol{T}\right)\sum_{i=0}^{\infty}\boldsymbol{M}_{i,s_0}\bar{s}^i = \bar{s}\widetilde{\boldsymbol{V}} + s_0\widetilde{\boldsymbol{V}}. \tag{3.3-8}$$

The moments $\boldsymbol{M}_{i,s_0}$ can then be found by equating powers of $\bar{s}$ on both sides of (3.3-8).

$$\bar{s}^0: \quad \left(\widetilde{\boldsymbol{P}} + \bar{s}\boldsymbol{T}\right)\boldsymbol{M}_{0,s_0} = \bar{s}\widetilde{\boldsymbol{V}} + s_0\widetilde{\boldsymbol{V}} \longrightarrow \boldsymbol{M}_{0,s_0} = \widetilde{\boldsymbol{P}}^{-1}s_0\widetilde{\boldsymbol{V}} \tag{3.3-9}$$

$$\bar{s}^1: \quad \left(\widetilde{\boldsymbol{P}} + \bar{s}\boldsymbol{T}\right)\left(\boldsymbol{M}_{0,s_0} + \bar{s}\boldsymbol{M}_{1,s_0}\right) = \bar{s}\widetilde{\boldsymbol{V}} + s_0\widetilde{\boldsymbol{V}} \longrightarrow \boldsymbol{M}_{1,s_0} = \widetilde{\boldsymbol{P}}^{-1}\left(\widetilde{\boldsymbol{V}} - \boldsymbol{T}\boldsymbol{M}_{0,s_0}\right) \tag{3.3-10}$$

$$\bar{s}^2: \quad \left(\widetilde{\boldsymbol{P}} + \bar{s}\boldsymbol{T}\right)\left(\boldsymbol{M}_{0,s_0} + \bar{s}\boldsymbol{M}_{1,s_0} + \bar{s}^2\boldsymbol{M}_{2,s_0}\right) = \bar{s}\widetilde{\boldsymbol{V}} + s_0\widetilde{\boldsymbol{V}} \longrightarrow \boldsymbol{M}_{2,s_0} = -\widetilde{\boldsymbol{P}}^{-1}\boldsymbol{T}\boldsymbol{M}_{1,s_0} \tag{3.3-11}$$

$$\bar{s}^3: \left(\widetilde{\boldsymbol{P}} + \bar{s}\boldsymbol{T}\right)\left(\boldsymbol{M}_{0,s_0} + \bar{s}\boldsymbol{M}_{1,s_0} + \bar{s}^2\boldsymbol{M}_{2,s_0} + \bar{s}^3\boldsymbol{M}_{2,s_0}\right) = \bar{s}\widetilde{\boldsymbol{V}} + s_0\widetilde{\boldsymbol{V}} \longrightarrow \boldsymbol{M}_{3,s_0} = -\widetilde{\boldsymbol{P}}^{-1}\boldsymbol{T}\boldsymbol{M}_{2,s_0} \tag{3.3-12}$$

$$\vdots$$

To summarize equations (3.3-9)-(3.3-12) and subsequent powers of $\bar{s}$, let

$$\boldsymbol{A} = -\widetilde{\boldsymbol{P}}^{-1}\boldsymbol{T} \tag{3.3-13}$$

$$\boldsymbol{R} = \widetilde{\boldsymbol{P}}^{-1}\left(\widetilde{\boldsymbol{V}} - \boldsymbol{T}\boldsymbol{M}_{0,s_0}\right) \tag{3.3-14}$$

then,

$$\boldsymbol{M}_{0,s_0} = \widetilde{\boldsymbol{P}}^{-1} s_0 \widetilde{\boldsymbol{V}} \tag{3.3-15}$$

and

$$\left[\boldsymbol{M}_{1,s_0}, \boldsymbol{M}_{2,s_0}, \boldsymbol{M}_{3,s_0}, \dots, \boldsymbol{M}_{i,s_0}\right] = \left[\boldsymbol{R}, \boldsymbol{A}\boldsymbol{R}, \boldsymbol{A}^2\boldsymbol{R}, \dots, \boldsymbol{A}^{i-1}\boldsymbol{R}\right]. \tag{3.3-16}$$

Comparing the results in (3.3-13)-(3.3-16) to those in (2.5-7)-(2.5-9), it can be observed that the multiplication by s on the right side of the initial matrix equation seen in (3.3-2) means that the zeroth moment must now be computed explicitly in order to form the matrix $\boldsymbol{Q}$ which is to be used to reduce the size of the original $N_e \times N_e$ system. With this zeroth moment computed, $\boldsymbol{A}$ and $\boldsymbol{R}$ can then be computed and used in the Arnoldi algorithm outlined in Figure 2.5-2 to create the matrix $\boldsymbol{Q}$. The zeroth moment can then be incorporated into the orthogonal basis $\boldsymbol{Q}$ by using standard QR decomposition since this moment has already been computed.

Matrix $\boldsymbol{Q}$ can now be used to reduce the expanded system using the methods described in equations (2.5-19)-(2.5-21) to create the reduced system in (2.5-22). This system can then be solved at many frequencies and expanded using (2.5-23) to produce the expanded vector $\tilde{\boldsymbol{I}}(s)$. All but the first N_e rows of $\tilde{\boldsymbol{I}}(s)$ can then be discarded, as it is only these rows which form the desired $\boldsymbol{I}(s)$ vector seen in equation (3.3-1).

This process works, however can be made more efficient. As seen in the above equations, the matrix $\widetilde{\boldsymbol{P}}$ must be inverted. Recall that in the case where the Taylor Series expansion was centred at zero, as in (3.3-1) and (3.3-2), inverting $\boldsymbol{P}$ is not a substantial burden since the additional "expanded" elements are all identity matrices along the diagonal. In the above derivation however, the Taylor series expansion was centred around an arbitrary frequency s_0. As a result, $\widetilde{\boldsymbol{P}}$ must be inverted, which does represent a considerable burden to invert, especially as the number of Chebyshev polynomials required to approximate $\boldsymbol{Z}$ increases. It is thus desirable to come up with a way to construct the matrix $\boldsymbol{Q}$ without having to explicitly compute, and thus invert, any of the expanded (those of size larger than the original system) matrices and vectors ($\boldsymbol{A}$, $\boldsymbol{R}$, $\widetilde{\boldsymbol{P}}$, $\widetilde{\boldsymbol{V}}$, $\boldsymbol{P}$, $\boldsymbol{T}$, and $\boldsymbol{M}_{0,s_0}$). This "efficient" MOR process will be explained in the following section.

3.3.1 Efficient Model Order Reduction

The first step in the MOR process outlined in the previous section is to compute the zeroth moment $\boldsymbol{M}_{0,s_0}$ defined in (3.3-15). The computation of this moment takes the following form

$$\begin{bmatrix} \boldsymbol{Z}_0 + s_0\boldsymbol{Z}_1 & s_0\boldsymbol{Z}_2 & s_0\boldsymbol{Z}_3 & & s_0\boldsymbol{Z}_{N_c+1} \\ -s_0\mathbb{I}_{N_e} & \mathbb{I}_{N_e} & \boldsymbol{0} & \cdots & \\ \boldsymbol{0} & -s_0\mathbb{I}_{N_e} & \mathbb{I}_{N_e} & & \vdots \\ & \vdots & & \ddots & \\ \boldsymbol{0} & \boldsymbol{0} & \cdots & -s_0\mathbb{I}_{N_e} & \mathbb{I}_{N_e} \end{bmatrix} \begin{bmatrix} \boldsymbol{M}_{0,s_0}^0 \\ \boldsymbol{M}_{0,s_0}^1 \\ \boldsymbol{M}_{0,s_0}^2 \\ \vdots \\ \boldsymbol{M}_{0,s_0}^{N_c} \end{bmatrix} = \begin{bmatrix} s_0\boldsymbol{V} \\ \boldsymbol{0} \\ \boldsymbol{0} \\ \vdots \\ \boldsymbol{0} \end{bmatrix}. \tag{3.3-17}$$

Expanding the first equation in (3.3-17) yields

$$(\boldsymbol{Z}_0 + s_0\boldsymbol{Z}_1)\boldsymbol{M}_{0,s_0}^0 + s_0\boldsymbol{Z}_2\boldsymbol{M}_{0,s_0}^1 + s_0\boldsymbol{Z}_3\boldsymbol{M}_{0,s_0}^2 + \cdots + s_0\boldsymbol{Z}_{N_c+1}\boldsymbol{M}_{0,s_0}^{N_c} = s_0\boldsymbol{V}. \tag{3.3-18}$$

One can note that equation (3.3-17) holds the same form as the matrix equation in (2.5-30). In *Section 2.5.3*, the unknowns in (2.5-30) were defined as recursive multiples of s. As such, it is known that in (3.3-17), $\boldsymbol{M}_{0,s_0}^1$ to $\boldsymbol{M}_{0,s_0}^{N_c}$ can be computed directly from $\boldsymbol{M}_{0,s_0}^0$. This means that the expanded $\boldsymbol{M}_{0,s_0}$ can be fully computed by knowing only $\boldsymbol{M}_{0,s_0}^0$.

$$\boldsymbol{M}_{0,s_0}^1 = s_0\boldsymbol{M}_{0,s_0}^0 \tag{3.3-19}$$

$$\boldsymbol{M}_{0,s_0}^2 = {s_0}^2\boldsymbol{M}_{0,s_0}^0 \tag{3.3-20}$$

$$\vdots$$

$$\boldsymbol{M}_{0,s_0}^{N_C} = {s_0}^{N_C}\boldsymbol{M}_{0,s_0}^0 \tag{3.3-21}$$

Substituting (3.3-19)-(3.3-21) into (3.3-18) yields

$$(\boldsymbol{Z_0} + s_0\boldsymbol{Z}_1)\boldsymbol{M}_{0,s_0}^0 + s_0\boldsymbol{Z_2}s_0\boldsymbol{M}_{0,s_0}^0 + s_0\boldsymbol{Z}_3{s_0}^2\boldsymbol{M}_{0,s_0}^0 + \cdots + s_0\boldsymbol{Z}_{N_C+1}{s_0}^{N_c}\boldsymbol{M}_{0,s_0}^0 = s_0\boldsymbol{V}. \tag{3.3-22}$$

Simplifying (3.3-22) ultimately leads to

$$\left[(\boldsymbol{Z}_0 + s_0\boldsymbol{Z}_1) + {s_0}^2\boldsymbol{Z}_2 + {s_0}^3\boldsymbol{Z}_3 + \cdots + {s_0}^{N_c+1}\boldsymbol{Z}_{N_c+1}\right]\boldsymbol{M}_{0,s_0}^0 = s_0\boldsymbol{V}. \tag{3.3-23}$$

$\boldsymbol{M}_{0,s_0}^0$ can thus be found as follows.

$$\boldsymbol{M}_{0,s_0}^0 = \left[(\boldsymbol{Z}_0 + s_0\boldsymbol{Z}_1) + {s_0}^2\boldsymbol{Z}_2 + {s_0}^3\boldsymbol{Z}_3 + \cdots + {s_0}^{N_c+1}\boldsymbol{Z}_{N_c+1}\right]^{-1} s_0\boldsymbol{V} \tag{3.3-24}$$

This result can then be used in (3.3-19)-(3.3-21) to generate the entire expanded vector $\boldsymbol{M}_{0,s_0}$ without having to invert the expanded matrix $\widetilde{\boldsymbol{P}}$. Also, one can observe from (3.3-24), that the term which is inverted is simply the $\boldsymbol{Z}$ matrix computed at s_0. Next, the $\boldsymbol{R}$ vector will be computed in a similar manner. The computation of this vector takes the following form.

$$\begin{bmatrix} \boldsymbol{Z}_0 + s_0\boldsymbol{Z}_1 & s_0\boldsymbol{Z}_2 & s_0\boldsymbol{Z}_3 & & s_0\boldsymbol{Z}_{N_c+1} \\ -s_0\mathbb{I}_{N_e} & \mathbb{I}_{N_e} & \boldsymbol{0} & \cdots & \\ \boldsymbol{0} & -s_0\mathbb{I}_{N_e} & \mathbb{I}_{N_e} & & \vdots \\ & \vdots & & \ddots & \\ \boldsymbol{0} & \boldsymbol{0} & \cdots & -s_0\mathbb{I}_{N_e} & \mathbb{I}_{N_e} \end{bmatrix} \begin{bmatrix} \boldsymbol{R}_0 \\ \boldsymbol{R}_1 \\ \boldsymbol{R}_2 \\ \vdots \\ \boldsymbol{R}_{N_c} \end{bmatrix}$$
$$= \left(\begin{bmatrix} \boldsymbol{V} \\ \boldsymbol{0} \\ \boldsymbol{0} \\ \vdots \\ \boldsymbol{0} \end{bmatrix} - \begin{bmatrix} \boldsymbol{Z}_1 & \boldsymbol{Z}_2 & \boldsymbol{Z}_3 & & \boldsymbol{Z}_{N_c+1} \\ -\mathbb{I}_{N_e} & \boldsymbol{0} & \boldsymbol{0} & \cdots & \\ \boldsymbol{0} & -\mathbb{I}_{N_e} & \boldsymbol{0} & & \vdots \\ & \vdots & & \ddots & \\ \boldsymbol{0} & \cdots & \boldsymbol{0} & -\mathbb{I}_{N_e} & \boldsymbol{0} \end{bmatrix} \begin{bmatrix} \boldsymbol{M}_{0,s_0}^0 \\ \boldsymbol{M}_{0,s_0}^1 \\ \boldsymbol{M}_{0,s_0}^2 \\ \vdots \\ \boldsymbol{M}_{0,s_0}^{N_c} \end{bmatrix} \right) \tag{3.3-25}$$

The right-side vector, denoted here as $\boldsymbol{B}$, of (3.3-25) can be computed as follows without computing the entire expanded matrix $\boldsymbol{T}$.

$$\boldsymbol{B} = \begin{bmatrix} \boldsymbol{B}_0 \\ \boldsymbol{B}_1 \\ \boldsymbol{B}_2 \\ \vdots \\ \boldsymbol{B}_{N_c} \end{bmatrix} = \begin{bmatrix} \boldsymbol{V} - (\boldsymbol{Z}_1\boldsymbol{M}_{0,s_0}^0 + \boldsymbol{Z}_2\boldsymbol{M}_{0,s_0}^1 + \boldsymbol{Z}_3\boldsymbol{M}_{0,s_0}^2 + \cdots + \boldsymbol{Z}_{N_c+1}\boldsymbol{M}_{0,s_0}^{N_c}) \\ \boldsymbol{M}_{0,s_0}^0 \\ \boldsymbol{M}_{0,s_0}^1 \\ \vdots \\ \boldsymbol{M}_{0,s_0}^{N_c-1} \end{bmatrix} \tag{3.3-26}$$

Now, the $\boldsymbol{R}$ vector can be rewritten as follows.

$$\begin{bmatrix} \boldsymbol{Z}_0 + s_0\boldsymbol{Z}_1 & s_0\boldsymbol{Z}_2 & s_0\boldsymbol{Z}_3 & & s_0\boldsymbol{Z}_{N_c+1} \\ -s_0\mathbb{I}_{N_e} & \mathbb{I}_{N_e} & \boldsymbol{0} & \cdots & \\ \boldsymbol{0} & -s_0\mathbb{I}_{N_e} & \mathbb{I}_{N_e} & & \vdots \\ & \vdots & & \ddots & \\ \boldsymbol{0} & \boldsymbol{0} & \cdots & -s_0\mathbb{I}_{N_e} & \mathbb{I}_{N_e} \end{bmatrix} \begin{bmatrix} \boldsymbol{R}_0 \\ \boldsymbol{R}_1 \\ \boldsymbol{R}_2 \\ \vdots \\ \boldsymbol{R}_{N_c} \end{bmatrix} = \begin{bmatrix} \boldsymbol{B}_0 \\ \boldsymbol{B}_1 \\ \boldsymbol{B}_2 \\ \vdots \\ \boldsymbol{B}_{N_c} \end{bmatrix} \tag{3.3-27}$$

Unlike in (3.3-17), the right-side vector in (3.3-27) is full. As a result, the relationship between the solution vector in (3.3-27) is not the same as that depicted in (3.3-19)-(3.3-21). Rather, the relationship is as follows.

$$\boldsymbol{R}_1 = s_0\boldsymbol{R}_0 + \boldsymbol{B}_1 \tag{3.3-28}$$

$$\boldsymbol{R}_2 = s_0\boldsymbol{R}_1 + \boldsymbol{B}_2 \tag{3.3-29}$$

$$\vdots$$

$$\boldsymbol{R}_{N_c} = s_0\boldsymbol{R}_{N_c-1} + \boldsymbol{B}_{N_c} \tag{3.3-30}$$

Expanding the first equation in (3.3-27) yields

$$(\boldsymbol{Z}_0 + s_0\boldsymbol{Z}_1)\boldsymbol{R}_0 + s_0\boldsymbol{Z}_2\boldsymbol{R}_1 + s_0\boldsymbol{Z}_3\boldsymbol{R}_2 + \cdots + s_0\boldsymbol{Z}_{N_c+1}\boldsymbol{R}_{N_c} = \boldsymbol{B}_0. \tag{3.3-31}$$

Substituting (3.3-28)-(3.3-30) into (3.3-31) leads to the following.

$$(\boldsymbol{Z}_0 + s_0\boldsymbol{Z}_1)\boldsymbol{R}_0 + s_0\boldsymbol{Z}_2(s_0\boldsymbol{R}_0 + \boldsymbol{B}_1) + s_0\boldsymbol{Z}_3(s_0\boldsymbol{R}_1 + \boldsymbol{B}_2) + \cdots + s_0\boldsymbol{Z}_{N_c+1}\left(s_0\boldsymbol{R}_{N_c-1} + \boldsymbol{B}_{N_c}\right) = \boldsymbol{B}_0 \tag{3.3-32}$$

The number of terms in equation (3.3-32) will depend on the number of Chebyshev polynomials N_c being used as a result of the recursive relationship of $\boldsymbol{R}_{N_c}$. As an example, let us assume that two Chebyshev polynomials are to be used. In that case, (3.3-32) can be rearranged as follows.

$$(\boldsymbol{Z}_0 + s_0\boldsymbol{Z}_1)\boldsymbol{R}_0 + {s_0}^2\boldsymbol{Z}_2\boldsymbol{R}_0 + s_0\boldsymbol{Z}_2\boldsymbol{B}_1 + {s_0}^2\boldsymbol{Z}_3(s_0\boldsymbol{R}_0 + \boldsymbol{B}_1) + s_0\boldsymbol{Z}_3\boldsymbol{B}_2 = \boldsymbol{B}_0 \tag{3.3-33}$$

$$(\boldsymbol{Z}_0 + s_0\boldsymbol{Z}_1)\boldsymbol{R}_0 + {s_0}^2\boldsymbol{Z}_2\boldsymbol{R}_0 + s_0\boldsymbol{Z}_2\boldsymbol{B}_1 + {s_0}^3\boldsymbol{Z}_3\boldsymbol{R}_0 + {s_0}^2\boldsymbol{Z}_3\boldsymbol{B}_1 + s_0\boldsymbol{Z}_3\boldsymbol{B}_2 = \boldsymbol{B}_0 \quad (3.3\text{-}34)$$

$$[(\boldsymbol{Z}_0 + s_0\boldsymbol{Z}_1) + {s_0}^2\boldsymbol{Z}_2 + {s_0}^3\boldsymbol{Z}_3]\boldsymbol{R}_0 = \boldsymbol{B}_0 - s_0\boldsymbol{Z}_2\boldsymbol{B}_1 - {s_0}^2\boldsymbol{Z}_3\boldsymbol{B}_1 - s_0\boldsymbol{Z}_3\boldsymbol{B}_2 \quad (3.3\text{-}35)$$

$$\boldsymbol{R}_0 = [(\boldsymbol{Z}_0 + s_0\boldsymbol{Z}_1) + {s_0}^2\boldsymbol{Z}_2 + {s_0}^3\boldsymbol{Z}_3]^{-1}(\boldsymbol{B}_0 - s_0\boldsymbol{Z}_2\boldsymbol{B}_1 - {s_0}^2\boldsymbol{Z}_3\boldsymbol{B}_1 - s_0\boldsymbol{Z}_3\boldsymbol{B}_2) \quad (3.3\text{-}36)$$

With $\boldsymbol{R}_0$ now known, the rest of the $\boldsymbol{R}$ vector can be constructed using the relationships in (3.3-28)-(3.3-30). It can again be observed from (3.3-36) that the term to be inverted is the $\boldsymbol{Z}$ matrix evaluated at s_0. For every additional Chebyshev polynomial that is used, additional terms will be present on the right side of equation (3.3-35). A generalized equivalent of (3.3-36) for any number of Chebyshev polynomials is shown in (3.3-37). This relationship is formulated in such a way that minimizes the number of matrix-vector products.

$$\boldsymbol{R}_0 = \boldsymbol{Z}(s_0)^{-1}\left[\boldsymbol{V} - \left(\boldsymbol{Z}_1\boldsymbol{M}_{0,s_0}^{0} + \sum_{i=2}^{N_c+1}\boldsymbol{Z}_{\boldsymbol{i}}\left(\boldsymbol{M}_{0,s_0}^{i-1} - \sum_{j=1}^{i-1} s_0^{i-j}\boldsymbol{M}_{0,s_0}^{j-1}\right)\right)\right] \quad (3.3\text{-}37)$$

With $\boldsymbol{R}$ now constructed, the first column of $\boldsymbol{Q}$ can be computed as was done in (2.5-12), namely

$$\boldsymbol{q}^{(1)} = \frac{\boldsymbol{R}}{\|\boldsymbol{R}\|}. \quad (3.3\text{-}38)$$

Finally, the key part of Arnoldi's algorithm is the multiplication of the $\boldsymbol{A}$ matrix with each successive vector $\boldsymbol{q}$, ultimately forming the orthogonal matrix $\boldsymbol{Q}$. This is why the Arnoldi algorithm pseudo-code presented in Figure 2.5-2 requires an input of the $\boldsymbol{A}$ matrix as well as the first $\boldsymbol{q}$ vector, $\boldsymbol{q}^{(1)}$. The full $\boldsymbol{A}$ matrix cannot be created efficiently as it is the product of two matrices, not a matrix and a vector, as is defined in (3.3-13). With that being said, the product of $\boldsymbol{A}$ and $\boldsymbol{q}_k$ (k representing the k^{th} column vector making up $\boldsymbol{Q}$) can be constructed without explicitly creating the expanded matrix $\boldsymbol{A}$ in much the same way as was done to compute the expanded vector $\boldsymbol{R}$. This product has the following form.

$$\begin{bmatrix} \boldsymbol{Z}_0 + s_0\boldsymbol{Z}_1 & s_0\boldsymbol{Z}_2 & s_0\boldsymbol{Z}_3 & & s_0\boldsymbol{Z}_{N_c+1} \\ -s_0\mathbb{I}_{N_e} & \mathbb{I}_{N_e} & \boldsymbol{0} & \cdots & \\ \boldsymbol{0} & -s_0\mathbb{I}_{N_e} & \mathbb{I}_{N_e} & & \vdots \\ & \vdots & & \ddots & \\ \boldsymbol{0} & \boldsymbol{0} & \cdots & -s_0\mathbb{I}_{N_e} & \mathbb{I}_{N_e} \end{bmatrix} \begin{bmatrix} \boldsymbol{Aq}_0^{(k)} \\ \boldsymbol{Aq}_1^{(k)} \\ \boldsymbol{Aq}_2^{(k)} \\ \vdots \\ \boldsymbol{Aq}_{N_c}^{(k)} \end{bmatrix} = - \begin{bmatrix} \boldsymbol{Z}_1 & \boldsymbol{Z}_2 & \boldsymbol{Z}_3 & & \boldsymbol{Z}_{N_c+1} \\ -\mathbb{I}_{N_e} & \boldsymbol{0} & \boldsymbol{0} & \cdots & \\ \boldsymbol{0} & -\mathbb{I}_{N_e} & \boldsymbol{0} & & \vdots \\ & \vdots & & \ddots & \\ \boldsymbol{0} & \cdots & \boldsymbol{0} & -\mathbb{I}_{N_e} & \boldsymbol{0} \end{bmatrix} \begin{bmatrix} \boldsymbol{q}_0^{(k-1)} \\ \boldsymbol{q}_1^{(k-1)} \\ \boldsymbol{q}_2^{(k-1)} \\ \vdots \\ \boldsymbol{q}_{N_c}^{(k-1)} \end{bmatrix} \tag{3.3-39}$$

The right-side vector, denoted here as $\boldsymbol{D}$, can be computed once again without computing the entire expanded matrix $\boldsymbol{T}$ as follows.

$$\boldsymbol{D} = \begin{bmatrix} \boldsymbol{D}_0 \\ \boldsymbol{D}_1 \\ \boldsymbol{D}_2 \\ \vdots \\ \boldsymbol{D}_{N_c} \end{bmatrix} = \begin{bmatrix} -(\boldsymbol{Z}_1\boldsymbol{q}_0^{(k-1)} + \boldsymbol{Z}_2\boldsymbol{q}_1^{(k-1)} + \boldsymbol{Z}_3\boldsymbol{q}_2^{(k-1)} + \cdots + \boldsymbol{Z}_{N_c+1}\boldsymbol{q}_{N_c}^{(k-1)}) \\ \boldsymbol{q}_0^{(k-1)} \\ \boldsymbol{q}_1^{(k-1)} \\ \vdots \\ \boldsymbol{q}_{N_c-1}^{(k-1)} \end{bmatrix} \tag{3.3-40}$$

Now, solving for the $\boldsymbol{Aq}^{(k)}$ vector can be rewritten as follows.

$$\begin{bmatrix} \boldsymbol{Z}_0 + s_0\boldsymbol{Z}_1 & s_0\boldsymbol{Z}_2 & s_0\boldsymbol{Z}_3 & & s_0\boldsymbol{Z}_{N_c+1} \\ -s_0\mathbb{I}_{N_e} & \mathbb{I}_{N_e} & \boldsymbol{0} & \cdots & \\ \boldsymbol{0} & -s_0\mathbb{I}_{N_e} & \mathbb{I}_{N_e} & & \vdots \\ & \vdots & & \ddots & \\ \boldsymbol{0} & \boldsymbol{0} & \cdots & -s_0\mathbb{I}_{N_e} & \mathbb{I}_{N_e} \end{bmatrix} \begin{bmatrix} \boldsymbol{Aq}_0^{(k)} \\ \boldsymbol{Aq}_1^{(k)} \\ \boldsymbol{Aq}_2^{(k)} \\ \vdots \\ \boldsymbol{Aq}_{N_c}^{(k)} \end{bmatrix} = \begin{bmatrix} \boldsymbol{D}_0 \\ \boldsymbol{D}_1 \\ \boldsymbol{D}_2 \\ \vdots \\ \boldsymbol{D}_{N_c} \end{bmatrix} \tag{3.3-41}$$

It is clear that (3.3-41) has the same form as (3.3-27). This means that the exact same process outlined in equations (3.3-28)-(3.3-37) can be used in this case on (3.3-41) to compute the components of $\boldsymbol{Aq}^{(k)}$ and thus each column vector making up the expanded orthogonal basis $\boldsymbol{Q}$, noting that (3.3-37) is modified to

$$\boldsymbol{Aq}_0^{(k)} = \boldsymbol{Z}(s_0)^{-1}\left[\boldsymbol{Z}_1\boldsymbol{q}_0^{(k-1)} + \sum_{i=2}^{N_c+1}\boldsymbol{Z}_i\left(\boldsymbol{q}_{i-1}^{(k-1)} - \sum_{j=1}^{i-1} s_0^{i-j}\boldsymbol{q}_{j-1}^{(k-1)}\right)\right]. \tag{3.3-42}$$

Since the $\boldsymbol{A}$ matrix is never explicitly computed, the Arnoldi algorithm must be modified slightly such that the above steps pertaining to equation (3.3-41) occur within the outer for-loop of the pseudo-code in Figure 2.5-2.

With that final step, the expanded orthogonal basis $\boldsymbol{Q}$ has now been constructed without explicitly computing any of the expanded matrices. Recall the zeroth moment was not included in the Arnoldi algorithm process due to the product of s on the right side of the original expanded matrix equation. An orthogonal vector corresponding to this moment is thus computed and incorporated into $\boldsymbol{Q}$ via QR decomposition. The number of iterations of the Arnoldi algorithm is thus $N_q - 2$.

This final basis can then be used to reduce the expanded $\boldsymbol{P}$, $\boldsymbol{T}$, and $\widetilde{\boldsymbol{V}}$ matrices in equation (3.3-2) as follows without explicitly computing them,

$$\begin{aligned}\boldsymbol{PQ} &= \begin{bmatrix} \boldsymbol{Z}_0 & \boldsymbol{0} & \boldsymbol{0} & & \boldsymbol{0} \\ \boldsymbol{0} & \mathbb{I}_{N_e} & \boldsymbol{0} & \cdots & \\ \boldsymbol{0} & \boldsymbol{0} & \mathbb{I}_{N_e} & & \vdots \\ & \vdots & & \ddots & \\ \boldsymbol{0} & & \cdots & & \mathbb{I}_{N_e} \end{bmatrix} \begin{bmatrix} \boldsymbol{q}^{(1)} & \boldsymbol{q}^{(2)} & \cdots & \boldsymbol{q}^{(N_q)} \end{bmatrix} \\ &= \begin{bmatrix} \boldsymbol{Z}_0 \boldsymbol{q}^{(1)}(1\!:\!N_e) & \boldsymbol{Z}_0 \boldsymbol{q}^{(2)}(1\!:\!N_e) & \cdots & \cdots & \boldsymbol{Z}_0 \boldsymbol{q}^{(N_q)}(1\!:\!N_e) \\ \boldsymbol{q}^{(1)}(N_e + 1\!:\!N_c N_e + N_e) & \boldsymbol{q}^{(2)}(N_E + 1\!:\!N_c N_e + N_e) & \cdots & \cdots & \boldsymbol{q}^{(N_q)}(N_e + 1\!:\!N_c N_e + N_e) \end{bmatrix}\end{aligned} \tag{3.3-43}$$

where the notation $(x\!:\!y)$ denotes a range of rows of $\boldsymbol{q}^{(k)}$. The reduced matrix, $\widehat{\boldsymbol{P}}$, is then

$$\widehat{\boldsymbol{P}} = \boldsymbol{Q}^{\mathrm{T}} \boldsymbol{PQ}. \tag{3.3-44}$$

The other reduced matrices are found in a similar manner.

$$\begin{aligned}\boldsymbol{TQ} &= \begin{bmatrix} \boldsymbol{Z}_1 & \boldsymbol{Z}_2 & \boldsymbol{Z}_3 & & \boldsymbol{Z}_{N_c+1} \\ -\mathbb{I}_{N_e} & \boldsymbol{0} & \boldsymbol{0} & \cdots & \\ \boldsymbol{0} & -\mathbb{I}_{N_e} & \boldsymbol{0} & & \vdots \\ & \vdots & & \ddots & \\ \boldsymbol{0} & \cdots & \boldsymbol{0} & -\mathbb{I}_{N_e} & \boldsymbol{0} \end{bmatrix} \begin{bmatrix} \boldsymbol{q}^{(1)} & \boldsymbol{q}^{(2)} & \cdots & \boldsymbol{q}^{(N_q)} \end{bmatrix} \\ &= \begin{bmatrix} \ddot{\boldsymbol{Z}} \boldsymbol{q}^{(1)} & \ddot{\boldsymbol{Z}} \boldsymbol{q}^{(2)} & \cdots & \ddot{\boldsymbol{Z}} \boldsymbol{q}^{(N_q)} \\ -\boldsymbol{q}^{(1)}(1\!:\!N_e) & -\boldsymbol{q}^{(2)}(1\!:\!N_e) & \cdots & -\boldsymbol{q}^{(N_q)}(1\!:\!N_e) \end{bmatrix}\end{aligned} \tag{3.3-45}$$

$$\ddot{\boldsymbol{Z}}\boldsymbol{q}^{(k)} = \boldsymbol{Z}_1\boldsymbol{q}^{(k)}(1\colon N_e) + \boldsymbol{Z}_2\boldsymbol{q}^{(k)}(N_e + 1\colon 2N_e) + \boldsymbol{Z}_3\boldsymbol{q}^{(k)}(2N_e + 1\colon 3N_e) + \cdots + \boldsymbol{Z}_{N_c+1}\boldsymbol{q}^{(k)}(N_cN_e + 1\colon (N_c + 1)N_e) \tag{3.3-46}$$

$$\widehat{\boldsymbol{T}} = \boldsymbol{Q}^{\mathrm{T}}\boldsymbol{T}\boldsymbol{Q} \tag{3.3-47}$$

$$\widehat{\boldsymbol{V}} = [\boldsymbol{q}^{(1)}(1\colon N_e) \quad \boldsymbol{q}^{(2)}(1\colon N_e) \quad \cdots \quad \boldsymbol{q}^{(N_q)}(1\colon N_e)]^{\mathrm{T}}\widetilde{\boldsymbol{V}} \tag{3.3-48}$$

The reduced solution vector $\hat{\boldsymbol{I}}$ can then finally be found using the same method that was described in *Section 2.5.2*, however with the additional product of s on the right-side vector as a result of the Chebyshev approximation.

$$\left(\widehat{\boldsymbol{P}} + s\widehat{\boldsymbol{T}}\right)\hat{\boldsymbol{I}}(s) = s\widehat{\boldsymbol{V}} \tag{3.3-49}$$

This reduced solution can then be expanded using the orthogonal basis and all, but the first N_e terms, can be discarded as

$$\boldsymbol{I}(s) \approx \left(\mathbb{e}_{1,N_{c+1}}^{\mathrm{T}} \otimes \mathbb{I}_{N_e}\right)\boldsymbol{Q}\hat{\boldsymbol{I}}(s) \tag{3.3-50}$$

where $\mathbb{e}_{m,M}^{T}$ denotes the m^{th} column of an identity matrix of size M.

3.3.2 Explicit Computation of the Orthogonal Basis

It was mentioned in *Section 2.5.2* that computing the moments is an ill-conditioned process which has led to the use of Arnoldi's algorithm in circuit simulation, enabling the construction of the orthogonal basis $\boldsymbol{Q}$ of the subspace spanned by the moments without having to compute the moments themselves. However, it is still possible to create $\boldsymbol{Q}$ via QR decomposition using explicitly computed moments, so long as the number of moments of $\boldsymbol{X}(s)$ (in the context of *Section 2.5.2*) is not exceedingly large. Pertaining to the MOR procedure and methodology described for the MoM, the moments can be explicitly computed using the Chebyshev approximated impedance matrix and (2.5-4) as follows.

$$\boldsymbol{M}_0 = \left(\sum_{i=0}^{N_c+1} \boldsymbol{Z}_i s_0^i \right)^{-1} s_0 \boldsymbol{V} \tag{3.3-51}$$

$$\boldsymbol{M}_1 = \left(\sum_{i=0}^{N_c+1} \boldsymbol{Z}_i s_0^i \right)^{-1} \left[\boldsymbol{V} - \left(\frac{d}{ds_0} \sum_{i=0}^{N_c+1} \boldsymbol{Z}_i s_0^i \right) \boldsymbol{M}_0 \right] \tag{3.3-52}$$

$$\boldsymbol{M}_n = \left(\sum_{i=0}^{N_c+1} \boldsymbol{Z}_i s_0^i \right)^{-1} \left[-\sum_{j=1}^{n} \frac{1}{j!} \left(\frac{d^j}{{ds_0}^j} \sum_{i=0}^{N_c+1} \boldsymbol{Z}_i s_0^i \right) \boldsymbol{M}_{n-j} \right], \qquad n = 2, 3, 4 \ldots. \tag{3.3-53}$$

While $\boldsymbol{M}_0$ can be computed rather simply as is shown in (3.3-51), the subsequent moments become increasingly more cumbersome to compute, as the n^{th} moment requires an additional n matrix-vector products of size N_e. *Section 3.5* will compare the time taken to solve the given problems using both the "implicit" method described in the previous section, as well as the "explicit" method explained here. It will become clear that while the MoM explicit MOR method is able to achieve accurate results in certain situations, the implicit method remains more efficient and more reliable.

3.4 SELECTING THE MODEL ORDER REDUCTION OPERATIONAL PARAMETERS

To use MOR three quantities must be determined: the number of Chebyshev polynomials N_c needed to approximate the impedance matrix over the desired frequency band, the size of the reduced order model (ROM) N_q, and the number of frequency expansion points N_m for which the ROMs are to be centred around. Having to determine these quantities by trial and error would obviously defeat the purpose of using MOR since the time needed to run many simulations would likely amount to more total time than just running a traditional MoM analysis. Therefore, a method is needed for quickly determining each of these quantities without having run any previous rigorous simulations or having any prior knowledge of what the antenna's frequency response (for any metric) will look like.

3.4.1 Determining N_c

In a typical mathematical context, the degree needed for a Chebyshev series to accurately approximate a function is found by examining successive Chebyshev coefficients. If several of these coefficients in a row fall below a threshold of approximately 10^{-15}, then the approximation is deemed to be sufficiently accurate [TREF 20]. Using such a threshold-style approach would mean simply that we can say a minimum N_c is achieved when the magnitude of the Chebyshev coefficients computed in (3.2-7) plateau (at around 10^{-15}), thus more coefficients added will no longer contribute to the approximation's accuracy. To test this approach, it is first important to identify from (3.2-7) and (3.2-5) that there are only two factors which will determine the minimum N_c that is needed to approximate $\boldsymbol{Z}(s)$: the frequency band over which the approximation is to be valid for, seen in Δ_m and Δ_p of (3.2-7), and the distance between the midpoint of a mesh triangle and the midpoint of one of the nine sub-triangles used for numerical integration as described in *Section 2.3.5*, contained within $\xi^{\pm} = \sqrt{\mu\varepsilon}\left|\vec{r}_m^{\,C\pm} - \vec{r}_n^{\,\pm\prime}\right|$. If we select the midpoint of a single sub-triangle within each mesh triangle for analysis, it would be reasonable to assume that the exponential function that would require the highest degree Chebyshev series would be that which spans the two mesh triangles which are furthest from each other, resulting in the greatest $\left|\vec{r}_m^{\,C\pm} - \vec{r}_n^{\,\pm\prime}\right|$. Therefore, whatever value of N_c is determined to accurately approximate this "extreme distance" exponential would suffice for all other exponentials.

As an example, later in this chapter, two antennas will be analyzed, a patch antenna and ground plane, and an array of eight patches above a ground plane. For the time being, the specific details of these antennas are not important (they will be properly characterized later). It is sufficient now just to say that we wish to analyze them over the same frequency band (1.5-6 GHz), and the extreme distance of the single patch is 117.3 mm, while that of the array is 447.9 mm. Figure 3.4-1 shows the magnitude of the Chebyshev coefficients, $|c_k|$, for $k = 0,1,2,\dots,100$, of both aforementioned antennas. From this plot we could conclude using the mathematical threshold approach that approximately 27 and 51 Chebyshev coefficients would suffice for the patch antenna and the antenna array, respectively. The issue with this conclusion is that these values of N_c are considerably higher than what is actually the minimum necessary for accurate antenna simulations. In fact, it was found that the optimal choices for the two antennas are $N_c = 5$ and $N_c = 9$, respectively (as seen by the red circles in Figure 3.4-1). These values are obviously substantially lesser than what was predicted mathematically and with N_c translating to the number of problem-sized matrices that must be constructed, the greater the difference between N_c and the actual minimum needed will result in significantly greater computation time and unnecessary additional memory requirement. One might suggest a solution to such an issue could be to increase the threshold at which we deem enough Chebyshev coefficients have been computed, however from the red circles in Figure 3.4-1 it is not obvious as to what such a new threshold should be. In fact, what is evident is that the actual threshold that yields the minimum N_c is problem dependent.

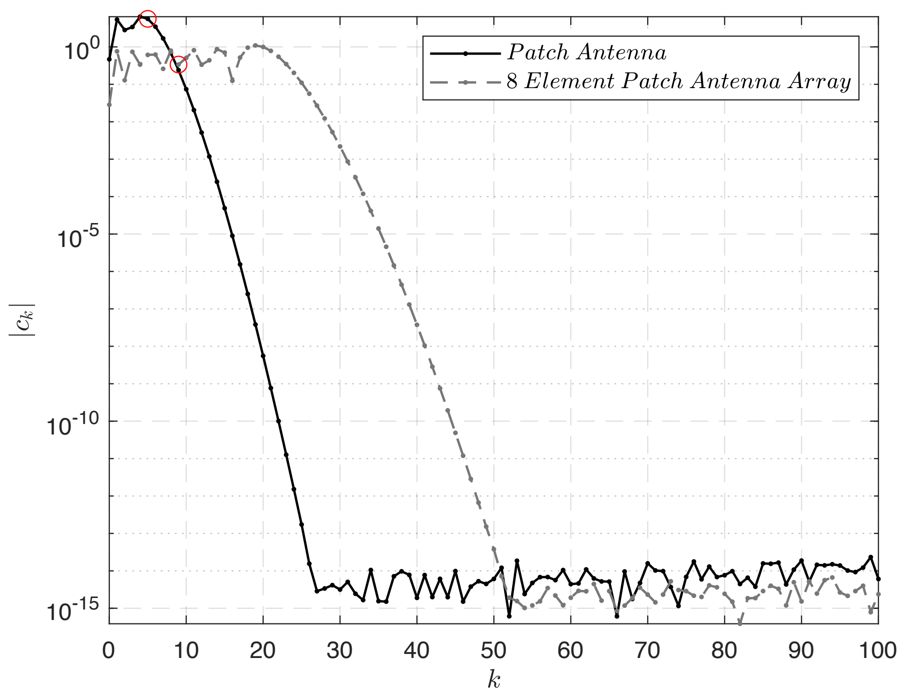

Figure 3.4-1. $|c_k|$ for $k = 0,1,2,\ldots,100$, of a patch antenna and patch antenna array.

To understand why considering only the extreme distance exponential as a bound for determining the minimum value of N_c results in such a great overestimation, we must recall that these exponential functions are scaled relative to the distance between basis functions as is dictated by the free-space Green's function below (pertaining to the particular MoM formulation of interest).

$$G\left(\bar{r}_m^{C\pm}, \bar{r}_n^{\pm\prime}\right) = \frac{e^{-jk\left|\bar{r}_m^{C\pm} - \bar{r}_n^{\pm\prime}\right|}}{4\pi\left|\bar{r}_m^{C\pm} - \bar{r}_n^{\pm\prime}\right|} \tag{3.4-1}$$

This means that the formulation puts more weight on the exponential terms which consider basis functions that are spaced closer to one another than on those considering further spaced mesh edges. The result is that it is not necessary to perfectly approximate the extreme distance exponentials to obtain accurate results since these functions are scaled down in (3.4-1) by this separation, thus explaining the overestimation seen in Figure 3.4-1.

This thesis now develops a graphical approach to circumvent this hurdle and determine the minimum, or at worst one greater than the minimum, value of N_c. The method works as follows. First, let

$$U = max\left(\left|c_{N_c-1}\right| \forall e^{-s\xi^{\pm}},\ \vec{r}^{\,C\pm}_{m,ext.} \in \xi^{\pm}\right). \tag{3.4-2}$$

Then compute U as in (3.4-2) for several values of N_c. This entails computing the magnitude of the $(N_c - 1)^{th}$ Chebyshev coefficient $\left|c_{N_c-1}\right|$ for all exponential functions that contain one of the two extreme triangles, denoted in (3.4-2) by the "ext." subscript, and then taking the maximum.

Computing U for a series of values of N_c (up to 30 in this case) will result in a curve that will likely lie within a shaded area of the plot in Figure 3.4-2. The legend in this figure indicates the minimum value of N_c that will be needed. The seven curves shown in Figure 3.4-2 that bound the shaded regions were determined via seven problems which are known to require that respective value of N_c to yield accurate results. Setting these known curves as the upper bound for each N_c region means that new curves are always rounded up one value of N_c. This means that at worst, it is possible that this method will select an N_c that is one higher than it could be. Furthermore, Figure 3.4-2 only goes up to $N_c = 9$, however this can be easily expanded upon through observation for simulations requiring more. An example showing specifically how this figure is used is shown in *Section 3.5* along with an account of the time needed to compute the necessary U curve, which is essentially negligible.

Of course, this method is making the large assumption that plotting U for the radiating structure and frequency band of interest will yield a curve similar to those in Figure 3.4-2 which lies within one of the shaded regions. It is impossible to say that this will always be so for every problem, however for the many that were considered in the making of this plot, as well as for those shown in all the subsequent sections in this thesis, the computed U curves remained consistently of this same nature.

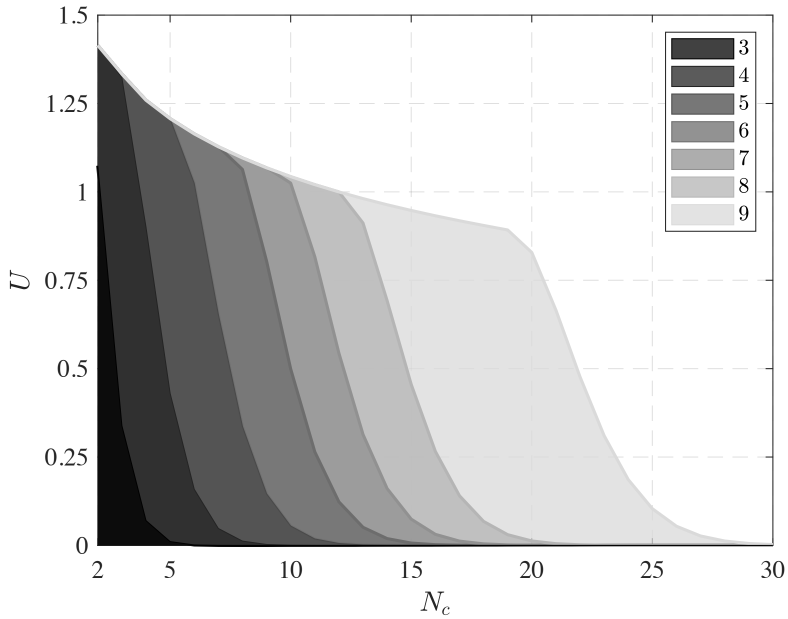

Figure 3.4-2. Equation (3.4-2) as a function of N_c. The shaded areas refer to the value of N_c that will be needed.

While a non-graphical, rigorous analytical solution to this problem linking a maximum error between the exact and approximate exponential functions that lead to a minimum number of Chebyshev coefficients needed for an accurate solution given a particular frequency band and size of structure may exist, the task of determining such a relationship would evidently hardly be straightforward.

3.4.2 Determining N_q and N_m

There are various methods in the MOR literature that describe how the size of reduced models and the number of expansion points can be determined, but not all are applicable in the present context. For instance, [NOUR 13b] details an approach that necessitates time domain simulations. That which could be applicable to this work is an adaptive binary search (ABS) scheme similar to that presented in [FENG 15]. In this method the entire frequency band over which the reduced order model is to apply is first defined via s_{min} and s_{max}. The exact “full-order” solution is then obtained at the midpoint of these two bounding frequencies (s_{mid} on "Line 1" of Figure 3.4-3). Reduced order models are then computed at s_{min} and s_{max} of size $N_{q,min}$. These are then used to determine approximations for the solution at the frequency midpoint and are compared with the exact solution. Should the solutions be sufficiently close, the algorithm is terminated, and the two reduced order models are used to compute the full response at frequencies within ranges $[s_{min}, s_{mid}]$ and $[s_{mid}, s_{max}]$, respectively. If the solutions are not sufficiently close, then N_q is increased from $N_{q,min}$ in increments of ΔN_q until a user specified $N_{q,max}$ is reached. It is important to note that for this work, when new columns of a previously constructed basis $\boldsymbol{Q}$ need to be computed, the stored $\boldsymbol{Q}$ must be that prior to when the zeroth moment is incorporated into $\boldsymbol{Q}$ via QR decomposition. As such, the zeroth moment for a given expansion point must always be stored. If N_q reaches $N_{q,max}$ without the solutions being sufficiently accurate, a new reduced order model is constructed at s_{mid} and new exact testing solutions are found at midpoints between $[s_{min}, s_{mid}]$ and $[s_{mid}, s_{max}]$, say $s_{mid,2}$ and $s_{mid,3}$, respectively, as on "Line 2" of Figure 3.4-3. The process is then repeated until every section of the frequency band of interest has a reduced order model that accurately covers it. This method of course allows for various ROM sizes that can cover unequal portions of the band.

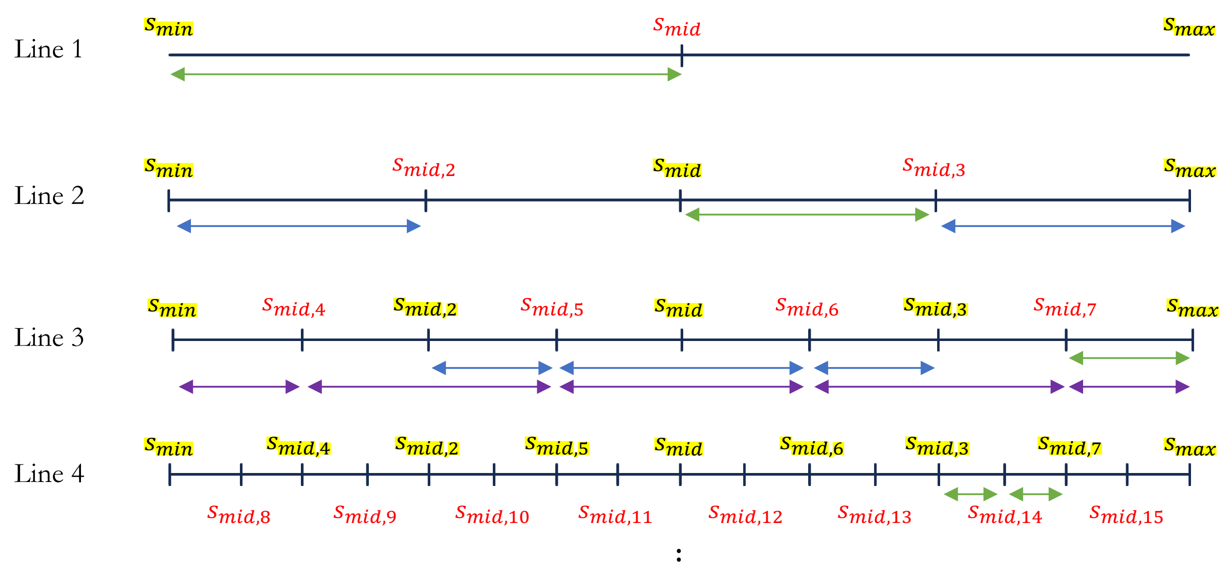

Figure 3.4-3. Diagram illustrating the frequency band splitting of the ABS technique. The frequencies highlighted in yellow show the expansion points of ROMs, while those in red show the location of the exact points used for checking the accuracy of the ROMs. The green, blue, and purple arrows are discussed in the following paragraph.

Solutions are determined to be sufficiently close if

$$\tau = mean\left\{\left|\frac{|I_{exact}| - |I_{MOR}|}{|I_{MOR}|}\right|\right\} \tag{3.4-3}$$

falls below a certain tolerance τ_{max}. When applied in the work of this thesis, it was observed that it is not uncommon for τ to stagnate when testing expansion points as N_q is increasing. To improve efficiency, a simple check was thus added to the algorithm that skips to the next expansion point if the solution obtained using an ROM of size $N_q + \Delta N_q$ results in a τ that is not less than that found from the solution using an ROM of size N_q. This ultimately means that $N_{q,max}$ can be set arbitrarily high so as to not worry about setting it too low and missing a potential termination, while also limiting wasted time computing unnecessary columns of $\boldsymbol{Q}$.

While the ABS technique described above will produce accurate results, it is simply too slow for present purposes. There are three reasons for this. The first concerns the number of LU decompositions that must be done. As an example, consider the green, blue, and purple arrows beneath the lines in Figure 3.4-3. Each of these coloured sets of arrows represents a possibility in which the ABS algorithm determines that five expansion points are necessary. The green arrows show the best-case scenario. Here, the ROM at s_{min} covers all frequencies in $[s_{min}, s_{mid}]$, the ROM at s_{mid} covers all frequencies in $[s_{mid}, s_{mid,3}]$, the ROM at $s_{mid,3}$ covers all frequencies in $[s_{mid,3}, s_{mid,14}]$, the ROM at $s_{mid,7}$ covers all frequencies in $[s_{mid,14}, s_{mid,7}]$, and finally the ROM at s_{max} covers all frequencies in $[s_{mid,7}, s_{max}]$. What is optimal about this arrangement is that all of the exact-check frequencies (those in red in Figure 3.4-3) get used as expansion points in subsequent lines (with the exception of $s_{mid,14}$) and thus the LU factors needed for the exact solutions at the checks will be reused to form ROMs at those frequencies. This ultimately means that for a certain number of expansion points N_m, the smallest number of LU decompositions needed will be $N_m + 1$, or in this case, six. However, the blue and purple arrow sets show other possibilities that would also result in five total expansion points. These, however, would require seven and nine LU decompositions, respectively. Consequently, in the vast majority of simulations done using this technique, the number of LU decompositions needed will significantly exceed N_m and thus significantly inflate the problem time, especially as the problem size increases and individual LU decompositions become more temporally demanding. This is easily conceptualized when realizing that the case of the green arrows, which requires the minimum number of LU decompositions, occurs only if the antenna's response fluctuates significantly in a very narrow band while barely fluctuating over the rest of the band. Exploratory runs show that it is far more common to see the scenario requiring the maximum number of LU decompositions, the purple set of arrows, in which the band is evenly split between the ROMs. The second reason relates to the number of checks that must be done, that is, the number of times an ROM has to be validated against an exact solution. For $N_m = 2$, the minimum number of checks needed is two, but for all subsequent values of N_m, the minimum number of checks increases by two from the previous N_m. Thus, the minimum number of checks for $N_m = 5$ is eight, which occurs in the situation depicted by the green arrows. Again though, this is only the minimum. The blue and purple arrow sets show examples where the number of checks increase to 10 and 14, respectively. The reason it is important to keep the number of checks low is that within each one of these checks, the entire process of increasing the size of the ROM from $N_{q,min}$ to $N_{q,max}$, or until τ stops improving or is within the predefined tolerance, must be repeated. This also includes the QR decomposition of the zeroth moment at every increment, contributing to what can take up a non-negligible amount of the total simulation time. The final issue with the ABS technique is that it does not support the possibility of needing only a single expansion point, which is quite commonly the optimal choice when considering a narrow band antenna. Of course, it would be possible for "Line 1" in Figure 3.4-3 to instead check an ROM at one expansion point located at s_{mid} against exact solutions at s_{min} and s_{max}, but this would require three LU decompositions, the same as if "Line 1" in Figure 3.4-3 is to be left as is.

To address these three issues, a simpler and more efficient method for determining N_q and N_m is developed here and similarly depicted in Figure 3.4-4. For this explanation, all mentions of certain "Line" numbers are with reference to Figure 3.4-4. This method works by splitting the band into evenly distributed intervals and placing expansion points at the centre of each. To start, as shown by "Line 1", an expansion point is placed in the centre of the entire band of interest. The ROM created at this point is then only tested and checked using (3.4-3) at s_{min}, again starting with $N_{q,min}$ and incrementally increasing to $N_{q,max}$, or until τ stops improving or is within the predefined tolerance, to conclude that the ROM is accurate. If τ does not fall below τ_{max}, then the method goes to the next line and repeats the same process. The band is split into two, as shown on "Line 2" and a ROM is constructed at the midpoint of the lowest frequency interval (the green dot on "Line 2"). That ROM is checked against only s_{min} once again. This process continues down each line until one of the ROMs computed yields sufficiently accurate results at s_{min}. Once this occurs, an ROM at each of the remaining expansion points (the blue dots on that line) are constructed, of the same size as that at the successful green dot. This method right away solves the compatibility issue with a single expansion point, in that one expansion point here would only require two LU decompositions and not three, as shown on "Line 1."

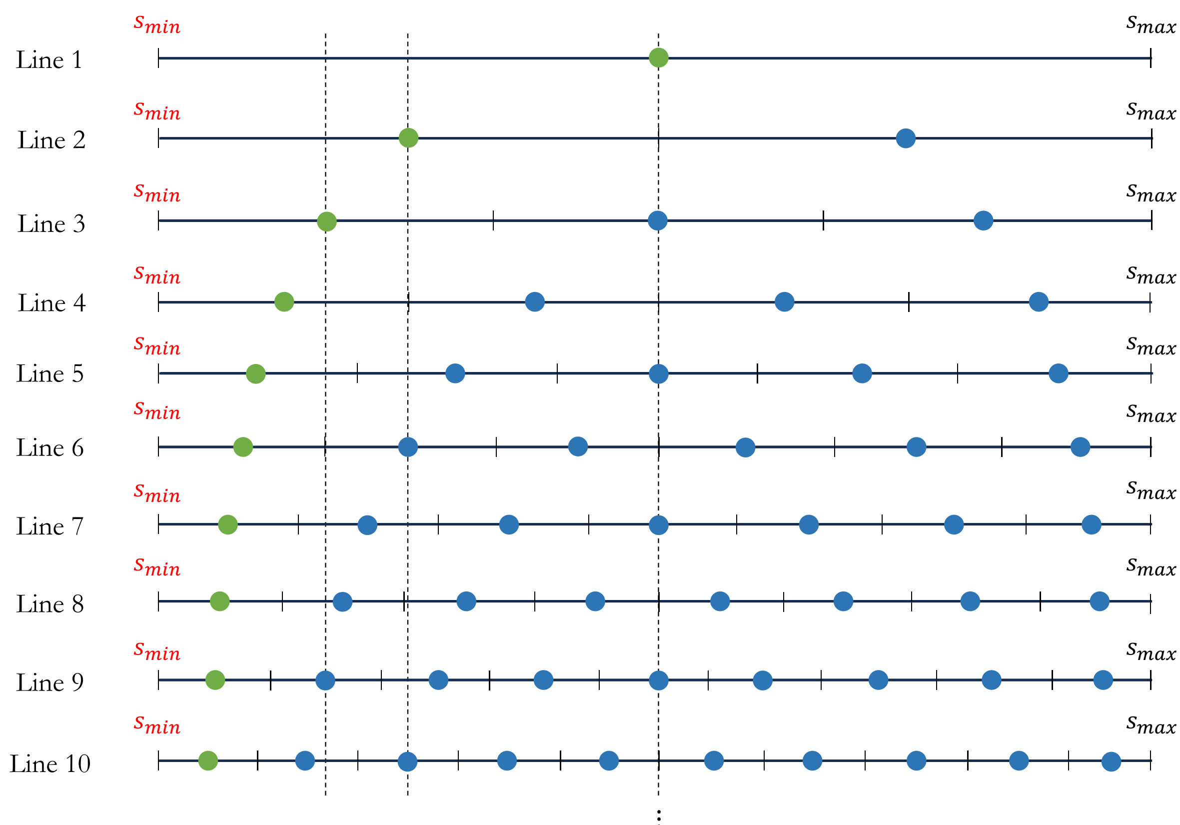

Figure 3.4-4. Diagram helping to illustrate a new method of determining N_q and N_m. Green dots represent the frequency on each line in which an ROM is created and checked against an exact solution at s_{min}, while blue dots show where final ROMs are to be created if a specific line's green dot ROM is deemed to be accurate. The vertical dashed lines show instances where green dots of one line occur at the same frequencies as blue dots on other lines.

Before addressing the other two issues, the method can be improved by noticing (via the vertical dashed lines in Figure 3.4-4) that some of the blue dots share frequencies with certain green ones, most noticeably that the basis used to create the first ROM on "Line 1" can always be reused to create an ROM at that same frequency should the method terminate on an odd numbered line. Table 3.4-1 shows how many LU decompositions and how many checks are needed if we consider all of these reuse cases when using all lines, as well as when only using even lines or only using odd lines.

Table 3.4-1. Number of LU decompositions and checks needed depending on what line is needed when all lines, only odd lines, and only even lines are reconsidered.

	LU Decompositions			Checks		
Line	All	Odd	Even	All	Odd	Even
1	2	2	-	1	1	-
2	4	-	3	2	-	1
3	5	4	-	3	2	-
4	8	-	6	4	-	2
5	9	7	-	5	3	-
6	11	-	8	6	-	3
7	13	10	-	7	4	-
8	16	-	12	8	-	4
9	16	12	-	9	5	-
10	19	-	14	10	-	5

This table shows that the number of LU decompositions can be significantly reduced when only considering either an odd or even number of expansion points. In fact, when only considering odd lines, the number of LU decompositions needed for a certain line is always less than the number needed for one less line when considering all lines. For example, when using only odd lines, five expansion points would always need seven LU decompositions which is less than the eight that are needed for four expansion points when considering all lines. As such, using only odd lines will always need fewer LU decompositions than when using all lines, even if it has to create an additional ROM. This is not so when using only even lines. In the latter case, in addition to not permitting a single ROM for the entire range, the total number of LU decompositions needed does not become less than that required when using all lines, until at least five expansion points are needed. For example, if a minimum of three expansion points are necessary, using all the lines would result in five LU decompositions, but using only even lines would necessitate four expansion points which would require six LU decompositions. This ultimately means that only using odd lines is the preferred route.

Compared to the ABS method the number of LU decompositions for a set number of expansion points is fixed here and not dependent on the antenna's response. As was mentioned earlier, for a set number of expansion points, such as five, the ABS technique could require fewer LU decompositions, as it could necessitate only six, however it can also require several more, in this case up to nine. The new technique described here would always need seven, meaning it usually needs either the same number, or often fewer, LU decompositions. It is also worth noting that the ROMs created using this technique are all used in their entirety since they are never constructed at s_{min} and s_{max}. In terms of checks, for five expansion points, the ABS technique needed a minimum of eight checks but could also need up to 14. Using this new method with only the "odd lines", five expansion points would require only three checks every time. This is a significant decrease.

Ultimately, as will be shown with numerical examples in *Section 3.5*, the new method described here, specifically when only considering odd lines, offers significant time saving over the ABS algorithm. At this stage concerns could be raised regarding the accuracy of this new method since not the entirety of the frequency band is being checked. However as will be shown in the next section, as long as the maximum tolerance is set to an appropriate level, no issues regarding accuracy are observed.

3.5 VERIFICATION OF THE MODEL ORDER REDUCTION SOLUTION

The purpose of this section will be to verify results achieved via the MOR methods defined in *Sections 3.2-3.4*. This section will then go on to compare and discuss the computational benefit of using model order reduction.

3.5.1 Test Case 1 - Air Substrate Patch and Ground Plane

The first test case that will be used is the single layer patch antenna and ground plane structure seen previously in Figure 2.3-1. This antenna is that presented in [HERS 98]. The dimensions of the patch antenna used here for testing are the same which are defined in [HERS 98], with the exception of the width of the pin whose dimension was not stated and was thus chosen to be 1.8 mm.

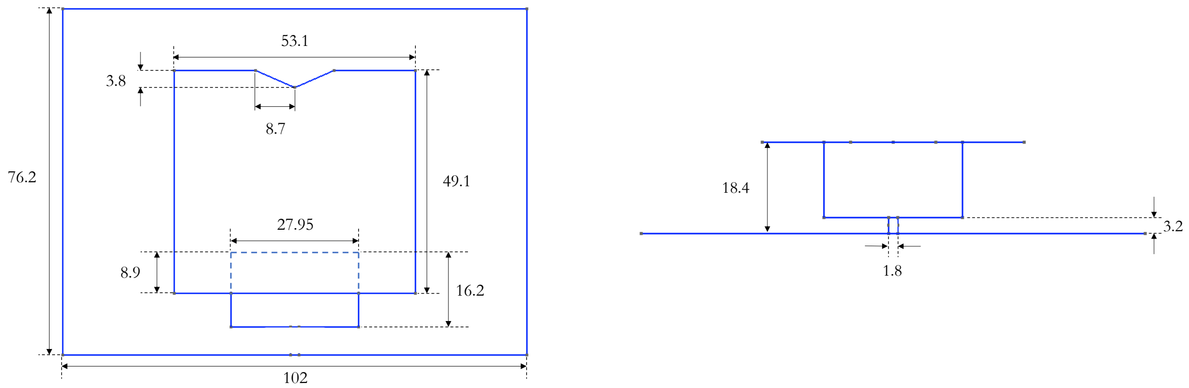

Figure 3.5-1. The dimensions (in mm) of the patch antenna and ground plane shown in the $x - y$ plane (left) and $x - z$ plane (right).

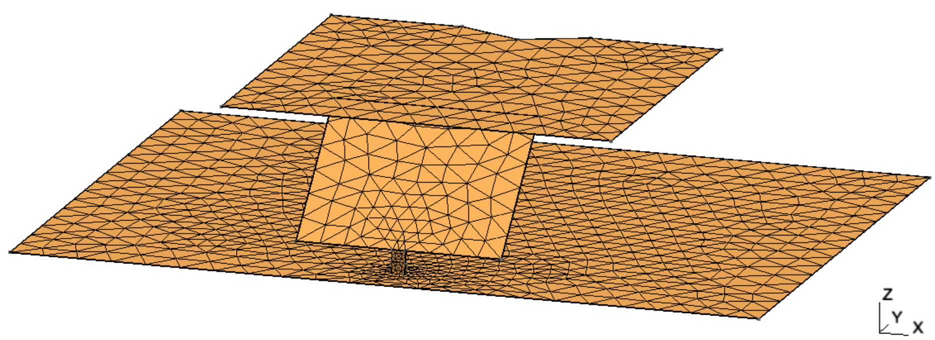

Figure 3.5-2. Patch antenna and ground plane mesh with air substrate created using Gmsh software [GEUZ 09].

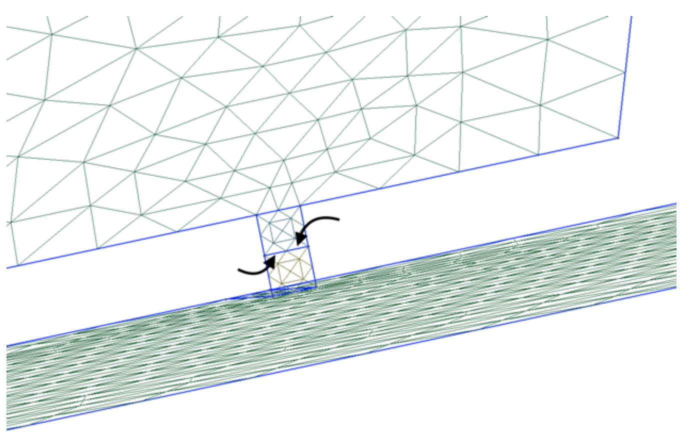

Figure 3.5-3. Patch antenna mesh of Figure 3.5-2 with black arrows indicating the feeding edges.

An overview of the structure and its dimensions are seen in Figure 3.5-1. The meshed structure is shown in Figure 3.5-2 which consists of 1684 triangles and 2455 inter-element edges. Figure 3.5-3 indicates which edges in the mesh in Figure 3.5-2 have been chosen as the feeding edges for the delta gap feeding model described in *Section 2.3.6*.

3.5.1.1 Test Case 1 Results

This section will compare results obtained via the "Exact" solution computed using (2.3-20), the "Chebyshev" solution computed using (3.2-28), and the "Implicit MOR" along with the "Explicit MOR" (using the procedure in *Section 3.3.2*) solutions found using both the ABS method and what will be called the "odd minimum check" (OMC) technique illustrated by only the odd lines in Figure 3.4-4. To start, it is necessary to determine the value of N_c needed for the Chebyshev and MOR methods. This will be done using the graphical approach described in *Section 3.4.1*. Computing U in (3.4-2) for values of N_c ranging from one to 30 given the mesh shown in Figure 3.5-2 and the desired frequency band of 1.5-6 GHz, the red curve in Figure 3.5-4 is obtained. It can be seen that this red curve falls within the $N_c = 5$ region. The total CPU time needed to generate this plot was 0.059 seconds.

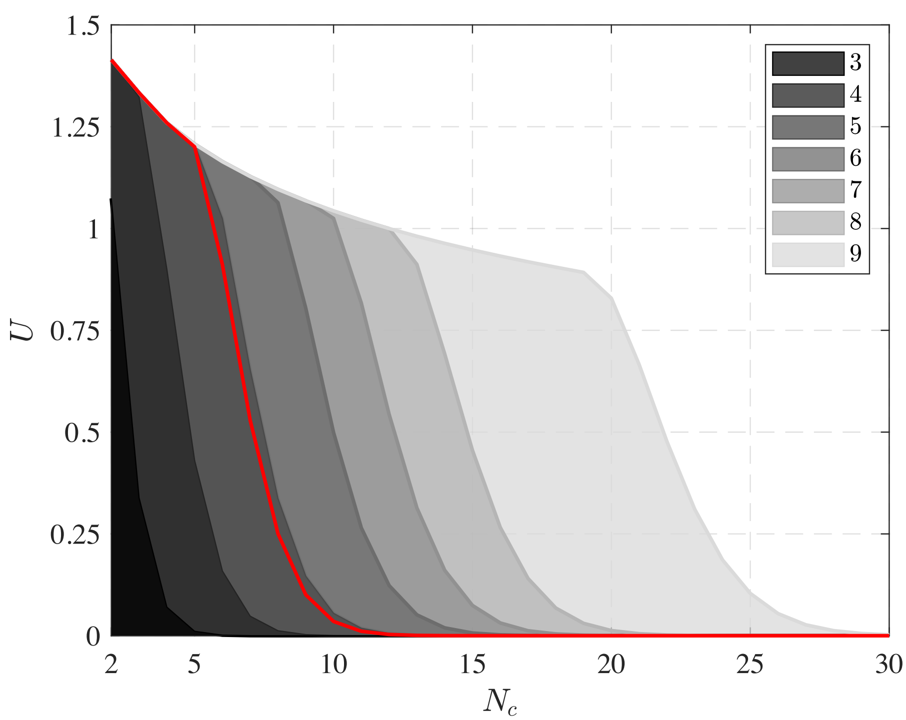

Figure 3.5-4. U curve of the patch antenna in Figure 3.5-2 for 1.5-6 GHz overlayed on top of Figure 3.4-2.

Figure 3.5-5 shows the input reflection coefficient as a function of frequency. The input impedance Z_{in} is calculated at each frequency using

$$Z_{in} = \frac{V_{in}}{I_{in}} = \frac{V_m}{{l_m}^2 I_m} \tag{3.5-1}$$

while the reflection coefficient Γ_{in} is calculated using (2.2-4) referenced to 50 Ω. In (3.5-1), l_m is the feeding edge length and I_m is the current coefficient corresponding to the feeding edge. Since the mesh in this example requires two feeding edges, (3.5-1) must be adjusted to consider both edges,

$$Z_{in} = \frac{V_{in}}{I_{in}} = \frac{V_{m,avg}}{l_{m1} I_{m1} + l_{m2} I_{m2}} \tag{3.5-2}$$

where

$$V_{in} = V_{m,avg} = \frac{\frac{V_{m1}}{l_{m1}} + \frac{V_{m2}}{l_{m2}}}{2}. \tag{3.5-3}$$

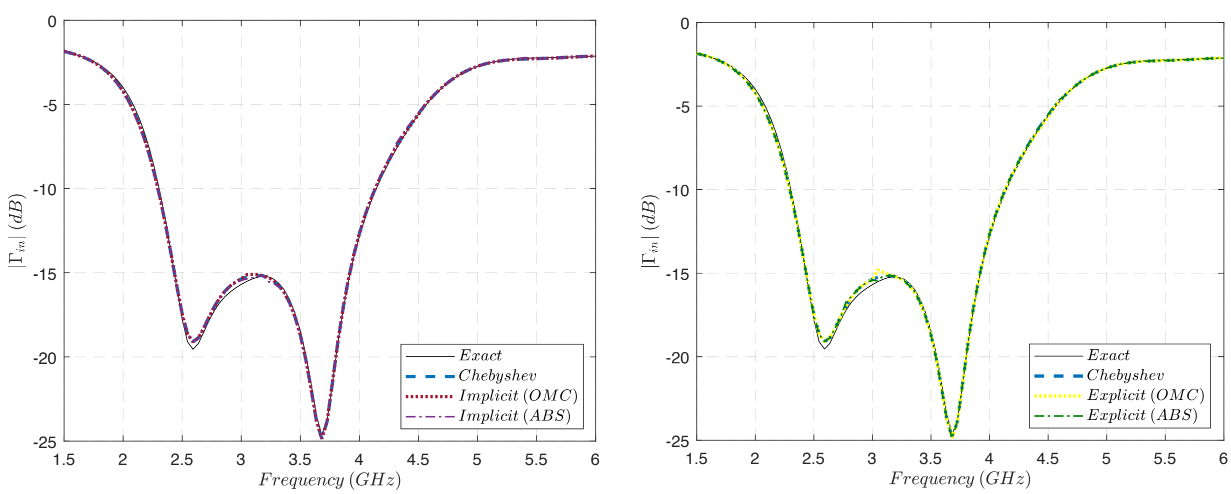

Figure 3.5-5. Input reflection coefficient as a function of frequency. For clarity, the left plot shows the implicit methods while the right plot shows the explicit methods.

Figure 3.5-6 shows the total directivity in the $x - z$ ($\phi = 0°$) and $y - z$ ($\phi = 90°$) plane at 2.5 GHz.

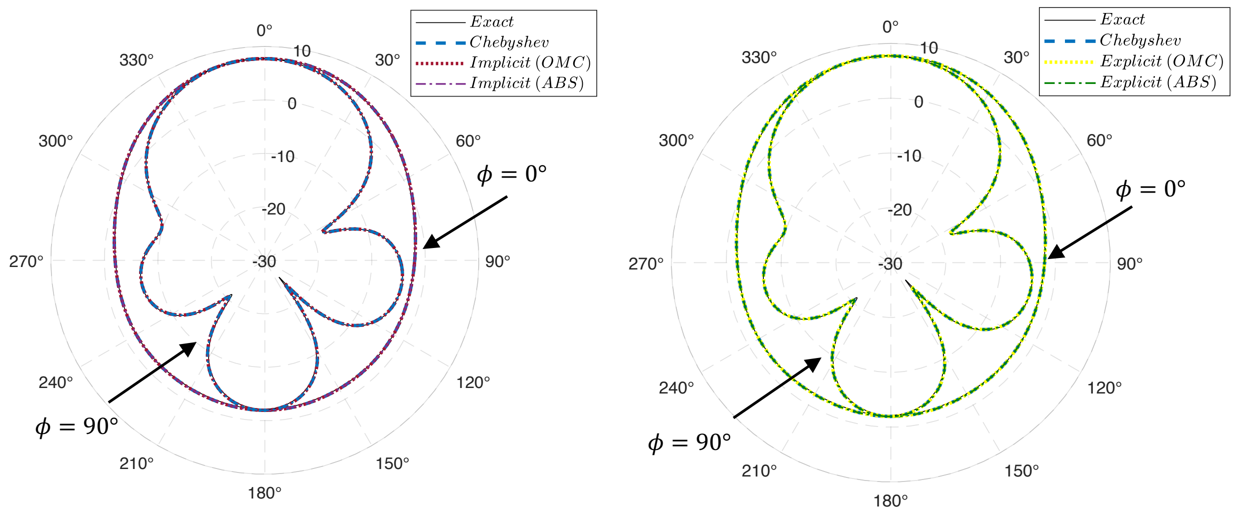

Figure 3.5-6. Total directivity in the $x - z$ ($\phi = 0°$) and $y - z$ ($\phi = 90°$) plane at 2.5 GHz. For clarity, the left plot shows the implicit methods while the right plot shows the explicit methods.

It can be seen from Figures 3.5-5 and 3.5-6 that the approximate results align almost perfectly with those calculated exactly with no Chebyshev polynomial approximations or matrix reductions. The upper bound on the accuracy of the MOR curves is the Chebyshev curve seeing as they all use the same value of N_c. Since the MOR curves are basically perfectly in line with the Chebyshev curve, if even less difference between the exact and MOR curves is desired, than the N_c values in the legends of Figures 3.4-2 and 3.5-4 can be adjusted accordingly.

3.5.1.2 Examination of the Test Case 1 Computation Time

Table 3.5-1 shows the operational parameters for each of the six curves shown in the previous section, as well as the MOR parameters that were determined by either the OMC or ABS selection algorithms. Figure 3.5-7 then shows the CPU time needed for the full CEM analysis as a function of the number of frequencies that were solved for each of the six curves. Figure 3.5-7 clearly shows the computational benefit of the MOR method. Since it is only the reduced system that is being inverted at each frequency point, additional frequency points translate to very little extra computation time. This is seen clearly by the relatively constant computation times of both the implicit and explicit MOR methods, contrastingly to the traditional "Exact" solution whose computation time increases near linearly as the number of frequency points is increased.

Table 3.5-1. Test Case 1 operational parameters

N_e = 2455	Chebyshev	Implicit MOR		Explicit MOR	
		OMC	ABS	OMC	ABS
N_c	5	5	5	5	5
N_m	-	3	7	3	16
{Expansion Frequency (GHz), N_q}	-	{2.25, 9} {3.75, 9} {5.25, 9}	{1.5, 5} {2.0625, 5} {2.625, 5} {3.75, 5} {4.875, 5} {5.4375, 5} {6, 5}	{2.25, 9} {3.75, 9} {5.25, 9}	{1.5, 3} {1.7812, 3} {2.0625, 3} {2.3438, 3} {2.2625, 3} {2.9062, 3} {3.1875, 3} {3.4688, 3} {3.75, 3} {4.0312, 3} {4.3125, 3} {4.875, 3} {5.1562, 3} {5.4375, 3} {5.7188, 3} {6, 3}
τ_{max}	-	5%	5%	1%	1%
$N_{q,min}$	-	5	5	3	3
$N_{q,max}$	-	45	45	43	43
ΔN_q	-	2	2	2	2

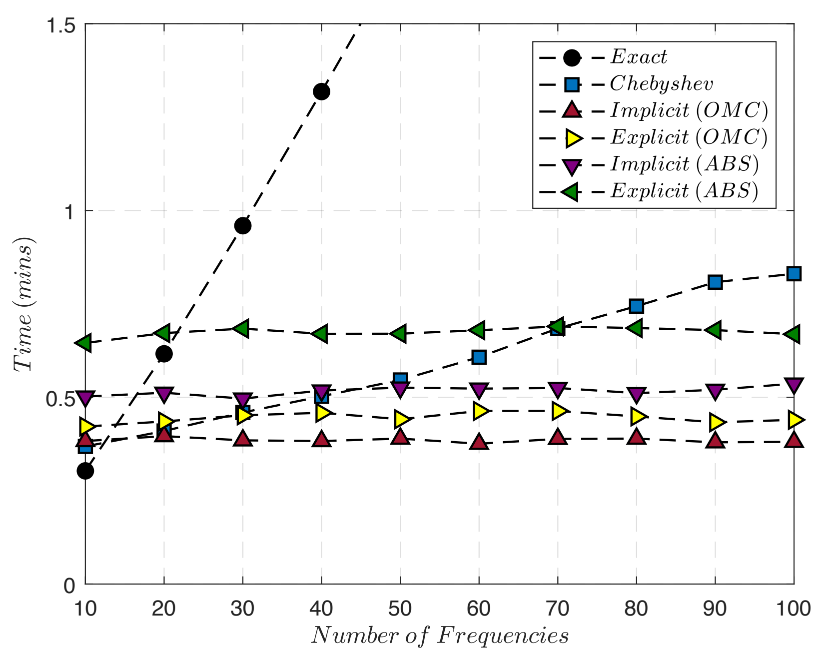

Figure 3.5-7. CPU time as a function of the number of computed frequency points. These times were found running MATLAB on a computer with an Intel Core i9 CPU and 128 GB of RAM.

When comparing the four MOR curves, implicit MOR is expectedly faster than its explicit counterpart. Table 3.5-1 shows that the OMC algorithm yielded the same number of expansion points and the same ROM size for both the implicit and explicit methods. While the difference in computation time for this example is not massive, the gap tends to widen as the antenna response becomes more complex and thus the explicit method is forced to compute more ROMs since computing additional moments stops contributing to the accuracy of the approximation (as was discussed in *Section 2.5.2*). We can begin to observe this in Table 3.5-1 where the explicit method needed a lower τ_{max} than the implicit method to achieve similar levels of accuracy. This issue also limits the effectiveness of the explicit method as the problem size increases since larger ROMs are naturally needed to continue achieving accurate results. This will become evident in the next section.

Next, from Table 3.5-1 it becomes quite evident that the OMC algorithm in this case is faster than the ABS algorithm simply due to requiring a lesser N_m. Despite both implicit algorithms having the same maximum tolerance, the OMC method proves that three expansion points is sufficient, however the ABS method does not. Why this is the case becomes clear when looking at Figures 3.4-3 and 3.4-4. Figure 3.4-3 shows that when the ABS algorithm is checking whether three expansion points is sufficient, the ROM constructed at s_{mid} is responsible for ensuring the accuracy of half of the total band. Figure 3.4-4 shows that since the OMC algorithm places the expansion points in the centres of sub-bands, each ROM is therefore responsible for a sub-band of equivalent size. As such, the three ROMs produced by the OMC algorithm on "Line 3" of Figure 3.4-4 for this test case, each covering a third of the band, were deemed to be accurate, whereas those three for the ABS algorithm were not and it was thus forced into constructing more ROMs than necessary.

Additionally, a general observation can be made that the majority of the time saved between the exact method and the MOR methods is a result of the Chebyshev approximation of the impedance matrix rather than the MOR itself given the "Chebyshev" result in Figure 3.5-7. While this is true for a small problem like this example, the computational benefit of MOR relative to the Chebyshev method increases as the problem size increases. This is because with relatively small problems the filling of the impedance matrices, whether that be the exact matrices at each frequency point or the

Chebyshev matrices, is dominant in terms of computation time compared to their inversions (or LU decompositions). As the system size increases, the time needed to invert the impedance matrices will become more prominent and will eventually dominate the matrix filling time, resulting in a greater benefit of MOR compared to just using the Chebyshev approximation since the Chebyshev approximation saves time only on impedance matrix filling when compared with the exact formulation, but not on matrix inversions. The second test case introduced in the following section confirms this intuition in practice.

3.5.2 Test Case 2 – Eight-Element Array Antenna of Air-Substrate Patches and Ground Plane

The purpose of this second test case is to analyze a problem of considerably larger size. This will be done by simulating an eight-element array antenna and ground plane. The radiating elements are those described in Figure 3.5-1, while the structure itself along with the dimensions of the platform can be seen below in Figure 3.5-8.

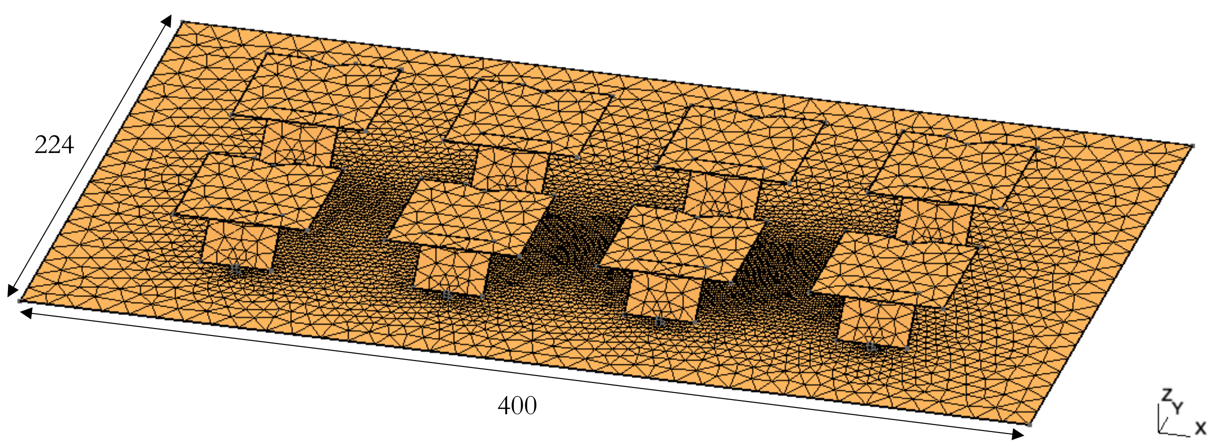

Figure 3.5-8. Eight-element array antenna of air-substrate patches above a ground plane. All dimensions are in mm.

3.5.2.1 Test Case 2 Results

Analogous to the results section for the previous test case, the following figure shows the input reflection coefficient and total directivity, respectively, obtained using the various methods. The reflection coefficient is taken at the port of the inside left element in the back row of Figure 3.5-8.

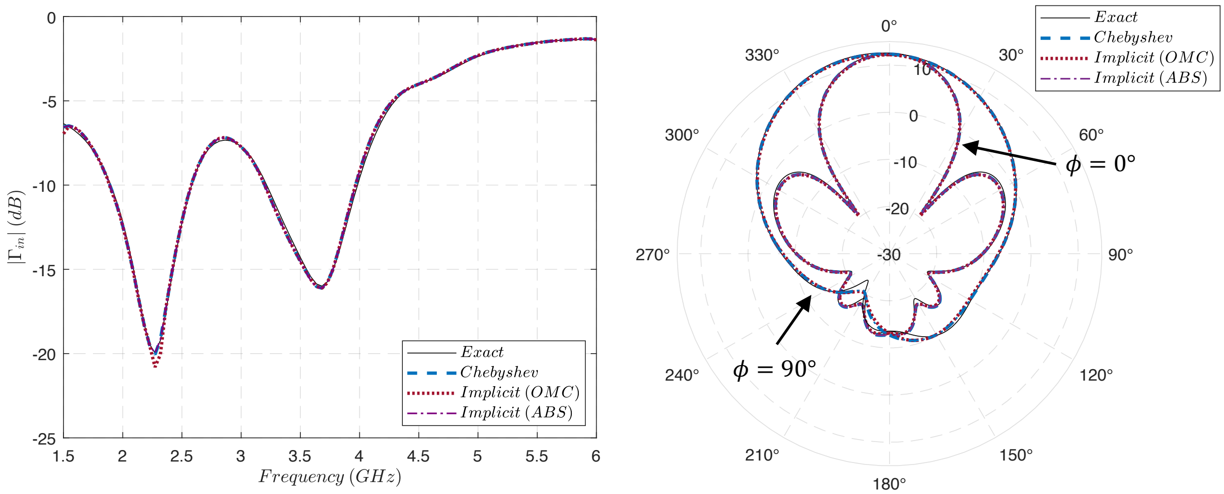

Figure 3.5-9. Input reflection coefficient as a function of frequency (left) and total directivity in the $x - z$ ($\phi = 0°$) and $y - z$ ($\phi = 90°$) plane at 2.5 GHz (right).

3.5.2.2 Examination of the Test Case 2 Computation Time

Table 3.5-2 shows the operational parameters for each of the four curves shown in the previous section, as well as the MOR parameters that were determined by either the OMC or ABS selection algorithms. Figure 3.5-10 then shows the CPU time as a function of the number of frequencies for each of the four curves. The computational benefit from MOR is again clear to see. The most notable difference in this example being the vast improvement in computation time between MOR using the OMC algorithm and the Chebyshev solution. This of course was expected given the much larger problem size than that of the previous example. It is also worth noting the huge difference between the OMC and ABS algorithms. This is largely due to τ_{max} for the ABS method needing to be reduced to 0.5% to achieve sufficiently accurate results, whereas the OMC method was able to remain at the same 5% that was used in the smaller problem. In fact, all four of the user-variable settings in the final four rows of Tables 3.5-1 and 3.5-2 were found to consistently provide sufficiently accurate results. More examples can be seen in *Chapter 4*.

3.6 CONLUDING REMARKS

In this chapter, model order reduction techniques well-established in the field of circuit simulation, but not so in the CEM landscape, have been enhanced so that they can be applied to the MoM formulation of electromagnetic scattering from PEC objects. The process first involves adapting

Table 3.5-2. Test Case 2 operational parameters

N_e = 23581	Chebyshev	Implicit MOR		Explicit MOR	
		OMC	ABS	OMC	ABS
N_c	9	9	9	N/A	N/A
N_m	-	11	31		
{Expansion Frequency (GHz), N_q}	-	{1.7045, 9} {2.1136, 9} {2.5227, 9} {2.9318, 9} {3.3409, 9} {3.75, 9} {4.1591, 9} {4.5682, 9} {4.9773, 9} {5.3864, 9} {5.7955, 9}	{1.5, 5} {1.5703, 5} {1.6406, 5} {1.7813, 5} {1.9219, 5} {2.0625, 5} {2.2031, 5} {2.3438, 5} {2.4844, 5} {2.6250, 5} {2.7656, 5} {2.8359, 5} {2.9063, 5} {3.0469, 5} {3.1875, 5} {3.3281, 5} {3.4688, 5} {3.6094, 5} {3.75, 5} {3.8906, 5} {4.0313, 5} {4.1719, 5} {4.3125, 5} {4.5938, 5} {4.875, 5} {5.0156, 5} {5.1563, 5} {5.4375, 5} {5.7188, 5} {5.8594, 5} {6, 5}		
τ_{max}	-	5%	0.5%		
$N_{q,min}$	-	5	5		
$N_{q,max}$	-	45	45		
ΔN_q	-	2	2		

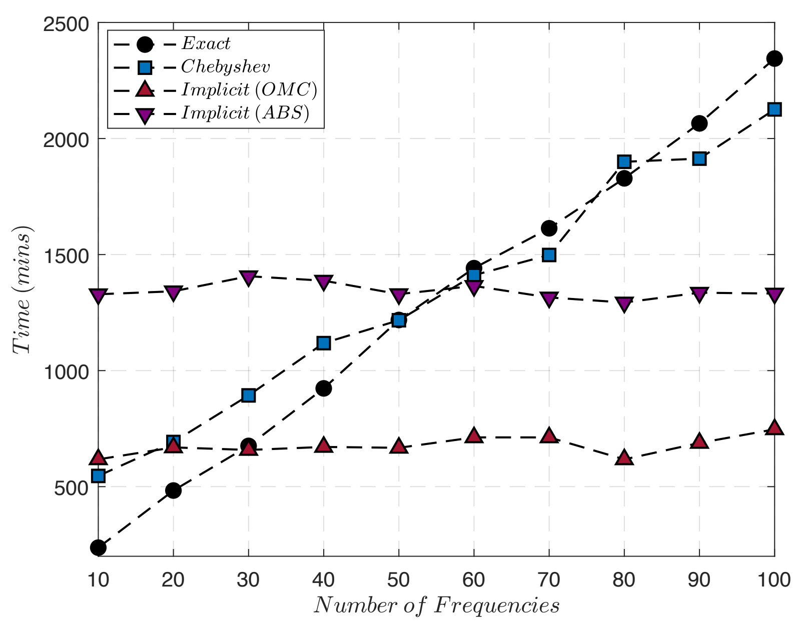

Figure 3.5-10. CPU time as a function of the number of computed frequency points. These times were found running MATLAB via the Digital Research Alliance of Canada's Narval compute node's [NARV 21] with two AMD EPYC 7413 (Zen 3) CPUs and 498 GB of RAM.

the MoM matrix into an MOR-compatible frequency power series form using a Chebyshev approximation. This necessary approximation step was shown to greatly expand the problem size in proportion to the number of Chebyshev coefficients needed to approximate the MoM impedance matrix. To alleviate this additional computational burden, a novel efficient MOR procedure was developed specifically for these types of problems, which obviates the need to construct or store any of the expanded problem matrices. Furthermore, new algorithms were developed to automatically determine the optimal or near-optimal (albeit problem-dependent) number of Chebyshev coefficients, reduced order model size, and number of expansion points, to ensure accurate results in an efficient manner without prior knowledge of the antenna's performance. All of the above aspects of the methodology were then verified through two examples of different problem sizes that highlighted the vast improvement in computational efficiency as the number of computed frequencies increases, while maintaining accuracy, all corroborated by comparison with traditional MoM simulations. The two chapters that now follow will present new antenna applications that benefit immensely from the developments of this chapter.

CHAPTER 4

Antenna-Circuit Co-Simulation Via Clustering Model Order Reduction

4.1 INTRODUCTION

With the process of applying model order reduction to a moment method formulation now laid out and verified for accuracy and speed, the following chapters will incorporate the methodology in *Chapter 3* into other antenna simulation applications. The first of which, covered in this chapter, is with regards to a system of equations which allows for the unification of integrated circuits alongside radiating elements. Such an approach is becoming increasingly sought after as the drive to use higher millimetre-wave frequencies in wireless communication technologies has created the necessity [WATA 21] to closely integrate arrays of individual radiating elements with the associated transceiver (RF electronics and beamformers, as depicted in Figure 4.1-1) due to increasingly limited physical access to the input ports of radiating elements.

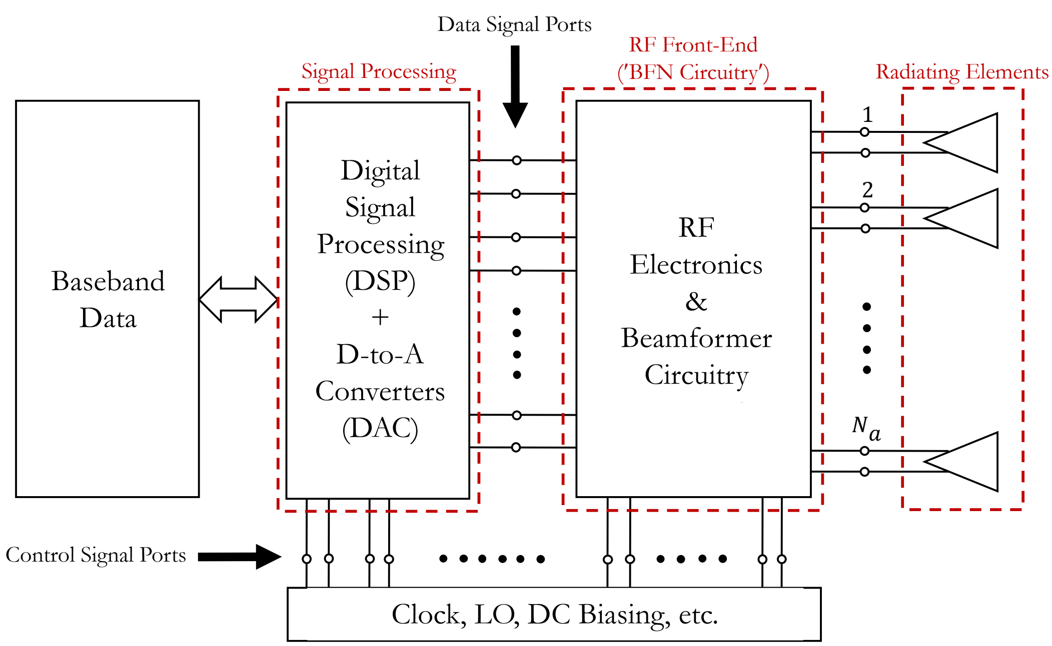

Figure 4.1-1. Depiction of a model of an imagined tightly integrated passive array antenna and accompanying beamforming circuits (possibly active, and containing non-linear components), in transmit mode. N_a is the number of radiating elements.

Indeed, [ZHAN 22b] alludes to the advantages of including both the antenna and circuitry in the same design analysis of such situations, so-called co-design. Thus, co-simulation approaches must evolve to treat the onboard electronics and radiating elements as a unified entity for analysis purposes in a computationally efficient manner.

Traditional metrics that evaluate passive array antenna performance, such as radiation patterns, directivity, and impedance-matching characteristics, can be determined, at least for moderately-sized arrays, using existing approaches in the literature [PAN 92], [WARN 18]. These are based on the viewpoint shown in Figure 4.1-2, in which the linear passive beamforming circuit does not include any transceiver electronics. Computational electromagnetics (CEM) is used to represent the radiating elements as a matrix $\boldsymbol{Z}_A$ of size $N_a \times N_a$. This $\boldsymbol{Z}_A$ is essentially a circuit model that describes the 'external' coupling between the array elements and can be determined via a sequence of CEM-based computations, as in [PAN 92] for instance. The linear passive beamformer circuit is then modeled [WARN 18] by another frequency-dependent matrix $\boldsymbol{Z}_G$, which together with the effective Thevenin sources, excites the array elements in the manner desired. Circuit analysis (combining the impedance matrices of multiports) is then used to determine the actual excitations at the array element ports; these are subsequently used as impressed sources in the CEM model of the radiating elements to find the radiation pattern characteristics. In the terminology of [JIN 19], this could be called a sequential coupling approach to the co-simulation.

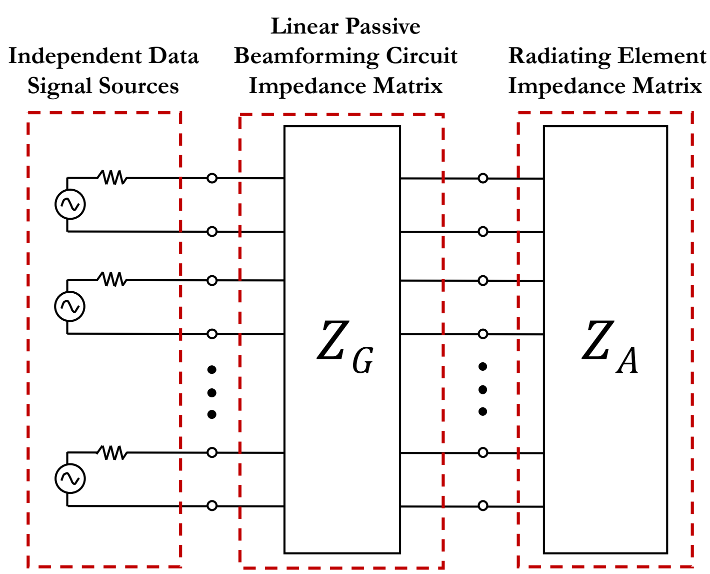

Figure 4.1-2. Diagram illustrating existing passive beamformer and array antenna modelling.

Although such conventional approaches remain successful in many applications that use array antennas, they would not adequately address the complexity of future array antenna platforms. One example is the fact that such an approach does not allow room for handling nonlinear devices in the transceiver/beamformer circuitry, and so exploitation of the antenna port properties, in addition to its radiating properties, to directly facilitate the design (e.g. [LIM 21]) of the entire antenna and circuit arrangement of Figure 4.1-1 would not be possible, for instance. Also, the limited access to the input ports of the individual radiating elements in highly integrated antenna designs has prompted the measurement of performance metrics that can capture the combined response of transceiver components and radiating elements, such as error vector magnitude [BROW 23a], [BROW 23b]. The computation of such quantities would thus also be needed during the design stage and would involve modulated-signal-based co-simulation. Many further reasons for adopting a co-design approach have been given (e.g. [NALL 19], [MARZ 22]). Thus, co-simulation methods are needed that have the computational efficiency to render feasible the large number of repeated simulations required in any design process. Difficulties in achieving this are accentuated by the disparity between the formulations that best suit lumped circuit analysis and the 3D full-wave analysis that is needed to accurately model significantly distributed non-radiating components and array radiating elements. Thus, [BELO 21] observes that antenna arrays have already been optimized for a given receiver but not the other way around, in part because receivers are optimized in circuit simulators and antennas in field simulators. It is for this reason that [BELO 21] proposes a more comprehensive circuit model for the array antenna. The co-simulation method presented in this section retains the circuit and direct field analyses for the respective parts in order to allow flexibility in the complexity of the antenna types used, and for which equivalent circuits and expressions for the relatively complicated radiation patterns (e.g. steered) are not straightforward.

In the interests of simplicity of description this section will discuss matters in terms of the transmit case of Figure 4.1-3, it being understood that similar considerations apply to the receive case. Although nothing in the formulation will in principle preclude the inclusion of the DSP portions, the presentation will have in mind the situation in Figure 4.1-3, with the DSP input to the RF electronics modelled as independent data signal sources. This approach formulates a unified system of equations which includes the MNA formulation form of the circuitry and the method of moments field modelling of the radiating elements. Recognizing that such an analysis would be computationally cumbersome for even moderately-sized arrays, multi-port MOR is applied to reduce the computational cost.

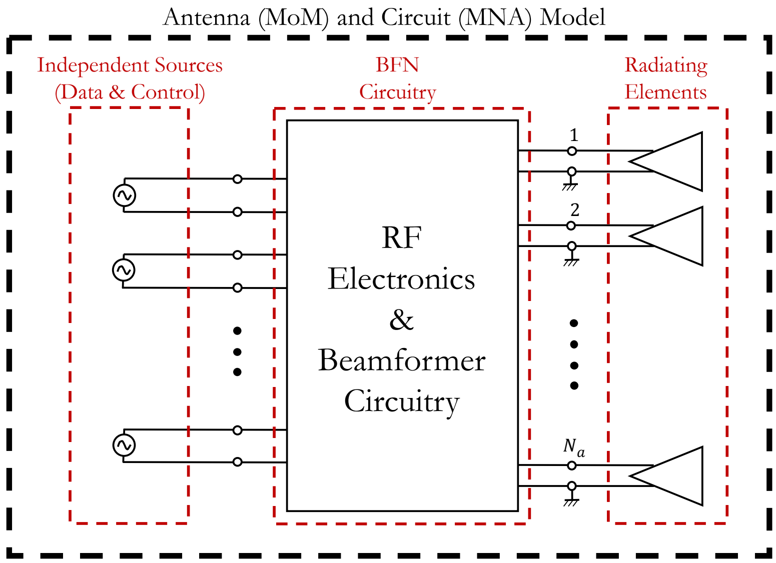

Figure 4.1-3. Antenna (MoM) and circuit (MNA) model. In the MNA model the Thevenin impedances of the equivalent sources are moved into the MNA model itself.

The above-mentioned formulation will be presented and demonstrated in this chapter through the following sections:

- Section 4.2: Unified Circuit and Radiating Elements Formulation
- Section 4.3: Numerical Simulation Results
- Section 4.4: Inclusion of Nonlinear Circuit Elements
- Section 4.5 Concluding Remarks

4.2 UNIFIED CIRCUIT AND RADIATING ELEMENTS FORMULATION

Firstly, Table 4.2-1 defines numerous parameters and notations used in this section which have been defined in previous sections but have been compiled here for convenience.

Table 4.2-1. Definitions of antenna-circuit co-simulation parameters and notations.

N_a	Number of radiating element ports
N_e	Number of edges in the antenna mesh
N_p	Number of ports in the circuit
N_c	Number of Chebyshev polynomials selected for the approximation of $\boldsymbol{Z}(s)$
N_q	Size of the reduced system
N_m	Number of expansion frequencies s_0 needed to approximate the solution over a certain frequency band using MOR
N_f	Desired number of sample frequencies in the band of interest
$\mathbb{I}_M$	Identity matrix of size $M \times M$
$\mathbb{e}_{m,M}$	m^{th} column of $\mathbb{I}_M$
$\{0, 1\}^{M \times N}$	$M \times N$ matrix whose entries are 0 or 1

4.2.1 Development of the Unified Formulation

The multi-port MNA and MoM matrix equations from *Chapter 2* are recalled here as

$$(\boldsymbol{G} + s\boldsymbol{C})\boldsymbol{X}(s) = \boldsymbol{B}_c\boldsymbol{U}(s) \tag{4.2-1}$$

and

$$\boldsymbol{Z}(s)\boldsymbol{I}(s) = \boldsymbol{B}_a\boldsymbol{V}(s) \tag{4.2-2}$$

respectively, where the right side of the MoM equation from (2.3-20) has been split up in a similar manner to that in (4.2-1) which was described in *Section 2.6*. $\boldsymbol{V}(s)$ is a vector of size $N_a \times 1$ containing the voltages applied to the feeding edges of the antenna and $\boldsymbol{B_a}$ is a matrix of size $N_e \times N_a$ which maps the voltages in $\boldsymbol{V}(s)$ to their corresponding feeding edges for each of the N_a radiating elements. The delta-gap feeding model described in *Section 2.3.6* is again being used here to feed the antenna structures, therefore the i^{th} column of matrix $\boldsymbol{B_a}$ is populated with the lengths of the sides of mesh triangles that are coincident with the i^{th} radiating element, but only for those entries whose row indices correspond to the location of those specific edges in the whole set of N_e edges of the mesh, and are zero otherwise. The product $\boldsymbol{B}_a\boldsymbol{V}(s)$ thus yields individual entries in the right-side vectors which are in line with those derived for the delta-gap model.

The unified antenna-circuit (field-circuit) formulation is then built upon the following observations.

1) The voltages, $\boldsymbol{V}(s)$, that drive the antenna elements, steering the radiation patterns, constitute a subset of the nodes in the beamforming network (BFN) circuitry $\boldsymbol{X}(s)$. This idea can be captured by defining a matrix $\boldsymbol{D} \in \{0,1\}^{N_k \times N_a}$, that makes $\boldsymbol{V}(s) = \boldsymbol{D}^{\mathrm{T}}\boldsymbol{X}(s)$.
2) The radiating elements load the BFN circuitry through the currents exchanged at the feeding edges. The currents in the radiating elements are encapsulated by the coefficients, in $\boldsymbol{I}(s)$, of the RWG basis functions that represent the surface current densities in A/m. Since the RWG basis functions have unity normal components at the edges of the mesh, and the subset of those edges that are fed by the BFN have their lengths in the matrix $\boldsymbol{B}_a$ defined in (4.2-2), it then follows that the currents exchanged between the BFN and the array elements at the feeding edges of the mesh are given by $\boldsymbol{B}_a^{\mathrm{T}}\boldsymbol{I}(s)$.
3) The $N_p > N_a$ ports of the BFN circuitry, represented in the columns of $\boldsymbol{B}_c$ in (4.2-1) are viewed as two distinct groups, those that are driven by external (independent) stimuli sources and those that drive the feeding edges of the N_a antenna elements. This notion is reflected by splitting $\boldsymbol{B}_c$ into two matrices, $\boldsymbol{B}_{ant} \in \{0,1\}^{N_k \times N_a} = \boldsymbol{D}$ that carries the ports which drive the antenna elements, and $\boldsymbol{B}_{ext} \in \{0,1\}^{N_k \times (N_p - N_a)}$ that channels the external independent sources.

These observations enable the assembly of the unified antenna-circuit formulation as

$$\begin{bmatrix} \boldsymbol{G} + s\boldsymbol{C} & \boldsymbol{B}_{ant}\boldsymbol{B}_a^{\mathrm{T}} \\ -\boldsymbol{B}_a\boldsymbol{B}_{ant}^{\mathrm{T}} & \boldsymbol{Z}(s) \end{bmatrix} \begin{bmatrix} \boldsymbol{X}(s) \\ \boldsymbol{I}(s) \end{bmatrix} = \begin{bmatrix} \boldsymbol{B}_{ext} \\ \boldsymbol{0} \end{bmatrix} \boldsymbol{U}_{ext}(s) \tag{4.2-3}$$

where $\boldsymbol{U}_{ext}(s)$ is the set of external sources that drive the circuit and the antenna. The matrices $\boldsymbol{B}_{ant}\boldsymbol{B}_a^{T}$ and $-\boldsymbol{B}_a\boldsymbol{B}_{ant}^{\mathrm{T}}$ provide the connection between the circuit variables and the currents at the ports of the antenna elements. The above formulation sets up an environment conducive to simultaneously simulating antenna arrays and their BFN circuitry, however, suffers from heavy computational burdens, particularly as the number of radiating elements N_a increases, as well as an inability to handle a BFN which contains nonlinear elements. The following sections address these issues.

4.2.2 Application of MOR to the Unified Antenna-Circuit Formulation

The application of MOR to (4.2-3) is done in much the same way as was covered in *Chapter 3*. The impedance matrix is first expanded via a Chebyshev approximation using the methodology in *Section 3.2* allowing for (4.2-2) to be written in the expanded form

$$\left(\begin{bmatrix} \boldsymbol{Z}_0 & \boldsymbol{0} & \boldsymbol{0} & & \boldsymbol{0} \\ \boldsymbol{0} & \mathbb{I}_{N_e} & 0 & \cdots & \\ \boldsymbol{0} & \boldsymbol{0} & \mathbb{I}_{N_e} & & \vdots \\ & \vdots & & \ddots & \\ \boldsymbol{0} & & \cdots & & \mathbb{I}_{N_e} \end{bmatrix} + s \begin{bmatrix} \boldsymbol{Z}_1 & \boldsymbol{Z}_2 & \boldsymbol{Z}_3 & & \boldsymbol{Z}_{N_c+1} \\ -\mathbb{I}_{N_e} & \boldsymbol{0} & \boldsymbol{0} & \cdots & \\ \boldsymbol{0} & -\mathbb{I}_{N_e} & \boldsymbol{0} & & \vdots \\ & \vdots & & \ddots & \\ \boldsymbol{0} & \cdots & \boldsymbol{0} & -\mathbb{I}_{N_e} & \boldsymbol{0} \end{bmatrix}\right) \begin{bmatrix} \boldsymbol{I}(s) \\ \boldsymbol{I}_1(s) \\ \boldsymbol{I}_2(s) \\ \vdots \\ \boldsymbol{I}_{N_c}(s) \end{bmatrix} = s \begin{bmatrix} \boldsymbol{B}_a \\ \boldsymbol{0} \\ \boldsymbol{0} \\ \vdots \\ \boldsymbol{0} \end{bmatrix} \boldsymbol{V}(s) \tag{4.2-4}$$

which is written compactly as

$$(\boldsymbol{P} + s\boldsymbol{T})\boldsymbol{\mathcal{I}}(s) = s\widetilde{\boldsymbol{B}}\boldsymbol{V}(s) \tag{4.2-5}$$

analogous to that in (3.3-2), however differing by the multi-port nature of the system in (4.2-4) identifiable by the matrix quantity on the right side as opposed to the vector quantity in the former. The moments of $\boldsymbol{\mathcal{I}}(s)$ can then be found at frequency s_0 in the same manner as was done in *Section 3.3* as

$$\boldsymbol{A} = -(\boldsymbol{P} + s_0\boldsymbol{T})^{-1}\boldsymbol{T} \tag{4.2-6}$$

$$\boldsymbol{R} = (\boldsymbol{P} + s_0\boldsymbol{T})^{-1}\left(\widetilde{\boldsymbol{B}} - \boldsymbol{T}\boldsymbol{M}_{0,s_0}\right) \tag{4.2-7}$$

$$\boldsymbol{M}_{0,s_0} = (\boldsymbol{P} + s_0\boldsymbol{T})^{-1}s_0\widetilde{\boldsymbol{B}} \tag{4.2-8}$$

$$\left[\boldsymbol{M}_{1,s_0}, \boldsymbol{M}_{2,s_0}, \boldsymbol{M}_{3,s_0}, \dots, \boldsymbol{M}_{i,s_0}\right] = \left[\boldsymbol{R}, \boldsymbol{A}\boldsymbol{R}, \boldsymbol{A}^2\boldsymbol{R}, \dots, \boldsymbol{A}^{i-1}\boldsymbol{R}\right]. \tag{4.2-9}$$

and the construction of the orthogonal basis spanning the space of the first N_q block moments is carried out using a modified version of the Arnoldi process from Figure 2.5-2 considering the block moments defined above. This modified Arnoldi process is shown in Figure 4.2-1.

Require: $\boldsymbol{Z}_i,\ i = 0, 1, \cdots, N_c + 1, s_0, \boldsymbol{B}_a$, and N_q
1: Initialize: $\boldsymbol{W} \leftarrow \phi$ $\{\phi$ is an empty set$\}$
2: Initialize: $\boldsymbol{M}_{0,s_0} \leftarrow (\boldsymbol{P} + s_0\boldsymbol{T})^{-1} s_0 \widetilde{\boldsymbol{B}}$
3: Solve: $\widetilde{\boldsymbol{W}} \leftarrow (\boldsymbol{P} + s_0\boldsymbol{T})^{-1}\left(\widetilde{\boldsymbol{B}} - \boldsymbol{T}\boldsymbol{M}_{0,s_0}\right)$
4: Normalize: $\boldsymbol{W_0} \leftarrow \frac{1}{\|\widetilde{\boldsymbol{W}}\|}\widetilde{\boldsymbol{W}}$
5: Append: $\boldsymbol{W} = [\boldsymbol{W} \quad \boldsymbol{W}_0]$
6: **for** $k = 1$ **to** $N_q - 1$ **do**
7:     **if** $j = N_q - 1$ **then**
8:         Assign: $\widetilde{\boldsymbol{W}} \leftarrow \boldsymbol{M}_{0,s_0}$
9:     **else**
10:         Solve: $\widetilde{\boldsymbol{W}} \leftarrow (\boldsymbol{P} + s_0\boldsymbol{T})^{-1}\, \boldsymbol{T}\, \boldsymbol{W}^{(k-1)}$
11:     **end if**
12:     **for** $i = 1$ **to** k **do**
13:         Compute: $\boldsymbol{H}_{ik} \leftarrow \boldsymbol{W}_i^H \widetilde{\boldsymbol{W}}$
14:         Orthogonalize: $\widetilde{\boldsymbol{W}} \leftarrow \widetilde{\boldsymbol{W}} - \boldsymbol{W}_i \boldsymbol{H}_{ik}$
15:     **end for**
16:     Normalize: $\boldsymbol{W}^{(k)} \leftarrow \frac{1}{\|\widetilde{\boldsymbol{W}}\|}\widetilde{\boldsymbol{W}}$
17:     Append: $\boldsymbol{W} = [\boldsymbol{W} \quad \boldsymbol{W}^{(k)}]$
18: **end for**

Figure 4.2-1. Modified block-Arnoldi pseudo code.

It is important to note that the calculations at lines 2, 3, and 10 of the pseudo code in Figure 4.2-1 are performed using the efficient procedure detailed in *Section 3.3.1*, however accounting for the fact that the moments are now block moments rather than single column vectors. The computation at line 2 is analogous to the single-port form shown in (3.3-17), however the right side will now be a matrix rather than a vector. Thus, the procedure to compute each column of the 0^{th} block moment $\boldsymbol{M}_{0,s_0}$ will constitute setting the right side of (3.3-17) as each successive column of the matrix $s_0\widetilde{\boldsymbol{B}}$ followed by computing (3.3-23). Similar deductions can be made for the calculations at lines 3 and 11. The single port equivalent of the calculation at line 3 is seen in (3.3-25). Now, the right side of (3.3-25) is the matrix $\left(\widetilde{\boldsymbol{B}} - \boldsymbol{T}\boldsymbol{M}_{0,s_0}\right)$ which is found through performing successive computations of (3.3-26) for each column of $\widetilde{\boldsymbol{B}}$ and its corresponding column of $\boldsymbol{M}_{0,s_0}$. Equation

(3.3-37) along with the relationship in (3.3-30) can then be used for each set of columns to fully characterize $\widetilde{\boldsymbol{W}}$. Line 10 is analogous to the single-port formulation of (3.3-39), however with matrices $\widetilde{\boldsymbol{W}}$ and $\boldsymbol{W}^{(k-1)}$ rather than vectors $\boldsymbol{Aq}^{(k)}$ and $\boldsymbol{q}^{(k-1)}$, respectively. Again, each individual column of $\widetilde{\boldsymbol{W}}$ can be computed using (3.3-39)-(3.3-42) using the corresponding column of $\boldsymbol{W}^{(k-1)}$. The efficient procedure thus allows once again for the computation of the basis $\boldsymbol{W}$ without needing to construct any of the larger expanded matrices in (4.2-5), needing instead only the Chebyshev coefficient matrices $\boldsymbol{Z}_i$ and the right-side matrix $\boldsymbol{B}_a$, both of which are the size of the original problem, N_e.

$\boldsymbol{W}$ is then be used to reduce the augmented system in (4.2-5) to form the reduced system

$$\left(\widehat{\boldsymbol{P}} + s\widehat{\boldsymbol{T}}\right)\widehat{\boldsymbol{\mathcal{I}}}(s) = s\widehat{\boldsymbol{B}} \tag{4.2-10}$$

where $\widehat{\boldsymbol{P}} = \boldsymbol{W}^{\mathrm{H}}\boldsymbol{PW}$, $\widehat{\boldsymbol{T}} = \boldsymbol{W}^{\mathrm{H}}\boldsymbol{TW}$, $\widehat{\boldsymbol{B}} = \boldsymbol{W}^{\mathrm{H}}\widetilde{\boldsymbol{B}}$, and $\boldsymbol{\mathcal{I}}(s) \approx \boldsymbol{W}\widehat{\boldsymbol{\mathcal{I}}}(s)$. Again, this reduction can be performed without computing matrices $\boldsymbol{P}$, $\boldsymbol{T}$, and $\widetilde{\boldsymbol{B}}$ by using the procedure in (3.3-43)-(3.3-48), recalling that each of $\left[\boldsymbol{q}^{(1)},\ \boldsymbol{q}^{(2)},\ \cdots \boldsymbol{q}^{(N_q)}\right]$ in these equations are now blocks of N_a columns $\left[\boldsymbol{W}^{(0)},\ \boldsymbol{W}^{(1)},\ \cdots \boldsymbol{W}^{(N_q-1)}\right]$. Incorporating the reduced system in (4.2-10) into the unified antenna-circuit formulation of (4.2-3) in place of the full MoM matrix $\boldsymbol{Z}(s)$ is carried out by recalling that $\boldsymbol{I}(s)$ and $\boldsymbol{B}_a$ are the first N_e entries in $\boldsymbol{\mathcal{I}}(s)$ and $\widetilde{\boldsymbol{B}}$, respectively. These facts are expressed mathematically as follows.

$$\boldsymbol{I}(s) \approx \left(\mathbb{e}_{1,N_c+1}^{\mathrm{T}} \otimes \mathbb{I}_{N_e}\right)\boldsymbol{W}\widehat{\boldsymbol{\mathcal{I}}}(s) \tag{4.2-11}$$

$$\boldsymbol{B}_a = \left(\mathbb{e}_{1,N_c+1}^{\mathrm{T}} \otimes \mathbb{I}_{N_e}\right)\widetilde{\boldsymbol{B}} \tag{4.2-12}$$

(4.2-12) can be further manipulated yielding,

$$\begin{aligned}
\boldsymbol{B}_a &= \widetilde{\boldsymbol{B}}^{\mathrm{T}}\left(\mathbb{e}_{1,N_c+1}^{\mathrm{T}} \otimes \mathbb{I}_{N_e}\right)^{\mathrm{T}} \\
\boldsymbol{B}_a &= \widetilde{\boldsymbol{B}}^{\mathrm{T}}\left(\mathbb{e}_{1,N_c+1} \otimes \mathbb{I}_{N_e}\right) \\
\boldsymbol{B}_a^{\mathrm{T}}\left(\mathbb{e}_{1,N_c+1}^{\mathrm{T}} \otimes \mathbb{I}_{N_e}\right) &= \widetilde{\boldsymbol{B}}^{\mathrm{T}}\left(\mathbb{e}_{1,N_c+1} \otimes \mathbb{I}_{N_e}\right)\left(\mathbb{e}_{1,N_c+1}^{\mathrm{T}} \otimes \mathbb{I}_{N_e}\right)
\end{aligned}$$

$$\boldsymbol{B}_a^{\mathrm{T}}\left(\mathbb{e}_{1,N_c+1}^{\mathrm{T}} \otimes \mathbb{I}_{N_e}\right) = \widetilde{\boldsymbol{B}}^{\mathrm{T}}\left(\mathbb{e}_{1,N_c+1}\mathbb{e}_{1,N_c+1}^{\mathrm{T}} \otimes \mathbb{I}_{N_e}\mathbb{I}_{N_e}\right)$$
$$\boldsymbol{B}_a^{\mathrm{T}}\left(\mathbb{e}_{1,N_c+1}^{\mathrm{T}} \otimes \mathbb{I}_{N_e}\right) = \widetilde{\boldsymbol{B}}^{\mathrm{T}}. \tag{4.2-13}$$

Next, (4.2-13) along with (4.2-5) can be used to rewrite (4.2-3) as

$$\begin{bmatrix} \boldsymbol{G} + s\boldsymbol{C} & \boldsymbol{B}_{ant}\boldsymbol{B}_a^{\mathrm{T}}\left(\mathbb{e}_{1,N_c+1}^{\mathrm{T}} \otimes \mathbb{I}_{N_e}\right) \\ -s\widetilde{\boldsymbol{B}}\boldsymbol{B}_{ant}^{\mathrm{T}} & \boldsymbol{P} + s\boldsymbol{T} \end{bmatrix} \begin{bmatrix} \boldsymbol{X}(s) \\ \boldsymbol{\mathcal{I}}(s) \end{bmatrix} = \begin{bmatrix} \boldsymbol{B}_{ext} \\ \boldsymbol{0} \end{bmatrix} \boldsymbol{U}_{ext}(s). \tag{4.2-14}$$

The theory of MOR maintains that the reduced set of current coefficient variables are related to the original set as $\boldsymbol{\mathcal{I}}(s) \approx \boldsymbol{W}\hat{\boldsymbol{\mathcal{I}}}(s)$. The system of lower dimension can thus be written as follows,

$$\begin{bmatrix} \boldsymbol{G} + s\boldsymbol{C} & \boldsymbol{B}_{ant}\widehat{\boldsymbol{B}}^{\mathrm{T}}\boldsymbol{W} \\ -s\boldsymbol{W}^{\mathrm{H}}\widetilde{\boldsymbol{B}}\boldsymbol{B}_{ant}^{\mathrm{T}} & \boldsymbol{W}^{\mathrm{H}}(\boldsymbol{P} + s\boldsymbol{T})\boldsymbol{W} \end{bmatrix} \begin{bmatrix} \boldsymbol{X}(s) \\ \hat{\boldsymbol{\mathcal{I}}}(s) \end{bmatrix} = \begin{bmatrix} \boldsymbol{B}_{ext} \\ \boldsymbol{0} \end{bmatrix} \boldsymbol{U}_{ext}(s) \tag{4.2-15}$$

or equivalently as

$$\begin{bmatrix} \boldsymbol{G} + s\boldsymbol{C} & \boldsymbol{B}_{ant}\widetilde{\boldsymbol{B}}^{\mathrm{T}} \\ -s\widehat{\boldsymbol{B}}\boldsymbol{B}_{ant}^{\mathrm{T}} & \left(\widehat{\boldsymbol{P}} + s\widehat{\boldsymbol{T}}\right) \end{bmatrix} \begin{bmatrix} \boldsymbol{X}(s) \\ \hat{\boldsymbol{\mathcal{I}}}(s) \end{bmatrix} = \begin{bmatrix} \boldsymbol{B}_{ext} \\ \boldsymbol{0} \end{bmatrix} \boldsymbol{U}_{ext}(s). \tag{4.2-16}$$

4.2.3 Clustered Multi-Port MOR of the Radiating Elements

The reduced dimension formulation in (4.2-16) matches the frequency-domain behaviour of the original array antenna MoM problem at all of its ports connecting to the BFN circuit. This was achieved through starting the Arnoldi process with the matrix $\widetilde{\boldsymbol{B}}$ and running it for q iterations to construct $\boldsymbol{W}$ used in building the reduced model. Consequently, matrices $\widehat{\boldsymbol{P}}$ and $\widehat{\boldsymbol{T}}$ that represent the model end up being of size $N_q N_a \times N_q N_a$ and dense. Recalling that N_a is the number of separate radiating elements in the array, these reduced metrices can become a significant computational burden in the analysis for a large number of radiating elements. This section therefore develops an approach whose objective is to address this growing computational burden as N_a increases following the clustering approach described in [NOUR 13a] and covered in *Section 2.6*, however now applied to the MoM formulation rather than for circuit simulation. To begin, the matrix $\boldsymbol{B}_a$ is expressed in terms of its columns $\boldsymbol{b}_i$ as

$$\boldsymbol{B}_a = [\boldsymbol{b}_1 \quad \boldsymbol{b}_2 \quad \cdots \quad \boldsymbol{b}_{N_a}]. \tag{4.2-17}$$

The superposition principle can be applied to rewrite $\boldsymbol{I}(s)$ of (4.2-2) as a summation of $\boldsymbol{I}_i(s)$, namely

$$\boldsymbol{I}(s) = \sum_{i=1}^{N_a} \boldsymbol{I}_i(s) \tag{4.2-18}$$

which are the solutions to the systems

$$\boldsymbol{Z}(s)\boldsymbol{I}_i(s) = \boldsymbol{b}_i V_i(s), \qquad i = 1, 2, \cdots, N_a \tag{4.2-19}$$

with $V_i(s)$ being the i^{th} component of $\boldsymbol{V}(s)$. The systems in (4.2-19) are single-port and therefore the efficient single-port MOR process described in *Section 3.3.1* can be applied to produce *i* bases spanning the moments of $\boldsymbol{\mathcal{I}}_i(s)$, which is the solution to the system

$$(\boldsymbol{P} + s\boldsymbol{T})\boldsymbol{\mathcal{I}}_i(s) = s\widetilde{\boldsymbol{b}}_i \tag{4.2-20}$$

where $\widetilde{\boldsymbol{b}}_i$ is defined as $\boldsymbol{b}_i$ appended by $N_e N_c$ zeros. The orthogonal bases obtained by executing the algorithm in Figure 4.2-1 starting with the vector $\boldsymbol{b}_i$ instead of matrix $\boldsymbol{B}_a$ are denoted by $\boldsymbol{W}^{[i]}$ and are of size $N_e(N_c + 1) \times N_q$. These bases are then used to obtain the reduced systems

$$\left(\widehat{\boldsymbol{P}}_i + s\widehat{\boldsymbol{T}}_i\right)\widehat{\boldsymbol{\mathcal{I}}}_i(s) = s\widehat{\boldsymbol{b}}_i \tag{4.2-21}$$

where $\widehat{\boldsymbol{P}}_i = {\boldsymbol{W}^{[i]}}^H \boldsymbol{P}\boldsymbol{W}^{[i]}$, $\widehat{\boldsymbol{T}}_i = {\boldsymbol{W}^{[i]}}^H \boldsymbol{T}\boldsymbol{W}^{[i]}$, $\widehat{\boldsymbol{b}}_i = {\boldsymbol{W}^{[i]}}^H \widetilde{\boldsymbol{b}}_i$, and $\boldsymbol{\mathcal{I}}_i(s) \approx \boldsymbol{W}^{[i]}\widehat{\boldsymbol{\mathcal{I}}}_i(s)$. Next, the antenna array must be modelled using the sequence of single-port reduced systems in (4.2-20) permitting their inclusions in the antenna-circuit formulation. This task seeks to derive a relation that approximates $\boldsymbol{I}(s)$ via the set of reduced dimension current coefficients $\widehat{\boldsymbol{\mathcal{I}}}_i(s)$. Considering the superposition relationship in (4.2-18) and the fact that $\boldsymbol{I}_i(s)$ consists of the first N_e rows of $\boldsymbol{\mathcal{I}}_i(s)$, the desired relation is given as

$$\boldsymbol{I}(s) = \sum_{i=1}^{N_a} \left(\mathbb{e}_{1,N_c+1}^{\mathrm{T}} \otimes \mathbb{I}_{N_e}\right) \boldsymbol{W}^{[i]} \hat{\boldsymbol{\mathfrak{J}}}_i(s). \tag{4.2-22}$$

The above relation can be utilized to recast the product $\boldsymbol{B}_a^{\mathrm{T}} \boldsymbol{I}(s)$ as

$$\begin{aligned}
\boldsymbol{B}_a^{\mathrm{T}} \boldsymbol{I}(s) &= \left(\left(\mathbb{e}_{1,N_c+1}^{\mathrm{T}} \otimes \mathbb{I}_{N_e}\right) \widetilde{\boldsymbol{B}}\right)^{\mathrm{T}} \boldsymbol{I}(s) \\
&= \widetilde{\boldsymbol{B}}^{\mathrm{T}} \left(\mathbb{e}_{1,N_c+1}^{\mathrm{T}} \otimes \mathbb{I}_{N_e}\right) \boldsymbol{I}(s) \\
&= \widetilde{\boldsymbol{B}}^{\mathrm{T}} \left(\mathbb{e}_{1,N_c+1} \otimes \mathbb{I}_{N_e}\right) \left(\mathbb{e}_{1,N_c+1}^{\mathrm{T}} \otimes \mathbb{I}_{N_e}\right) \sum_{i=1}^{N_a} \boldsymbol{W}^{[i]} \hat{\boldsymbol{\mathfrak{J}}}_i(s) \\
&= \widetilde{\boldsymbol{B}}^{\mathrm{T}} \left(\mathbb{e}_{1,N_c+1} \mathbb{e}_{1,N_c+1}^{\mathrm{T}} \otimes \mathbb{I}_{N_e}\right) \sum_{i=1}^{N_a} \boldsymbol{W}^{[i]} \hat{\boldsymbol{\mathfrak{J}}}_i(s) \\
&= \left(\begin{bmatrix} 1 & 1 & \cdots & 1 \end{bmatrix}_{N_a} \otimes \widetilde{\boldsymbol{B}}^{\mathrm{T}}\right) \boldsymbol{\Psi} \hat{\boldsymbol{\mathcal{J}}}(s)
\end{aligned} \tag{4.2-23}$$

where

$$\boldsymbol{\Psi} = \begin{bmatrix} \boldsymbol{W}^{[1]} & \mathbf{0} & \cdots & \mathbf{0} \\ \mathbf{0} & \boldsymbol{W}^{[2]} & \cdots & \mathbf{0} \\ \vdots & \vdots & \ddots & \vdots \\ \mathbf{0} & \mathbf{0} & \cdots & \boldsymbol{W}^{[N_a]} \end{bmatrix} \tag{4.2-24}$$

and

$$\hat{\boldsymbol{\mathcal{J}}}(s) = \begin{bmatrix} \hat{\boldsymbol{\mathfrak{J}}}_1(s)^{\mathrm{T}} & \hat{\boldsymbol{\mathfrak{J}}}_2(s)^{\mathrm{T}} & \cdots & \hat{\boldsymbol{\mathfrak{J}}}_{N_a}(s)^{\mathrm{T}} \end{bmatrix}^{\mathrm{T}}. \tag{4.2-25}$$

The representation of $\boldsymbol{B}_a^{\mathrm{T}} \boldsymbol{I}(s)$ in (4.2-23) enables the current coefficients in the reduced domain, $\hat{\boldsymbol{\mathcal{J}}}(s)$, to be coupled to the space of the BFN circuit variables via multiplication by the matrix $\boldsymbol{B}_{ant}$, as shown in the upper right block of the now rewritten version of (4.2-16) as

$$\begin{bmatrix} \boldsymbol{G} + s\boldsymbol{C} & \boldsymbol{B}_{ant}\left(\begin{bmatrix} 1 & 1 & \cdots & 1 \end{bmatrix}_{N_a} \otimes \widetilde{\boldsymbol{B}}^{\mathrm{T}}\right) \boldsymbol{\Psi} \\ -s\boldsymbol{\Psi} \begin{bmatrix} \widetilde{\boldsymbol{b}}_1 \\ \vdots \\ \widetilde{\boldsymbol{b}}_{N_a} \end{bmatrix} \boldsymbol{B}_{ant}^{\mathrm{T}} & \begin{bmatrix} \widehat{\boldsymbol{P}}_1 + s\widehat{\boldsymbol{T}}_1 & \cdots & \mathbf{0} \\ \vdots & \ddots & \vdots \\ \mathbf{0} & \cdots & \widehat{\boldsymbol{P}}_{N_a} + s\widehat{\boldsymbol{T}}_{N_a} \end{bmatrix} \end{bmatrix} \begin{bmatrix} \boldsymbol{X}(s) \\ \hat{\boldsymbol{\mathcal{J}}}(s) \end{bmatrix} = \begin{bmatrix} \boldsymbol{B}_{ext} \\ \mathbf{0} \end{bmatrix} \boldsymbol{U}_{ext}(s). \tag{4.2-26}$$

Similarly, the sequence of reduced systems in (4.2-21) are used to provide the coupling of the BFN circuit variables with the space of the reduced current coefficients $\widehat{\mathcal{J}}(s)$. This coupling is shown in the lower left block of the same matrix in (4.2-26).

The reduced size formulation of the antenna-circuit problem shown in (4.2-26) provides the clustered alternative to the reduced size problem of (4.2-16). Figure 4.2-2 contrasts the structures of the matrices arising from these two formulations. Blocks on the sketch filled with solid black colour denote full matrix blocks. Sparse blocks are indicated with few small points representing non-zero entries. This figure highlights the fact that the matrix in the bottom right in the cluster-based multi-port MOR structure is block diagonal as opposed to the same matrix being full for the un-clustered multi-port formulation, both versions being of the same total size.

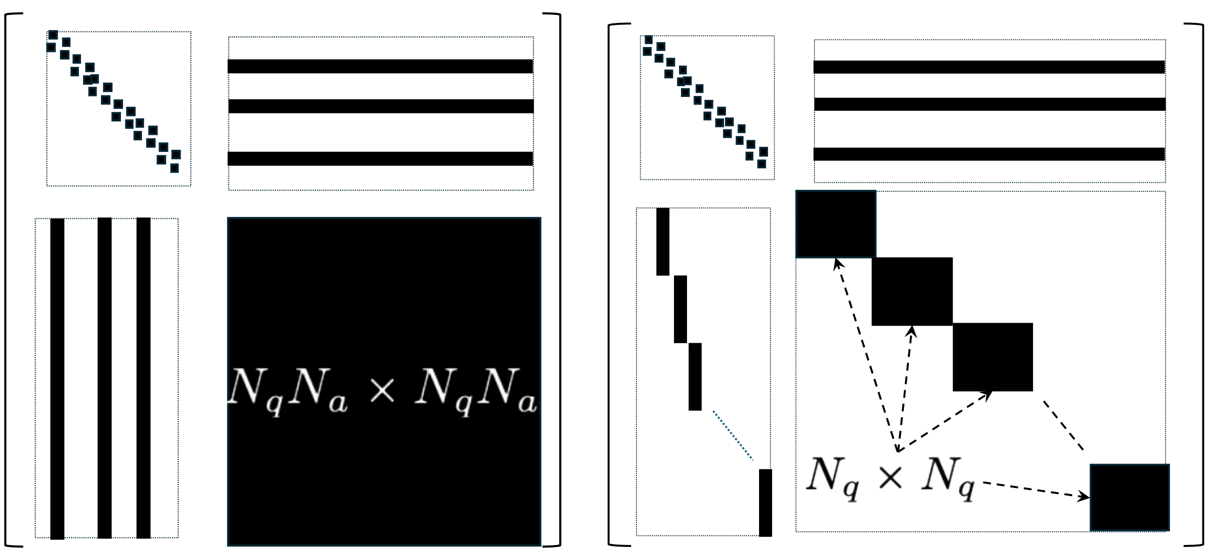

Figure 4.2-2. Illustration describing the structure of the matrix in the reduced-size antenna-circuit formulations using multi-port MOR (left) and clustered multi-port MOR (right).

4.3 NUMERICAL SIMULATION RESULTS

Two examples are presented to validate the above defined clustered multi-port MOR formulation for its accuracy and to demonstrate its computational efficacy. The results presented here will compare the "MOR" formulation of (4.2-26) with the "Exact" formulation of (4.2-3), and the "Chebyshev" formulation

$$\begin{bmatrix} \boldsymbol{G} + s\boldsymbol{C} & \boldsymbol{B}_{ant}\boldsymbol{B}_a^T \\ -s\boldsymbol{B}_a\boldsymbol{B}_{ant}^{\mathrm{T}} & \sum_{i=0}^{N_c+1} \boldsymbol{Z}_i s^i \end{bmatrix} \begin{bmatrix} \boldsymbol{X}(s) \\ \boldsymbol{I}(s) \end{bmatrix} = \begin{bmatrix} \boldsymbol{B}_{ext} \\ \boldsymbol{0} \end{bmatrix} \boldsymbol{U}_{ext}(s). \tag{4.3-1}$$

The two examples are not intended to represent optimized antenna designs in any way.

4.3.1 Patch Antenna on a Box-Shaped Platform

The example analyzed in this section is illustrated in Figure 4.3-1.

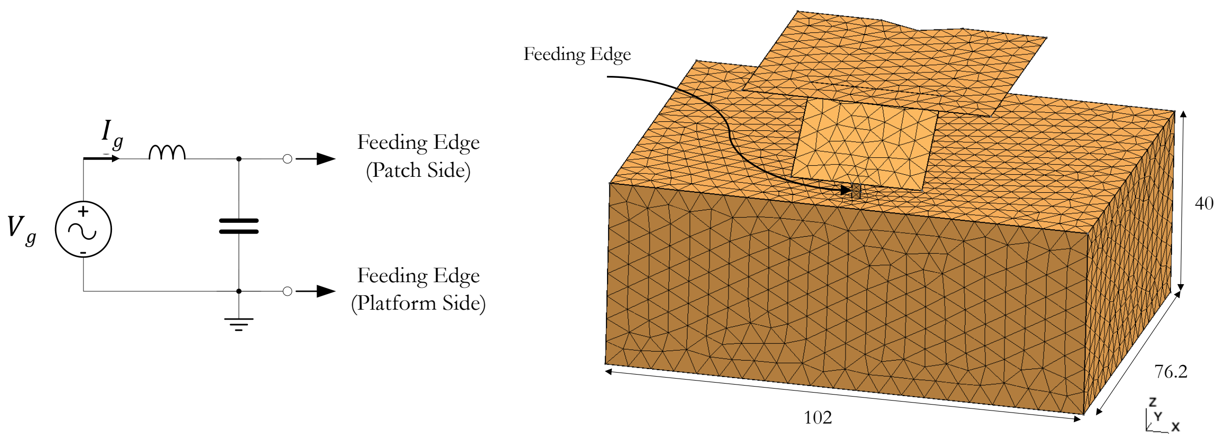

Figure 4.3-1. L-section matching network (left) and patch antenna with an air substrate on a box-shaped platform (right). All dimensions are in mm.

The circuit is a simple matching network designed to match the input impedance of the antenna to 50 Ω at 3 GHz. The circuit component values are 1.69 nH and 0.79 pF. The dimensions of the patch and feeding strip are the same as those in Figure 3.5-1. With the inclusion of the independent voltage source in the circuit, the current through this source is included as one of the MNA circuit variables in $\boldsymbol{X}(s)$. As such, the input impedance of the circuit is computed as $Z_{in}(s) = I_g(s)^{-1}$ given that the voltage source is set as $V_g = 1$. The reflection coefficient is then found from $Z_{in}(s)$ with reference to 50 Ω. The input reflection coefficient Γ_{in} is plotted versus frequency in Figure 4.3-2 (left) and the total directivity as a function of θ in the $x - z$ ($\phi = 0°$) and $y - z$ ($\phi = 90°$) plane at 2 GHz is shown in Figure 4.3-2 (right). Furthermore, Figure 4.3-3 illustrates the normalized magnitude of the surface current density on the antenna and platform at 2 GHz.

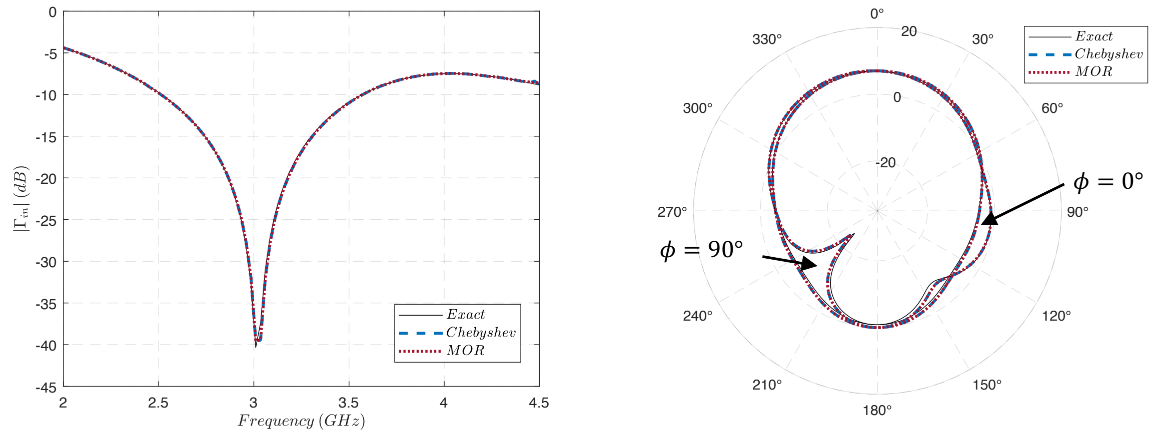

Figure 4.3-2. Input reflection coefficient (left) and total directivity (right) at 2 GHz in two planes of the circuit and antenna combination in Figure 4.3-1.

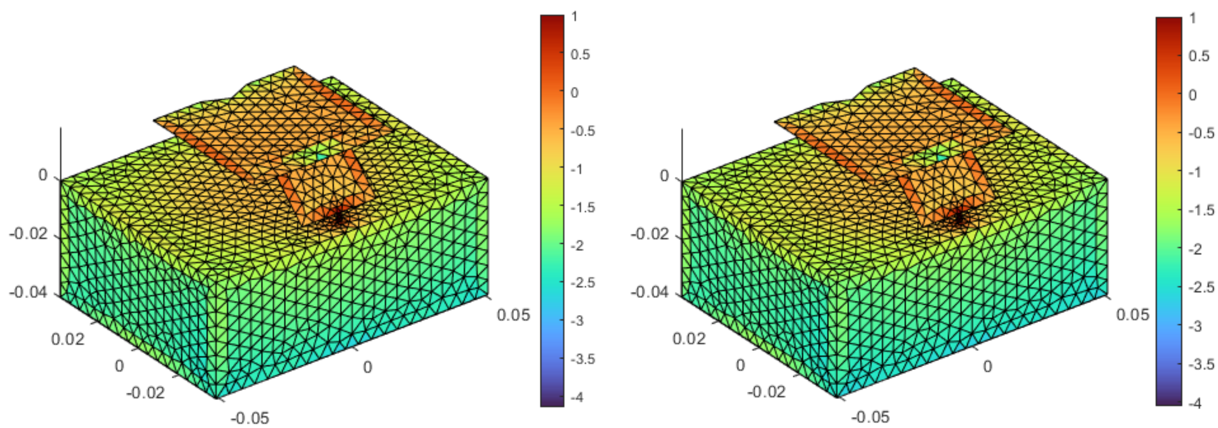

Figure 4.3-3. Normalized surface current density magnitude of the antenna in Figure 4.3-1 computed at 2 GHz via the exact formulation (left) and the MOR formulation (right). Dimensions are in m.

This current distribution is computed using (2.3-11), where $\bar{\rho}_n^{\pm}$ in (2.3-12) is taken at the centre of the plus and minus triangle associated with each edge. The current distribution over each triangular mesh element is thus the sum of the contributions from each of its inter-element edge boundaries. The all but identical values of these metrics validate the accuracy of the MOR-based antenna-circuit formulations.

4.3.2 Four-Element Linear Array of Air-Substrate Patches on a Finite Ground Plane

The second example is summarized in the following figures.

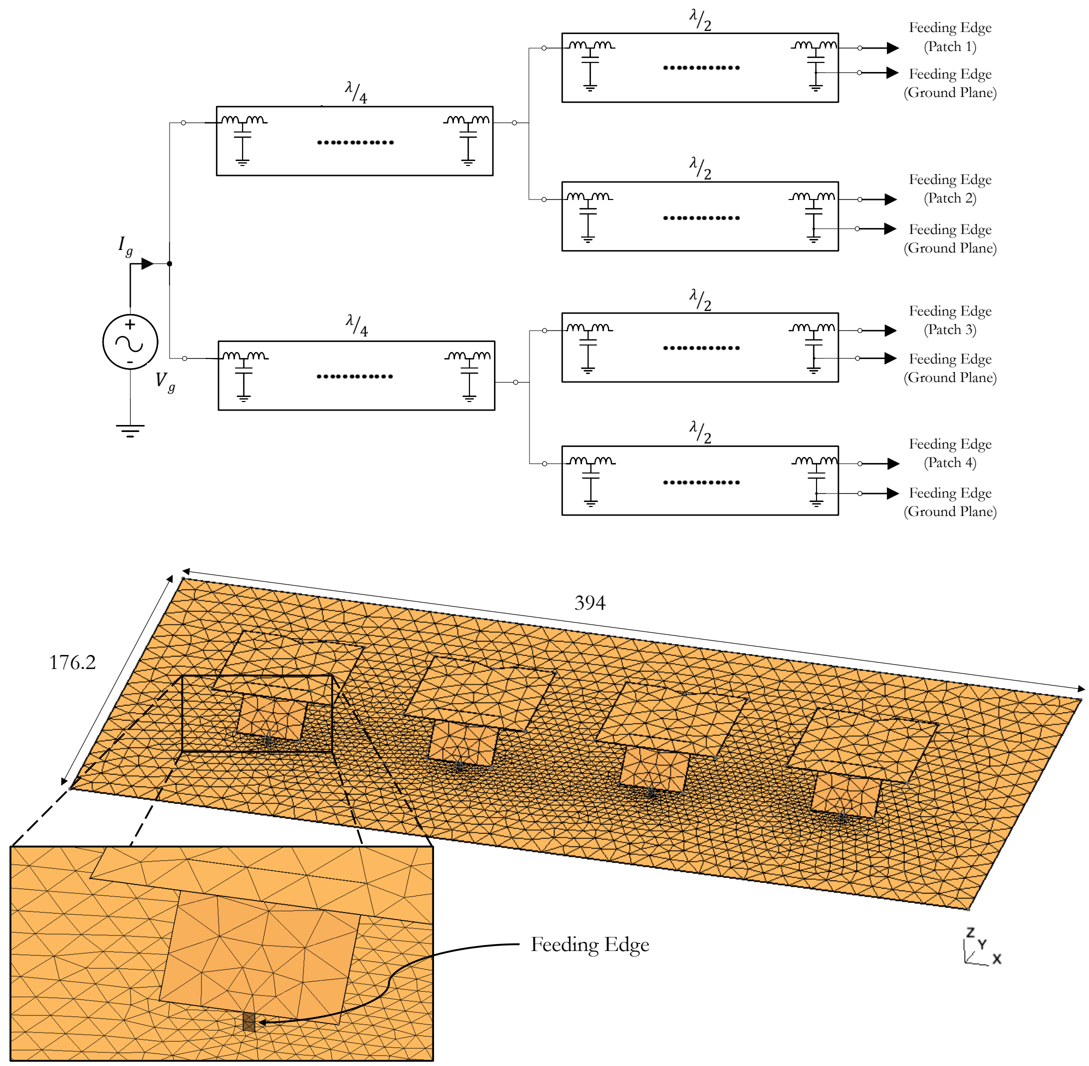

Figure 4.3-4. Lumped equivalent circuit of an ideal transmission line BFN (top) and four-element linear array of air-substrate patches and ground plane (bottom). All dimensions are in mm.

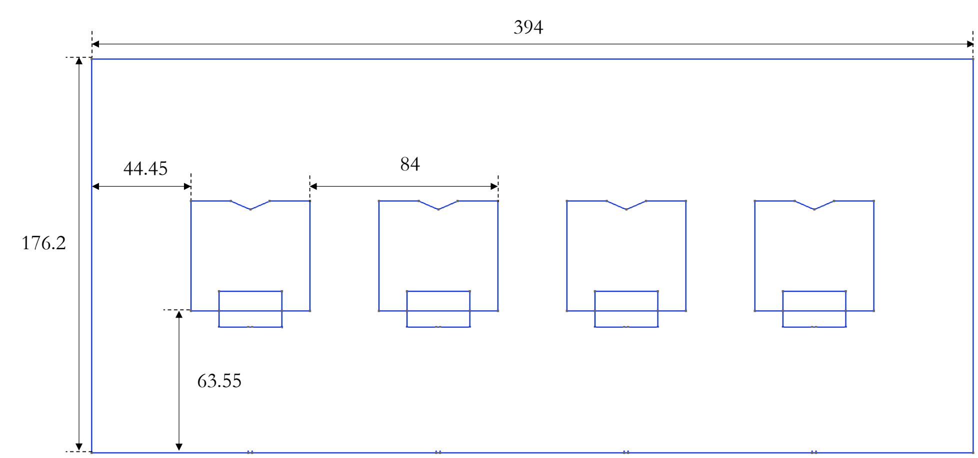

Figure 4.3-5. Position of the patch elements relative to the ground plane. All dimensions are in mm.

The dimensions of the patch elements and feeding strips in Figures 4.3-4 and 4.3-5 are once again the same as those in Figure 3.5-1. The circuit in Figure 4.3-4 is a power-divider consisting of idealized transmissions lines (distributed circuits) matched at its input to a reference impedance of 50 Ω when terminated by each of the four patches at its outputs. This network consists of a half-wavelength transmission line connected to each patch followed by two quarter-wavelength transmission lines to transform the input impedance as needed, at 2.46 GHz. In order to fit this into the MNA lumped circuit analysis framework, each half- and quarter-wavelength distributed transmission line segment was represented by a cascade of 10 lumped-component T-networks, each T-network consisting of two series inductors of value L and a shunt capacitor of value C, as illustrated in Figure 4.3-4 (top). The same L and C values are used for all T-networks representing a certain transmission line segment. The fixed values of L and C are needed for the lumped equivalent circuit to faithfully reproduce the behaviour of the "true" distributed sections over the frequency band of interest. These component values were determined for each transmission line segment by using a genetic algorithm to minimize the function

$$F(L,C) = \sum_{n=1}^{N_f} \sum_{i=1}^{2} \sum_{j=1}^{2} \left| S_{ij}^{(Distributed)}(f_n) - S_{ij}^{(Lumped)}(f_n, L, C) \right|^2 \qquad (4.3\text{-}2)$$

where the quantities $S_{ij}^{(Distributed)}$ and $S_{ij}^{(Lumped)}$ are the S-parameters of the distributed TL section predicted by circuit theory and the S-parameters of the equivalent circuit consisting of cascaded lumped T-networks, respectively. Figure 4.3-6 shows the reflection coefficient and directivity analogous to those in Figure 4.3-2 for this example, while Figure 4.3-7 shows the exact and MOR computed surface current density. These results further validate the accuracy of the MOR approach.

4.3.3 Computational Comparison

Table 4.3-1 provides the parameters used in each example, while Figure 4.3-8 plots the execution times for each example as a function of the total number of frequencies N_f at which we wish to perform the antenna-circuit co-simulation. The expansion frequencies are not listed in Table 4.3-1 since the MOR method uses the OMC algorithm and thus they are fixed for a given N_m.

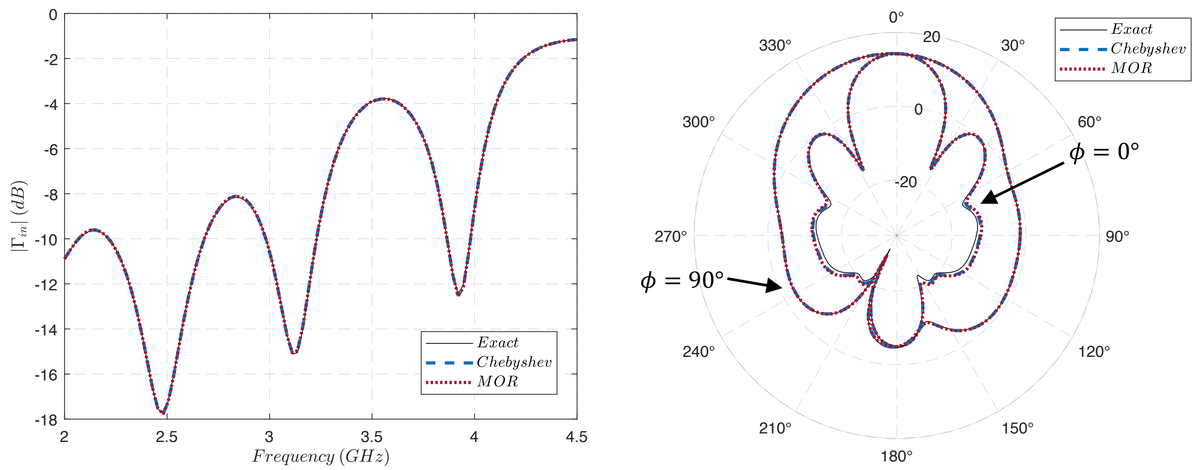

Figure 4.3-6. Input reflection coefficient (left) and total directivity at 2 GHz in two planes (right) of the circuit and antenna in Figure 4.3-4.

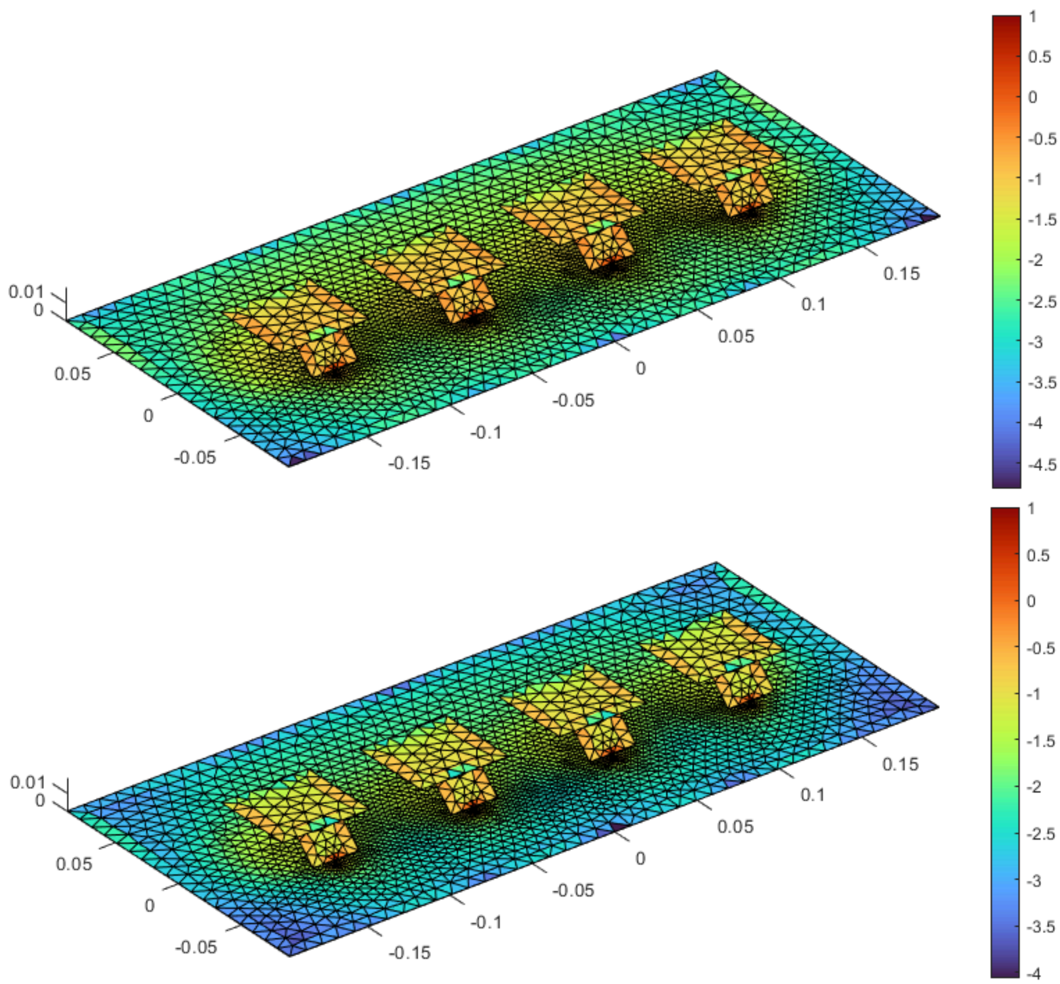

Figure 4.3-7. Normalized surface current density magnitude of the antenna in Figure 4.3-4 computed at 2 GHz via the exact formulation (top) and the MOR formulation (bottom). Dimensions are in m.

Table 4.3-1. Parameters used for the analysis of the antenna-circuit examples.

Example	4.3.1		4.3.2	
N_e	5402		8131	
N_a	1		4	
	Chebyshev	MOR	Chebyshev	MOR
N_c	4	4	7	7
N_q	-	9	-	13
N_m	-	3	-	5
τ_{max}	-	5%	-	5%
$N_{q,min}$	-	5	-	5
$N_{q,max}$	-	45	-	45
ΔN_q	-	2	-	2

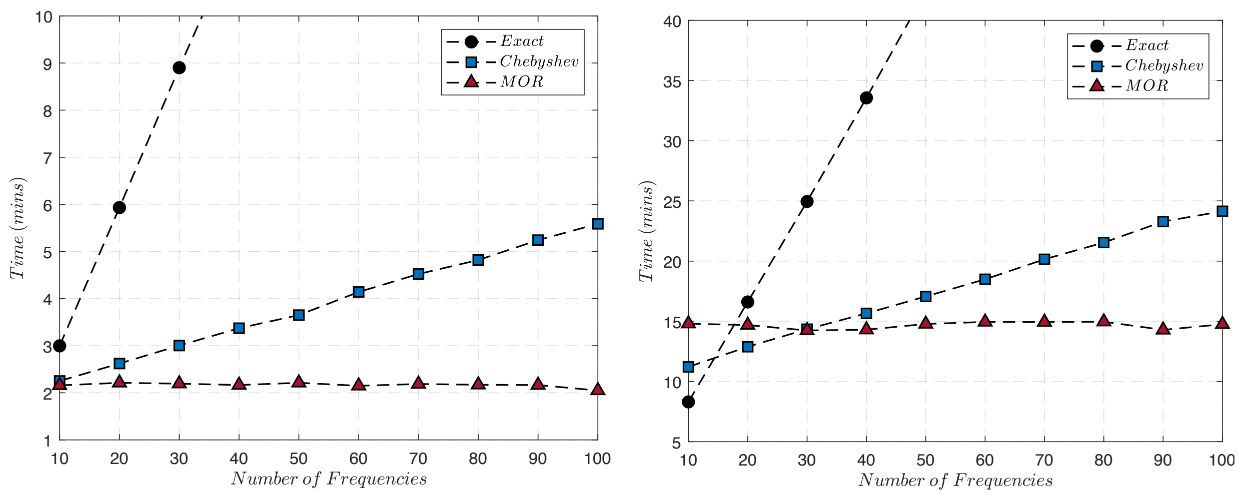

Figure 4.3-8. Comparison of the CPU time versus the number of frequencies for the antenna-circuit combinations in *Section 4.3.1* (left) and *Section 4.3.2* (right). These times were found running MATLAB on a computer with an Intel Core i9 CPU and 128 GB of RAM.

As was the case in *Section 3.5*, the advantage of MOR is evident, particularly as the number of frequency points increases. By analyzing the two plots in Figure 4.3-8, it is observed that the intersection between the MOR curves and the exact and Chebyshev curves is problem dependent. The example is *Section 4.3.1* has frequency and angular responses that vary far less than those of the example in *Section 4.3.2*. As would be expected, more expansion points are therefore required in the second example despite the frequency sweep of both examples covering the same band, resulting in intersection points at a higher number of frequencies. It could thus be concluded that for small to medium sized problems MOR will see its greatest benefit when the antenna's response is less varying, however even when this is not the case, as is so for the array example, MOR is still observed to provide ample speed-up after only about 30 frequencies are computed.

4.4 INCLUSION OF NON-LINEAR CIRCUIT ELEMENTS

The unified circuit-radiating elements formulation presented in the previous sections is of course limited to the use of linear circuit elements. The inclusion of non-linear circuit elements in the MNA formulation would necessitate the addition of the non-linear vector $\boldsymbol{F}(\boldsymbol{x}(t))$ as is shown in (2.4-1) and thus must be solved in the time domain. By observation, (4.2-26) can easily be converted to the following time domain system of differential equations which includes the aforementioned additional non-linear vector.

$$\begin{bmatrix} \boldsymbol{G} & \boldsymbol{B}_{ant}\left([1 \quad 1 \quad \cdots \quad 1]_{N_a} \otimes \widetilde{\boldsymbol{B}}^{\mathrm{T}}\right)\boldsymbol{\Psi} \\ \boldsymbol{0} & \begin{bmatrix} \widehat{\boldsymbol{P}}_1 & \cdots & \boldsymbol{0} \\ \vdots & \ddots & \vdots \\ \boldsymbol{0} & \cdots & \widehat{\boldsymbol{P}}_{N_a} \end{bmatrix} \end{bmatrix} \begin{bmatrix} \boldsymbol{x}(t) \\ \boldsymbol{j}(t) \end{bmatrix} + \begin{bmatrix} \boldsymbol{C} & \boldsymbol{0} \\ -\boldsymbol{\Psi}\begin{bmatrix} \widetilde{\boldsymbol{b}}_1 \\ \vdots \\ \widetilde{\boldsymbol{b}}_{N_a} \end{bmatrix}\boldsymbol{B}_{ant}^{\mathrm{T}} & \begin{bmatrix} \widehat{\boldsymbol{T}}_1 & \cdots & \boldsymbol{0} \\ \vdots & \ddots & \vdots \\ \boldsymbol{0} & \cdots & \widehat{\boldsymbol{T}}_{N_a} \end{bmatrix} \end{bmatrix} \begin{bmatrix} \frac{\partial \boldsymbol{x}(t)}{\partial t} \\ \frac{\partial \boldsymbol{j}(t)}{\partial t} \end{bmatrix} + \begin{bmatrix} \boldsymbol{F}(\boldsymbol{x}(t)) \\ \boldsymbol{0} \end{bmatrix} = \begin{bmatrix} \boldsymbol{B}_{ext} \\ \boldsymbol{0} \end{bmatrix} \boldsymbol{u}_{ext}(t) \qquad (4.4\text{-}1)$$

The issue with (4.4-1) is that $\boldsymbol{\Psi}$, $\widehat{\boldsymbol{P}}_i$, $\widehat{\boldsymbol{T}}_i$, and $\widetilde{\boldsymbol{b}}_i$ are matrices containing complex quantities arising from the method of moments formulation of the radiating elements. This leads to instability and thus lack of convergence when solving using Newton iterations. A different approach has therefore been taken to tackle this problem. A sequential step is added before performing the co-simulation. That is, the procedure for handling circuits with non-linear elements is split into two steps. The first step involves computing a frequency sweep of the antenna on its own with unity voltages applied to its ports. Clustering MOR is of course used to do this for maximum efficiency. The resulting MoM currents at each of the antenna ports are then used as samples within the vector fitting (VF) procedure described in *Section 2.8*. This algorithm yields a transfer function modelling the port currents directly (given the unity voltage inputs) after multiplying the current densities at each feeding edge by their respective lengths. The poles and residues can then be used to build the state space matrices $\boldsymbol{A}$, $\boldsymbol{B}$, $\boldsymbol{C}$, and $\boldsymbol{D}$ seen in (2.8-9) such that the transfer function can be represented in the equivalent form of (2.8-8). To avoid confusion with other quantities, the four state space matrices will be denoted here as $\boldsymbol{\mathcal{A}}$, $\boldsymbol{\mathcal{B}}$, $\boldsymbol{\mathcal{C}}$, and $\boldsymbol{\mathcal{D}}$, respectively. The benefit of this approach is that the VF algorithm enforces stability during its iterations by inverting the sign of the real part of a pole estimation if said estimation is unstable, ensuring a stable approximation of the port currents [TRIV 20]. The second step then uses these matrices as the representation of the radiating elements in the co-simulation along with the MNA representation of the circuit in a transient time domain solver. These steps are illustrated in the flowchart in Figure 4.4-1.

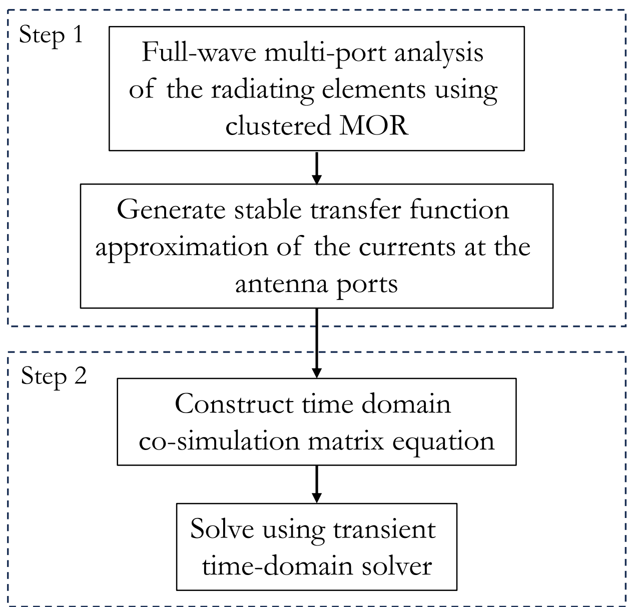

Figure 4.4-1. Flowchart depicting the antenna-circuit simulation procedure when there are non-linear elements in the circuitry.

4.4.1 Non-Linear Antenna-Circuit Formulation

The VF model and state-space matrices yield the following model of the currents at the ports of the radiating elements, $\boldsymbol{I}_a(s)$,

$$\boldsymbol{I}_a(s) = \left[\boldsymbol{\mathcal{D}} + \boldsymbol{\mathcal{C}}\left(s\mathbb{I}_{\tilde{n}N_a} - \boldsymbol{\mathcal{A}}\right)^{-1}\boldsymbol{\mathcal{B}}\right]\boldsymbol{V}(s) = \left[\boldsymbol{\mathcal{D}} + \boldsymbol{\mathcal{C}}\left(s\mathbb{I}_{\tilde{n}N_a} - \boldsymbol{\mathcal{A}}\right)^{-1}\boldsymbol{\mathcal{B}}\right]\boldsymbol{B}_{ant}^{\mathrm{T}}\boldsymbol{X}(s) \qquad (4.4\text{-}2)$$

where $\boldsymbol{\mathcal{A}}$ is of size $\tilde{n}N_a \times \tilde{n}N_a$, $\boldsymbol{\mathcal{B}}$ is of size $\tilde{n}N_a \times N_a$, $\boldsymbol{\mathcal{C}}$ is of size $N_a \times \tilde{n}N_a$, and $\boldsymbol{\mathcal{D}}$ is of size $N_a \times N_a$, recalling from *Section 2.8* that $\tilde{n}$ is the order of the VF model. From here, $\boldsymbol{Y}(s)$ is introduced as

$$\boldsymbol{Y}(s) = \left(s\mathbb{I}_{\tilde{n}N_a} - \boldsymbol{\mathcal{A}}\right)^{-1} \boldsymbol{\mathcal{B}}\boldsymbol{B}_{ant}^{\mathrm{T}}\boldsymbol{X}(s) \tag{4.4-3}$$

which lets $\boldsymbol{I}_a(s)$ be written as

$$\boldsymbol{I}_a(s) = \boldsymbol{\mathcal{D}}\boldsymbol{B}_{ant}^{\mathrm{T}}\boldsymbol{X}(s) + \boldsymbol{\mathcal{C}}\,\boldsymbol{Y}(s). \tag{4.4-4}$$

Formulating (4.4-3), (4.4-4), as well as the linear MNA equations into a single matrix equation gives us

$$\begin{bmatrix} \boldsymbol{G} + s\boldsymbol{C} & \boldsymbol{0} & \boldsymbol{B}_{ant} \\ -\boldsymbol{\mathcal{B}}\boldsymbol{B}_{ant}^{\mathrm{T}} & s\mathbb{I}_{\tilde{n}N_a} - \boldsymbol{\mathcal{A}} & \boldsymbol{0} \\ \boldsymbol{\mathcal{D}}\boldsymbol{B}_{ant}^{\mathrm{T}} & \boldsymbol{\mathcal{C}} & -\mathbb{I}_{N_a} \end{bmatrix} \begin{bmatrix} \boldsymbol{X}(s) \\ \boldsymbol{Y}(s) \\ \boldsymbol{I}_a(s) \end{bmatrix} = \begin{bmatrix} \boldsymbol{B}_{ext} \\ \boldsymbol{0} \\ \boldsymbol{0} \end{bmatrix} \boldsymbol{U}_{ext}(s). \tag{4.4-5}$$

By observation, (4.4-5) can then be converted into a time domain set of differential equations including the non-linear MNA vector as follows.

$$\begin{aligned} &\begin{bmatrix} \boldsymbol{G} & \boldsymbol{0} & \boldsymbol{B}_{ant} \\ -\boldsymbol{\mathcal{B}}\boldsymbol{B}_{ant}^{\mathrm{T}} & -\boldsymbol{\mathcal{A}} & \boldsymbol{0} \\ \boldsymbol{\mathcal{D}}\boldsymbol{B}_{ant}^{\mathrm{T}} & \boldsymbol{\mathcal{C}} & -\mathbb{I}_{N_a} \end{bmatrix} \begin{bmatrix} \boldsymbol{x}(t) \\ \boldsymbol{y}(t) \\ \boldsymbol{i}_a(t) \end{bmatrix} + \begin{bmatrix} \boldsymbol{C} & \boldsymbol{0} & \boldsymbol{0} \\ \boldsymbol{0} & \mathbb{I}_{\tilde{n}N_a} & \boldsymbol{0} \\ \boldsymbol{0} & \boldsymbol{0} & \boldsymbol{0} \end{bmatrix} \begin{bmatrix} \dfrac{\partial \boldsymbol{x}(t)}{\partial t} \\ \dfrac{\partial \boldsymbol{y}(t)}{\partial t} \\ \dfrac{\partial \boldsymbol{i}_a(t)}{\partial t} \end{bmatrix} + \begin{bmatrix} \boldsymbol{F}\left(\boldsymbol{x}(t)\right) \\ \boldsymbol{0} \\ \boldsymbol{0} \end{bmatrix} \\ &= \begin{bmatrix} \boldsymbol{B}_{ext} \\ \boldsymbol{0} \\ \boldsymbol{0} \end{bmatrix} \boldsymbol{U}_{ext}(t) \end{aligned} \tag{4.4-6}$$

4.4-2 Dual Polarized Patch Antenna Link

To demonstrate the formulation in (4.4-6), this section will consider the verification of a dual polarized patch antenna link with a switching circuit. The antennas used in this example are shown in Figure 4.4-2. These are modified versions of the patch antenna seen in Figure 3.5-2, however the patches themselves and the ground planes have been made square such that single excitations to port 1 or port 2 in Figure 4.4-2 will result in near identical fields. The antenna link itself is shown in Figure 4.4-3, while the modified dimensions of these antennas are shown in Figure 4.4-4. The objective of this example will be to switch between feeding antenna 1 at either port 1 or port 2 (at a switching frequency less than the RF source frequency). The link and associated circuitry can be verified by observing the voltages induced at the ports of antenna 2. Since these antennas are linearly polarized, when port 1 of antenna 1 is being powered we should see a higher voltage at the similarly oriented port on antenna 2 (port 3) and a lower voltage at the other port on antenna 2 that is rotated 90° (port 4), and vice versa when the voltage is being applied to port 2 of antenna 1.

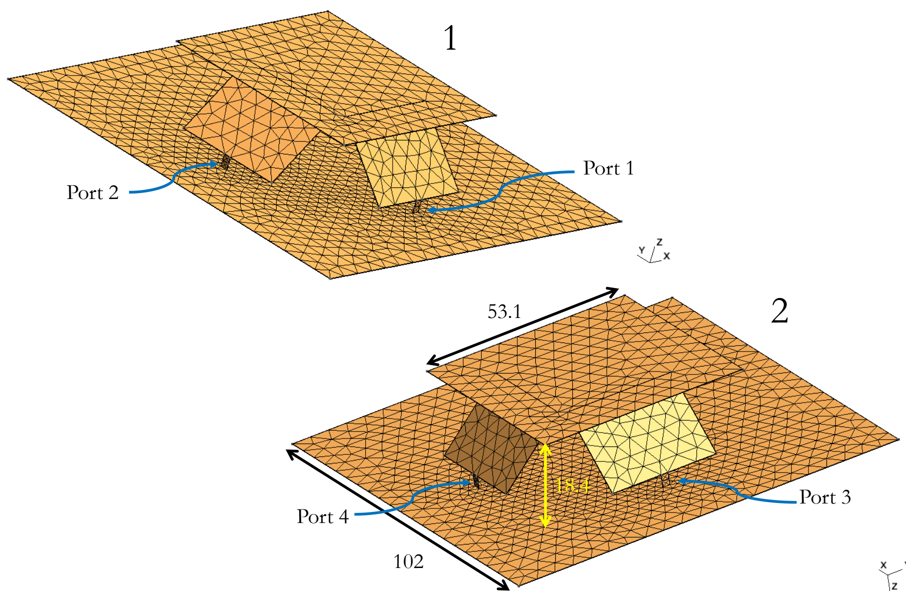

Figure 4.4-2. Two identical patch antennas. The indicated ports are feeding edges halfway up each feeding pin spanning the pin's width. The dimensions shown on antenna 2 are in mm.

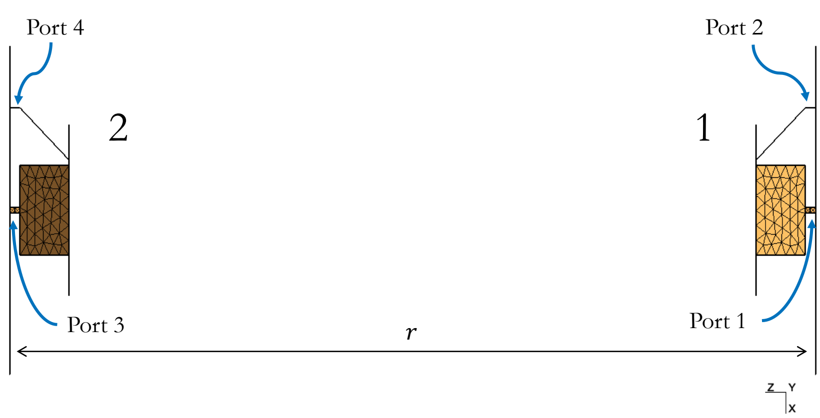

Figure 4.4-3. Antenna link showing the positioning of the two patch antennas. Note that the distance r (ground plane to ground plane) is 0.5 m, however for clarity is not shown to scale in this figure relative to the size of the antennas.

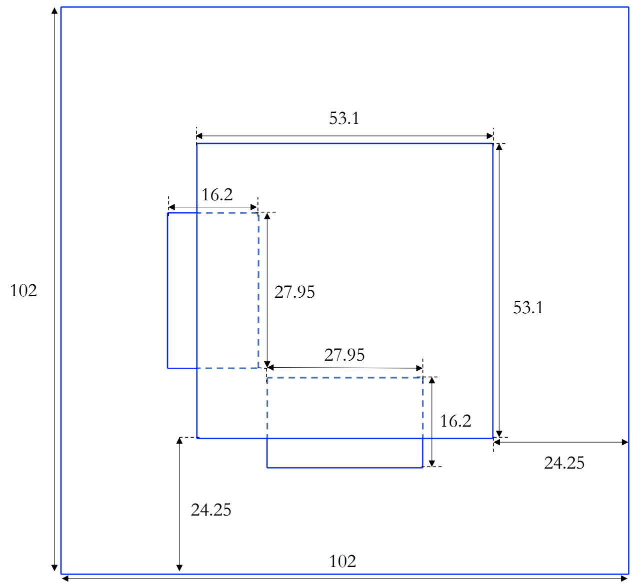

Figure 4.4-4. The dimensions (in mm) of the patch antenna seen from above. The dimensions of the feeding strip and pin are the same as those in the right diagram of Figure 3.5-1.

To achieve a circuit that accurately provides this switching capability, BSIM (level 54) models are used for NMOS and PMOS transistors. Such models would be cumbersome to code into MATLAB thus it is desirable to integrate the formulation in (4.4-6) into HSPICE. To verify that such a time-domain integration is working as intended, the linear circuit shown below in Figure 4.4-5 is considered.

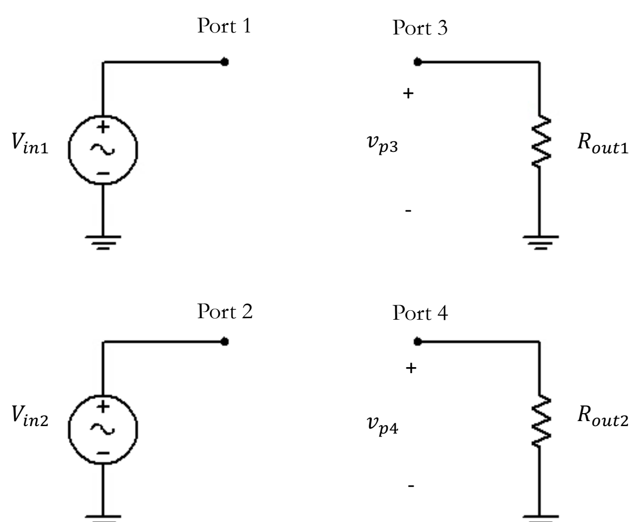

Figure 4.4-5. Linear test circuit driving the antenna link.

The ports in Figure 4.4-5 are connected to their respective terminals of the antenna link shown in Figures 4.4-2 and 4.4-3. Since this is a linear circuit, the frequency domain formulation described in *Section 4.2* can be used to observe the port voltages on the receive side of the antenna link (that is at ports 3 and 4). At 2.5 GHz the results of such a simulation are shown in Table 4.4-1.

Table 4.4-1. Operational parameters and frequency domain results of the linear test circuit connected to the antenna link.

Test Case	$R_{out1,2}$	V_{in1}	V_{in2}	v_{p3}	v_{p4}
1	50 Ω	0.5 V	0 V	**0.027 V**	**0.012 V**
2	50 Ω	0 V	0.5 V	**0.012 V**	**0.027 V**

The results in Table 4.4-1 show that the voltage at the receive port oriented in the same direction as that which is being fed on the transmit side does indeed have a greater voltage than the other receive port. A VF model of $\boldsymbol{\mathcal{A}}$, $\boldsymbol{\mathcal{B}}$, $\boldsymbol{\mathcal{C}}$, and $\boldsymbol{\mathcal{D}}$ matrices is then computed to accurately model behaviour at the ports of the four radiating elements at 2.5 GHz according to (4.4-2). Integrating this model into HSPICE along with the same circuit in Figure 4.4-5 yields the time domain results shown in Figure 4.4-6 given a sinusoidal source with a 1 V input amplitude and a frequency of 2.5 GHz. The amplitudes of these output waveforms agree with the frequency domain results of Table 4.4-1.

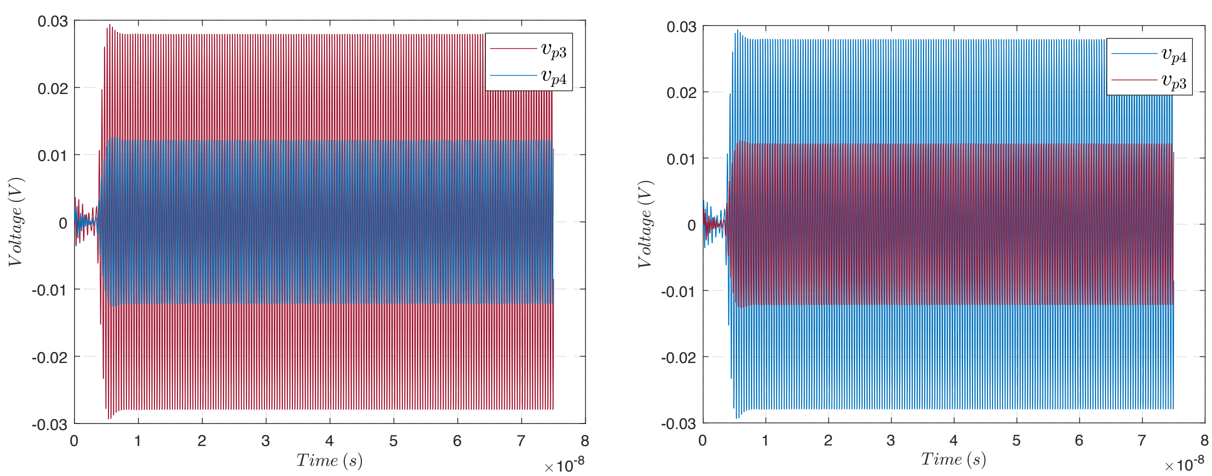

Figure 4.4-6. Time domain output port voltages given a 1 V sinusoidal input signal applied to port 1 (left) and port 2 (right).

With the time domain simulation of the VF model of the radiating elements along with a circuit in HSPICE verified, the actual nonlinear switching circuit can be included into the HSPICE netlist. Such a circuit is shown below in Figure 4.4-7.

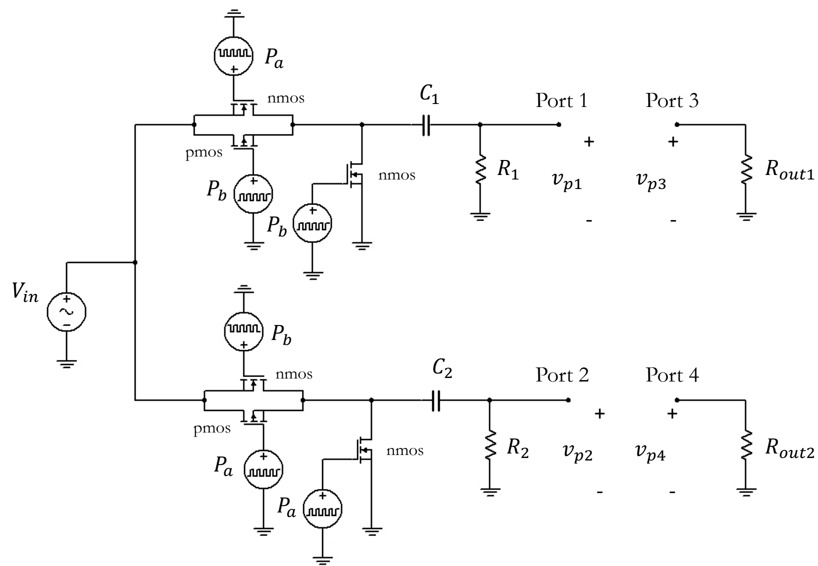

Figure 4.4-7. Switching circuit driving the antenna link.

The above circuit element details are shown in Table 4.4-2 while Table 4.4-3 shows the MOR and vector fitting parameters needed to run the time domain co-simulation.

Table 4.4-2. Element details of the circuit in Figure 4.4-7.

V_{in}	$sin(2\pi(2.5 \times 10^9)t)$
P_a	Initial value = 1.8 V, Pulsed value = 0 Delay time = 0 s Rise time = Fall time = 0.01 μs Pulse width = 200 ns Period = 400 ns, Frequency = 2.5 MHz
P_b	Initial value: 0 V, Pulsed value = 1.8 V Delay time = 0 s Rise time = Fall time = 0.01 μs Pulse width = 200 ns Period = 400 ns, Frequency = 2.5 MHz
nmos	BSIM nmos model (level = 54)
pmos	BSIM pmos model (level = 54)
C_1, C_2	10 nF
R_1, R_2	10 kΩ
R_{out1}, R_{out2}	50 Ω

Table 4.4-3. MOR and vector fitting parameters.

N_e	6918
N_f	50
N_a	4
N_c	10
N_q	9
N_m	7
τ_{max}	0.001%
$N_{q,min}$	5
$N_{q,max}$	45
ΔN_q	2
$\tilde{n}$	25

The MOR parameters defined in the above table render the VF model accurate over the 2-3 GHz band, a wide enough range to account for the circuit's nonlinearities. The OMC method for determining N_q and N_m was used here, however the graphical method for determining N_c, while sufficient for an accurate frequency domain simulation, underestimates the number of Chebyshev coefficients needed for time domain simulations, and thus additional coefficients were needed. Also, the maximum tolerance τ_{max} had to be significantly reduced to generate an accurate VF model. Furthermore, in addition to approximating the MoM current coefficients between 2-3 GHz, a DC solution of zero was forced upon the VF model such that the port currents of the antenna at DC are known for the initial guess of the time domain simulation.

Figure 4.4-8 shows the magnitude of the current computed at each port given a unity excitation applied to port 1. This plot compares these quantities computed via an exact frequency domain formulation and that using (4.4-2) where $\boldsymbol{\mathcal{A}}$, $\boldsymbol{\mathcal{B}}$, $\boldsymbol{\mathcal{C}}$, and $\boldsymbol{\mathcal{D}}$ are found using MOR with the parameters in Table 4.4-3. This plot confirms the accuracy of the stable transfer function approximation needed for "Step 1" outlined in Figure 4.4-1. One could of course also construct the VF model using the exact currents, however doing so in this case takes about 41 minutes compared to 19 minutes using MOR. Figure 4.4-9 then shows the results of the co-simulation in "Step 2" of Figure 4.4-1 by depicting the voltage as a function of time at each of the four antenna ports. These results confirm the function of the circuit and antenna link given the switching of high-level voltages between ports 1 and 2 corresponding to the respective switching of high-level voltages between ports 3 and 4.

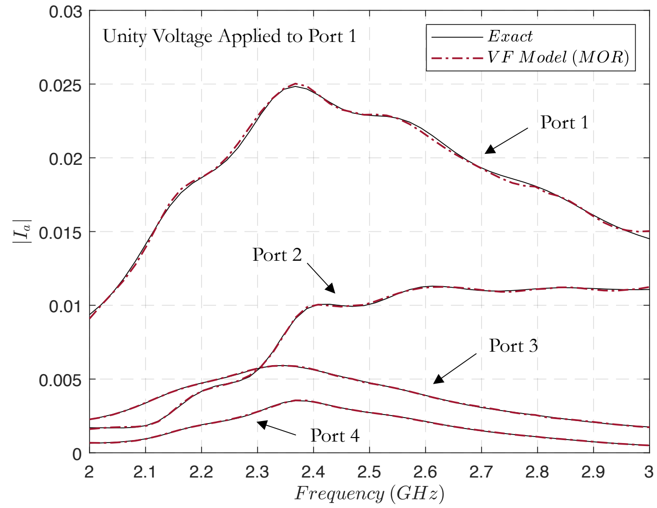

Figure 4.4-8. Current magnitude at each port given a unity voltage excitation applied to port 1 computed using the exact MoM formulation and the VF model constructed using MOR acquired samples. Altering the port in which the voltage is applied yields no change other than to the curve port labels.

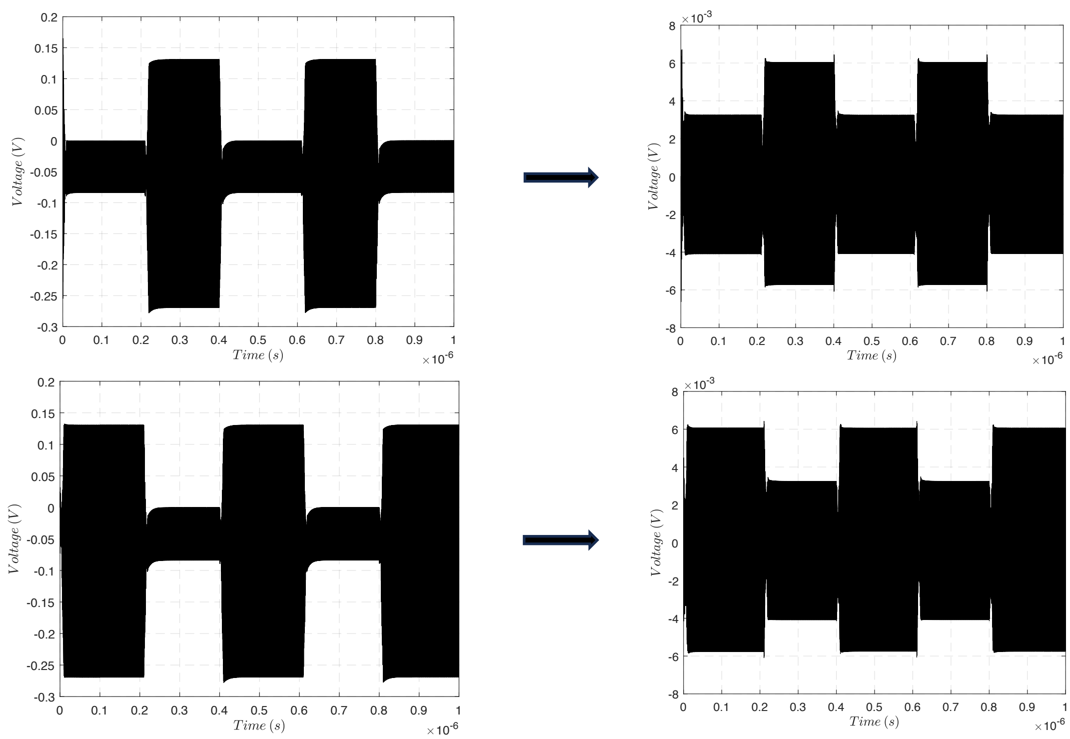

Figure 4.4-9. Time domain port 1 (top-left), port 2 (bottom-left), port 3 (top-right), and port 4 (bottom-right) voltages of the antenna link modelled using VF with samples taken from the MOR MoM formulation while driven by the circuit shown in Figure 4.4-7.

4.5 CONCLUDING REMARKS

A new idea that targets the co-simulation of an antenna array modelled via a MoM-MOR field analysis, and a transceiver/beamformer modelled using lumped circuit analysis (MNA), has been described. A unified field-circuit system has been developed in a form that has allowed the use of a clustered multiport MOR approach for the MoM-based field-analysis part of the problem to be devised that (very importantly) allows use of the efficient Arnoldi-like process for its implementation. Many groundbreaking acceleration methods become computationally superior to conventional MoM-based methods only for problems that are very large (in terms of the number of unknowns). The field-circuit clustered multiport MOR method arrived at here has been shown through examples to offer significant computational advantages for even small to medium sized field analysis problems.

Furthermore, while the inclusion of non-linear elements in the antenna circuitry necessitates an initial sequential step prior to the simultaneous simulation, the example in the previous section provides a baseline of how such a formulation may be useful in analyzing antenna links. Of course, further digital signal processing, digital to analog/analog to digital converters, and signal modulation circuitry can be included in the model at both the transmit and receive ends of the link to fully quantify specific system metrics (e.g. error vector magnitude). Ultimately, this non-linear circuit formulation serves as an addendum to the co-simulation technique described in *Section 4.2* that describes one possible method that uses both MOR and a co-simulation matrix equation, albeit sequentially, to quickly and accurately handle the modelling of antenna-circuit systems that include non-linear elements.

CHAPTER 5

Antenna Subtractive-Mask Shape Synthesis

5.1 INTRODUCTION

We recall from *Section 2.11* that existing antenna shaping techniques have three main drawbacks. The first arises from non-gradient optimizers used in discrete-pixelation methods struggling to identify global minima in the objective function space due to the very large number of pixels that would be necessary to achieve sufficient geometrical resolution. This limits the use of most pixelation-based methods to structures that are of intermediate or small electrical size. Continuous versions of pixelation methods solve this issue by permitting the use of gradient-based algorithms that allow for a huge number of design variables; however in their current state these methods run into the second drawback. While rapidly determining gradient information for port parameters, modal fields, radiated fields, and antenna gain has been reported, no such information has appeared as of yet for composite objective functions. Furthermore, issues have been reported of these methods leading to less-than-optimal solutions when the continuous material parameters must be pushed towards the complete binarization needed for fabrication. The final drawback, and arguably the most important, is the immense computation time needed to complete shaping routines, particularly for medium to large sized geometries. This is most prominently seen in the subtractive shaping technique described in *Section 2.11* and which was introduced in [MOHA 22], to avoid some of the drawbacks of pixelation methods by defining subtractive objects as a relatively small number of shapes (relative to the size of the mesh) that indicate portions of the initial structure to be removed. This limits the number of optimization variables such that non-gradient optimizers can be safely used while also allowing for a high geometrical resolution. However, after each new subtractive shape orientation is created, the structure must be re-meshed before CEM analysis can be performed, leading to extremely long simulation times.

In this section the new antenna subtractive-mask shape synthesis procedure will be introduced. It is best described as comprising of three components. (a) It uses subtractive objects as in the method in [MOHA 22], however the shape of each object is imagined to be a part of a mask that is projected onto the mesh of the CEM model of the starting conductive material distribution, and it is these mesh elements that lie within the projection (and their occupying conductor) that must be removed. (b) Instead of actually removing these elements of the mesh (and hence the material there), these mesh elements are effectively removed by leveraging an idea from [CAPE 19]. This obviates the need to re-mesh the remaining structure or re-size the operator matrix of the associated CEM forward analysis. (c) A customized form of the Arnoldi-based model order reduction technique described in previous sections is used. Numerical simulations will demonstrate that each of these components enhances the efficiency of the overall shape synthesis methodology. This method will be presented in this chapter as follows:

- Section 5.2: Existing Subtractive Shape Synthesis Methodology
- Section 5.3: Subtractive-Mask Shape Synthesis
- Section 5.4: Numerical and Experimental Results
- Section 5.5: Concluding Remarks

5.2 EXISTING SUBTRACTIVE SHAPE SYNTHESIS METHODLOGY

The existing subtractive shape synthesis process is illustrated in Figure 5.2-1. This figure depicts an initial conductor S_0 that is progressively modified by removing a set of $\mathcal{R}_i$ standard geometrical objects for $i = 1, 2, \ldots, N_S$. The (usually fixed) ports are not shown. The shaping process is carried out by iteratively modifying the dimensions and location of the geometrical objects through a non-gradient optimization technique such as a genetic algorithm (GA) to reach a shape with the desired performance metrics. By parameterizing the shapes with only a few parameters, the optimization problem can be formulated with a greatly reduced set of decision variables. In each iteration, for the existing form of the subtractive approach [MOHA 22], the surface is re-meshed anew after removing the objects from S_0. Such an approach is amenable for use with any commercial computational electromagnetics code that permits automated control of its geometry by a shaping script through its application programming interface. In the following section, not only will an extension of this method be proposed, but it will also be more directly integrated within the CEM analysis allowing for significant computational gains using MOR.

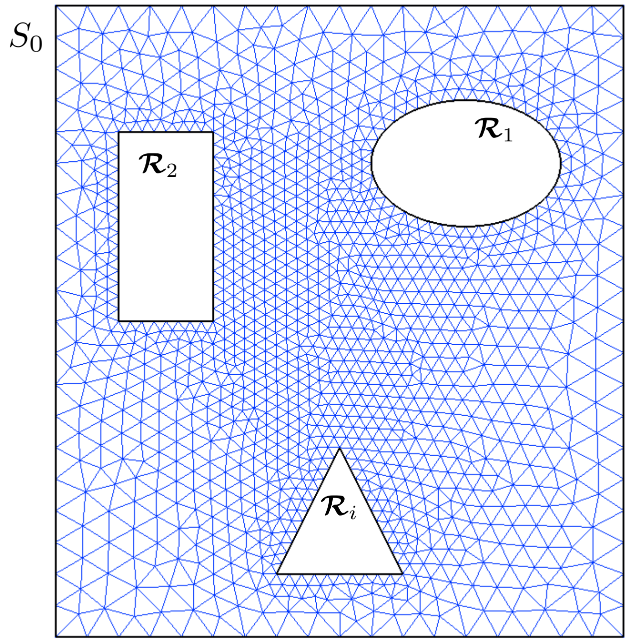

Figure 5.2-1. Illustration of the concept of subtractive shape synthesis where the $\mathcal{R}_i$ objects are actually removed from the conducting surface S_0, which need not be planar.

5.3 SUBTRACTIVE-MASK SHAPE SYNTHESIS

The idea of subtractive-mask shape synthesis (SMSS) is encapsulated in Figure 5.3-1 where subtractive objects dictate regions of the initial surface S_0 to be removed. Compared to Figure 5.2-1, the proposed method operates on edges of a far denser mesh that must be generated only once.

This formulation begins by associating a set of parameters $\boldsymbol{\mathcal{P}}_i$ that uniquely identifies every projective object $\mathcal{R}_i$, where $i = 1, 2, \dots, N_S$, with N_S being the number of projective objects used in the optimization. Without loss of generality, each $\boldsymbol{\mathcal{P}}_i$ is comprised of six variables: $\boldsymbol{\mathcal{P}}_i = \{s_i, x_i, y_i, z_i, w_i, h_i\}$, where s_i is an index specifying the type of object (rectangle, ellipse, or triangle), the triple (x_i, y_i, z_i) denotes the centroid coordinates of a particular mesh triangle in which the object is to be placed around, and the pair (w_i, h_i) specifies two dimensions of $\mathcal{R}_i$ (those dimensions depending on the type of shape). For a given $\boldsymbol{\mathcal{P}} = \{\boldsymbol{\mathcal{P}}_1, \boldsymbol{\mathcal{P}}_2, \dots, \boldsymbol{\mathcal{P}}_{N_S}\}$ the shape S_C is defined. The optimization problem is thus defined as the determination of the configuration $\boldsymbol{\mathcal{P}}^*$ that minimizes the problem's error function [BAND 88], $F(\boldsymbol{\mathcal{P}}; f_l)$, for all frequencies f_l. This can then be formally stated as the search for the parameter set

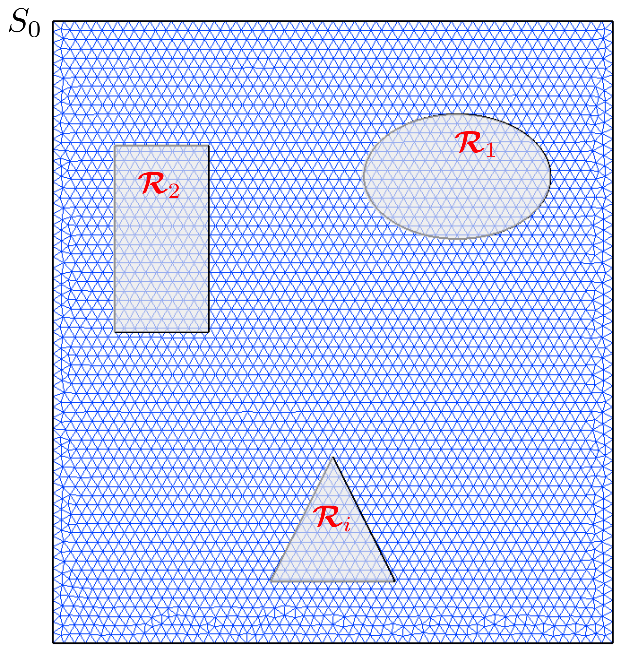

Figure 5.3-1. Representation of the idea of projective subtractive shape synthesis (left). The $\mathcal{R}_i$ are geometrical objects whose projections onto S_0 (which need not be planar) dictate mesh edges to remove.

$$\boldsymbol{\mathcal{P}}^* = \left\{\boldsymbol{\mathcal{P}}_1^*, \boldsymbol{\mathcal{P}}_2^*, \dots, \boldsymbol{\mathcal{P}}_{N_S}^*\right\} \tag{5.2-1}$$

such that, subject to fabrication and other physical design constraints,

$$\boldsymbol{\mathcal{P}}^* = \underset{\boldsymbol{\mathcal{P}}}{\operatorname{argmin}} \sum_{l=1}^{N_f} F(\boldsymbol{\mathcal{P}}; f_l) = \underset{\boldsymbol{\mathcal{P}}}{\operatorname{argmin}}\left(F^*(\boldsymbol{\mathcal{P}})\right) \tag{5.2-2}$$

where $F^*(\boldsymbol{\mathcal{P}})$ is the objective function which measures how close each of the N_f error functions are to the required performance at their specific frequency and "argmin" is defined as "argument of the minimum", which in this case is used in equating $\boldsymbol{\mathcal{P}}^*$ to the set of parameters $\boldsymbol{\mathcal{P}}$ that minimizes $F^*(\boldsymbol{\mathcal{P}})$. The shaping process then proceeds according to the following strategy:

1) **Fixed, dense triangulation:** At the outset of synthesis, a dense triangular mesh is generated and remains unchanged throughout the entirety of the shaping procedure. All inter-element edges are assigned unique indices in advance. This mesh sets the fineness of the geometrical resolution afforded by the shaping process.

2) **Object selection constraints:** The GA used in the optimization is purposefully restricted so that the centroid triplets (x_i, y_i, z_i) of any projective object $\mathcal{R}_i$ may only be assigned a value equal to the centroid of one of the mesh triangles. This is done by assigning each mesh triangle an integer value that is linked to its respective centroid triplet. The object's dimensions (w_i, h_i) are continuous variables that are limited only by the physical constraints placed on the problem. These constraints will be specified further on.
3) **Edge-flagging during evaluation:** At every iteration, when computing $F(\boldsymbol{\mathcal{P}}; f_l)$, the algorithm scans each edge in turn. An edge is flagged if and only if both of its nodes lie inside $\mathcal{R}_i$. This strategy is used instead of say, flagging an edge if its midpoint lies inside $\mathcal{R}_i$, which would be faster to check, however would result in more isolated edges (those not part of an entirely removed mesh triangle) leading to a design that is more cumbersome to fabricate. This is demonstrated in Figure 5.3-2. The collection of unique edges identified for all N_S objects are then stored.

The above strategy can be implemented as a specific update to the MoM impedance matrix $\boldsymbol{Z}(s)$ that is constructed at the beginning of the shaping process in accordance with the initial dense mesh. The update in $\boldsymbol{Z}(s)$ reflects the fact that all the edges located in the "shadow" of $\mathcal{R}_i$ are to be removed. It has been shown in [CAPE 19] that the operation of removing one edge is captured by a scalar operation on the diagonal of $\boldsymbol{Z}(s)$. More precisely, if the n^{th} edge, $n = 1, 2, \dots, N_e$, is selected for removal, then this entails updating the matrix $\boldsymbol{Z}(s)$ by adding a large real value, R_∞, on its diagonal element, $Z_{nn}(s)$. The approach here extends this idea to the bulk removal of all the edges that lie in $\mathcal{R}_i$. To this end, denote by $\boldsymbol{\mathcal{E}}_i^{(k)}$ the set of indices of the mesh elements that fall within the boundary of $\mathcal{R}_i$ at the k^{th} optimization iteration. The update in $\boldsymbol{Z}(s)$ is then formulated as

$$\boldsymbol{Z}(s) \Leftarrow \boldsymbol{Z}(s) + \boldsymbol{P}_k \tag{5.2-3}$$

where

$$\boldsymbol{P}_k = \sum_{i=1}^{N_S} \sum_{j \in \boldsymbol{\mathcal{E}}_i^{(k)}} \left(\mathbb{e}_{j,N_e}\right) R_\infty \left(\mathbb{e}_{j,N_e}\right)^{\mathrm{T}}. \tag{5.2-4}$$

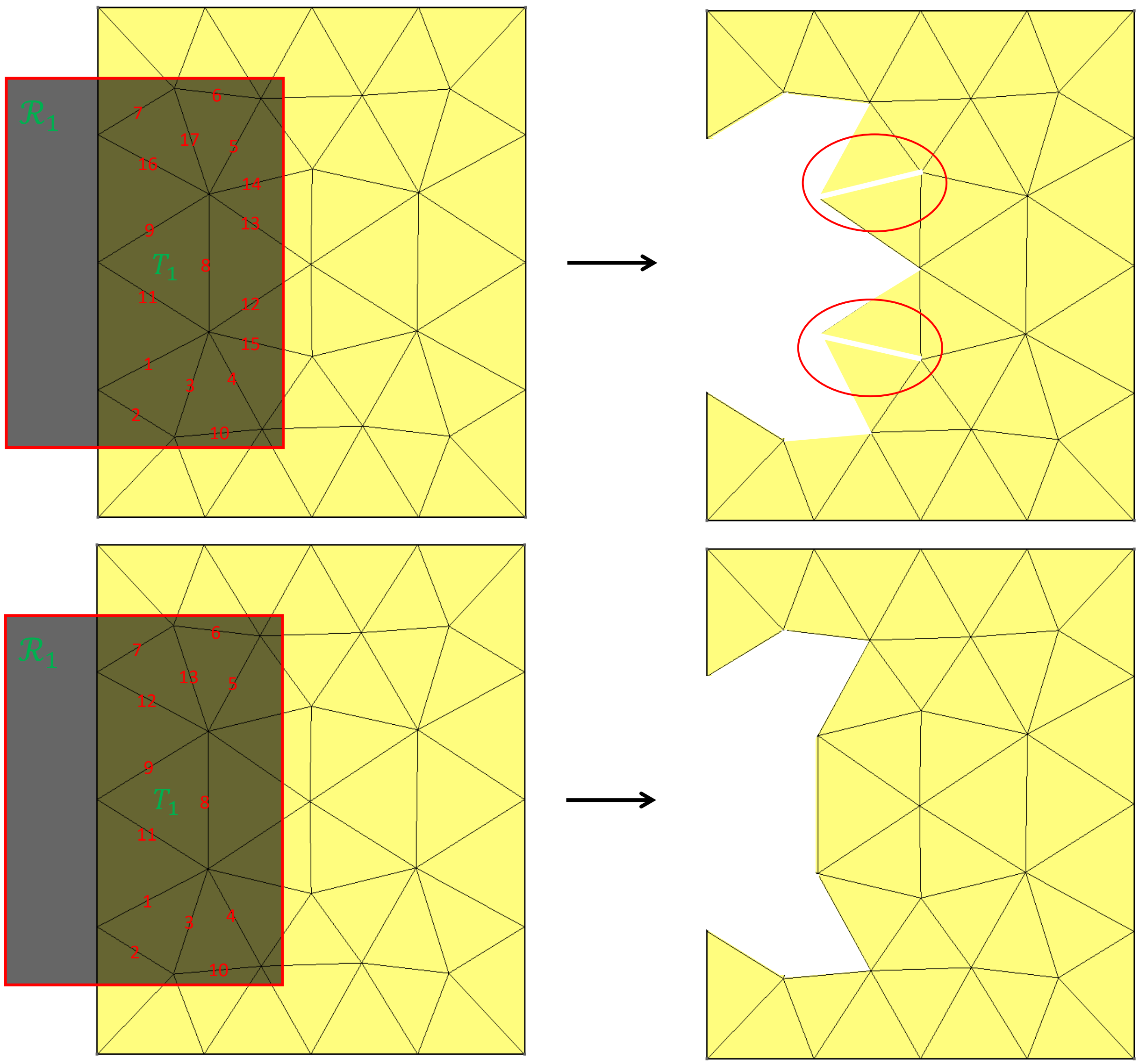

Figure 5.3-2. Mesh with projective object $\mathcal{R}_1$ centred around triangle T_1 removing 17 edges if the flagging criteria is the midpoint of the edge (top-left). The resulting shape (top-right) has two isolated edges (circled in red) that would require narrow cuts to be made in fabrication. Dense meshes could result in many such isolated edges. The same mesh and projective object if the flagging criteria are the edge nodes (bottom-left). This lowers the chance of having isolated edges as shown by the resulting shape (bottom-right).

This idea is easily adapted to suit the multi-port MOR formulation described previously. MOR enables the efficient evaluation of the error functions $F(\boldsymbol{\mathcal{P}}; f_i)$, and hence the objective function. Incorporating the k^{th} update matrix $\boldsymbol{P}_k$ into the MOR framework is straightforward. This is carried out by noting that the update to $\boldsymbol{Z}(s)$ in (5.2-3) requires modification of the power series representation in (3.2-28). Specifically, one may write

$$\boldsymbol{Z}(s) = \boldsymbol{Z}_0 + \boldsymbol{P}_k + \sum_{i=1}^{N_c+1} \boldsymbol{Z}_i(s) s^i. \tag{5.2-5}$$

This modification propagates solely through the augmented matrix $\boldsymbol{P}$ in (3.3-2), where the original leading block is simply replaced by $\boldsymbol{Z}_0 + \boldsymbol{P}_k$, with all other blocks remaining unchanged. Additionally, [CAPE 19] demonstrates the application of the Sherman-Morisson-Woodbury formula to update the moment method admittance matrix when a single basis function is being removed. The result is given as

$$\widetilde{\boldsymbol{Y}} = \boldsymbol{Y} - \frac{\boldsymbol{y}_n \boldsymbol{y}_n^{\mathrm{T}}}{Y_{nn}} \tag{5.2-6}$$

where $\boldsymbol{Y}$ is the admittance matrix, $\boldsymbol{y}_n$ is the n^{th} column of the admittance matrix, Y_{nn} is the n^{th} diagonal element of the admittance matrix, n is the index of the basis function to be removed, and $\widetilde{\boldsymbol{Y}}$ is the updated admittance matrix. The SMSS technique can make use of this idea by expanding (5.2-6) to update the admittance matrix given the bulk removal of edges. The general matrix-vector product $\boldsymbol{I} = \boldsymbol{Y}\boldsymbol{V}$, with the indices of the basis functions to be removed defined by $\boldsymbol{\mathcal{E}}^{(k)} = \boldsymbol{\mathcal{E}}_1^{(k)} \cup \boldsymbol{\mathcal{E}}_2^{(k)} \cup \ldots \cup \boldsymbol{\mathcal{E}}_{N_S}^{(k)}$, is updated using the algorithm in Figure 5.3-3.

Require: $\boldsymbol{Y}, \boldsymbol{V}, \boldsymbol{I}$ and $\boldsymbol{\mathcal{E}}^{(k)}$
Define: $\boldsymbol{M}_{\boldsymbol{j}}$ as the columns of $\boldsymbol{M}$ defined by the indices $\boldsymbol{j}$
Define: $\boldsymbol{M}_{\boldsymbol{i}}$ as the rows of $\boldsymbol{M}$ defined by the indices $\boldsymbol{i}$
1: Initialize: $\mathbb{C} \leftarrow \boldsymbol{Y}_{\boldsymbol{j}} \ \{\boldsymbol{j} = \boldsymbol{\mathcal{E}}^{(k)}\}$
2: Initialize: $\mathbb{R} \leftarrow \boldsymbol{Y}_{\boldsymbol{i}} \ \{\boldsymbol{i} = \boldsymbol{\mathcal{E}}^{(k)}\}$
3: Initialize: $\mathbb{N} \leftarrow \mathbb{C}_{\boldsymbol{i}} \ \{\boldsymbol{i} = \boldsymbol{\mathcal{E}}^{(k)}\}$
4: Solve: $\mathbb{Q} \leftarrow \mathbb{N}^{-1}\mathbb{R}\boldsymbol{V}$
5: Compute: $\boldsymbol{I} \leftarrow \boldsymbol{I} - \mathbb{C}\mathbb{Q}$

Figure 5.3-3. Algorithm for the matrix-vector product $\boldsymbol{Y}\boldsymbol{V}$ given the bulk removal of basis functions.

MOR can make use of this algorithm at each iteration of the optimization process by computing and storing the admittance matrix of the original structure at each of the N_m expansion points. Then once a set of edges $\boldsymbol{\mathcal{E}}^{(k)}$ has been determined for the k^{th} iteration, instead of recomputing (3.3-24), (3.3-37), and (3.3-42) to obtain $\boldsymbol{M}_{0,s_0}$, $\boldsymbol{R}$, and $\boldsymbol{Aq}^{(k)}$, respectively, by pre-multiplying their respective vector quantities by $\boldsymbol{Z}(s_0)^{-1}$, this time however with $\boldsymbol{Z}(s_0)$ replaced by (5.2-5), necessitating an additional matrix LU decomposition at each expansion point for every optimization iteration, the algorithm in Figure 5.3-3 can be applied to instead update the product of the admittance matrix and each of the aforementioned three vector quantities. These changes would be applied within lines 2, 3, and 10 of the pseudo code in Figure 4.2-1. It is important to note that the update $\boldsymbol{Z}_0 + \boldsymbol{P}_k$ is still necessary in order to compute the reduced matrix $\widehat{\boldsymbol{P}}$ as seen in (3.3-43). Since making use of this algorithm obviously provides a substantial computational benefit, one may envisage that instead of using MOR altogether, the admittance matrix at every frequency can be computed and stored for the initial structure and are then updated using the above algorithm to find the value of the objective function for each iteration. While this would have the obvious drawback of costing more memory, it is also slower than incorporating Figure 5.3-3 into MOR for the problems of interest. Computation times for each of these methods will be compared in *Section 5.4.2*. Finally, a generalized overview of the shaping procedure is summarized in the flowchart in Figure 5.3-4. In this figure, $\emptyset$ is used to indicate an empty set in the initial error and objective functions given these are the values of the initial structure S_0, and $\boldsymbol{Z}_0^{(int)}$ denotes the $\boldsymbol{Z}_0$ matrix of S_0. Furthermore, the characterization of $\boldsymbol{\mathcal{P}}_i$ from the GA is done so by selecting a single value from each of the four columns within the large curly brackets. The triangle index column contains numbers in the set $\{1, 2, \dots, N_v\}$ where N_v is the number of valid triangles, that being those which are part of a surface of the antenna that is permitted to be shaped. From this index, the centroid triplet (x_i, y_i, z_i) is then easily obtained. Finally, the dimension parameters w_i and h_i are assigned an upper and lower limit, denoted here by (α_L, α_U) and (β_L, β_U), respectively, such that $\alpha_L \leq w_i \leq \alpha_U$ and $\beta_L \leq h_i \leq \beta_U$, for all $i = 1, 2, \dots, N_S$.

The process through which a subtractive object is constructed on any flat surface of the antenna in three dimensions, and who is characterized around the centroid of a mesh triangle with specific dimensions, as well as how it is determined whether or not the endpoints of an edge lie within that object, is explained in *Appendix A*.

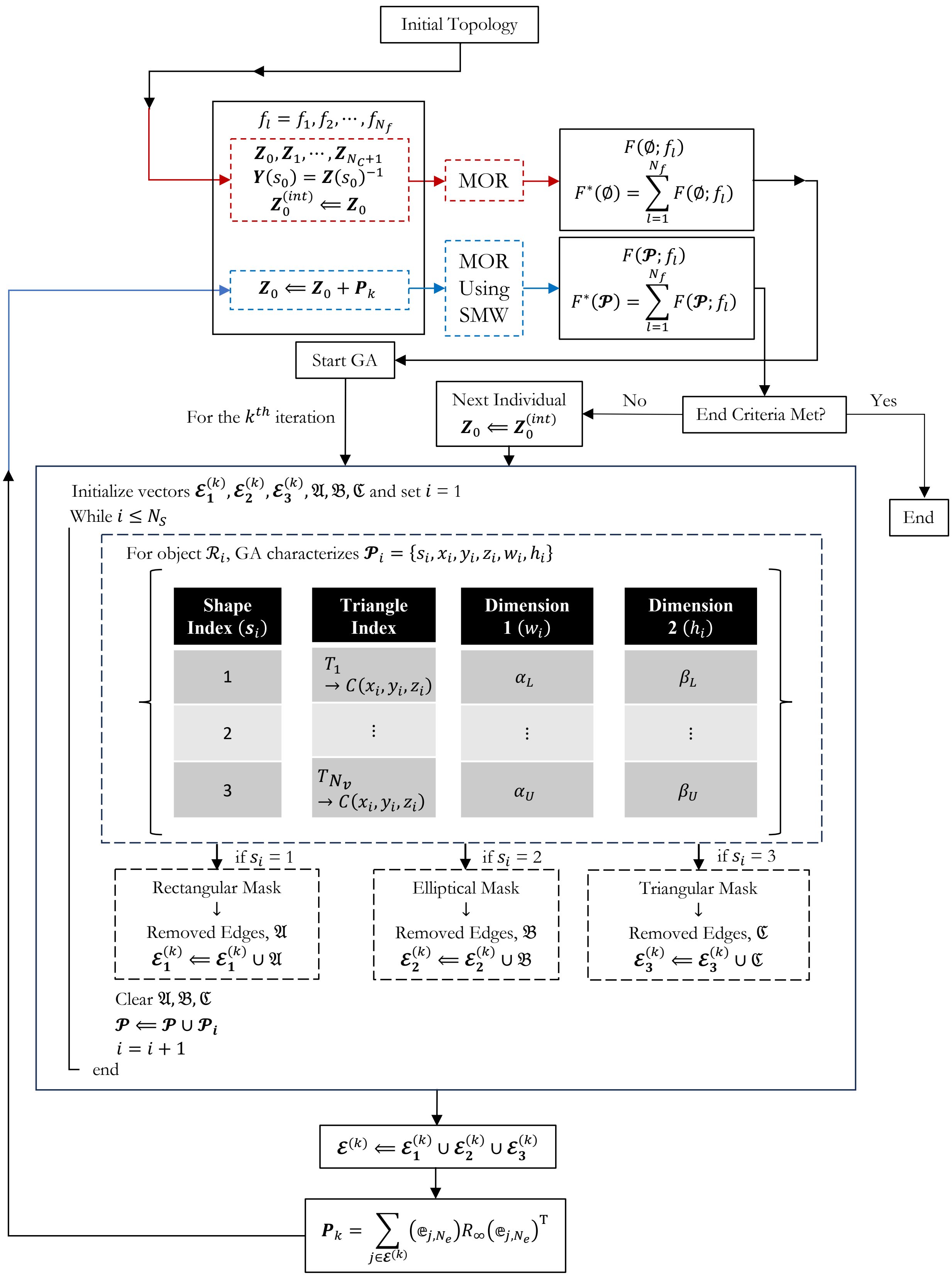

Figure 5.3-4. Flowchart illustrating the generalized projective shaping procedure.

5.4 NUMERICAL AND EXPERIMENTAL RESULTS

This section presents three examples used to demonstrate the effectiveness of the SMSS method. The first two examples examine individual air-substrate patch antennas situated above a ground plane, while the third example considers the performance of a patch antenna embedded within a linear array configuration. The first example will be used to highlight the accuracy and computational efficiency achieved through using the MOR component of the proposed framework. The second example then provides experimental validation of the methodology via fabrication and measurements. Finally, the third example is used to address a more complex optimization scenario involving a more intricate objective function.

5.4.1 Implementation Details

Prior to presenting the examples, this section details important operational parameters which were found empirically to be efficient in driving the shaping process. Firstly, the GA employed is implemented using populations of N_P individuals per generation for the number of generations N_G. Each individual represents a unique parameter configuration, $\boldsymbol{\mathcal{P}}$. For the upcoming examples, the upper limits of the two dimensions α_U and β_U are specified as 20% of the largest dimension of the initial conducting surface S_0, while the lower limits α_L and β_L are set very close to zero.

Next, particular end criteria was applied to all of the upcoming examples. That is, the number of subtractive objects is set to an initial value upon starting the optimization process, $N_S = N_{Si}$. If the GA exhibits stagnation, defined as no improvement in the objective function over N_{stag} consecutive generations, then N_S is incremented by N_{S+} additional projective objects, effectively expanding the design space. After such an increment, the next generation is initialized by preserving the configuration that yielded the best objective function value for the previous number of projective objects, while the newly introduced objects are assigned initial values of negligible dimension. This guarantees that should the addition of projective objects not result in an improved objective function, the best result across the entire optimization routine is maintained. Optimization proceeds until stagnation is detected at or beyond the initial predefined total number of generations N_G.

Thirdly, the error functions used in the optimization process at a single frequency point f_l follow the formulation introduced in [KHAN 22], namely

$$F(\mathcal{P}; f_l) = -\sum_{n=1}^{N_O} \left[H_n\big(X_n(\mathcal{P}, f_l)\big) \prod_{\substack{m=1 \\ m \neq n}}^{N_O} [\operatorname{logsig}(X_m(\mathcal{P}, f_l) - B_m)] \right], \tag{5.4-1}$$

where X_m represents a specific performance metric (e.g. input reflection coefficient) computed for the physical structure synthesized using configuration $\boldsymbol{\mathcal{P}}$ at frequency f_l. B_m denotes a minimum activation value of the corresponding metric, while N_O is the total number of metrics set for optimization. The functions $H_n\big(X_n(\boldsymbol{\mathcal{P}}, f_l)\big)$ are tailored for each performance metric. The specific definitions of $X_n(\boldsymbol{\mathcal{P}}, f_l)$ and $H_n\big(X_n(\boldsymbol{\mathcal{P}}, f_l)\big)$ are detailed individually in the upcoming sections for each of the three examples. The explicit dependence of X_m on $\boldsymbol{\mathcal{P}}$ and f_l will be supressed from this point onwards for notational convenience.

Finally, the operational parameters for all examples are shown in Table 5.4.1.

Table 5.4.1. Parameters used for the examples in *Sections 5.4.2-5.4.4*.

Ex.	N_e	N_f	MOR Parameters			Shaping Parameters										
			N_c	N_q	N_m	N_v	N_{Si}	N_{S+}	N_{stag}	N_O	w_i		h_i		N_P	N_G
											α_L	α_U	β_L	β_U		
5.4.2	3612	50	5	10	2	1294	10	10	50	2	10^{-4}	23	10^{-4}	23	250	250
5.4.3	5338	50	5	10	2	1610	5	5	50	3	10^{-4}	23	10^{-4}	23	250	250
5.4.4	7829	50	5	12	2	1962	20	10	40	6	10^{-4}	36	10^{-4}	36	200	200

The MOR parameters in this table were not determined using the methods explained in *Section 3.4* but rather were determined through a trial-and-error comparison with the exact solution. The reason for this was to guarantee that the exact and MOR shaping routines (specifically for example 5.4.2) terminated in the same final shape so that fair conclusions could be drawn from their computation times. This means that the MOR parameters for these examples lead to an unnecessarily high level of accuracy, however since the route the optimization takes generation to generation depends on any improvement in the objective function, no matter how slight, a lesser level of MOR accuracy would have resulted in an entirely different final shape after a differing number of total generations. This does not mean that the results from such a shape would be inaccurate, just that they could not be compared fairly to the exact result. This is all to say that if the comparisons between the MOR and exact method was not necessary to this section, then the methodology in *Section 3.4* would be used.

5.4.2 Air Substrate Patch and Finite Ground Plane

The initial antenna structure used in this example is a slightly modified version of that in [CHAN 01], with the difference being in the feeding method. The structure, along with its dimensions, is given in Figure 5.4-1. The objective of this example is to minimize the input reflection coefficient and maximize the total broadside directivity of the below antenna over the 2.775-3.225 GHz (15%) band.

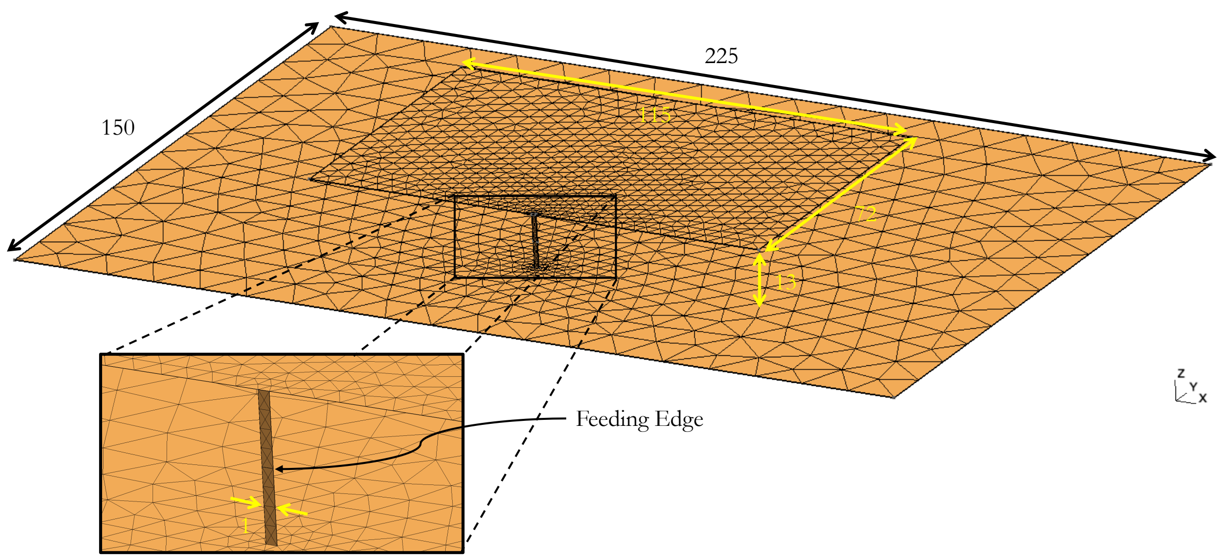

Figure 5.4-1. Air substrate patch and ground plane. All dimensions are in in mm.

As such, two metrics ($N_O = 2$) are used in the objective function. These are defined as

$$X_1 = |\Gamma_{in,dB}|, \quad X_2 = D_{dBi}(0, \phi) \tag{5.4-2}$$

where $\Gamma_{in,dB}$ is the input reflection coefficient and $D_{dBi}(0,\phi)$ is the total broadside directivity. The minimum activation values are given as $B_1 = 15$ and $B_2 = 5$, while the functions $H_1(X_1)$ and $H_2(X_2)$ are given as

$$H_1(X_1) = 15 \tanh\left(\frac{X_1}{15}\right) \tag{5.4-3}$$

$$H_2(X_2) = 0.5(X_2 - 10) + \frac{15}{1 + e^{(-1.5(X_2 - 7))}} + 5. \tag{5.4-4}$$

Figure 5.4-2 plots $H_1(X_1)$ and $H_2(X_2)$. The dashed vertical lines illustrate the activation or minimum values of X_n, B_n. The green markers then show reasonable target values of X_n, that is $X_1 = 15$ and $X_2 = 7$, which at those points yield about the same value of $H_n(X_n)$ (equal contribution to the objective function) shown by the horizontal black dotted line. The blue curve shows that $H_2(X_2)$ will still benefit significantly should X_2 increase beyond seven (up to about 10 before it begins to taper). However, $H_1(X_1)$ increases far less as X_1 surpasses 15, indicating that once $X_1 \geq B_1$, the optimizer should focus on X_2 rather than on further improving X_1, since further improvement in the reflection coefficient beyond -15 dB is deemed to be unnecessary.

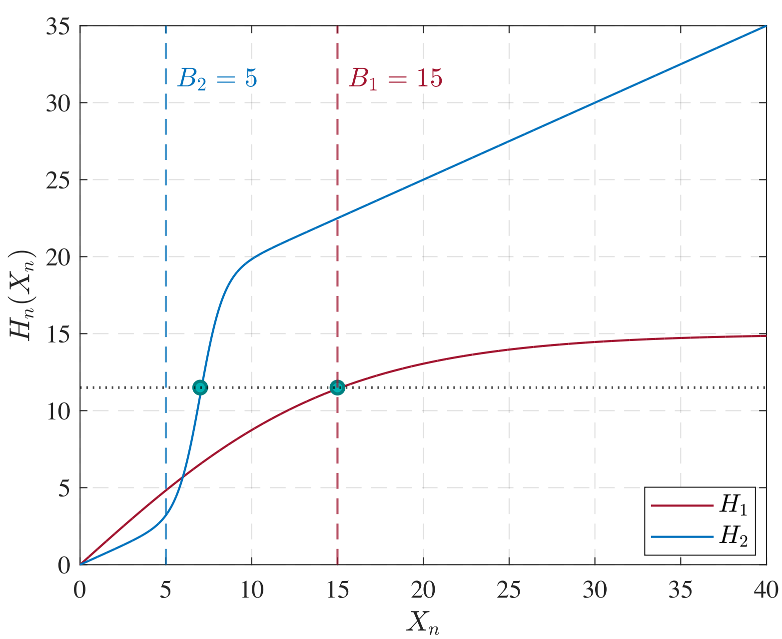

Figure 5.4-2. Plot of the two components of the objective function.

Figure 5.4-3 shows the final shaped antenna design.

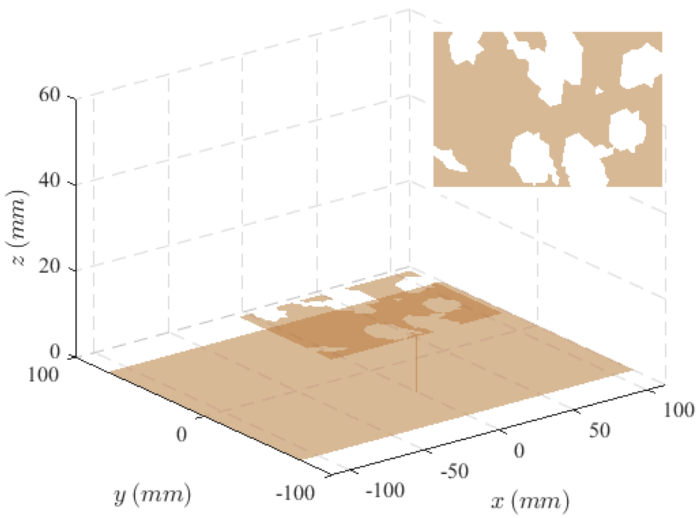

Figure 5.4-3. Final shaped antenna design. Note that the shaping was restricted to the patch element S_0, whose design can be seen in the upper right corner.

Figure 5.4-4 then shows the total broadside directivity and input reflection coefficient as a function of frequency, while Figure 5.4-5 shows the total directivity in the two principal planes at various frequencies. Each of these plots reveals the vast improvement in performance from the initial to the final geometry.

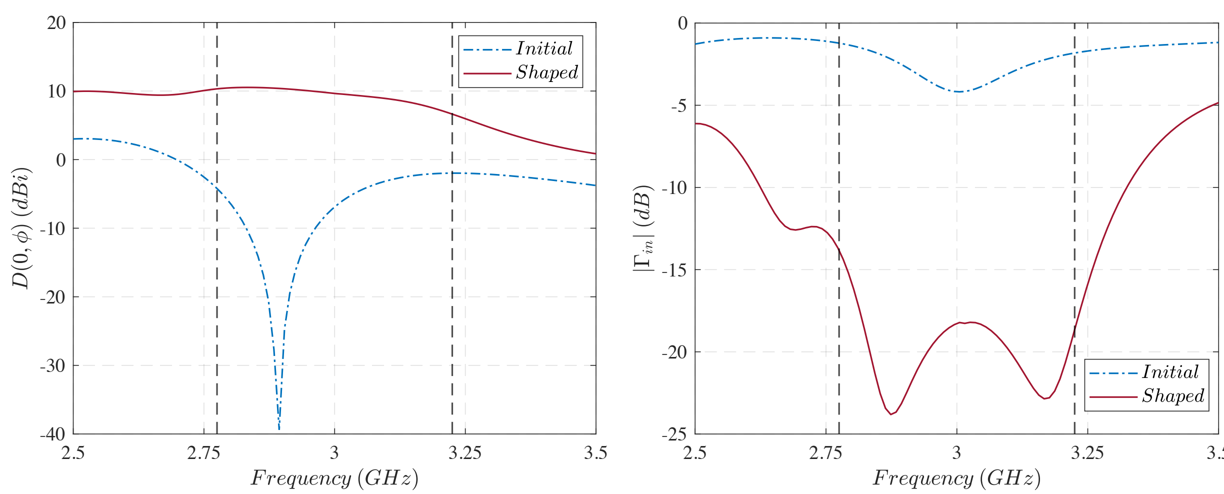

Figure 5.4-4. Total broadside directivity $D_{dBi}(0, \phi)$ (left) and input reflection coefficient $\Gamma_{in,dB}$ (right) as a function of frequency. The band over which the performance was optimized is that seen between the two dashed lines.

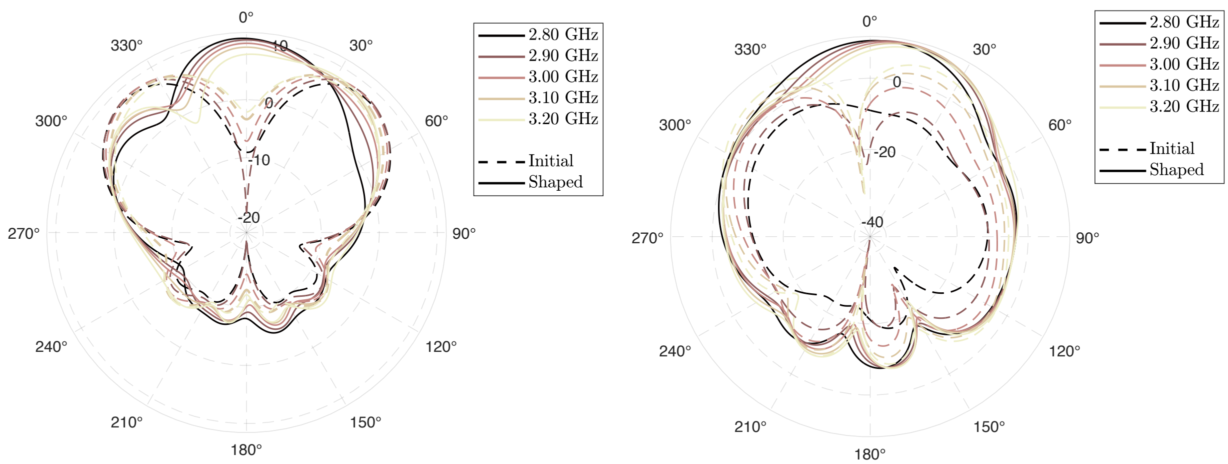

Figure 5.4-5. Total broadside directivity in the $\phi = 0°$ (left) and (b) $\phi = 90°$ (right) plane at various frequencies within the optimization band.

Finally, Figure 5.4-6 shows the progression of the objective function as a function of the GA generation. The proposed method, which incorporates MOR, completed after 501 generations, denoted as G_{MOR}, and as indicated by the green arrow. This optimization process required approximately 51 hours and was executed on a MATLAB platform using parallel computing on a workstation equipped with an Intel Core i9-14900 processor (2.00 GHz), 5 available cores, and 128 GB of RAM. To assess the impact of MOR, the same optimization problem was solved without MOR under identical computational conditions, however with a set time limit of 51 hours. In this case, the exact method, denoted G_{exact}, was only able to complete 30 generations within the allocated time, as indicated by the yellow arrow in the plot below. Although the computational time per generation varies depending on the characteristics of the individuals, a conservative estimate suggests that the use of MOR accelerated the optimization process by a factor of approximately $501/30 \approx 16.7$. It is important to also note that this speed-up estimate does not account for the increasing computational cost (per individual population member) associated with higher values of N_S, as the exact method did not progress beyond the initial 10 shapes. As such, the actual performance advantage provided by the MOR-based approach is likely greater than the estimated value. Figure 5.4-6 also compares the MOR approach with a strictly Sherman-Morrison-Woodbury (SMW) formulation denoted as G_{SMW} and indicated by the red arrow. While this formulation was able to finish 485 generations in the allotted 51 hours, the time it needed to complete the entire optimization was approximately 67 hours, meaning that the MOR process was still faster by a significant factor of about $67/51 \approx 1.3$ times.

As a point of comparison, [CAPE 23b] presents an example shaping a spherical shell to minimize Q-factor. The problem size is given as 2304, 250 generations are considered with a population size of 64, and with only a single frequency being optimized. Using their optimization method, they reported that this problem took 46 hours using parallel processing with 16 available cores. The problem presented above was of greater size (3612), went for more than twice the number of generations (501), used populations of almost four times the size (250), optimized over many frequencies (50), and used parallel processing with just 5 available cores. Despite this, the optimization took only slightly longer at 51 hours.

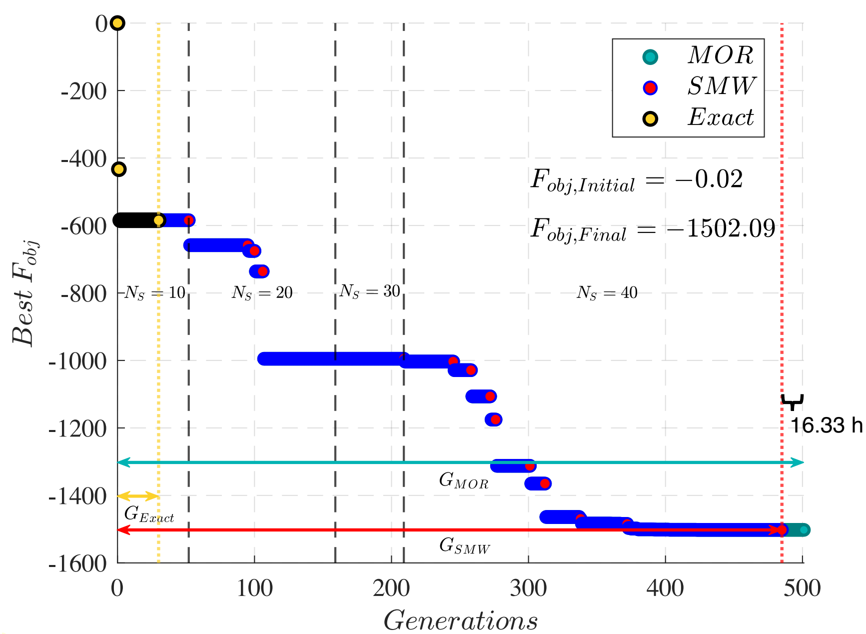

Figure 5.4-6. Progression of the best objective function as a function of the GA generation. The dashed lines indicate the regions of various N_S with that region's respective N_S overlayed within the section.

5.4.3 Circularly Polarized Air Substrate Patch and Ground Plane

The performance of circularly-polarized single-feed (simple probe or L-probe) air-substrate microstrip patches has been studied in [YANG 08]. Those authors observed that, with a simple probe feed, the presence of a U-slot allowed bandwidths of 12% for an axial ratio less than 3 dB and around 7% for an input reflection coefficient less than -10 dB, but that these bands are not necessarily coincident. This work defines a benchmark for what can be achieved with a conventional design approach and can thus be compared to what is achievable using the proposed shaping methodology in a way it would likely be used in design practice.

This example uses the same structure as that seen in Figure 5.4-1, however the height of the patch above the ground plane has been decreased from 13 mm to 9.5 mm. In addition to optimizing the total broadside directivity and the reflection coefficient, this example will also seek to minimize the axial ratio over the prescribed 15% band (2.775-3.225 GHz) such that the antenna becomes circularly polarized. As such, $N_O = 3$ with metrics given by

$$X_1 = \left|\Gamma_{in,dB}\right|, \quad X_2 = D_{dBi}(0,\phi), \quad X_3 = AR_{dB}(0,\phi) \tag{5.4-5}$$

where $AR_{dB}(0,\phi)$ is the axial ratio in dB to be minimized to below a threshold of 3 dB to be considered sufficiently circularly polarized. The minimum activation values for this example are $B_1 = 15$, $B_2 = 5$, and $B_3 = 3$. The medium electrical size of the starting structure is such that requiring maximization of the total broadside directivity to be 5 dBi or more will be sufficient to ensure a single main lobe. Since B_3 is a desired maximum activation value rather than a minimum, the logsig functions in (5.4-1) containing B_3 must be adjusted to $\text{logsig}\big(-(X_3 - B_3)\big)$. The H functions are then given by

$$H_1(X_1) = 15\tanh\left(\frac{X_1}{15}\right) \tag{5.4-6}$$

$$H_2(X_2) = 0.5(X_2 - 10) + \frac{15}{1 + e^{-1.5(X_2 - 7)}} + 5 \tag{5.4-7}$$

$$H_3(X_3) = -1.5(X_3 - 10) + \frac{10}{1 + e^{2(X_3 - 4)}} + 3. \tag{5.4-8}$$

Figure 5.4-7 plots the above three objective function coefficients analogous to Figure 5.4-2 in the previous section. $H_1(X_1)$ and $H_2(X_2)$ are the same as those plotted in Figure 5.4-2 and have the same activation values. $H_3(X_3)$ in this example is the objective function component that considers the axial ratio as is shown in (5.4-5). The marker on the orange curve in Figure 5.4-7 illustrates that the target value of the axial ratio is equal to that of the activation value and has a greater weight than that of the other two components. This was found to be necessary since the desired axial ratio is confined to a much tighter bound as a result of the steep drop off in $H_3(X_3)$ beyond $X_3 = 3$.

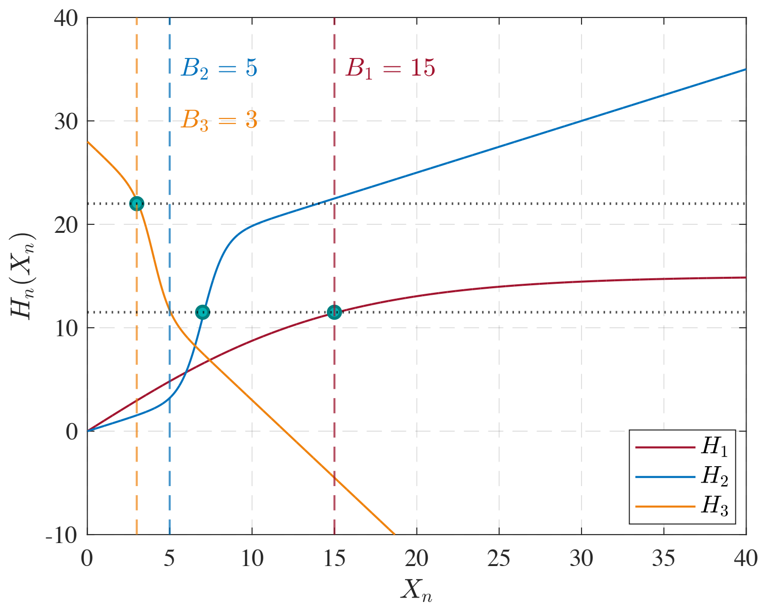

Figure 5.4-7. Plot of the three components of the objective function.

Next, since it is known that a rectangular patch antenna with a single feed location can be made circularly polarized by cutting away a pair of diagonally opposite corners, bilateral anti-symmetry has been enforced on this problem about a y-directed line through the centre of the patch. That is to say that only half (left or right) of the patch is being shaped with the other half being a copy of the shaped half translated (left or right) and rotated 180°. This is reflected in the distinct halves of the mesh shown in Figure 5.4-8. It is also worth noting from this figure that the mesh has been made denser for this example than for the previous one. Figure 5.4-9 shows the final shaped antenna design.

To verify this design, the results of the shaped antenna will be compared both with a simulated version of the final structure (that is, a mesh constructed specifically from the final design of the optimization, denoted as "simulated") as well as with measurements of the fabricated design.

While measurements only really serve as an indication of the accuracy of the computational electromagnetics model used, they nevertheless act as a confidence check for any work. Figure 5.4-10 shows both of these comparison structures.

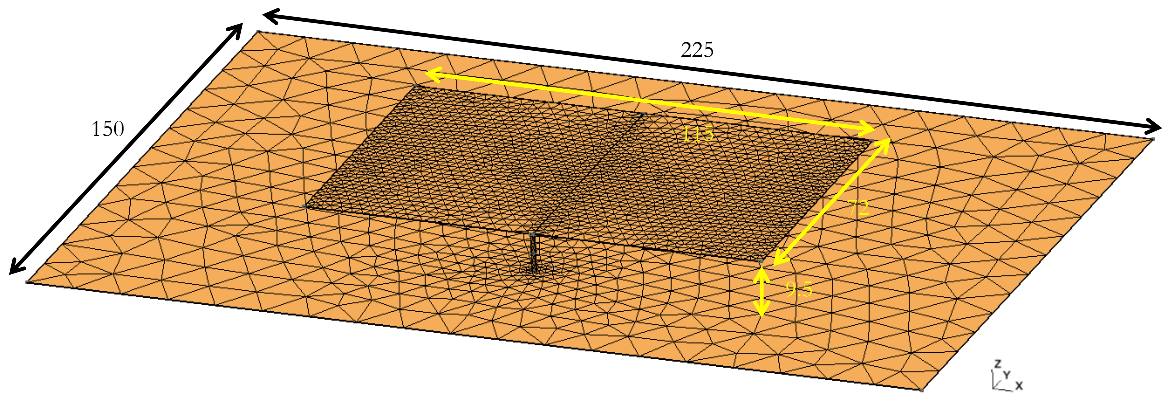

Figure 5.4-8. Air substrate patch and ground plane. The patch mesh is bilaterally anti-symmetrical. Only the left half is shaped.

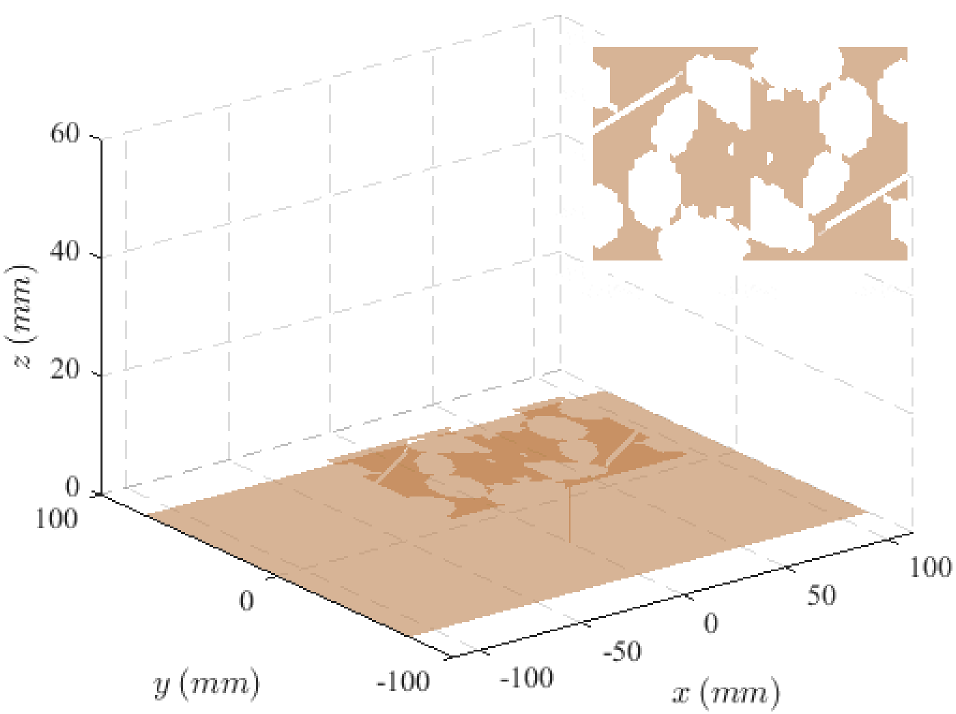

Figure 5.4-9. Final shaped antenna design. Note that the shaping was restricted to the left half of the patch element S_0, whose design can be seen in the upper right corner.

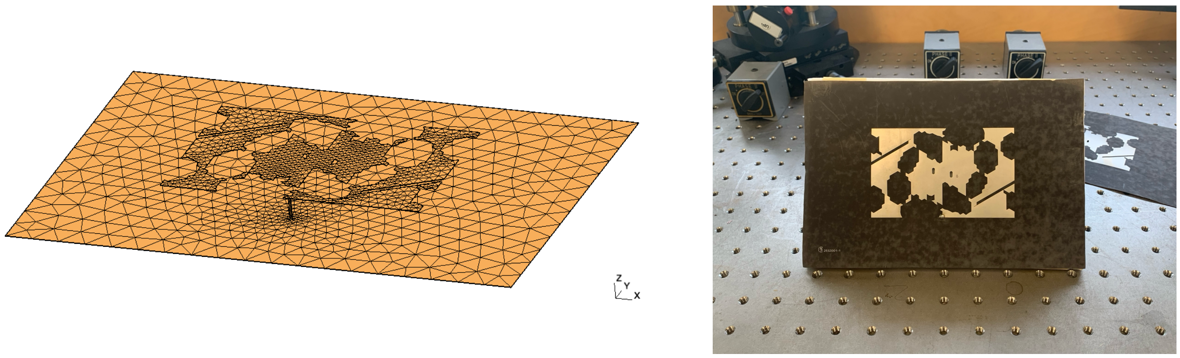

Figure 5.4-10. Mesh structure (left) and fabricated antenna (right) of the final shaped antenna design. The fabricated antenna was printed on a thin 0.127 mm RT/Duroid 5880 substrate ($\varepsilon_r = 2.2$) and placed on a Rohacell HF ($1.047 < \varepsilon_r < 1.067$) foam spacer to obtain the required patch-to-ground plane spacing.

Figure 5.4-11 shows the total broadside directivity as a function of frequency, the input reflection coefficient as a function of frequency, and the axial ratio as a function of frequency.

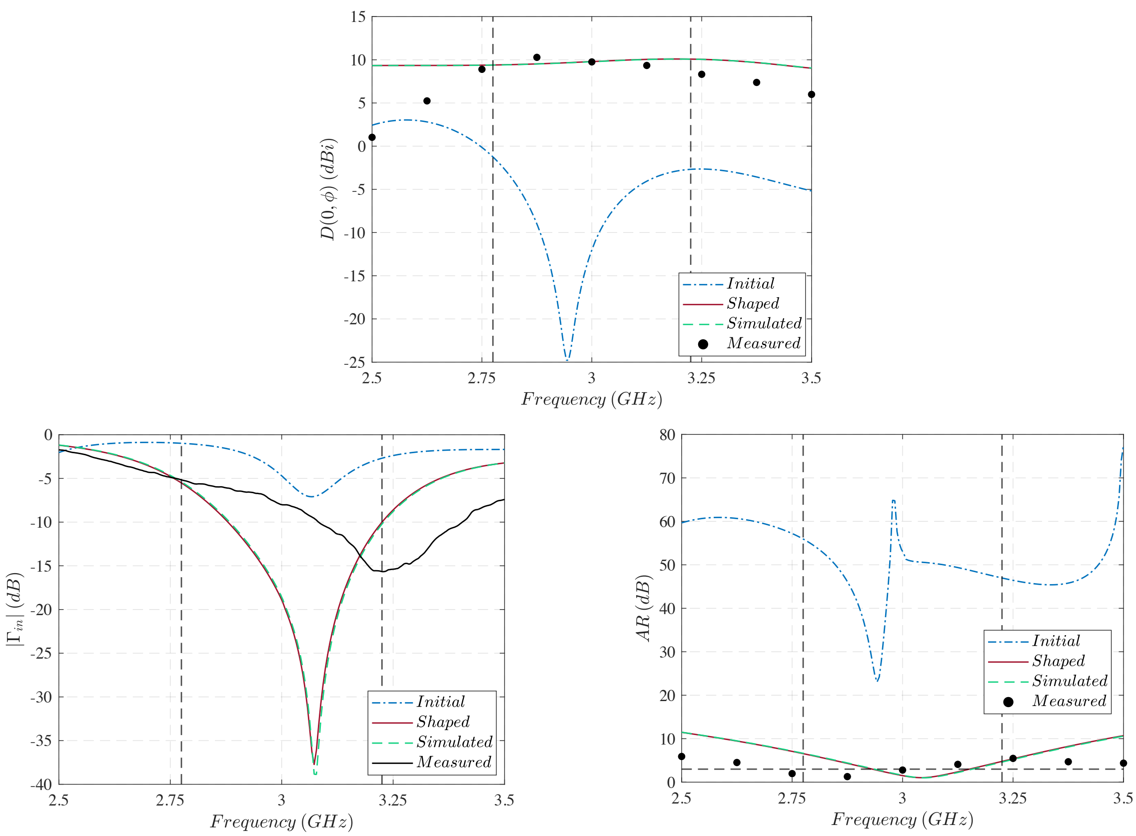

Figure 5.4-11. Total broadside directivity $D_{dBi}(0,\phi)$ as a function of frequency (top), input reflection coefficient $\Gamma_{in,dB}$ as a function of frequency (bottom left), and axial ratio as a function of frequency (bottom right). The band over which the performance was optimized is shown between the two dashed lines.

For further characterization, Figure 5.4-12 shows the normalized surface current density magnitude of the shaped design, while Figure 5.4-13 and Figure 5.4-14 show the total directivity and axial ratio in the two principal planes at various frequencies, respectively. Finally, Figure 5.4-15 shows the progression of the objective function as a function of the GA generation.

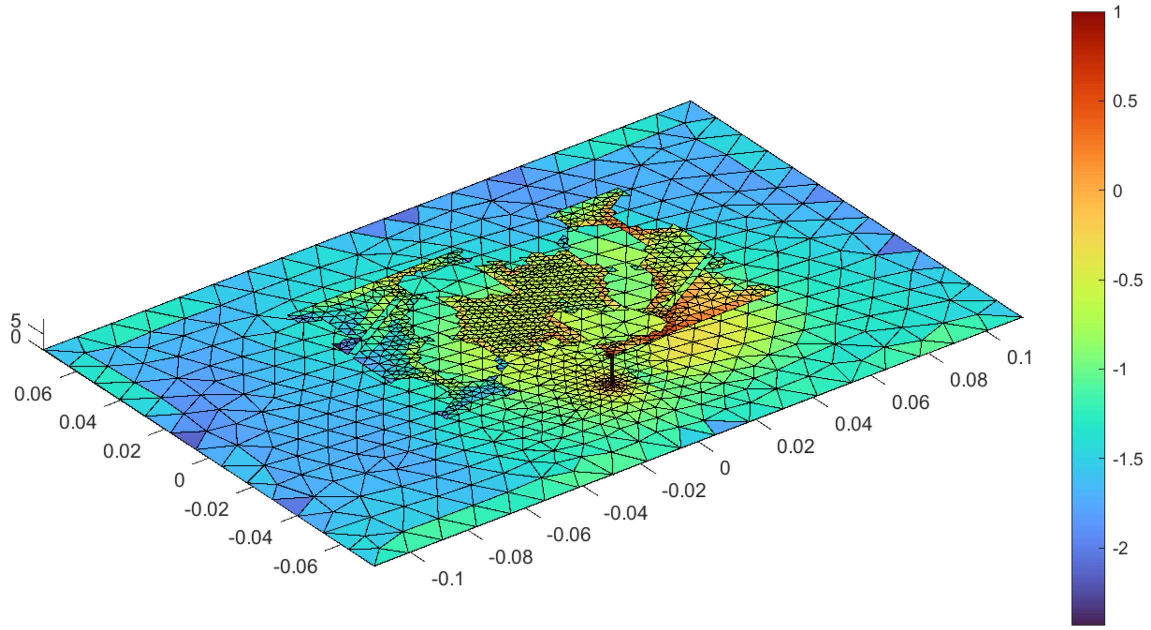

Figure 5.4-12. Normalized surface current density magnitude of the shaped antenna computed at 3 GHz. Dimensions are in m.

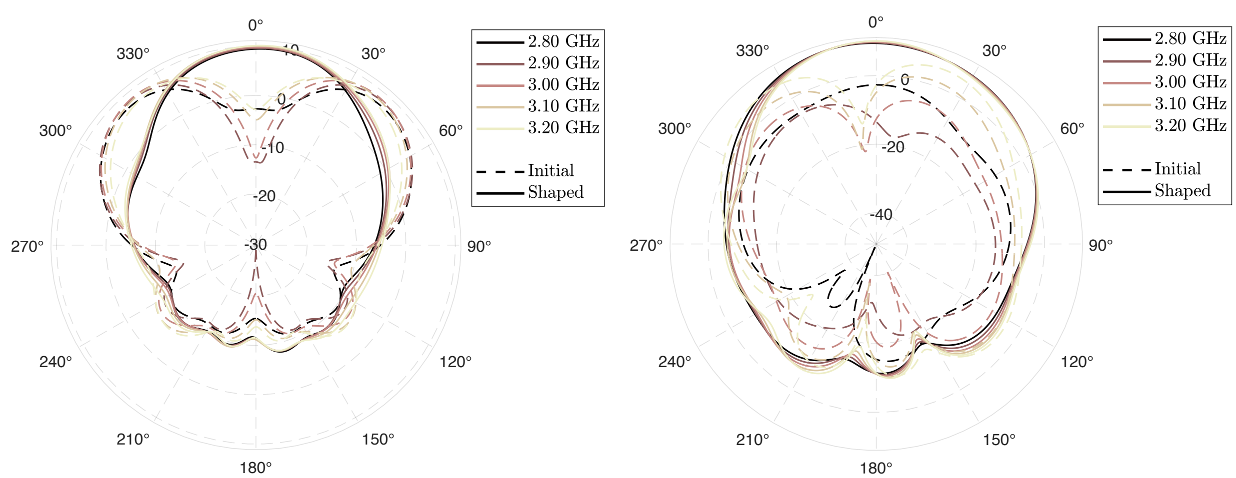

Fig. 5.4-13. Total directivity as a function of θ in the $\phi = 0°$ (left) and $\phi = 90°$ (right) plane at various frequencies within the optimization band.

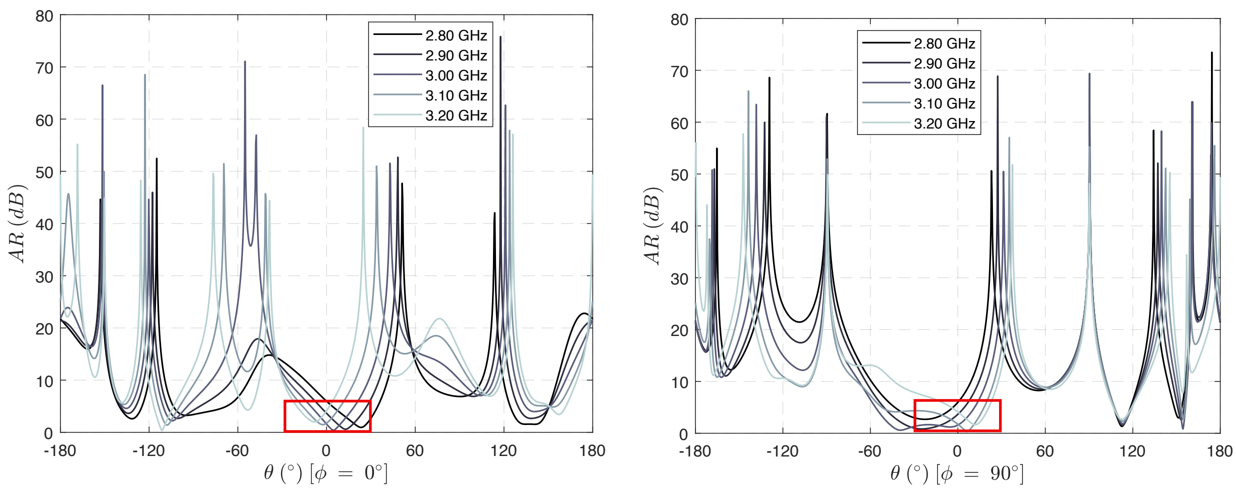

Fig. 5.4-14. Axial ratio as a function of θ in the (a) $\phi = 0°$ and (b) $\phi = 90°$ plane at various frequencies within the optimization band. The red boxes highlight the low axial ratios around $\theta = 0°$.

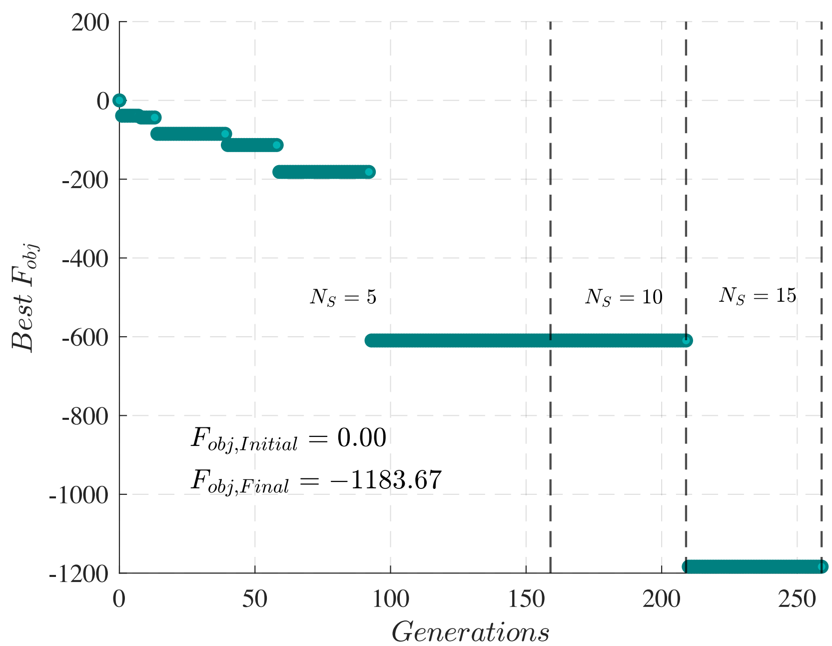

Figure 5.4-15. Progression of the best objective function as a function of the GA generation. The dashed lines indicate the regions of various N_S with that region's respective N_S overlayed within the section. Due to the enforced bilateral anti-symmetry, these numbers pertain to subtractive objects restricted to half of the geometry.

The measured directivity and axial ratio are in good agreement with the computed performance. The reflection coefficient expectedly deviated the most given the inherent difficulty in replicating the exact feeding mechanism used in the simulation, particularly in the machining of a narrow, flat feeding strip, as well as ensuring the very thin substrate that the conductor is printed on remains flush with the foam substrate around the feeding pin connection. We can see that by using SMSS, an approximately 12-13% 10 dB input return loss bandwidth was achieved coincidentally with an approximately 9% bandwidth containing an axial ratio of less than 3 dB, while also ensuring a full 15% ancillary total broadside directivity bandwidth of approximately 10 dBi (more so if the frequencies beyond the optimization band are considered).

5.4.4 Shape Synthesis of an Air Substrate Patch as an Embedded Element in a Linear Array

The final example will consider the design of an embedded patch within a linear array, motivated by what was done in [THOR 05] for a patch in an infinite planar periodic structure environment. In this case we are interested in decreasing the E-plane mutual coupling between the centre patch (representative of a patch embedded within a large linear array) and the patches on either side. Since the same shaped design will be enforced on every patch, it is then reasonable to surmise that additional patches added to the linear array would also exhibit minimal mutual coupling since they experience a similar environment. Figure 5.4-16 shows a diagram of the antenna structure along with its dimensions. The array is a modified version of that seen in [SUN 21].

As can be seen in the upper left of Figure 5.4-16, the ground plane has been segmented into identical portions beneath each of the three elements, each of which are identically meshed. For this example, the central patch and its corresponding ground plane segment will be considered for shaping. This shape will then be copied over to the other two element and ground plane combinations. The feeding strips again are not permitted to be shaped, as well as the leftmost and rightmost pieces of the ground plane in Figure 5.4-16. Additional patches and ground plane segments can thus be inserted into the linear array should they be needed.

This example considers six metrics ($N_O = 6$) defined by

$$X_1 = |S_{11,dB}|,\ X_2 = |S_{21,dB}|,\ X_3 = |S_{31,dB}|,\ X_4 = D_{dBi}(0,\phi),\ X_5 = BW_{(x-z)},\ X_6 = BW_{(y-z)}. \tag{5.4-9}$$

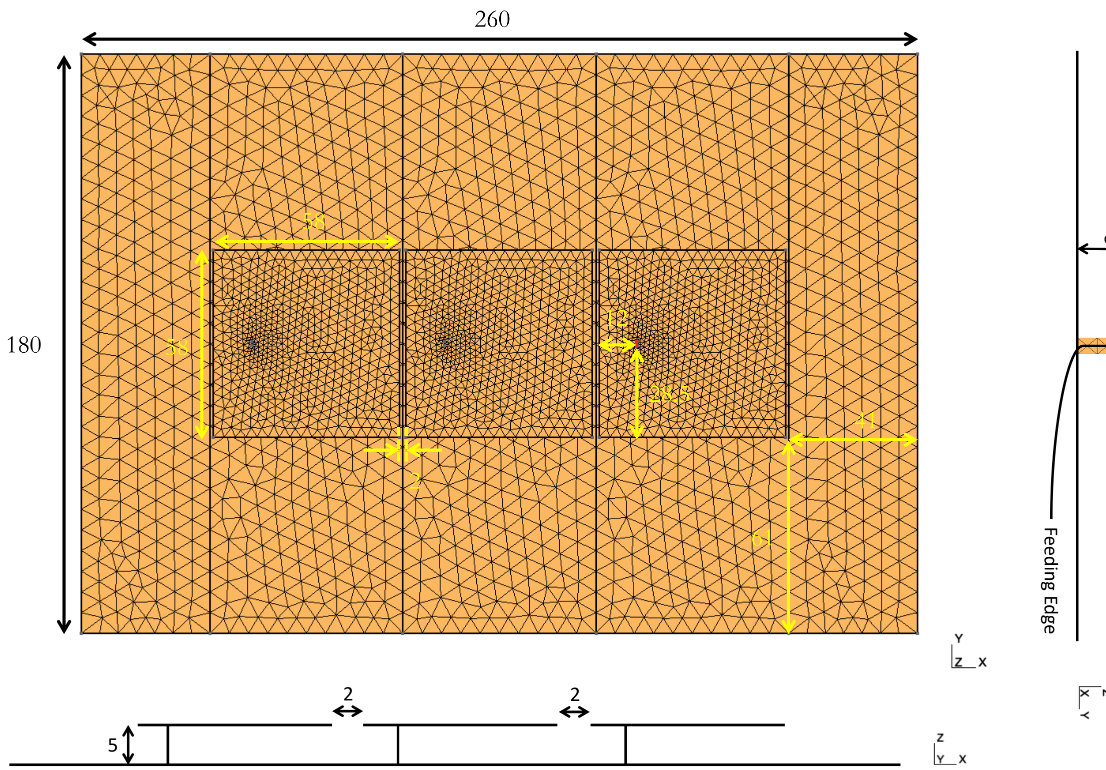

Figure 5.4-16. Linear array of the unshaped patch antennas and ground plane viewed in the $x-y$ plane (top left), $x-z$ plane (bottom left), and $z-y$ plane (right). The diagram in the bottom left and on the right are not to scale but have been adjusted for clarity. All dimensions are in mm. The elements are numbered 3, 1, and 2 from left to right.

The broadside directivity in X_4 is that of the central element and BW refers to the 3 dB main lobe beamwidth of the central element in either the $x-z$ or $y-z$ plane. It is desired that the embedded element pattern remains sufficiently broad in both principal planes while achieving the maximum broadside directivity possible. The activation values for this example are $B_1 = 15$, $B_2 = B_3 = 20$, $B_4 = 8$, and $B_5 = B_6 = 40$. The objective function components are then the following.

$$H_1(X_1) = 25\tanh\left(\frac{X_1}{15}\right) \tag{5.4-10}$$

$$H_2(X_2) = 20tanh\left(\frac{X_2}{25}\right) \tag{5.4-11}$$

$$H_3(X_3) = 20tanh\left(\frac{X_2}{25}\right) \tag{5.4-12}$$

$$H_4(X_4) = 0.5(X_4 - 10) + \frac{10}{1 + e^{-1.5(X_4 - 10)}} + 5.5 \tag{5.4-13}$$

$$H_5(X_5) = 0.2(X_5 - 40) + \frac{10}{1 + e^{-0.7(X_5 - 60)}} + 2 \tag{5.4-14}$$

$$H_6(X_6) = 0.2(X_6 - 40) + \frac{10}{1 + e^{-0.7(X_6 - 60)}} + 2 \tag{5.4-15}$$

The above functions are plotted in Figure 5.4-17.

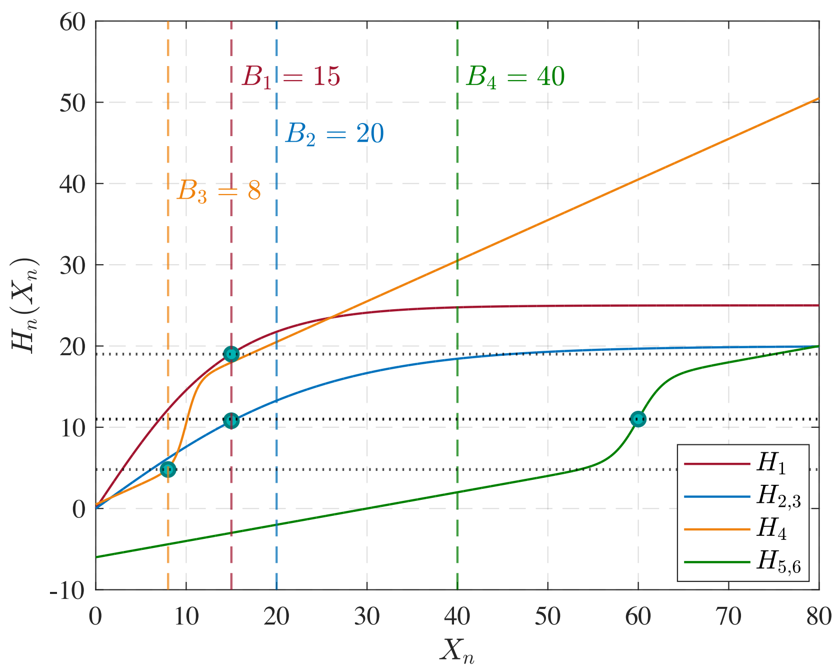

Figure 5.4-17. Plot of the six objective function components.

The first thing to note is that S_{11} was given a higher weight than S_{21} and S_{31}. As will be shown in Figure 5.4-19, the initial antenna's S_{11} over frequency is on average further from the desired activation value (-15 dB) than that of S_{21} and S_{31} (-20 dB). Furthermore, through several trial runs, it was found that S_{11} was the quantity that the GA most struggled to optimize which is why it has the greatest weight relative to not only the other S-parameters, but to all of the optimization metrics. Next, despite the expectation that the total broadside directivity of the embedded element will be less than that of the previous two examples (given the smaller size of starting patch), it was found that a greater activation value and a slightly different function was necessary to achieve the desired results. This was simply to keep the weight of $H_4(X_4)$ in line with the other functions, that is to say that (5.4-7) sometimes lead to structures with suboptimal directivities. Finally, an activation value of 40º was set for the 3 dB beamwidths in each principal plane. By using a similar function to that used for the directivity, a target value of 60º was set by offering a larger increase in the value of the objective function should the beamwidth surpass about 55º up to about 65º. It was found that this setup offered a good balance between beamwidth and directivity, thus any greater beamwidth was considered unnecessary so it's contribution to the objective function decreases beyond about 65º.

The final shaped antenna design can be seen below in Fig. 5.4-18. Note that each patch element and its associated ground plane segment are identically shaped.

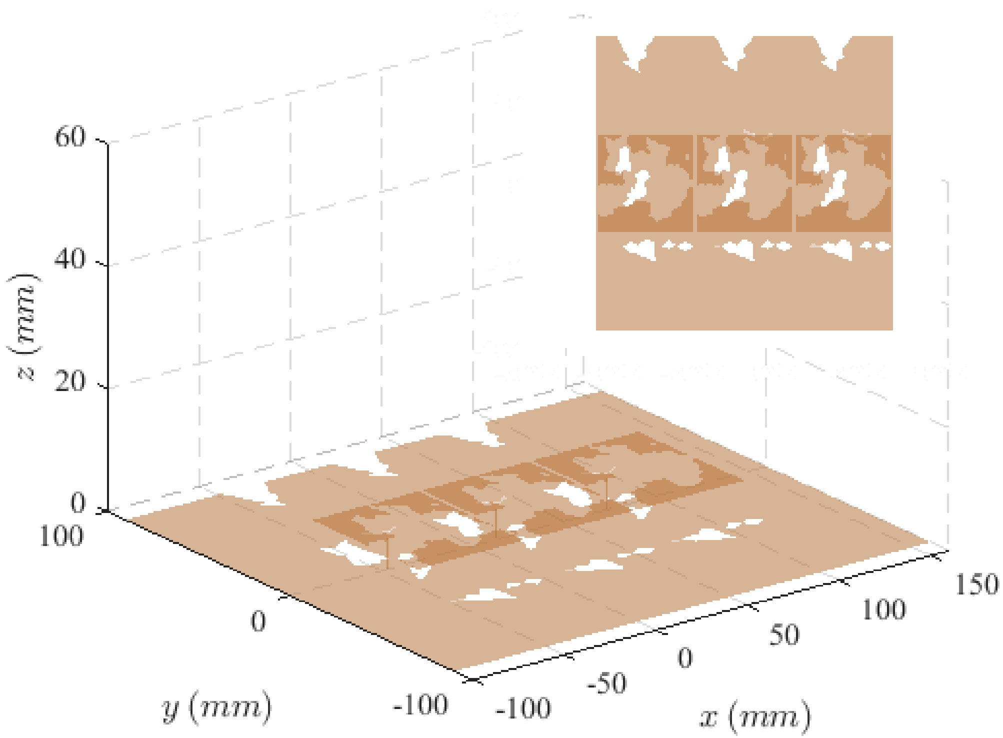

Figure. 5.4-18. Final shaped antenna design. A top-down view is shown in the upper right corner.

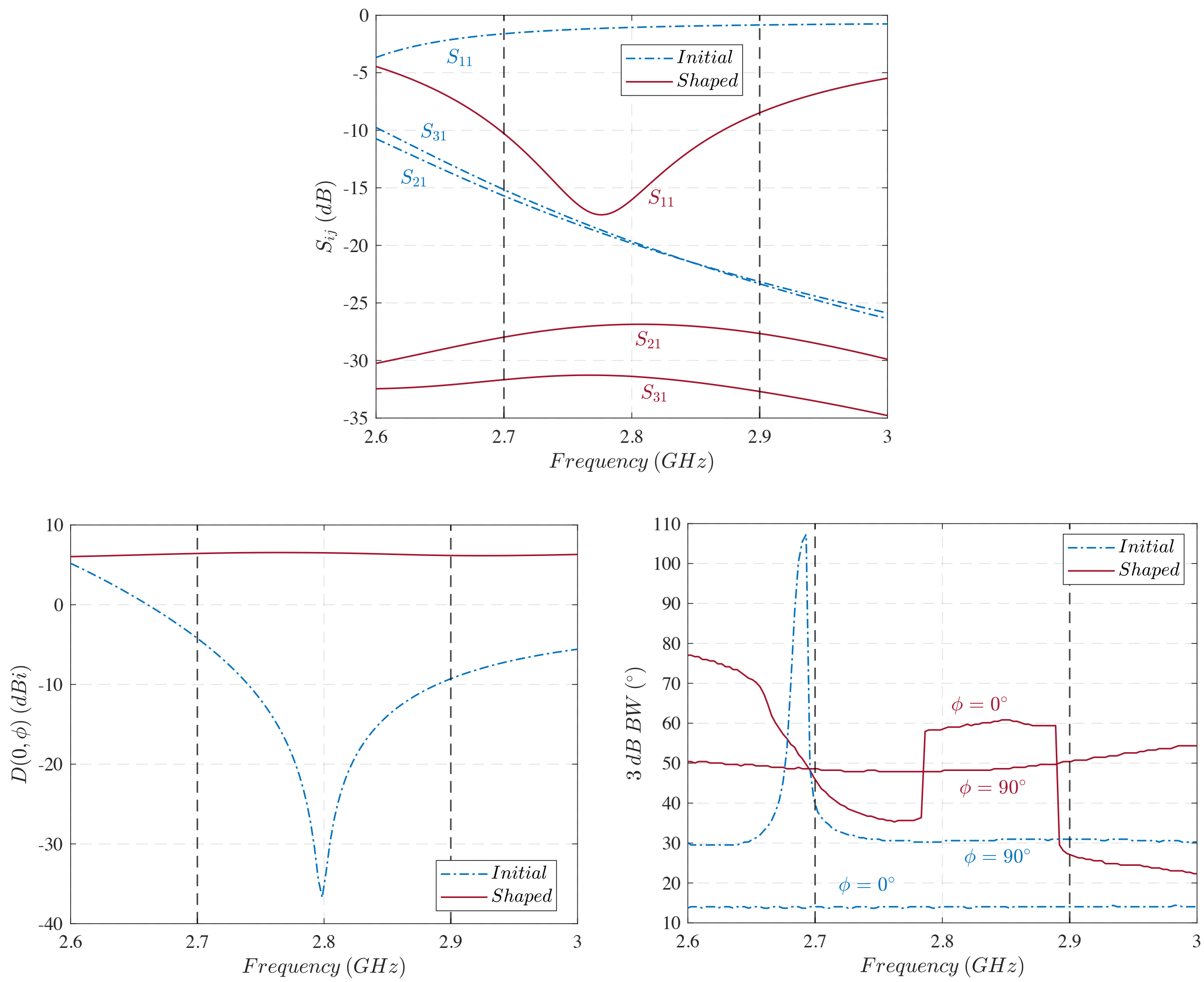

Figure 5.4-19. S_{11}, S_{21}, and S_{31} as a function of frequency (top), total broadside directivity $D_{dBi}(0, \phi)$ as a function of frequency (bottom left), and 3 dB beamwidth as a function of frequency (bottom right). The band over which the performance was optimized is that shown between the two black dashed lines

Figure 5.4-19 above shows S_{11}, S_{21}, and S_{31} as a function of frequency for the initial and shaped array, the broadside total directivity over frequency, along with the 3 dB beamwidth versus frequency. Figure 5.4-20 shows the total directivity at various frequencies in the $x - z$ and $y - z$ planes, respectively, where both planes exhibit the broad patterns desired for an embedded element. Finally, Figure 5.4-21 displays the progression of the objective function throughout each GA generation.

It is always possible to define shape synthesis problems with a tough set of performance metrics, however it is often difficult to achieve the desired optimization across all such metrics. This example has demonstrated that the subtractive-mask approach, combined with MOR, renders such problems do-able with modest computational resources.

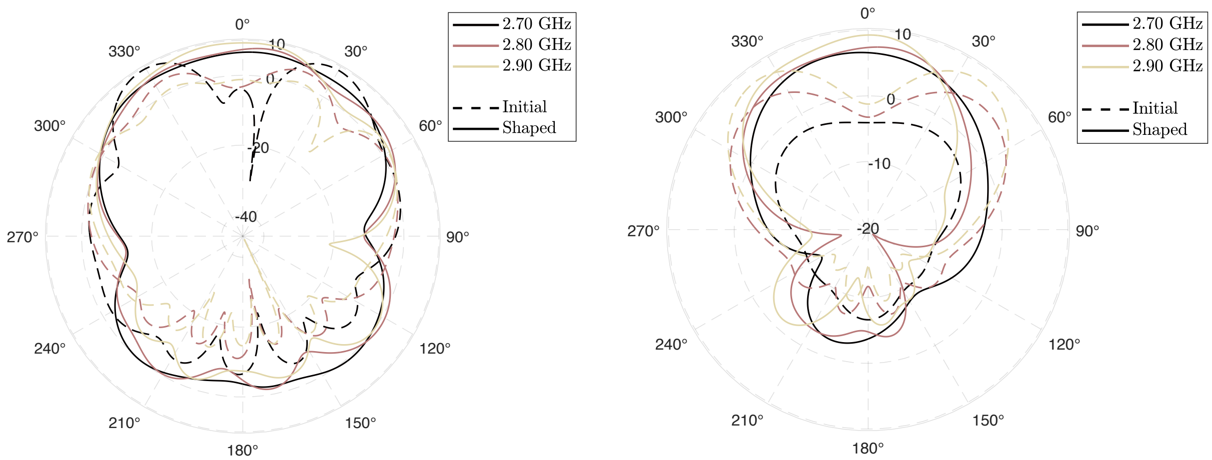

Figure 5.4-20. Total directivity in the $\phi = 0°$ (left) and $\phi = 90°$ (right) plane at various frequencies.

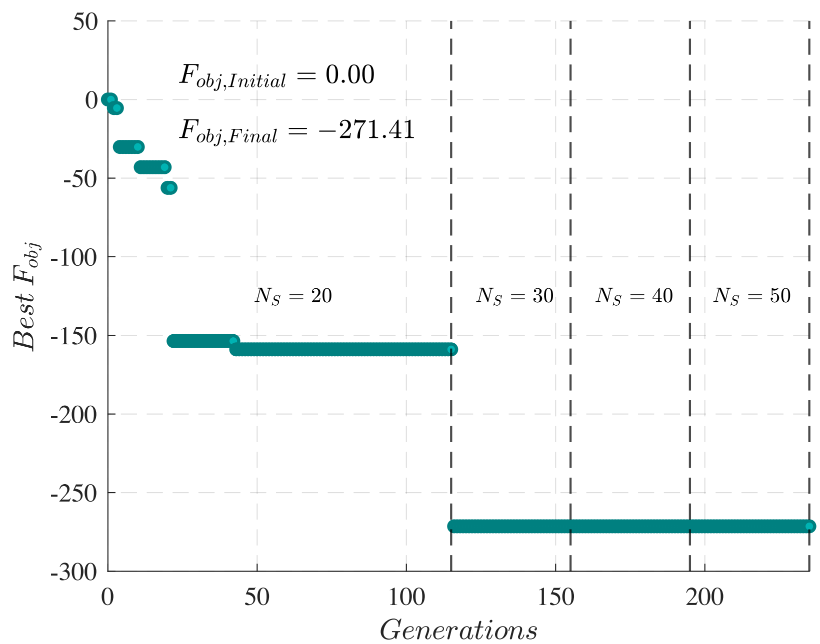

Figure 5.4-21. Progression of the best objective function as a function of GA generation. Since the patch and ground plane section is being shaped in this example, N_{Si} was set to 20 to account for the greater shaping area.

5.5 CONCLUDING REMARKS

The key attribute of the subtractive-mask shape synthesis method presented in this chapter is its ability to apply a provenly effective subtractive shaping methodology (through various adaptations to the original approach) while obviating the need for remeshing during each iteration. This means that throughout the entirety of the problem, only the initial structure needs to be meshed and formulated. This improvement to the original subtractive shaping approach alone is significant, and constitutes a massive reduction in computation time. To put this into perspective, let us consider the circularly polarized patch antenna example of *Section 5.4.3*. By no longer needing to re-mesh each new structure at every GA iteration, a new impedance matrix need not be computed. For this example, the time needed to fill the Chebyshev-approximated ($N_c = 5$) impedance matrices (seven matrices in total) of the final meshed design, shown on the left of Figure 5.4-10, is approximately 40 seconds. If a Chebyshev approximation of the impedance matrix is not used (conventional approach), filling the 50 impedance matrices ($N_f = 50$) takes approximately 160 seconds. Each generation of the GA results in a population of 250 different structures that have varying MoM problem sizes with slightly different matrix fill times. However, if we use the fill time of the final meshed design as an estimated average, then with the 64750 antenna shape possibilities that were considered in this synthesis example, utilization of the new subtractive-mask approach saves approximately 719 hours (30 days) of matrix fill time if the Chebyshev approximation is used, or about 2878 hours (120 days) of matrix fill time if the MoM matrix is computed in the conventional way at each frequency. Although even the improvement afforded by the subtractive-mask technique alone provides a substantial reduction in the computation time needed for the shape synthesis process, the shaping of non-electrically-small antennas is shown in this chapter to be rendered feasible only with the use of MOR compounded with the aforementioned obviated re-meshing.

The subtractive-mask shape synthesis process thus ultimately allows for the rapid shaping of medium- to large-sized antenna problems with complex composite objective functions that yield directly manufacturable final designs that were validated in this chapter through both simulation and measurement.

CHAPTER 6

Conclusion

The **first contribution** of this thesis was detailed in *Chapter 3*. There, the idea of model order reduction, historically used in circuit simulation, was adapted to create reduced order models of CEM analyses which allow for such problems (of fundamentally any size) to be solved at essentially any number of frequencies without costing additional computation time beyond the first solution. Achieving this was done through multiple steps:

- To start, the frequency dependent MoM impedance matrix had to be recast in such a way to allow it to be equivalently written as a linear polynomial with respect to frequency. This was done by taking a Chebyshev approximation of the exponential terms within the computation of each impedance matrix element. The result, however, was a power series representation of the impedance matrix with frequency independent coefficient matrices whose number, and thus the order of the polynomial, was determined by the number of Chebyshev coefficients needed for an accurate approximation. Such a polynomial was then linearized by expanding the size of the matrix equation by derivatives of the solution vector.
- Arnoldi's algorithm, and thus what was termed implicit MOR in this thesis, could then be employed, albeit in a painstakingly slow and inefficient capacity due to the much larger system of equations now being considered. An alternative computationally efficient procedure was thus developed to utilize Arnoldi's algorithm to compute the ROMs from only matrices and vectors of the original problem size, thus circumventing this computational hurdle.
- This formulation was then finalized by developing new methods precise to antenna applications that allow for the automatic determination of all of the necessary MOR operational parameters, ensuring that an accurate result can be achieved without having to brute-force such a result through repeated trial runs. These parameters being the number of

Chebyshev polynomials needed to approximate the impedance matrix, the optimal size of the reduced order models, and the number and location of expansion points.

Prior to this work, the literature surrounding the application of model order reduction to the method of moments analysis of radiating structures was incredibly limited if not non-existent, which was certainly the case when considering electric field integral equation modelling using the spatial-domain free-space Green's function. This thesis has extended this literature by developing an MOR formulation for such class of MoM scattering problems from perfectly conducting objects.

Chapter 4 and *Chapter 5* then made use of this MOR formulation to enable a novel antenna-circuit co-simulation framework and shape synthesis algorithm, respectively, that would otherwise have been computationally cumbersome.

Thus the **second contribution**, namely the formulation developed in *Chapter 4*, which simultaneously solves a MoM field analysis along with the MNA circuit formulation of the feeding circuitry, linking the voltages and currents at the circuit ports and antenna feed points. The multi-port nature of the MOR formulation allows for what is effectively a "library" of ROMs to be created for varying antenna structures over different frequency bands. This means that any circuit can be connected to a ROM and can be simulated for a full-wave solution without having to recompute the ROM, allowing for repeated rapid simulations of the entire antenna-circuit combination as the circuit is being iteratively designed. Such a library is of particular value when dealing with higher frequency applications which in turn lead to tightly-integrated array antennas that do not easily allow for measurements at individual element ports (or even the array antenna port), making measurements of the combined antenna array/transceiver circuitry increasingly essential. Two examples in this chapter showed off this idea to be both accurate and computationally efficient when working with a linear circuit. Non-linear circuits were then considered by adding in a sequential step, along with a vector-fitting algorithm, to combat the numerical instability and lack of convergence when dealing with this type of problem in the time domain. A third example in this chapter showed how this type of formulation can be used, using an antenna link as a vehicle. Although not shown here, this approach can easily include any signal processing and modulation circuitry involved at either end of the link to quantify system-specific metrics.

Finally, from the onset of this research, the goal was to improve the computational efficiency of antenna shape synthesis, an antenna design technique which, while promising in its concept, has yet to become adopted as a common industry practice. The reason was evident from the computational comparison shown for the first example of *Chapter 5* where traditional MoM computations (the exact formulation) would take far too long to complete. This is why the comparison was done by halting the process (when using the exact MoM) after it had taken as long as the MOR-based process took. A conservative estimate for the time needed for the exact method to finish this example would have been approximately 35 days, but likely more given this estimate is based on the number of generations the exact method completed while using only the minimum number of subtractive objects (as was explained in *Section 5.4.2*), and that it was done for only the duration for the smallest of the three problems presented in this thesis. However, by using MOR in conjunction with this novel SMSS methodology, the **third contribution** of the thesis, the time needed to shape medium-sized antenna structures with composite objective functions balancing several design metrics was cut down from weeks or months to just a few days, ultimately increasing the viability for such a technique to be used as part of standard design practice. Of course, computational efficiency is hardly relevant if the methodology yields sub-optimal or inaccurate results, but the examples in *Chapter 5* proved this was not the case for the MOR-based SMSS method which was able to achieve strong results relative to what would be expected as an upper bound for the performance metrics, given the initial structure's size. One of these examples was also fabricated and assembled to confirm the method's validity, while also providing measurements that fundamentally confirm the accuracy of the CEM model used throughout this thesis. As a whole, the SMSS method addresses many of the issues plaguing current antenna shape synthesis techniques beyond just exhaustive computation times. It provides easily manufacturable designs, scalable geometrical resolution (defined by the density of the mesh) without inflating the number of design variables or the computation time. It can easily handle any type of objective function, and has relatively few optimization variables making it ideal for non-gradient optimizers.

To conclude, there do remain some points discussed throughout this thesis in which further investigation would prove useful. The first is the determination of the minimum number of Chebyshev coefficients needed to accurately represent the impedance matrix. While the graphical approach covered here is functional, a rigorous analytical relationship between the minimum number of Chebyshev coefficients, the frequency band of interest, and the maximum dimension of the antenna structure may exist. Its determination is a more complicated task then was initially thought, for the reasons mentioned in *Section 3.4.1*, but would certainly prove useful to uncover. The second is related to the antenna-circuit co-simulation methodology when handling circuits with non-linear elements. As was mentioned in *Section 4.4*, the sequential step and subsequent necessity for the vector fitting algorithm was due to convergence and stability issues that were encountered when attempting to solve the co-simulation formulation in the time domain via Newton iterations, and stemmed from the complex nature of the reduced MoM matrices. A few attempts were made throughout the research to model these matrices in an equivalent real-valued manner to try to alleviate this issue, but a solution was not found. Future further research into this area would very likely lead to a solution allowing for a full co-simulation framework with non-linear circuit elements as was presented here for strictly linear circuits. Lastly, the obvious and largest next step in the application of MOR to the MoM analysis of radiating structures would be to broaden the class of problem in which MOR can be used to beyond just perfect electrical conducting surfaces in free space to ones which also include dielectric materials. PEC materials were chosen in this work simply as a test case for the methodology. Common design practice entails initially assuming a PEC structure and then later considering losses via a perturbation approach to see what the effect is on the final design. However, given how beneficial MOR has been demonstrated to be throughout this thesis, expanding its application in the field of CEM analysis would undoubtedly be worth investigating.

REFERENCES

[ACHA 01] R. Achar and M. S. Nakhla, "Simulation of high-speed interconnects," in Proceedings of the IEEE, vol. 89, no. 5, pp. 693-728, May 2001.

[ALAK 21] A. Alakhras and D. McNamara, “The shape synthesis of 3D electrically-small conducting surface antennas,” Electronics Letters, vol. 57, no. 8, pp. 311–313, 2021.

[ANTO 01] C. Antoulas and D. C. Sorensen, “Approximation of large-scale dynamical systems: an overview,” in Int. J. Appl. Math. Comput. Sci., co. 11, no. 5, pp. 1093-1121, 2001.

[AOKI 11] Y. Aoki, H. Deguchi, and M. Tsuji, “Reflectarray with arbitrarily-shaped conductive elements optimized by genetic algorithm,” in 2011 IEEE International Symposium on Antennas and Propagation (APSURSI), 2011, pp. 960–963.

[AYGÜ 04] K. Aygün, B. Fischer, J. Meng, B. Shanker, and E. Michielssen, “A fast hybrid field-circuit simulator for transient analysis of microwave circuits,” *IEEE Transactions on Microwave Theory and Techniques*, vol. 52, no. 2, pp. 573–583, 2004.

[BALA 05] C. A. Balanis, “Antenna theory: analysis and design,” 3rd ed, John Wiley, 2005.

[BAND 88] J. Bandler and S. Chen, “Circuit optimization: the state of the art,” IEEE Transactions on Microwave Theory and Techniques, vol. 36, no. 2, pp. 424–443, 1988.

[BELO 21] L. Belostotski, A. T. Sutinjo, A. Madanayake, and M. Okoniewski, “Framework for the cosimulation of antenna arrays and receivers,” *IEEE Transactions on Antennas and Propagation*, vol. 69, no. 8, pp. 5090– 5094, 2021.

[BENN 08] P. Benner, L. Feng, and E. B. Rudnyi, “Using the superposition property for model reduction of linear systems with a large number of inputs,” in *Proceedings of the 18th International Symposium on Mathematical Theory of Networks & Systems*. Citeseer, 2008.

[BROW 23a] D. Brown and Y. Rahmat-Samii, "Error vector magnitude as a performance standard for Antennas in the millimeter-wave era: part 1: metric comparisons and measurement concepts," in *IEEE Antennas and Propagation Magazine*, vol. 65, no. 5, pp. 25-34, Oct. 2023.

[BROW 23b] D. Brown and Y. Rahmat-Samii, "Error vector magnitude as a performance standard for antennas in the millimeter-wave era: part 2: modeling, simulation, and measurement methods," in *IEEE Antennas and Propagation Magazine*, vol. 65, no. 6, pp. 10-24, Dec. 2023.

[CAPE 19] M. Capek, L. Jelinek, and M. Gustafsson, “Shape synthesis based on topology sensitivity,” in *IEEE Trans. on Antennas and Propagation*, vol. 67, no. 6, June 2019.

[CAPE 23a] M. Capek, L. Jelinek, P. Kadlec, and M. Gustafsson, “Optimal inverse design based on memetic algorithms – part I: theory and implementation,” *IEEE Transactions on Antennas and Propagation*, vol. 71, no. 11, Nov. 2023.

[CAPE 23b] M. Capek, L. Jelinek, P. Kadlec, M. Gustafsson, “Optimal inverse design based on memetic algorithms – part II: examples and properties,” *IEEE Transactions on Antennas and Propagation*, vol. 17 no. 11, Nov. 2023.

[CHAN 01] F.-S. Chang and K.-L. Wong, “A broadband probe-fed patch antenna with a thickened probe pin,” in APMC 2001. 2001 Asia-Pacific Microwave Conference (Cat. No.01TH8577), vol. 3, 2001, pp. 1247–1250 vol.3.

[CHEN 22] W.-J. Chen, S. Sun, L. Lei, and J. Hu, “A-EFIE with model-order reduction technique for fast analysis of circuit simulation,” *IEEE Microwave and Wireless Components Letters*, vol. 32, no. 10, pp. 1143–1146, 2022.

[DAI 17] Q. I. Dai, H. U. I. Gan, Q. S. Liu, and W. C. Chew, “Characteristic mode and reduced order modeling at low frequencies,” *IEEE Transactions on Components, Packaging and Manufacturing Technology*, vol. 7, no. 5, pp. 669–677, 2017.

[FENG 15] L. Feng, J. G. Korvink, and P. Benner, “A fully adaptive scheme for model order reduction based on moment matching,” IEEE Trans. Compon. Packag. Manuf. Technol., vol. 5, no. 12, pp. 1872–1884, 2015.

[GAN 19] H. H. Gan, Q. I. Dai, T. Xia, Q. Liu, and W. C. Chew, “Reduced-order model with equivalence surface for scattering problems,” *IEEE Antennas and Wireless Propagation Letters*, vol. 18, no. 2, pp. 308–312, 2019.

[GEDE 23] J. Gedeon, E. Hassan, and A. Cal` a Lesina, “Time-domain topology optimization of arbitrary dispersive materials for broadband 3d nanophotonics inverse design,” ACS Photonics, vol. 10, no. 11, pp. 3875–3887, 2023.

[GEUZ 09] C. Geuzaine and J. F. Remacle, “Gmsh: a three-dimensional finite element mesh generator with built-in pre- and post-processing facilities,” International Journal for Numerical Methods in Engineering 79(11), pp. 1309-1331, 2009. Accessed on February 19, 2023.

[GHAS 13] M. Ghassemi, M. Bakr, and N. Sangary, “Antenna design exploiting adjoint sensitivity-based geometry evolution,” IET Microwaves, Antennas & Propagation, vol. 7, no. 4, pp. 268–276, 2013.

[GUO 23] H. Guo and X. Ding, “Topology optimization design of antennas with complex radiation characteristics,” Microwave and Optical Technology Letters, vol. 66, no. 1, p. e33649, 2023.

[HADJ 25] N. Hadjiantoni, D. Feng, M. Navarro-Cía, and S. M. Hanham, “Topological optimization framework for the automated design of 3D printable THz lens antennas,” IEEE Journal on Multiscale and Multiphysics Computational Techniques, vol. 10, pp. 218–226, 2025.

[HAMM 22] A. M. Hammond, A. Oskooi, M. Chen, Z. Lin, S. G. Johnson, and S. E. Ralph, “High-performance hybrid time/frequency-domain topology optimization for large-scale photonics inverse design,” Opt. Express, vol. 30, no. 3, pp. 4467–4491, Jan 2022.

[HAMM 25] A. M. Hammond, A. Oskooi, I. M. Hammond, M. Chen, S. E. Ralph, and S. G. Johnson, “Unifying and accelerating level-set and density-based topology optimization by subpixel-smoothed projection,” Opt. Express, vol. 33, no. 16, pp. 33 620–33 642, Aug 2025.

[HASS 14] E. Hassan, E. Wadbro, and M. Berggren, “Topology optimization of metallic antennas,” IEEE Transactions on Antennas and Propagation, vol. 62, no. 5, pp. 2488–2500, 2014.

[HERS 98] N. Herscovici, "A wide-band single-layer patch antenna," in *IEEE Transactions on Antennas and Propagation*, vol. 46, no. 4, pp. 471-474, April 1998.

[HOCH 14] A. Hochman, J. F. Villena, A. G. Polimeridis, L. M. Silveira, J. K. White, and L. Daniel, “Reduced-order models for electromagnetic scattering problems,” *IEEE Transactions on Antennas and Propagation*, vol. 62, no. 6, pp. 3150–3162, 2014.

[HONG 04] J.-S. G. Hong and M. J. Lancaster, Microstrip filters for RF/microwave applications. John Wiley & Sons, 2004.

[IOAN 21] D. Ioan, G. Ciuprina, and W. H. A. Schilders, “Complexity reduction in electromagnetic systems,” in *Model Order Reduction*, P. Benner, S. Grivet-Talocia, A. Quarteroni, G. Rozza, W. Schilders, and L. M. Silveira, Eds. De Gruyter, 2021, vol. 3, ch. 5, pp. 174–196.

[JIN 19] J.-M. Jin and S. Yan, “Multiphysics modeling in electromagnetics: Technical challenges and potential solutions,” *IEEE Antennas and Propagation Magazine*, vol. 61, no. 2, pp. 14–26, 2019.

[JIN 21] J. Jin, F. Feng, J. Zhang, J. Ma, and Q.-J. Zhang, “Efficient EM topology optimization incorporating advanced matrix Pade ́ via Lanczos and genetic algorithm for microwave design,” *IEEE Transactions on Microwave Theory and Techniques*, vol. 69, no. 8, pp. 3645–3666, 2021.

[JOHN 90] W. A. Johnson, D. R. Wilton, and R. M. Sharpe, “Modelling scattering from and radiation by arbitrary shaped objects with the electric field integral equation triangular surface patch code,” Electromagnetics, 10:1, 41-63, 1990.

[JOHN 99] J. M. Johnson and Y. Rahmat-Samii, “Genetic algorithms and method of moments (GA/MOM) for the design of integrated antennas,” *IEEE Transactions on Antennas and Propagation*, vol. 47, no. 10, 1999.

[KATA 14] J. Kataja, S. Järvenpää, J. I. Toivanen, R. A. E. Mäkinen, and P. Ylä-Oijala, “Shape sensitivity analysis and gradient-based optimization of large structures using MLFMA,” IEEE Transactions on Antennas and Propagation, vol. 62, no. 11, pp. 5610–5618, 2014.

[KHAN 22] M. R. Khan, C. L. Zekios, S. Bhardwaj, and S. V. Georgakopoulos, “Multiobjective fitness functions with nonlinear switching for antenna optimizations,” *IEEE Open Journal of Antennas and Propagation*, 2022.

[KUMA 18] N. Kumar, K. J. Vinoy, and S. Gopalakrishnan, “Improved well- conditioned model order reduction method based on multilevel Krylov subspaces,” *IEEE Microwave and Wireless Components Letters*, vol. 28, no. 12, pp. 1065–1067, 2018.

[LI 14] P. Li, L. J. Jiang, and H. Bağcı, “Cosimulation of electromagnetics- circuit systems exploiting DGTD and MNA,” *IEEE Transactions on Components, Packaging and Manufacturing Technology*, vol. 4, no. 6, pp. 1052–1061, 2014.

[LIM 21] J. G. Lim, H. Yu, E. Traore, M. Almoneer, J. Xia, and S. Boumaiza, "Modulated-signal-based EM/RF/DSP co-simulation framework for predictive analysis of fully digital MIMO transmitters," in *2021 51st European Microwave Conference (EuMC)*, 2022, pp. 454–457.

[LUCC 22] F. Lucchini, R. Torchio, V. Cirimele, P. Alotto, and P. Bettini, "Topology optimization for electromagnetics: A survey," IEEE Access, vol. 10, pp. 98 593–98 611, 2022.

[MAKA 02] S. N. Makarov, "Receiving antenna: the scattering algorithm," in *Antenna and EM Modelling with MATLAB*, 2002, pp. 18.

[MARZ 22] L. Marzall and Z. Popović, "Nonlinear co-simulations for transmit broadband phased arrays," in *2022 IEEE International Symposium on Antennas and Propagation and USNC-URSI Radio Science Meeting (AP-S/URSI)*, 2022, pp. 133–134.

[MOHA 22] A. E. A. M. Mohammed, "A new physical shape synthesis method for planar microwave circuits," Ph.D. dissertation, Université d'Ottawa/University of Ottawa, 2022.

[MOLE 18] S. Molesky, Z. Lin, A. Y. Piggott, W. Jin, J. Vuckovi´ c, and A. W. Rodriguez, "Inverse design in nanophotonics," Nature Photonics, vol. 12, no. 11, pp. 659–670, 2018.

[NAJM 10] F. N. Najm, "Circuit simulation," 2010.

[NALL 19] S. N. Nallandhigal and K. Wu, "Unified and integrated circuit antenna in front end—a proof of concept," *IEEE Transactions on Microwave Theory and Techniques*, vol. 67, no. 1, pp. 347–364, 2019.

[NARV 21] Narval. https://docs.alliancecan.ca/wiki/Narval/en. 2021.

[NIKO 04] N. Nikolova, J. Bandler, and M. Bakr, "Adjoint techniques for sensitivity analysis in high-frequency structure CAD," IEEE Transactions on Microwave Theory and Techniques, vol. 52, no. 1, pp. 403–419, 2004.

[NIKO 06] N. Nikolova, J. Zhu, D. Li, M. Bakr, and J. Bandler, "Sensitivity analysis of network parameters with electromagnetic frequency-domain simulators," IEEE Transactions on Microwave Theory and Techniques, vol. 54, no. 2, pp. 670–681, 2006.

[NOUR 13a] B. Nouri, M. S. Nakhla, and R. Achar, "Efficient reduced-order macromodels of massively coupled interconnect structures via clustering," *IEEE Trans. on Compon., Packag. and Manuf. Technol.*, vol. 3, no. 5, May 2013.

[NOUR 13b] B. Nouri, M. S. Nakhla, and R. Achar, "Optimum order estimation of reduced macromodels based on a geometric approach for projection-based MOR methods," in IEEE Transactions on Components, Packaging and Manufacturing Technology, vol. 3, no. 7, pp. 1218-1227, July 2013.

[NOUR 14] S. B. Nouri, "Advanced model-order reduction techniques for large-scale dynamical systems," Ottawa-Carleton Institutes for Electrical and Computer Engineering, Carleton University, 2014.

[NOUR 20] B. Nouri, E. Gad, M. Nakhla, and R. Achar, "Model order reduction in microelectronics," *Model Oreder Reduction, Volume 3, Applications*, pp. 111-143, De Gruyter, 2020.

[PAN 92] S.-G. Pan and I. Wolff, "Computation of mutual coupling between slot-coupled microstrip patches in a finite array," *IEEE Transactions on Antennas and Propagation*, vol. 40, no. 9, pp. 1047-1053, 1992.

[PETE 97] A. F. Peterson, S. L. Ray, R. Mittra, "Computational methods for electromagnetics," *Vol. 4*. John Wiley & Sons.

[PETE 07] A. F. Peterson and C. A. Balanis, "Antenna modeling using integral equations and the method of moments." In *Modern Antenna Handbook*, pp. 1461-1494, 2007.

[PRES 92] W. H. Press, S. A. Teukolsky, W. T. Vetterling, and B. P. Flannery, "Numerical recipes in C," 2nd ed, 1992.

[RAO 82] S. M. Rao, D. R. Wilton, and A. W. Glisson, "Electromagnetic scattering by surfaces of arbitrary shape," in IEEE Transactions on Antennas and Propagation, vol. AP-30, no. 3, 1982.

[SUN 21] L. Sun, Y. Li, and Z. Zhang, "Decoupling between extremely closely spaced patch antennas by mode cancellation method," IEEE Transactions on Antennas and Propagation, vol. 69, no. 6, pp. 3074–3083, 2021.

[THOR 05] B. Thors, H. Steyskal, and H. Holter, "Broad-band fragmented aperture phased array element design using genetic algorithms," IEEE Transactions on Antennas and Propagation, vol. 53, no. 10, pp. 3280–3287, 2005.

[TOIV 10] J. I. Toivanen, R. Mäkinen, J. Rahola, S. Järvenpä, and P. Ylä-Oijala, "Gradient-based shape optimisation of ultra-wideband antennas parameterised using splines," IET microwaves, antennas & propagation, vol. 4, no. 9, pp. 1406–1414, 2010.

[TREF 20] Trefethen, L. N., & Society for Industrial and Applied Mathematics, publisher. (2020). *Approximation theory and approximation practice* (Extended edition.). Society for Industrial and Applied Mathematics SIAM, 3600 Market Street, Floor 6, Philadelphia, PA 19104.

[TRIV 20] P. Triverio, "Vector Fitting", *Model Order Reduction, Volume 1, System- and Data-Driven Methods and Algorithms*, pp. 275-310, De Gruyter, 2020.

[TUCE 23] J. Tucek, M. Capek, L. Jelinek, and O. Sigmund, "Density-based topology optimization in method of moments: Q-factor minimization," IEEE Transactions on Antennas and Propagation, vol. 71, no. 12, pp. 9738–9751, 2023.

[TUCE 24] J. Tucek, M. Capek, and L. Jelinek, "Preliminary study on gain maximization via density-based topology optimization," in 18th European Conference on Antennas and Propagation (EuCAP), Glasgow, UK, Mar. 2024.

[TUCE 25] J. Tucek, "Private communication," Czech Technical University, Prague, Czech Republic, private Communication.

[VISS 12] H. J. Visser, "Antenna theory and applications," John Wiley & Sons, 2012.

[WANG 09] R. Wang and J.-M.Jin, "Incorporation of multiport lumped networks into the hybrid time-domain finite-element analysis," *IEEE Transactions on Microwave Theory and Techniques*, vol. 57, no. 8, pp. 2030–2037, 2009.

[WANG 17] J. Wang, X.-S. Yang, X. Ding, and B.-Z. Wang, "Antenna radiation characteristics optimization by a hybrid topological method," IEEE Transactions on Antennas and Propagation, vol. 65, no. 6, pp. 2843–2854, 2017.

[WANG 25] L-L. Wang and X-S. Yang, "Adjoint sensitivity analysis based on well-conditioned asymptotic waveform evaluation for broadband antenna topology optimization acceleration," *IEEE Transactions on Antennas and Propagation*, vol. 73, no. 1, Jan. 2025.

[WARN 18] K. F. Warnick, R. Maaskant, M. V. Ivashina, D. B. Davidson, and B. D. Jeffs, "Phased arrays for radio astronomy, remote sensing, and satellite communications." Cambridge University Press, 2018.

[WATA 21] A. O. Watanabe, M. Ali, S. Y. B. Sayeed, R. R. Tummala, and M. R. Pulugurtha, "A review of 5G front-end systems package integration," *IEEE Transactions on Components, Packaging and Manufacturing Technology*, vol. 11, no. 1, pp. 118–133, 2021.

[WEIL 01] D. Weile, E. Michielssen, and K. Gallivan, "Reduced-order modeling of multiscreen frequency-selective surfaces using krylov-based rational interpolation," *IEEE Transactions on Antennas and Propagation*, vol. 49, no. 5, pp. 801–813, 2001.

[WHIT 22] E. B. Whiting, G. Mackertich-Sengerdy, S. D. Campbell, S. Soltani, M. P. Haack, J. P. Barrett, J. W. Withrow, J. A. Bossard, and D. H. Werner, "Adjoint sensitivity optimization of three-dimensional directivity-enhancing, size-reducing GRIN lenses," IEEE Antennas and Wireless Propagation Letters, vol. 21, no. 11, pp. 2166–2170, 2022.

[YANG 08] S. Yang, K.-F. Lee, A. Kishk, and K.-M. Luk, "Design and study of wideband single feed circularly polarized microstrip antennas," Progress In Electromagnetics Research, vol. 80, pp. 45–61, 2008.

[YILM 05] A. Yilmaz, J.-M. Jin, and E. Michielssen, "A parallel FFT accelerated transient field-circuit simulator," *IEEE Transactions on Microwave The- ory and Techniques*, vol. 53, no. 9, pp. 2851–2865, 2005.

[ZHAN 16] H. H. Zhang, L. J. Jiang, and H. M. Yao, "Embedding the behavior macromodel into tdie for transient field-circuit simulations," *IEEE Transactions on Antennas and Propagation*, vol. 64, no. 7, pp. 3233– 3238, 2016.

[ZHAN 22a] T. Zhang, H. Bao, P. Gu, D. Ding, D. H. Werner, and R. Chen, "An arbitrary high-order DGTD method with local time-stepping for nonlinear field-circuit cosimulation," *IEEE Transactions on Antennas and Propagation*, vol. 70, no. 1, pp. 526–535, 2022.

[ZHAN 22b] Y. P. Zhang, "Antenna and array technologies for future wireless ecosystems," in *Antenna-in-Package Design for Wireless System on a Chip*, Y. J. Guo and R. W. Ziolkowski, Eds. Wiley Online Library, 2022.

APPENDIX A – Edge Removal

The subtractive-mask shaping algorithm allows for the removal of basis functions enclosed within a rectangle, an ellipse, or a triangle superimposed on the antenna geometry regardless of its orientation. Each shape is defined based on the midpoint of a triangle in the mesh and two dimensions.

A-1. Rectangle Removal

The genetic algorithm produces first an index corresponding to the center of a triangle in the mesh. This point is used as the center of the rectangle. Since the index indicates the triangle number, the coordinates of the vertices of the triangle that contains this centroid are known. From these coordinates, two vectors $\bar{v}_1$ and $\bar{v}_2$ can be constructed coinciding with two edges of the mesh triangle. The cross product of these vectors thus yields a vector $\bar{n}$ normal to the plane containing the triangle. The rectangle is defined surrounding the midpoint of the triangle by four corners as is depicted in Figure A-1. The coordinates of a particular corner can be determined by solving for the translation vector $\bar{t}$. Since the orientation of the plane containing the mesh triangle is not restricted in any way, $\bar{t}$ in general will have components t_x, t_y, and t_z.

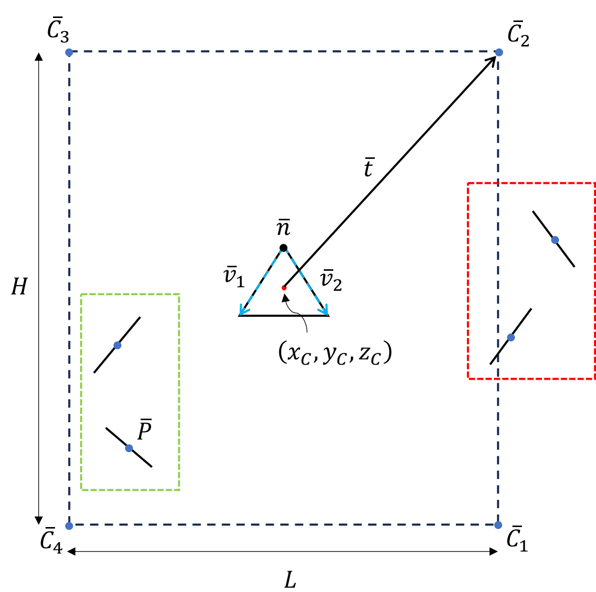

Figure A-1. Example of a removal rectangle centred around a mesh triangle. The green box shows examples of edges which would be removed while the red box shows examples of edges which would not be removed.

Solving for the components of $\bar{t}$ requires three equations. Firstly, the magnitude of $\bar{t}$ is known given that the dimensions of the rectangle are known.

$$|\bar{t}| = \sqrt{\left(\frac{L}{2}\right)^2 + \left(\frac{H}{2}\right)^2} = \sqrt{t_x{}^2 + t_y{}^2 + t_z{}^2} \tag{A-1}$$

Furthermore, since the corners must lie in the same plane as the mesh triangle,

$$\bar{t} \cdot \bar{n} = t_x n_x + t_y n_y + t_z n_z = 0. \tag{A-2}$$

Finally, since the genetic algorithm does not provide an orientation for the rectangle (how it is angled with respect to some axis), the third equation must define one of the components of the translation vector directly. In this case, the selection is as follows.

$$t_x = \frac{L}{2} \tag{A-3}$$

It is important to note that this selection will only work if the plane in which the rectangle is on is not parallel to the y-z plane or on a plane that was parallel to the y-z plane but has been tilted in the x direction. It is evident that in these situations, t_x must either be zero or a specific value that corresponds to the tilt of the plane which is likely not exactly the distance in (A-3). In such cases no real solution for the translation vector exists. As such, if no real solution is detected, (A-3) is changed to either

$$t_y = \frac{L}{2} \tag{A-4}$$

or

$$t_z = \frac{L}{2}. \tag{A-5}$$

Solving equations (A-1), (A-2), and one of (A-3)-(A-5) will yield two solutions for the components of the translation vector corresponding to two of the rectangle's corners. The translation vectors corresponding to the other two corners are found by solving the same system of equations however with the negative of (A-3)-(A-5). The coordinates of the four corners are then calculated as follows where $\bar{P}_C$ is a vector from the origin to the midpoint of the triangle and $\bar{C}_i$ are vectors from the origin to each of the rectangle's corners.

$$\bar{C}_1 = \bar{P}_C + \bar{t}_1 \tag{A-6}$$

$$\bar{C}_2 = \bar{P}_C + \bar{t}_2 \tag{A-7}$$

$$\bar{C}_3 = \bar{P}_C + \bar{t}_3 \tag{A-8}$$

$$\bar{C}_4 = \bar{P}_C + \bar{t}_4 \tag{A-9}$$

Once the corners of the rectangle are known, the endpoints of an edge are determined to be within the rectangle if the sum of the area of four triangles formed by connecting each neighbouring corner pair to an endpoint, respectively, equals the total area of the rectangle. If the edge is outside of the triangle, the sum of the areas will be greater than the area of the rectangle. The areas of the four triangles are easily found as follows considering as an example the triangle formed between points at the ends of vectors $\bar{C}_3$, $\bar{C}_4$, and $\bar{P}$ in Figure A-1.

$$Area = \frac{1}{2}|(\bar{P} - \bar{C}_3) \times (\bar{C}_4 - \bar{C}_3)| \tag{A-10}$$

A-2. Ellipse Removal

When removing edges within an ellipse, the ellipse is defined by the genetic algorithm which again produces a midpoint of a triangle in the mesh, as well as two dimensions, which in this case correspond to the major and minor axes of the ellipse. Similar to the case of the rectangle, the midpoint of the mesh triangle is taken to also be the midpoint of the ellipse. Like in the previous section, from the coordinates of the mesh triangle vertices, two vectors $\bar{v}_1$ and $\bar{v}_2$ can be constructed. Their cross product then yields a vector $\bar{n}$ normal to the plane containing the triangle. If the following inequality is true, then it is known that a point (x, y) lies within the ellipse, where A and B are the major and minor axes lengths respectively.

$$\frac{x^2}{A} + \frac{y^2}{B} \leq 1 \tag{A-11}$$

The equation of the ellipse above is clearly only applicable for an ellipse which lies in the x-y plane. Since the ellipse in this case can be superimposed on a plane oriented in any way, a local coordinate system is defined such that the ellipse always lies in the x'-y' plane of the local coordinate system (that with the primed notation). The edge endpoints that are to be tested can then be converted from the global coordinate system to the local coordinate system of the ellipse allowing for (A-11) to be used. Figure A-2 shows an example of said situation. The local cartesian coordinate system must be defined by three unit vectors in terms of the global coordinate system. Since the ellipse must lie in the x'-y' plane, the unit vector in the z' direction can simply be taken in the direction of $\bar{n}$. The unit vector in the x' or y' direction must be in the plane of the mesh triangle, therefore it is arbitrarily chosen that

$$\hat{x}' = \frac{\bar{T}_1 - \bar{P}_C}{|\bar{T}_1 - \bar{P}_C|} \tag{A-12}$$

where $\bar{T}_1$ is a vector spanning from the origin of the global coordinate system to one of the vertices of the mesh triangle and $\bar{P}_C$ is a vector spanning from the origin of the global coordinate system to the midpoint of the mesh triangle. The unit vector in the y' direction $\hat{y}'$ can then be found by taking the cross product of $\hat{x}'$ and $\hat{z}'$.

Any point in the global coordinate system (x, y, z) can then by converted to a point in the local coordinate system of the ellipse (x', y', z') using the following relationship,

$$\begin{bmatrix} x' \\ y' \\ z' \end{bmatrix} = \begin{bmatrix} x'_x & x'_y & x'_z \\ y'_x & y'_y & y'_z \\ z'_x & z'_y & z'_z \end{bmatrix} \begin{bmatrix} x - x_C \\ y - y_C \\ z - z_C \end{bmatrix} \tag{A-13}$$

where the 3×3 matrix contains the global x, y, and z components of the local unit vectors. The coordinate pair (x', y') can then be inserted into (A-11) to verify whether an edge endpoint is within the ellipse. Since (A-11) has no z' dependence, it must also be checked that the point lies in the same plane as the ellipse. This is the case if $z' = 0$.

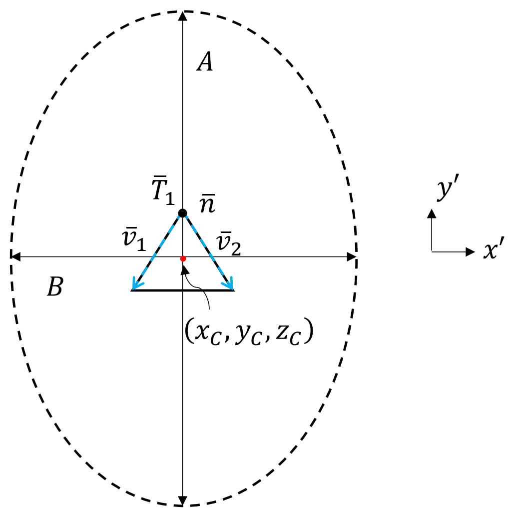

Figure A-2. Example of a removal ellipse centred around a mesh triangle.

A-3. Triangle Removal

When the genetic algorithm decides to remove a triangular shape, it defines said triangle again by the midpoint of a mesh triangle as well as two dimensions. Unlike with the two previous shapes, the midpoint of the mesh triangle does not need to be the midpoint of the removal triangle. The two dimensions that the genetic algorithm provides are two of the triangles side lengths. Again, from the vertices of the mesh triangle, two vectors $\bar{v}_1$ and $\bar{v}_2$ can be constructed. The angle between these vectors can be computed as follows.

$$\theta = cos^{-1}\left(\frac{\bar{v}_1 \cdot \bar{v}_2}{|\bar{v}_1||\bar{v}_2|}\right) \tag{A-14}$$

Cosine law can then be used to determine the length of the third side of the triangle *c*, where *a* and *b* are those given by the genetic algorithm.

$$c = \sqrt{a^2 + b^2 - 2ab\cos\theta} \tag{A-15}$$

Figure A-3 shows an example of the situation described in this section. Since θ is computed from the mesh triangle, it is being taken that one angle of the removal triangle is the same as that of the mesh triangle. The length of the median AM taken from the vertex with the common angle θ can be computed as follows.

$$AM = \sqrt{\frac{2a^2 + 2b^2 - c^2}{4}} \tag{A-16}$$

A translation vector $\bar{t}$ must now be constructed in order to determine the location of one of the vertices of the removal triangle. Since the removal triangle could theoretically be placed in any orientation surrounding the mesh triangle, an assumption regarding its orientation will have to be made. It is thus taken that the distance between the common angle vertices of the removal and mesh triangle are equal to the distance of the longer segment of the median if the centroid of the triangle was the midpoint of the mesh triangle. This distance *d* could then be calculated as follows.

$$d = \frac{2}{3}AM \tag{A-17}$$

Since the vertex A of the removal rectangle is aligned with the midpoint of the mesh triangle and one of the vertices of the mesh triangle, a unit vector $\hat{u}$ pointing in the direction of the midpoint of the mesh triangle to said mesh triangle vertex would also be pointing in the direction of vertex A. Since all points of the mesh triangle are known this unit vector is easily constructed. The translation vector and subsequently the coordinates of vertex A can then be found.

$$\bar{t} = d\hat{u} \tag{A-18}$$

$$\bar{A} = \bar{P}_C + \bar{t} \tag{A-19}$$

The coordinates of vertices B and C can then be found from vertex A knowing that AB and AC are directed in the same way as $\bar{v}_1$ and $\bar{v}_2$ respectively.

$$\bar{B} = \bar{A} + b\hat{v}_1 \tag{A-20}$$

$$\bar{C} = \bar{A} + a\hat{v}_2 \tag{A-21}$$

With the coordinates of the triangle now known, the same method used for the rectangle removal to determine whether a point is inside the triangle or not can be applied here. In this case, if a point is inside the triangle, then the sum of the area of three triangles formed by connecting each neighbouring corner pair to that point, respectively, will equal the total area of the triangle. If the edge is outside of the triangle, the sum of the areas will be greater than the area of the triangle. The areas of these three triangles can be found in the same way as described in (A-10). The total area of the removal triangle can be found as

$$Area = \frac{1}{4}\sqrt{4a^2b^2 - (a^2 + b^2 - c^2)^2} \tag{A-22}$$

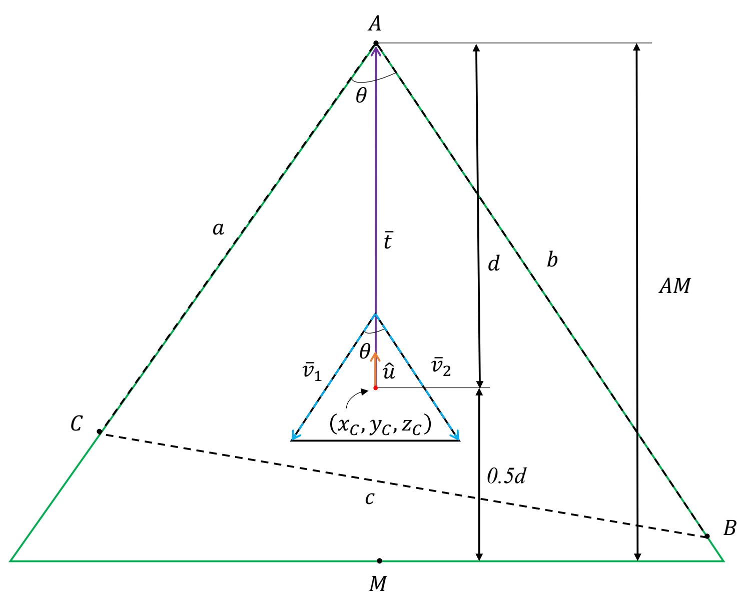

Figure A-3. Example of a triangle removal described in this section. The black dashed triangle is the general removal triangle with unequal edges, while the green triangle is one which has the midpoint of the mesh triangle as its centroid.